

Measurement of the Z boson cross-section in the dimuon channel in pp collisions at $\sqrt{s} = 7$ TeV

A dissertation presented

by

Lashkar Mohammad Kashif

to

The Department of Physics

in partial fulfillment of the requirements

for the degree of

Doctor of Philosophy

in the subject of

Physics

Harvard University

Cambridge, Massachusetts

November 2010

©2010 - Lashkar Mohammad Kashif

All rights reserved.

Thesis advisor
Professor John Huth

Author
Lashkar Mohammad Kashif

Measurement of the Z boson cross-section in the dimuon channel in pp collisions at $\sqrt{s} = 7$ TeV

Abstract

We measure the production cross-section of the Z boson in the dimuon decay channel in pp collisions at $\sqrt{s} = 7$ TeV. The measurement is based on data collected by the ATLAS experiment at the CERN Large Hadron Collider between April and July 2010. The amount of data collected was 331 nb^{-1} , containing 109 Z boson candidates decaying to muons. The background level for our measurement is very small, which we estimate using Monte Carlo simulation. We use data-driven techniques to extract experimental efficiencies as well as the muon momentum scale and resolution. We measure $\sigma_{Z/\gamma^*} \times BR(Z/\gamma^* \rightarrow \mu^+\mu^-) = 0.87 \pm 0.08$ (stat) ± 0.05 (sys) ± 0.10 (lum) nb, which is in agreement with the Standard Model expectation at next-to-next-to-leading-order accuracy in QCD.

Contents

Title Page	i
Abstract	iii
Table of Contents	iv
List of Figures	viii
List of Tables	xi
Acknowledgments	xiii
1 Introduction and Theoretical Overview	1
1.1 Introduction	1
1.2 The Standard Model	4
1.2.1 The Higgs mechanism	6
1.3 Proton-proton collisions and Z boson production at the LHC	8
1.3.1 Internal structure of a proton and parton distributions functions	8
1.3.2 Renormalization of the strong coupling	11
1.3.3 QCD hard scattering and factorization	12
1.3.4 Hadronization	15
1.4 Z boson production at the LHC	16
1.5 Current state of theoretical calculation of the Z cross-section	19
1.5.1 Sources of theoretical errors	22
1.5.2 Current status of PDFs	26
1.5.3 PDF measurements in ATLAS	28
1.5.4 Overall theoretical error in Z cross-section and acceptance	31
1.5.5 Summary	33
2 The Accelerator and the Experiment	34
2.1 The Large Hadron Collider	34
2.2 A Toroidal LHC Apparatus (ATLAS)	36
2.2.1 The magnet system	38
2.2.2 The Inner Detector (ID)	41
The Pixel Detector	41
The Semiconductor Detector (SCT)	43
The Transition Radiation Tracker (TRT)	43

2.2.3	The Calorimetry	45
	The Liquid Argon (LAr) Electromagnetic Calorimeter	45
	The Hadronic Calorimeter	49
	The Liquid Argon Forward Calorimeter	50
2.2.4	The Muon Spectrometer	51
	Precision measurement technologies	53
	Trigger technologies	55
	Magnetic field in the muon system	60
	Alignment of muon chambers	61
2.2.5	Trigger and Data Acquisition System (TDAQ)	62
3	Luminosity Measurement at the LHC and in ATLAS	66
3.1	Luminosity measurement using beam parameters	67
3.1.1	Crossing angle	69
3.1.2	Offset beams with finite crossing angle	70
3.1.3	Hourglass effect	71
3.2	Determination of beam parameters relevant to luminosity measurement	72
3.2.1	Beam current measurement at the LHC	72
3.2.2	Beam size measurement using Van der Meer scans	75
3.2.3	Beam profile measurement	76
3.2.4	Beam position monitors	80
3.2.5	The BRAN detectors for relative luminosity measurement	82
3.3	Luminosity monitoring in ATLAS	83
3.3.1	ALFA	84
3.3.2	LUCID	88
3.3.3	BCM	90
3.3.4	Offline relative luminosity monitoring in ATLAS	91
3.3.5	Summary	93
4	Data Collection and Event Reconstruction	94
4.1	Data Collection and Integrated Luminosity	94
4.2	Event Reconstruction in ATLAS	95
4.2.1	Reconstruction in the Inner Detector	97
	Inside-out track reconstruction	98
	Outside-in track reconstruction	100
	TRT-only track reconstruction	100
	Vertex reconstruction	101
	Reconstruction of photon conversions	105
	Beamline reconstruction	106
	Electron reconstruction in the inner detector	109
4.2.2	Reconstruction in the Calorimeters	111
	Jet reconstruction	114

	Electron reconstruction in the calorimeter	120
	Photon reconstruction in the calorimeter	121
	Reconstruction of missing transverse energy	122
4.2.3	Reconstruction in the Muon Spectrometer	124
	Standalone muon reconstruction	125
	Combined muon reconstruction	134
	Inner detector based muon tagging	136
	Calorimeter-based muon tagging	137
4.2.4	Efficiencies in the muon system	138
	Drift tube efficiency	139
	Reconstruction efficiency of combined muon tracks	143
5	Monte Carlo Simulation	152
5.1	Overview of Monte Carlo event generation and simulation	152
5.2	Monte Carlo generators used in this analysis	154
5.2.1	Pythia	154
5.2.2	POWHEG	155
5.2.3	FEWZ	156
5.2.4	Monte Carlo samples used in this analysis	157
5.2.5	The ATLAS detector simulation	157
6	Event Selection	160
6.1	Z event selection	160
6.1.1	Properties of the preselected sample	165
	Hit distributions	165
	Kinematic distributions	171
6.2	Z signal acceptance and efficiencies	171
6.2.1	Monte Carlo event reweighting owing to pile-up	174
6.2.2	Acceptance of Z selection from Monte Carlo cutflow	175
6.2.3	Factorizing the acceptance: A_Z and C_Z	177
	Fiducial acceptance A_Z	177
	Event detection efficiency C_Z	178
6.2.4	Estimation of efficiency scale factors	180
	Trigger efficiency for single muons	180
	Trigger efficiency and scale factor for $Z \rightarrow \mu\mu$ events	185
	Reconstruction efficiency and scale factor for $Z \rightarrow \mu\mu$ events	188
6.2.5	Muon momentum scale and resolution	189
	Muon momentum scale and resolution from cosmic events	192
	Effect of momentum scale and resolution on $Z \rightarrow \mu\mu$ acceptance	199
6.2.6	Isolation cut efficiency for $Z \rightarrow \mu\mu$ events	200
6.2.7	Theoretical uncertainty on C_Z	202
6.2.8	Summary of systematic uncertainties	202

6.2.9	Summary of acceptance and efficiency	203
6.2.10	Decomposition of C_Z	204
7	Background Estimation	207
7.1	QCD background	208
7.1.1	Data-driven QCD background estimation	208
	Exponential fit to the $M_{\mu\mu}$ distribution	208
	Template fitting with 3.37 pb^{-1}	209
7.2	Electroweak backgrounds	217
7.2.1	$t\bar{t}$ background	217
7.2.2	$Z \rightarrow \tau\tau$ background	218
7.2.3	$W \rightarrow \mu\nu$ backgrounds	218
7.3	Cosmic ray background	219
7.4	Summary of backgrounds	222
8	Properties of Z bosons and measurement of $Z \rightarrow \mu\mu$ cross-section	223
8.1	Z candidate events	223
8.1.1	Properties of $Z \rightarrow \mu\mu$ events	224
	Hit distributions	225
	Kinematic distributions	227
8.1.2	Fitting the Z peak and extraction of Z mass resolution	228
8.2	Cross-section measurement	234
9	Discussion and Outlook	235
9.1	Comparison with theoretical prediction	235
9.2	Outlook	238
A	Event list	244
B	Comparison of muon curvature in cosmic events	248
	Bibliography	250

List of Figures

1.1	Proton structure	9
1.2	PDF fits	10
1.3	Schematic structure of a hard scattering process.	13
1.4	Z boson production	17
1.5	Higher-order Z production	17
1.6	Production cross-sections at the LHC and the Tevatron	18
1.7	Flavor decomposition in Z production	20
1.8	Z p_T comparison	25
1.9	W/Z cross-section comparison	29
2.1	Schematic of the CERN accelerator complex.	35
2.2	Cutaway view of the ATLAS detector	38
2.3	Schematic of the ATLAS magnet system	40
2.4	Cutaway view of the ATLAS inner detector	42
2.5	Structure of the ATLAS calorimetry	46
2.6	Schematic of a liquid argon barrel module	48
2.7	Structure of the ATLAS forward calorimeter	50
2.8	Cutaway view of the ATLAS muon system	52
2.9	Structure of a barrel MDT chamber	54
2.10	Schematic of a muon drift tube	55
2.11	rz view of the ATLAS muon system	57
2.12	Schematic of the ATLAS muon trigger system	59
2.13	Block diagram of ATLAS TDAQ system	64
3.1	Schematic view of two bunches colliding at a non-zero crossing angle.	69
3.2	Illustration of the hourglass effect	71
3.3	Operating principle of a fast beam current transformer.	73
3.4	Vertex rate in Van der Meer scan	75
3.5	Beam size measurement using OTR	77
3.6	LHC beam on scintillator screen	78
3.7	Configuration of beam profile monitors	79

3.8	Button pickups	81
3.9	TAN absorber and BRAN monitors at Point 5	82
3.10	Elastic scattering cross-sections	85
3.11	Roman Pot concept	86
3.12	ATLAS Roman Pot unit	87
3.13	LUCID configuration	88
3.14	BCM stations	91
3.15	BCM configuration	92
4.1	Integrated luminosity	96
4.2	Track seeds per event	99
4.3	Vertex topologies	102
4.4	Vertex resolution	103
4.5	Conversion radius of photon conversions	107
4.6	Distribution of primary vertices	108
4.7	QCD event with four jets	117
4.8	Flowchart of jet reconstruction	119
4.9	Moore flowchart	126
4.10	MDT segment building	129
4.11	Muon segment addition	131
4.12	Efficiency vs drift radius in MDT tube	141
4.13	Overall efficiency of MDT tubes	142
4.14	Muon reco efficiency from MS hit method	145
4.15	Tag-probe schematic	148
4.16	Muon reco efficiency from tag-probe method	150
6.1	Background vs signal efficiency for isolation cut	165
6.2	MDT hits/track at preselection	166
6.3	RPC hits/track at preselection	168
6.4	TGC hits/track at preselection	169
6.5	Pixel hits/track at preselection	170
6.6	SCT and TRT hits/track at preselection	171
6.7	Muon kinematics at preselection	172
6.8	Track isolation and invariant mass at preselection	173
6.9	Vertex distribution	175
6.10	L1_MU6 trigger efficiency vs p_T	183
6.11	L1_MU6 trigger efficiency vs η	183
6.12	L1_MU6 trigger efficiency vs ϕ	184
6.13	Momentum scale and resolution	191
6.14	Scale and resolution in barrel and endcap	192
6.15	MS-ID momentum resolution fits on cosmics (positive tracks)	195
6.16	MS-ID momentum resolution fits on cosmics (negative tracks)	196

6.17	Muon p_T scale from cosmics	198
6.18	Muon p_T resolution from cosmics	198
6.19	p_T distribution of muons with and without smearing	200
7.1	Invariant mass spectrum in data after high- p_T selection	210
7.2	invariant mass spectra for isolated and non-isolated muons	211
7.3	Template fit for QCD background estimation	212
7.4	Ensemble test results	214
7.5	χ^2 distributions from ensemble test	215
7.6	Input vs measured QCD fraction	217
8.1	MDT hits/track after Z selection	225
8.2	RPC hits/track after Z selection	226
8.3	TGC hits/track after Z selection	226
8.4	Pixel hits/track after Z selection	227
8.5	SCT and TRT hits/track after Z selection	228
8.6	Muon kinematics after Z selection	229
8.7	Muon p_T vs invariant mass	230
8.8	Track isolation and invariant mass	230
8.9	Invariant mass in various regions	231
8.10	Z p_T and rapidity	232
8.11	Mass fit	233
9.1	Cross-section measured vs predicted	238
9.2	Cross-section vs CM energy	239
9.3	Mass fit 3pb	240
9.4	Muon kinematics 3 pb	242
9.5	Muon p_T vs invariant mass 3 pb	243
9.6	Z p_T and rapidity 3 pb	243
B.1	Muon curvature in cosmic events	249

List of Tables

1.1	Theoretical uncertainties in W/Z cross-section	32
2.1	Design parameters of the Large Hadron Collider.	36
2.2	Beam parameters of the Large Hadron Collider	36
4.1	Integrated luminosity in run periods	95
4.2	Event selection in MS hit method for muon reco efficiency	144
4.3	Prompt muon fractions using template fit	146
4.4	Muon reco efficiency using factorized method	147
4.5	Final results for MS hit method	147
4.6	Tag-probe selection for muon reco efficiency	149
4.7	Final results from tag-probe method	151
5.1	Monte Carlo samples used in analysis	158
6.1	Event selection for Z candidates.	162
6.2	Vertex weights	176
6.3	Selection cutflow on $Z \rightarrow \mu\mu$ MC	176
6.4	Summary of geometrical acceptance values	179
6.5	Selection cuts for trigger efficiency	180
6.6	Trigger systematics	185
6.7	Final results for trigger efficiency	185
6.8	Z events in barrel and endcap	187
6.9	Event trigger efficiencies in barrel and endcap	187
6.10	Trigger efficiency scale factor for $Z \rightarrow \mu\mu$ events with errors.	188
6.11	Reconstruction efficiency scale factor for $Z \rightarrow \mu\mu$ events with errors.	189
6.12	Measured scale and resolution parameters	192
6.13	Result of the p_T resolution fits on cosmic events	197
6.14	Selection cuts for isolation efficiency using tag-probe	201
6.15	Measured isolation cut efficiency	202
6.16	Systematic uncertainties on $Z \rightarrow \mu\mu$ acceptance	203
6.17	Total and factorized acceptances for Z events	203

6.18	Decomposition of C_Z	206
7.1	Input and measured QCD fractions in ensemble tests	216
7.2	Cutflow in unpaired bunch crossings	221
7.3	Background summary	222
8.1	Z selection cutflow on the data.	224
8.2	Event summary	224
8.3	Mass fit parameters	232
8.4	Cross-sections	234
9.1	Theoretical cross-sections	236
9.2	Theoretical uncertainties studied	237
9.3	Fit parameters 3 pb	240
A.1	Z candidate list	245
A.2	Z candidate list <i>cont'd.</i>	246
A.3	Z candidate list <i>cont'd.</i>	247

Acknowledgments

I wish to express my gratitude to the many physicists in the W/Z subgroup of the Standard Model group, and in particular of the W/Z with *Muons* working group, for the fast and efficient work they did which led to the submission of the cross-section measurement paper within half a year of first 7 TeV collisions. In particular, I thank the individuals who calculated the muon reconstruction and trigger efficiencies, the muon momentum scale and resolution, and the theoretical acceptance. I use their results in this thesis.

My advisor Prof. John Huth has been a tower of strength and support over the years. He had time to sit down with me and talk whenever needed; I have learnt much from his insight into physics, particularly about details of QCD which is essential know-how for anyone working at a hadron collider. But more importantly, he provided necessary moral support as the LHC schedule got pushed back over and over again. This thesis would not have been written without John's continuing encouragement. In the middle of all this, he also gave me great advice on running.

I am very specially indebted to Prof. Guimaraes da Costa, who tirelessly egged me on with my analysis from the time we had first data. Without his frequent comment of '*So you think you're done?*', I might not have been...done.

Profs. Franklin and Morii have given me good advice on my work on many occasions and helped me learn how to think critically. I am grateful to them, and to George Brandenburg for his aid with the analysis for my qualifying exam. Prof. Black, while a post-doc in the Harvard group, assisted me on countless occasions with physics insights as well as code debugging. The other post-docs in the group, specifically Alberto and Corrinne, answered my physics questions and helped with technical issues at many points during the analysis. Alberto, in addition, provided essential respite by pointing me to guitar works by Jeff Loomis, whom I liked, and Paco de Lucia, whom I did not like! Not the least, I want to thank the other students in the group for their fellowship when I needed it.

My collaborations with physicists outside my group have been very instructive over the years. I gained invaluable hardware experience working on muon chamber commissioning under the supervision of Prof. Zhou, Prof. Bensinger and the late Alex Marin. My first major analysis project was with Dan Levin. My former office-

mate Niels van Eldik was seminal in my understanding of how muon reconstruction works. Matthias Schott has been a great friend and colleague over five years; I have borrowed a number of ideas from his graduate work on Z cross-section measurement. My sincere thanks goes to all of these individuals.

Finally, I thank my mother for all her patience, hard work and unfailing emotional support in times good and bad. This thesis is dedicated to her.

Chapter 1

Introduction and Theoretical Overview

1.1 Introduction

The long-awaited Large Hadron Collider (LHC) at CERN is now operational. ATLAS and CMS, the two general-purpose experiments at the LHC, are set up to probe the fundamental laws of physics at the multi-TeV energy scale, corresponding to a distance scale of 10^{-19} m.

The vast amount of experimental data collected by numerous high-energy physics experiments during the 20th century is well explained by the Standard Model of particle physics. Unifying the electromagnetic, the weak and the strong interactions, this theory has stood a wealth of tests over a large range of energy scales. The theory of strong interactions, Quantum Chromodynamics (QCD), has proven more difficult to test precisely than the electroweak theory. Because the strong coupling grows large at small momentum transfers, perturbative calculations become inapplicable at low energies and non-perturbative methods must be used (see Section 1.2 below). Nevertheless, measurements to date have shown no significant divergence from QCD

predictions at the energy scales probed.

In spite of its success, we know that the Standard Model is not the final theory of nature. Unanswered questions from both particle physics and cosmology point to the existence of deeper symmetries and/or dynamic mechanisms that remain to be uncovered (for example, see [33], [36]). Indeed, a major aim of the LHC is to throw light on Beyond the Standard Model (BSM) physics.

Before we can move into the discovery regime, we want to be confident that we can use our detector to observe and measure properties of processes that are already familiar from experiments at other facilities. Such processes include, for example, the W and Z gauge bosons of the Standard Model and the top quark. In this thesis, we measure the production cross-section of the Z gauge boson. We describe the methodology used and present the results obtained for the Z production cross-section in proton-proton collisions at a center-of-mass energy of 7 TeV. The measurements are made on data taken by the ATLAS (A Toroidal LHC ApparatuS) experiment during April-July 2010. We use events in which the Z boson decays into two muons, because these events are easy to separate from various background processes.

The motivations for Z boson observation and cross-section measurement are several:

- **Benchmarking ATLAS:** As mentioned above, before we start looking for new particles and interactions, we must satisfy ourselves that we understand our detector. To this end, we want to rediscover the Standard Model, i.e., reproduce known measurements. Z boson production is a standard ‘benchmark’ process, enabling us to measure reconstruction and trigger efficiencies, detector

resolution, lepton energy scale etc. For example, discrepancies in the width of the observed Z peak from Monte Carlo expectations can point to significant misalignment in various detector components.

- Test of theoretical predictions: QCD corrections substantially modify the total Z cross-section (see [74] for a concise review of QCD corrections). New predictions combining electroweak and QCD corrections are now emerging; these predictions can be tested by comparing with the measured Z cross-section and p_T spectrum.

It is already possible to achieve the above two goals with the dataset used in this analysis. With larger datasets, we can go further:

- Inferring properties of the $Z \rightarrow \nu\nu$ decay: The invisible $Z \rightarrow \nu\nu$ decay is a background to many processes involving missing transverse energy, such as Supersymmetry and extra-dimension models where a graviton escapes into the higher-dimensional ‘bulk’. The $Z \rightarrow \mu\mu$ decay can be used to indirectly measure the rate and properties of the invisible mode.
- Luminosity measurement: Z production can be used as a ‘standard candle’ to monitor and measure luminosity. This requires a precise measurement of the total cross-section and a good understanding of the p_T spectrum.

In the remainder of this chapter, we summarize some relevant aspects of the Standard Model and of proton-proton collisions that must be understood for any analysis at a hadron collider. We also discuss in some depth the current state of

theoretical calculation of W/Z cross-sections. In Chapter 2, we briefly describe the LHC and the various subsystems of the ATLAS detector. Chapter 3 contains a detailed discussion of the measurement of luminosity by the LHC as well as by the ATLAS detector. Details of data collection and event reconstruction can be found in Chapter 4, together with the measurement of muon reconstruction efficiency. Chapter 5 summarizes the Monte Carlo generators and samples we use in the analysis. We discuss Z event selection criteria and related acceptance and efficiencies in Chapter 6. In Chapter 7, we study the principal backgrounds to our signal channel and the procedures adopted to minimize them. In Chapter 8, we show the results of the Z boson selection and the measurement of the Z cross-section. Finally, in Chapter 9, we compare our results with theoretical predictions. In this chapter, we also show properties of Z bosons obtained with a data sample larger than that used for the analysis.

Note that all data distributions shown in this thesis have statistical error bars only unless otherwise specified. The size of the error bars corresponds to a 68.3% confidence interval. Also, the term ‘ $Z \rightarrow \mu\mu$ cross-section’ will refer to the cross-section of Z/γ^* production multiplied by the branching fraction ($Z/\gamma^* \rightarrow \mu^+\mu^-$), unless otherwise stated.

1.2 The Standard Model

The Standard Model of particle physics describes particles and their interactions in terms of at least 19 free parameters [45]. The Model is invariant under local transformations of the gauge group $SU(3)_C \times SU(2)_L \times U(1)_Y$. It contains three

families of quarks and leptons, which are massive spin- $\frac{1}{2}$ fermions, as well as spin-1 (vector) bosons which mediate the electroweak and strong interactions. The Standard Model does not incorporate gravity.

Quantum Electrodynamics (QED), which was developed in the 1940s and 50s, describes electromagnetic interactions in terms of an exchange mechanism [42]. It requires the existence of a massless gauge boson, *i.e.*, the photon. In the 1970s, the electromagnetic interaction was successfully unified with the weak interaction [108], which is mediated by the massive vector bosons W^\pm and Z^0 . The electroweak theory is invariant under $SU(2)_L \times U(1)_Y$ transformations, its couplings being parametrized by two dimensionless constants.

Quantum Chromodynamics, described by the group $SU(3)_C$, contains an octet of massless gluons as force mediators. Unlike the mediators of the electroweak force, gluons can interact among themselves. A consequence of this self-interaction is that the QCD coupling α_s decreases as the energy scale of the interaction increases, leading to the so-called *asymptotic freedom* of the theory [109]. Gluon self-interaction also means that colored objects such as free quarks and gluons cannot be observed; only colorless bound states are experimentally observable.

In the electroweak sector, the quarks are able to *mix* via the Kabibbo-Kobayashi-Maskawa (CKM) mixing matrix, which contains three mixing angles and a phase [22]. A similar mixing matrix exists in the neutrino sector, containing three angles and three phases (e.g., see [9] and references therein). Mixing is also possible in the QCD sector, but the mixing parameter in this case very close, if not identical, to zero (e.g., [37]).

1.2.1 The Higgs mechanism

The Standard Model is hypothesized to contain a spin-0 (scalar) called the Higgs boson which is responsible for generating masses for the fermions and the massive vector bosons via the spontaneous breaking of electroweak symmetry. Spontaneous symmetry breaking is necessary to generate masses for the W and Z bosons, while keeping the theory renormalizable¹. Since the weak interaction is known to be a short-range force, the three mediators of the force (the W^\pm and the Z) must be massive. However, adding mass terms for these bosons to the Standard Model Lagrangian violates local $SU(2) \times U(1)$ gauge invariance.

To generate masses for three gauge bosons while keeping the photon massless, one introduces a complex $SU(2)$ doublet of scalars with a mass term $\mu^2 < 0$ (see [20] for a recent overview of the Higgs mechanism). The corresponding scalar potential has its minimum along a circle in the complex plane. To investigate the behavior of the field near the minimum, one must choose a particular point in the circle. Consequently, the symmetry of the Lagrangian governing the dynamics of the field is no longer present in the solutions. This fact is known as *spontaneous symmetry breaking*. Upon being expanded around the chosen point, the Lagrangian contains terms for one massive scalar, corresponding to the Higgs boson, but also terms corresponding to three massless scalars, the so-called *Goldstone bosons*. This is a consequence of the Goldstone theorem, which states that whenever a continuous symmetry is spontaneously broken, the theory will contain massless scalars [50], the number of scalars being equal to the

¹Fermion masses can be generated within the Standard Model without requiring a Higgs scalar, for example, via chiral symmetry breaking. It is elegant, however, to have all masses generated with a single mechanism.

number of broken generators. In this case, we break three continuous symmetries and therefore have as many Goldstone bosons.

The Goldstone fields act as longitudinal components of the vector fields, allowing them to transform to the Goldstone fields during propagation. One must perform a diagonalization to arrive at the physical eigenstates of the vector fields; the diagonalization in this case is a $SU(2)$ gauge transformation. Since the initial Lagrangian was gauge invariant, it remains gauge invariant after the transformation. The end result is three physical vector bosons with mass, and therefore with longitudinal polarization states, as well as one massless vector boson. The longitudinal polarizations of the former are due to the transformation that eliminated the Goldstone fields, so that the massive vector bosons are said to have ‘absorbed’ the Goldstone bosons.

All particles of the Standard Model other than the Higgs boson have been experimentally observed. With the exception of the neutrinos, their masses have been measured to varying degrees of accuracy. However, as mentioned before, the Standard Model is not a complete theory of nature. Its parameters, *i.e.*, the nine fermion masses, the four parameters of the CKM matrix, the strong mixing parameter, the three coupling constants, and the Higgs vacuum expectation value and self coupling, are all *free*, in the sense that their values cannot be derived from the theory and have to be chosen to agree with experiment. In addition, the Model suffers from a *naturalness problem*, due to the fact that the mass of the Higgs boson requires extreme fine-tuning to keep it at the electroweak scale.

1.3 Proton-proton collisions and Z boson production at the LHC

In this thesis, we are concerned with the production of Z bosons in hard pp collisions. Hard processes can include interactions that involve small and large transfers of momentum, and we need to understand the effects of both in order to be able to extract theoretical predictions for the Z cross-section. We need to know the momentum distributions of *partons*, *i.e.*, quarks and gluons, inside the colliding protons. Furthermore, since perturbative calculations are made as an expansion in the strong coupling α_s , we need knowledge of the renormalization procedure used to extract α_s at a given momentum scale. In this section, we review these topics in some detail.

1.3.1 Internal structure of a proton and parton distributions functions

Protons are composed of quarks and gluons. In low energy interactions, the proton's internal structure can be described as a collection of three *valence* quarks: two of the *up* type and one of the *down* type, which interact via gluon exchange (see Figure 1.1). The valence quarks determine the quantum numbers of the proton. In addition, gluons can self-interact to produce quark-antiquark pairs as well as further gluons. The additional $q\bar{q}$ pairs thus produced are known as *sea quarks*.

As mentioned in Section 1.2, the strength of the strong interaction decreases with increasing energy scale of the interaction. Consequently, for *hard interactions*, *i.e.*, interactions involving large momentum transfers, the partons inside a proton can be considered as being effectively free. Each parton carries a fraction of the proton's total momentum, and we can express the momentum of the i th parton as:

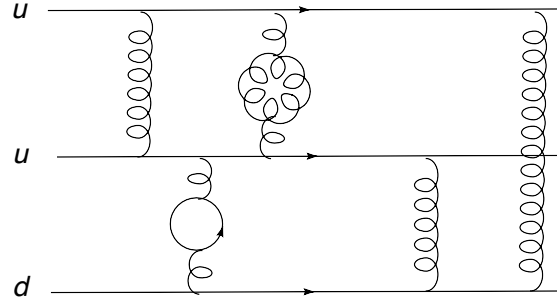


Figure 1.1: The three valence quarks in a proton interacting via gluon exchange. Gluon self-interaction and the formation of ‘sea quarks’ are also shown.

$$p_i = xp_{proton} \quad (1.1)$$

where x is the fraction of the proton’s total momentum carried by the parton. The probability that a parton will carry a given fraction of the proton’s momentum can be expressed in terms of a probability distribution, referred to as a *parton distribution function* (PDF) [40]. It is as yet not possible to calculate PDFs from the theory; they are extracted from fits to experimental data (for example, see [80]). Figure 1.2 shows a fit to deep inelastic scattering (DIS) data from the ZEUS experiment [29].

Note in Figure 1.2 that the PDFs are scale-dependent, *i.e.*, the fitting is done at a particular momentum scale Q^2 . The scale-dependence of PDFs is logarithmic and arises, as we shall see below (Section 1.3.3), because logarithmically divergent gluon emission terms are absorbed into the definition of PDFs. For a given momentum fraction x , the PDF $f_i(x, Q^2)$ expresses the density of the i th type of parton in the proton integrated over a momentum range of 0 to Q .

Knowing the PDF of parton i , we can formulate a set of *structure functions* for the proton as a function of x and Q^2 . For example,

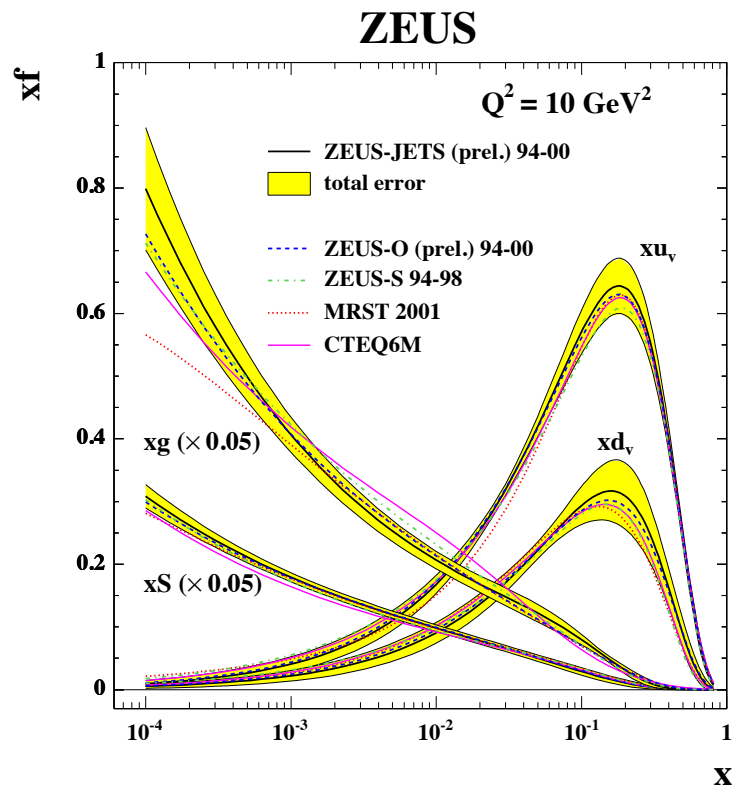


Figure 1.2: PDF fits to deep inelastic scattering data from the ZEUS experiment at a momentum transfer scale of $Q^2 = 10 \text{ GeV}^2$. Comparison to various other fits is also shown.

$$F_2(x, Q^2) = \sum_i q_i^2 f_i(x, Q^2)x \quad (1.2)$$

where q_i is the electric charge on the i th parton type and the sum is over all parton types. Constraints on the structure functions can be obtained by utilizing the conserved quantum numbers of the proton. As an example, since the proton has an electric charge of +1, the *charge sum rule* must hold:

$$\int_0^1 \left(\frac{2}{3}[u_v(x, Q^2)] - \frac{1}{3}[d_v(x, Q^2)] \right) dx = 1 \quad (1.3)$$

where u_v and d_v are PDFs for the valence up and down quarks respectively.

The PDFs can be measured at some momentum scale using, *e.g.*, deep inelastic scattering processes. They can then be *evolved* to any other momentum scale using a set of integro-differential equations formulated by Dokshitzer, Gribov, Lipatov, Altarelli and Parisi (the DGLAP equations) [10].

1.3.2 Renormalization of the strong coupling

Owing to vacuum effects, the value of the strong coupling ‘constant’ α_s must be *renormalized* or reparametrized [32] in order to avoid infinities in measurable quantities. As a result, the coupling is not constant, but ‘runs’ logarithmically with the momentum scale Q^2 . The running can be expressed as:

$$\alpha_s(Q^2) = \frac{12\pi}{(33 - 2n_f)\ln(Q^2/\Lambda_{QCD}^2)} \quad (1.4)$$

where n_f is the number of quark flavors with masses below the scale Q^2 , and Λ_{QCD} is the *QCD scale*². The scale Q^2 is referred to as the *renormalization scale*, μ_R .

² Λ_{QCD} can be thought of as the energy scale at which the coupling becomes large, *i.e.*, approaches unity.

In higher-order QCD calculations, the value of α_S depends not only on μ_R , but also on the renormalization *scheme*, *i.e.* , how the various divergences that arise during the calculation are regulated. The *modified minimal subtraction* or \overline{MS} scheme [91] is the most widely used renormalization scheme.

1.3.3 QCD hard scattering and factorization

The *factorization theorem* states that cross-sections for a large number of processes can be factored into a process-dependent part, which is calculable in perturbative QCD, and a universal part, which can be measured at a given energy scale for a given process and then evolved to any other scale for any process.

Drell and Yan [34] showed in 1971 that a hadronic interaction can be separated into two parts: the distribution of partons inside the hadron, and an interaction between two partons. More formally, if hadrons A and B interact to produce X , the cross-section for the process $\sigma_{AB \rightarrow X}$ can be calculated by convolving the cross-section $\hat{\sigma}$ for the parton-parton process $ab \rightarrow X$ with the PDFs of the hadron:

$$\sigma_{AB} = \int dx_a dx_b f_{a/A}(x_a) f_{b/B}(x_b) \hat{\sigma}_{ab \rightarrow X} , \quad (1.5)$$

where $f_{a/A}(x_a)$ is the PDF for parton a in hadron A , and similarly for $f_{b/B}(x_b)$. When perturbative corrections from gluon emission are included in this expression, divergent logarithmic terms appear from very soft gluons and gluons emitted collinearly with the incoming partons [24]. The factorization theorem was derived [28] to show that these large logarithmic terms can be factored into renormalized parton distributions, so that the perturbative expansion converges. In equation 1.5, the PDFs are then written as $f_{a/A}(x_a, Q^2)$ and $f_{b/B}(x_b, Q^2)$, where Q^2 is the momentum scale characterizing the

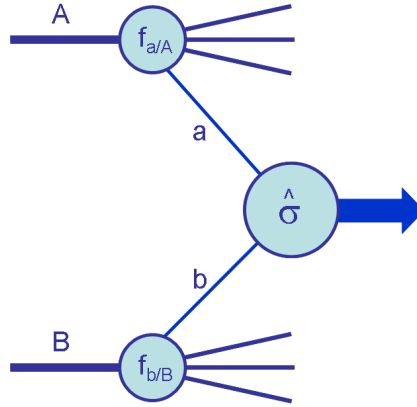


Figure 1.3: Schematic structure of a hard scattering process.

hard scattering of interest. For example, for Z boson production, $Q^2 = M_Z^2$. The PDFs are often also written as $f(x, \mu_F^2)$, where μ_F is the *factorization scale*, which can be described as the scale separating the perturbative from the non-perturbative regime.

A generic hard scattering process is shown in Figure 1.3.

After the logarithmic terms have been factored in, there are process-dependent finite corrections left, which are included in the partonic cross-section for a given process. These corrections are expressed as a power-series expansion in α_S , and are referred to as the *leading order* (LO), *next-to-leading-order* (NLO) etc terms:

$$\hat{\sigma}_{ab \rightarrow X} = \alpha_S^k(\mu_R^2) [\hat{\sigma}^{LO} + \alpha_S(\mu_R^2) \hat{\sigma}^{NLO} + \alpha_S^2(\mu_R^2) \hat{\sigma}^{NNLO} + \dots]_{ab \rightarrow X} \quad (1.6)$$

where $k = 0, 2, \dots$. The perturbation series always converges if contributions from all diagrams at all orders of α_S are included. But since this is not possible, $\hat{\sigma}$ can be approximated by calculating the contributions to a given order in α_S , *e.g.*, to

order NNLO, which corresponds to inclusion up to the $\mathcal{O}(\alpha_S^2)$ term in Eq. 1.6. As the calculation is performed to higher orders, the dependence on the unphysical renormalization and factorization scales decreases, and so does the theoretical uncertainty of the result.

Resummation: Fixed-order predictions can break down near phase space boundaries. An example is the transverse momentum distribution of vector bosons in hadron collisions [24], in the calculation of which logarithms appear as $\alpha_S^n \ln^{2n-1}(Q^2/p_T^2)$. For small p_T , these terms can diverge and the finite-order calculation is no longer valid. However, it is possible to single out the dominant contributions from each order in the perturbation series and sum them explicitly using an evolution equation. This process is called *resummation*. Various resummation methods are available (see, e.g., [68]).

Fixed-order calculation and resummation each provide a good description of event properties in certain regions of the phase space. The former is more accurate at high energy and p_T scales, while the latter provides better results in the low- p_T regime. By matching the two in the overlap region, the accuracy of each can be improved.

The program ResBos [19] provides NLO resummed predictions for bosonic processes at hadron colliders. Recently, the programs *FEHiP* and *FEWZ* [11] have become available, which calculate production cross-sections for the SM Higgs and the W and Z bosons respectively to NNLO accuracy.

Parton shower: Another approach to avoid the calculation of higher and higher orders in the perturbative expansion is the so-called *parton shower* method. Parton shower is widely used by many Monte Carlo event generators to simulate hadronic

processes. The method relates partons produced at a high energy scale to partons at a low scale near Λ_{QCD} . Using the DGLAP equations, parton shower algorithms allow the evolution of parton fragmentation to any energy scale³. The solution of the DGLAP equations can be written in terms of the *Sudakov form factor* [27], which gives the probability that a parton at a given energy scale will evolve to a lower scale without the emission of a gluon with p_T greater than a given value⁴. The shower development stops when the energy of the partons falls below a cut-off value.

1.3.4 Hadronization

Hadronization is the process by which color singlet hadrons are formed from colorless partons. This is an essentially non-perturbative process. Three popular models are available for describing hadronization, namely, the independent fragmentation model [43], the Lund string fragmentation model [76] and the cluster model [52].

The independent fragmentation model: This model of hadronization is due to Feynman and Field [43]. In this model, a quark-antiquark pair is generated for each initial quark q_0 from the parton shower. Mesons are formed with a fraction of the longitudinal momentum of q_0 and a Gaussian distributed transverse momentum. Baryons are formed by generating diquarks and combining them with antiquarks. For each new quark/antiquark, the procedure is repeated until the available momentum is used up.

This simple model correctly describes energetic hadrons in a jet, but does not

³For parton shower from initial state quarks/gluons, the evolution is done backwards from the hard scattering scale to the low scale.

⁴Sudakov form factors are in fact a basis of both resummation and parton shower approaches.

conserve energy or flavor. Momentum rescaling is therefore necessary at the end of the hadronization process.

The Lund string model: The color field lines between a quark-antiquark pair can be thought of as a tube, or a string in one dimension, with a constant string tension $k \approx 1 \text{ GeV/fm}$. As the partons move apart, the tension in the string increases until there is enough energy to produce a $q\bar{q}$ pair. Consequently, two color-singlet $q\bar{q}$ pairs form that can fragment again, and so on until only on-shell hadrons remain. In this model, baryons are generated by diquark-antiquark production.

The Lund model is intuitively appealing and physically motivated. The PYTHIA [92] Monte Carlo program uses it for hadronization.

The cluster model: This model works by following the color structure of a parton shower such that, at the end of the showering process, color-singlet *clusters* are formed. The model splits all gluons into quark-antiquark and diquark-antidiquark pairs, forming clusters with predominantly small masses. The light clusters decay to hadrons, while the heavier clusters are split into lighter ones.

The advantage of the cluster model is that the properties of the hadrons are determined by the properties of the parton shower. However, it runs into problems with baryon production. The HERWIG [46] Monte Carlo program makes use of this model.

1.4 Z boson production at the LHC

The main Z boson production mechanism at the LHC is the Drell-Yan process $q\bar{q} \rightarrow Z \rightarrow \mu^+\mu^-$, as illustrated in Figure 1.4. This process may or may not involve

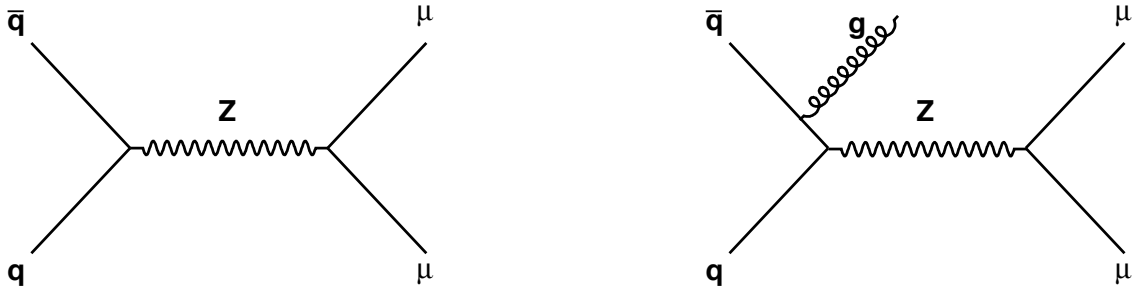


Figure 1.4: *Left:* Z boson production through the Drell-Yan channel, *i.e.*, $q\bar{q}$ annihilation. *Right:* Drell-Yan Z boson production accompanied by initial-state gluon radiation. This is an NLO process.

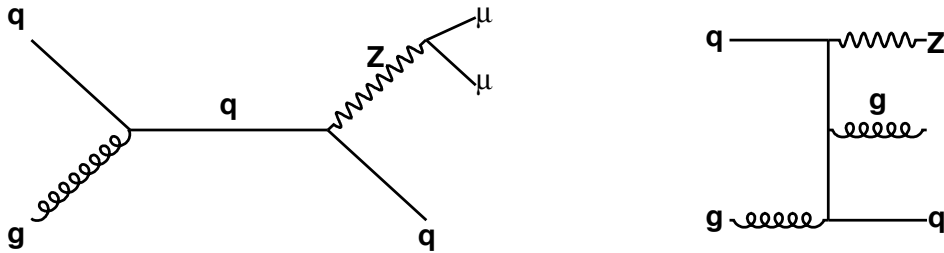


Figure 1.5: *Left:* Z boson production through gluon Compton scattering. This is a $Z + 1 \text{ jet}$ event. *Right:* A $Z + 2 \text{ jet}$ event, an NNLO process.

initial-state gluon radiation. Higher-order processes with multiple radiated gluons in the final state have a small contribution.

Figure 1.6 shows the production cross-sections for various Standard Model processes as a function of the center-of-mass energy, calculated to NLO accuracy in perturbative QCD [24]. As can be seen, the total Z production cross-section at a collision energy of 7 TeV is ≈ 30 nb. The *branching fraction* of the decay $Z \rightarrow \mu\mu$ is $\approx 3.366\%$ [40], which gives a cross-section of ≈ 1 nb for the inclusive decay mode $Z \rightarrow \mu\mu + X$, where X represents any other final state particle/s.

Figure 1.7 shows the contributions of different quark flavors to Drell-Yan Z boson

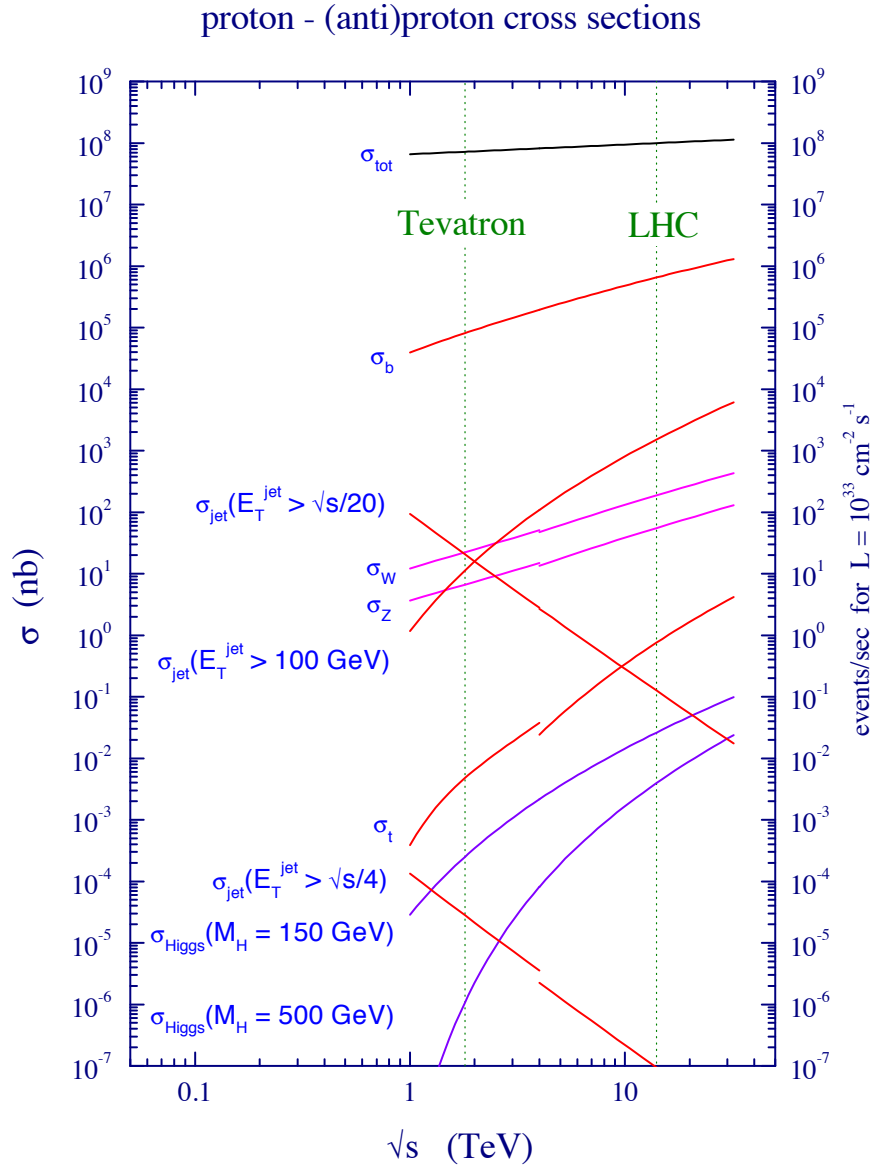


Figure 1.6: Total cross-sections for a number of SM processes at the Tevatron and at the LHC. The right axis shows the number of events expected per second at an instantaneous luminosity of $10^{33} \text{ cm}^{-2} \text{ s}^{-1}$.

production [73]. At 7 TeV, $u\bar{u}$ and $d\bar{d}$ each contribute about 40% to the leading-order process (left diagram in Figure 1.4). Contributions from $s\bar{s}$ and $c\bar{c}$ are $\approx 15\%$ and $\approx 5\%$ respectively.

The QCD prediction of the Z boson production cross-section must be tested by experiment. Experiments at the Tevatron accelerator at Fermilab have measured this quantity in $p\bar{p}$ collisions at a center-of-mass energy of 1.96 TeV, and their results agree well with predictions. The CERN LHC, with pp collisions at a center-of-mass energy of 7 TeV (and at 14 TeV starting ≈ 2013), provides an opportunity to test these predictions in a new kinematic regime.

1.5 Current state of theoretical calculation of the Z cross-section

As mentioned before, the production rate of Z boson can be used to estimate the absolute luminosity per luminosity block or run, provided that the production cross-sections are known with high accuracy. Given the large cross-sections of these processes at LHC energies, the statistical uncertainty in cross-section determination will quickly become very small, and systematic errors will be dominant. As the detector is understood better and better, the experimental systematics will decrease as well, such that errors arising from theoretical sources will set the limiting accuracy for the cross-section measurements, and thus for the use of these processes as ‘standard candles’ for luminosity measurement. In what follows, we discuss the theoretical uncertainties associated with the measurement of Z cross-section in ATLAS.

The theoretical input to a cross-section analysis comes in through the acceptance correction: any detector has a finite geometrical and kinematic acceptance, so that

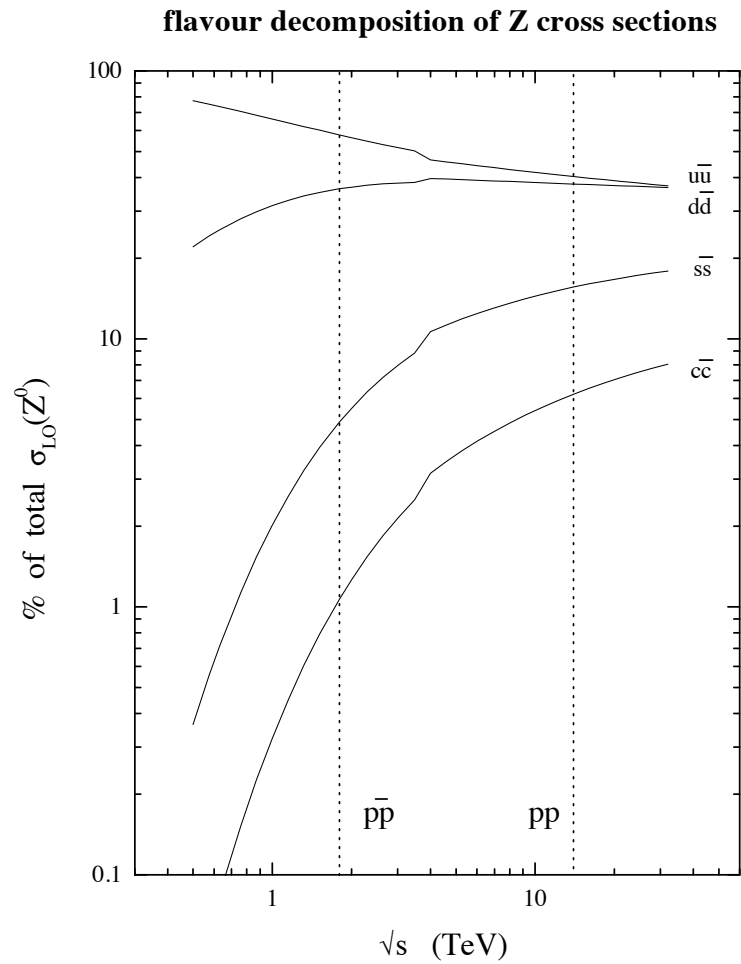


Figure 1.7: Flavor decomposition of Drell-Yan Z production as a function of the center-of-mass energy. The vertical lines indicate contributions at the Tevatron energy of 1.96 TeV and the LHC design energy of 14 TeV.

not all events of a given type (e.g., events in which a Z is produced) can be observed. Therefore, to measure the total production cross-section of a particle, the observed cross-section must be corrected for the acceptance. The correction factors are derived using a simulated or ‘Monte Carlo’ (MC) sample of the process in question⁵, produced with an event generator which uses theoretical tools and calculations to model interactions. A number of event generators are available, differing in their use of computational schemes and accuracy of calculations⁶.

There are four main classes of theoretical errors in such calculations, arising from:

- QCD corrections
- electroweak corrections
- QCD scale dependence
- parton distribution functions (PDFs)

In this section, we discuss these errors in the context of specific MC generators that are or can be used to simulate Z boson events at the LHC. We give an estimate of the error arising from each source in the cross-section prediction and acceptance calculation, and the overall theoretical error that can be expected from current calculations. As we will see, PDFs are presently the major source of theoretical uncertainty; we devote a separate subsection to discussing their present status and what measurements

⁵We note here that detector simulation is in general imperfect, and can potentially introduce a large systematic error in the acceptance calculation. The accuracy of a detector simulation can be estimated by first making a measurement (e.g., muon reconstruction efficiency) with detector data without any reliance on Monte Carlo, then repeating the measurement on a Monte Carlo sample, and comparing the two results (see Section 4.2.4, for example).

⁶Chapter 5 of this thesis contains an overview of MC event generation and simulation, as well as brief reviews of the MC generators used in our analysis.

at the LHC can help constrain them. We briefly describe the other improvements that will be needed to reduce the overall theoretical error to the level of a percent.

1.5.1 Sources of theoretical errors

QCD corrections: QCD calculations to NLO accuracy have been available for a long time. The event generator MC@NLO [84], for example, combines NLO QCD matrix elements with the HERWIG [46] parton shower algorithm. The fixed-order matrix element calculation gives a good description of processes where the partons are energetic and widely separated, while parton showers provide an excellent description of processes dominated by soft and collinear gluon emission. A tool that combines both types of calculation is therefore very useful.

MC@NLO calculates W/Z boson production cross-sections including $\gamma - Z$ interference as well as spin correlations among leptonic decay products. It can be interfaced with a particular detector simulation. For example, it has been interfaced with the ATLAS simulation via the *Athena* computing framework.

Recently, NNLO QCD calculations have become available for some processes. The program FEWZ [67] calculates W/Z production cross-sections through NNLO including finite-width effects, $\gamma - Z$ interference and spin correlations. The program RESBOS [19] resums soft and collinear initial-state gluon emission to all orders, giving an accurate description of processes in the low- p_T regime. It can also (optionally) include initial-state NLO corrections. Both of these programs use VEGAS [72] for evaluating phase-space integrals.

The authors of [75] recently studied the theoretical uncertainties in W/Z cross-

section determination. They investigated the error introduced by using NLO rather than NNLO QCD calculations by comparing cross-sections and acceptances obtained from MC@NLO with those obtained from FEWZ. Since MC@NLO (coupled with HERWIG Monte Carlo) includes parton showering and FEWZ does not, results from the two cannot be directly compared. Instead, the authors derive a K -factor using NLO and NNLO results from FEWZ, multiply the NLO result from MC@NLO by the K -factor, and compare the resulting numbers with NNLO results obtained from FEWZ. The Z cross-section values differ by $\approx 1\%$ between the two, while the acceptances differ by $\approx 2.4\%$ [75].

Electroweak (EW) corrections: At LHC energies, $\alpha_{EW} \approx \alpha_s^2$, so that NLO EW corrections appear at the same order as NNLO QCD corrections⁷. Hence, to reach an accuracy of $\approx 1\%$ in W/Z cross-section measurements, both types of corrections must be taken into account.

The most important EW correction with respect to W/Z production is expected to be from final-state photon radiation. The event generator HORACE [25] includes initial- and final-state photon radiation in a photon shower approximation as well as exact NLO EW corrections, though not higher-order QCD corrections. RESBOS-A [81], an upgrade of the ResBos program, includes final-state photon radiation in addition to gluon resummation. PHOTOS [77] is an add-on program that generates multi-photon emission in events created by a host program. The host program can be any event generator such as MC@NLO.

To study the effect of adding EW corrections, the authors of [75] use the HO-

⁷As a numerical example, at the Z pole, $\alpha_{EW} \approx \frac{1}{129} \approx 7.8 \times 10^{-3}$, and $\alpha_s^2 \approx 13.8 \times 10^{-3}$.

RACE generator to compare the Z cross-section and acceptance in three scenarios:

1. HORACE without EW corrections, and with parton showering performed with HERWIG
2. HORACE without EW corrections, but this time showered with both HERWIG and PHOTOS (QCD and photon showers)
3. HORACE with full EW corrections, and showered with HERWIG

For the Z production cross-section, the difference between scenarios 1) and 3), i.e., no EW correction vs. exact EW correction to NLO, is found to be 1.2%. The difference between scenarios 2) and 3), i.e., multi-photon shower vs. exact NLO EW corrections, is 0.16%. For the acceptance, the difference is 1.7% between scenarios 1) and 3), and 0.74% between scenarios 2) and 3).

Clearly, results from using PHOTOS to perform final-state photon radiation agree with the full NLO EW corrected results to within 1%. In view of the discussion in the previous subsection, MC@NLO (or equivalently POWHEG [44]) interfaced with PHOTOS seems to be a good event generator to use for Z cross-section estimation, and indeed was adopted in the analysis described in this thesis. We note, however, that calculations from RESBOS-A are more reliable in the low- p_T region than exact NLO calculations, since RESBOS-A performs soft and collinear gluon resummation. For example, Figure 1.8 [75] shows a comparison of the Z p_T spectra from the two programs in the region $p_T^Z < 50$ GeV. The two spectra differ significantly, in particular in the Sudakov region ($p_T^Z < 10$ GeV). A good strategy to adopt in a Z p_T analysis is

to reweight the MC@NLO or POWHEG Z p_T spectrum to match the RESBOS-A spectrum.

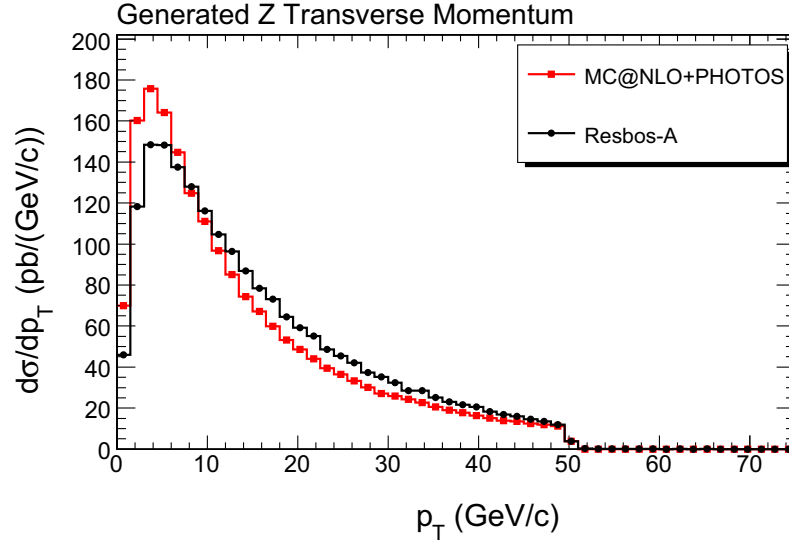


Figure 1.8: Z differential cross-section in p_T bins from MC@NLO using PHOTOS for final-state photon showering (red) and RESBOS-A (black). The effect of gluon resummation in RESBOS-A can be seen clearly.

QCD scale dependence: As already mentioned, any perturbative QCD calculation uses a factorization scale μ_F and a renormalization scale μ_R at which PDFs and α_s are respectively evaluated. In an all-order calculation, there is no dependence on these scales, but any fixed-order calculation necessarily has scale dependence, and the choice of one scale as opposed to another introduces an uncertainty in the results.

The effect of the choice of scale on Z production cross-section and acceptance was investigated using NLO and NNLO results from FEWZ [75]. Calculations were performed at three different scales: $\mu_{F,R} = \frac{M_Z}{2}, M_Z$ and $2M_Z$. Scale dependence of the cross-section was found to be $\approx 2.5\%$ at NLO and $\approx 1\%$ at NNLO. Scale dependence

of the acceptance was $\approx 0.1\%$ at NLO⁸ and $\approx 1\%$ at NNLO [75].

1.5.2 Current status of PDFs

As discussed in Section 1.3.1, the cross-section for a process is theoretically calculated by convolving the partonic cross-section for the process with the proton PDFs. The PDFs are extracted in the framework of perturbative QCD from a global analysis of hard-scattering data from a number of fixed-target and collider experiments. Relevant processes include deep inelastic scattering (DIS), Drell-Yan (DY) and inclusive jet production. PDF parameterizations are available from global fits at leading order (LO), NLO, and recently NNLO⁹ in QCD. Two major groups, CTEQ [78] and MSTW [49] (formerly MRST) provide regular updates of proton PDFs using the latest data and theoretical advances.

Information about quark distributions is provided by DIS and DY data. The only processes in which gluon distributions enter directly at leading order are hadron-hadron scattering with jet final states. At low partonic momentum fraction x , gluon distributions may be determined from scaling violations in quark distributions, but direct measurements are necessary for extracting the distributions at moderate and high x values. Currently, the best direct gluon PDF measurements are from jet production data at the Tevatron [24], which are limited by statistics, especially at high E_T .

PDF uncertainties have systematic components in addition to statistical ones,

⁸Note that the scale dependence of NLO acceptances is reduced drastically due to correlations between cross-sections before and after applying cuts.

⁹But not all processes used in the global fits are yet available at NNLO. In particular, an NNLO treatment of inclusive jet production was not available until very recently [24].

and these uncertainties propagate to cross-section calculations. The errors are large in the very low x and high x regions but, unsurprisingly, the gluon distribution has the largest error. Two methods have traditionally been used to estimate PDF errors, namely the Lagrange Multiplier technique and the Hessian technique [63]. The latter provides a more general framework for estimating the PDF uncertainty for any cross-section calculation.

Below, we are going to discuss recent advances in PDF calculation and error estimation with reference to CTEQ PDF sets as an illustrative example.

Global PDF analyses have traditionally used structure function data from DIS experiments, which necessarily involved model-dependent assumptions used to extract the structure functions. Recently, DIS experiments at DESY have published detailed cross-section data, which allows a model-independent analysis and thus yield more accurate PDFs. The CTEQ6.5 PDFs were the first ones to use this cross-section data [106].

Another recent development involves the use of heavy quark mass effects in PDF analyses. Conventionally, the factorization theorem has been taken to be valid at energy scales far above all quark mass thresholds, so that quark masses could be neglected in perturbative QCD calculations. This is known as the zero-mass (ZM) formalism, and is unreliable at energy scales close to the heavy quark masses (mainly c and b quarks). Recently, the factorization theorem has been generalized to take into account non-zero quark masses [64]. This is known as the general-mass (GM) factorization scheme, and calculations done therein are substantially more accurate

than the ZM approach¹⁰. The CTEQ6.5M PDFs were the first ones derived using the GM formalism[106].

The impact of the new formalism is prominent for u and d quark distributions in the low- x region, for $x < \approx 10^{-3}$ [78]. Since Z production at the LHC occurs predominantly through light quark interactions at small x ($\approx 10^{-3} < x < \approx 10^{-2}$), the predicted cross-section is enhanced significantly, by as much as 7% compared to earlier calculations [78], [106]. Moreover, the latest PDF sets from the CTEQ collaboration (CTEQ6.6, CT10) includes new DIS data [78], [56], so that the Hessian error in Z cross-sections has decreased from $\approx 5\%$ to 3.5%. The error is driven mainly by s , c and b quarks, which account for $\approx 20\%$ of Z production in NLO processes at the LHC.

In parallel with the CTEQ collaboration, MSTW have recently published their latest PDF set [49], which includes dimuon cross-sections from NuTeV. This PDF analysis included NNLO corrections for inclusive jet data for the first time. Figure 1.9 [78] shows a comparison of W and Z cross-sections at the LHC calculated with ResBos using PDF sets from CTEQ, MSTW and other groups.

1.5.3 PDF measurements in ATLAS

The LHC experiments aim to constrain the proton PDFs in the high and low x regions, where they are poorly known. The most important measurements for this purpose are the Z rapidity distribution, W asymmetry, $Z + b$ -jet production, inclusive jet production and direct photon production. We will briefly describe the

¹⁰The overall χ^2 , a measure of the goodness of fit, decreases by ≈ 200 for 2676 data points when fitted in the GM formalism instead of the older ZM formalism.

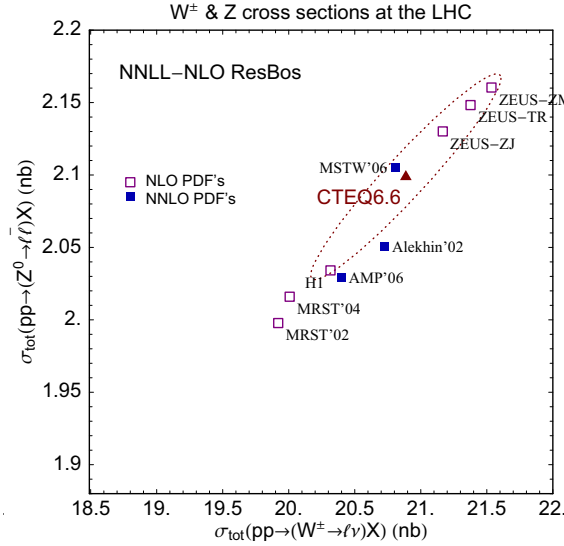


Figure 1.9: Comparison of W and Z production cross-sections at the LHC calculated with RESBOS using PDF sets from CTEQ, MSTW (MRST) and various other groups. The CTEQ6.6 90% confidence limit band is shown.

PDF constraining potential of some of these processes in ATLAS.

Z rapidity distribution: At rapidity $y \approx 0$, the colliding partons have small momentum fractions x . At larger values of $|y|$, one parton is typically at larger x and the other one at smaller x . However, over the measurable rapidity region in ATLAS ($|y| < \approx 2.5$), x values remain in the range $5 \times 10^{-4} < x < 5 \times 10^{-2}$. The colliding partons in this regime are predominantly sea partons which originate from gluon splitting. As a result, the rapidity spectrum of the Z provides information about the gluon distribution at low x . The gluon PDF uncertainty in this regime is currently $\approx 8\%$ at NLO [103]. A measurement of the Z rapidity spectrum down to 4% accuracy should start improving it.

To estimate how well ATLAS can constrain the gluon PDF, ATLAS pseudo-data was recently included in a ZEUS-S PDF fit [30]. The error on the λ parameter, which

controls small- x gluon distribution, decreased by 35% as a result.

W charge asymmetry: The quantity $A_W = \frac{W^+ - W^-}{W^+ + W^-}$ depends on the PDFs of valence u and d quarks at $x \approx 5 \times 10^{-3}$. This is because, at leading order, the expression reduces to:

$$A_W = \frac{u_v - d_v}{u_v + d_v + \bar{u} + \bar{d}} \quad (1.7)$$

Because of the missing neutrino, ATLAS cannot directly measure the W charge asymmetry, but rather the decay lepton charge asymmetry. Nevertheless, the sensitivity to valence u and d quark distributions should remain¹¹, and the measurement will give information about the distributions in a region of x of which there is no current knowledge. Indeed, a first measurement of this asymmetry is already underway using the 2010 data.

Before we can measure the physics-induced lepton charge asymmetry, we must ensure that we know detector-induced charge asymmetries very well. One way to account for the latter asymmetry is to use data from runs in which the solenoid and toroid polarities were alternately reversed. In this case, any charge bias from geometrical acceptance and alignment errors should cancel out. D0, for example, regularly reverses their magnet polarities, so that the magnets are in each polarity about half of the time [100]. ATLAS decided against using this technique in the 2010 run.

$Z + b$ -jet production: To measure the Z production cross-section to $\approx 1\%$ precision, the bottom quark PDF must be known to better than $\approx 20\%$ [103]. The

¹¹The lepton charge asymmetry is a convolution of the W charge asymmetry and the V - A asymmetry from the W decay. Assuming that W decay occurs via a pure V - A interaction, the lepton charge asymmetry remains sensitive to PDFs.

process $bg \rightarrow Zb + X$ is sensitive to the b quark PDF. With well-understood silicon vertexing, this decay may be observed soon in the Z leptonic decay channels.

Inclusive jet production: Uncertainty in high- x gluon distribution is the dominant systematics in high- E_T jet measurements, and can become as large as 60% at $E_T \approx 5$ TeV [103]. Hence, the high- x gluon PDF can be improved with high- E_T jet cross-section measurements. Such improvement may be possible with as little as 1 fb^{-1} of data from ATLAS, provided that the jet energy scale is known to good accuracy ($\approx 1\%$) [30].

Direct photon production: At leading order, direct photon production at the LHC occurs via the channels $qg \rightarrow \gamma q$ and $q\bar{q} \rightarrow \gamma g$. The photon and jet E_T distributions are highly sensitive to PDFs: the expected difference in this distribution using different PDF sets is as large as 18% [103]. Measurement of this process will constrain the gluon distribution in the moderate and high x regions. See [54] for a first measurement of prompt photon cross-section by ATLAS.

1.5.4 Overall theoretical error in Z cross-section and acceptance

The authors of [75] estimate the size of the overall theoretical error in Z cross-section and acceptance for a set of cuts typical of a cross-section analysis:

- dilepton invariant mass between 79 GeV and 104 GeV
- pseudorapidity of each lepton in the range $[-2.0, 2.0]$
- transverse momentum of each lepton greater than 20 GeV

Table 1.1 summarizes the error estimate from each source as well as the overall errors expected in the cross-section and acceptance. As expected from the above discussion, the dominant component of the PDF uncertainty comes from gluon distributions.

Source of uncertainty	cross-section uncertainty (%)	acceptance uncertainty (%)
Total QCD uncertainty, including missing NNLO corrections and scale dependence	1.57	2.55
Uncertainty due to missing NLO EW corrections	0.38	0.96
PDF uncertainty	3.52	1.85
Overall uncertainty	3.85	3.29

Table 1.1: Summary of theoretical uncertainties, derived in [75]. Note that the authors of [75] also quote errors *on the uncertainties* from QCD and EW sources. These derive mainly from the slow convergence of MC integration programs, which limits the precision of the results. They term it ‘technical error’, which we do not show in our table.

Hence, using current tools, it is possible to reach a precision of $\approx 4\%$ on the Z boson cross-section calculation and $\approx 3\%$ on acceptance estimation. We will come back to these numbers in Chapters 6 and 9 in the context of our analysis. To be able to improve these errors to the level of 1%, developments on several fronts will be needed:

- an event generator that combines NNLO QCD corrections with complete NLO EW corrections
- improved PDF constraints, especially for the gluon PDF, from new data
- PDF fits that include NNLO QCD and NLO EW corrections

- an event generator with adequately fast convergence, such that errors due to convergence are minimal

1.5.5 Summary

In this section, we have discussed the theoretical uncertainties involved in the measurement of Z cross-section in ATLAS. We have presented current estimates of errors arising from QCD and electroweak corrections and from our limited knowledge of PDFs, and summarized the improvements which will be needed to reduce the overall theoretical error to the level of a percent. In addition, we have briefly looked at measurements in ATLAS, some of them already being made with the 2010 data, that can help constrain proton PDFs.

Chapter 2

The Accelerator and the Experiment

2.1 The Large Hadron Collider

The Large Hadron Collider (LHC) is located partly in Switzerland and partly in France. It has been built and is managed by the European Council for Nuclear Research (CERN). It is a proton synchrotron, designed to collide protons with protons at a maximum center-of-mass energy of 14 TeV and a peak instantaneous luminosity in excess of 10^{34} protons $cm^{-2}s^{-1}$. The LHC is housed in the 26.7 km circumference tunnel that formerly contained the Large Electron Positron (LEP) collider.

A schematic view of the CERN accelerator complex is shown in Figure 2.1. Proton acceleration occurs in several different stages in this complex. The protons are initially obtained by ionizing gaseous hydrogen. They are accelerated in bunches in the linear accelerator (*LINAC2*) to an energy of 50 MeV. The following stage, the Proton Synchrotron Booster (*PSB*), boosts them up to 1.4 GeV, after which the Proton Synchrotron (*PS*) accelerates them to 26 GeV. The proton bunches are then injected into the Super Proton Synchrotron (*SPS*), which accelerates them to 450 GeV and

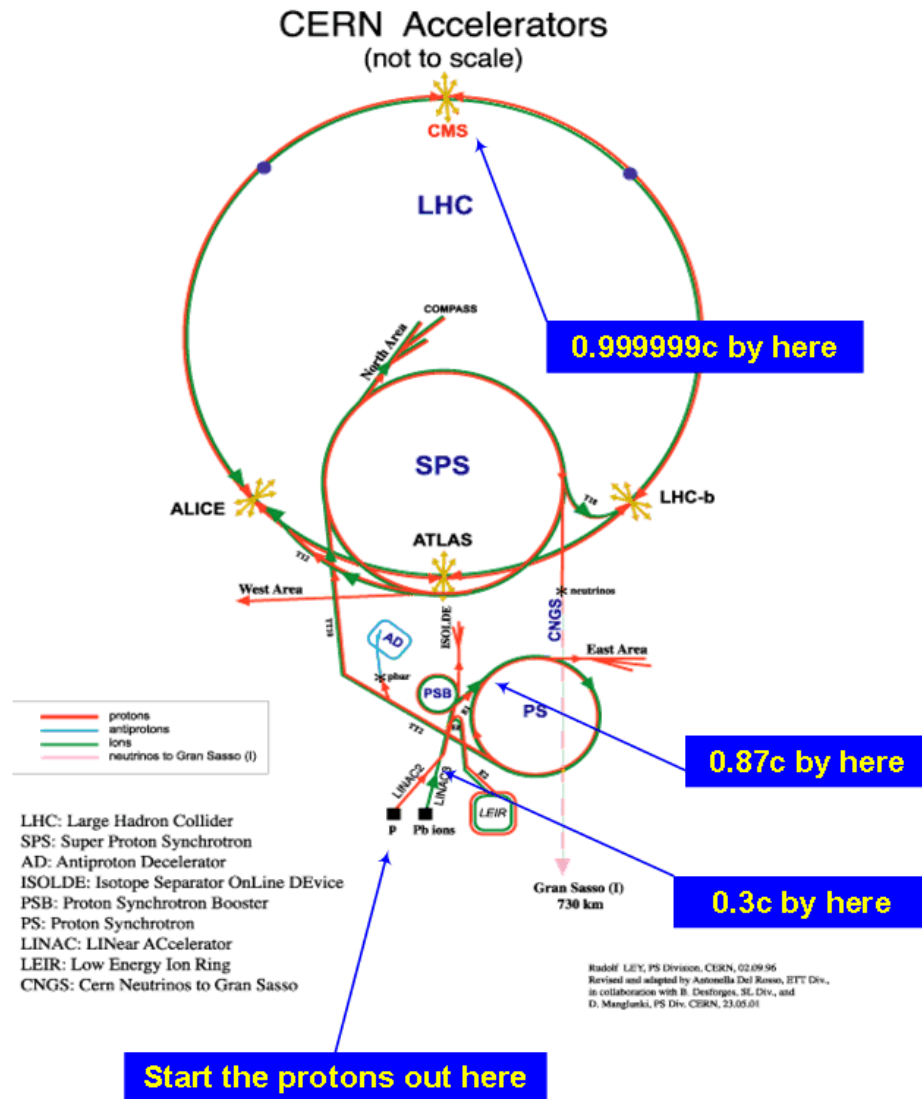


Figure 2.1: Schematic of the CERN accelerator complex.

injects them into the LHC for acceleration to higher energies, up to a maximum of 7 TeV. Inside the LHC, superconducting magnets are used for bending and focusing the proton bunches.

Some important parameters of the LHC and the proton beams are summarized in Tables 2.1 and 2.2.

Parameter name	Value
Circumference	26,659 m
Design energy per beam	7 TeV
Number of dipole magnets	1232
Number of quadrupole magnets	858
Dipole magnetic field at 7 TeV	8.33 T
Operating temperature	1.9 K

Table 2.1: Design parameters of the Large Hadron Collider.

Parameter name	Value
Maximum number of protons/bunch	10^{11}
Maximum number of bunches/beam	8
Beam orbit frequency	11.3 kHz
Peak instantaneous luminosity	$1.6 \times 10^{30} \text{ cm}^{-2} \text{ s}^{-1}$
Maximum number of interactions per bunch crossing	≈ 1.3

Table 2.2: Beam parameters of the Large Hadron Collider in the runs during April-July 2010.

2.2 A Toroidal LHC Apparatus (ATLAS)

To explore the wide variety of physics phenomena that should be accessible at the LHC, The ATLAS experiment was designed to measure the spatial position, energy

and momentum of leptons and jets with high precision, with almost 4π solid angle coverage. Design considerations were strongly motivated by the large event multiplicities expected per bunch crossing, the short bunch crossing intervals (see Table 2.2), and a high radiation environment. From initial design, through development and production, and finally to installation and commissioning of the detector took over fifteen years and the involvement of 3000 physicists and as many engineers and technicians.

As is usual with collider detectors, ATLAS has a cylindrical geometry, with tracking detectors closest to the interaction region followed by sampling calorimeters and a muon system. The inner trackers are in a solenoidal magnetic field, while the muon system is in a toroidal magnetic field. The beam direction is defined as the z axis, such that the plane perpendicular to the beam is the xy plane. Figure 2.2 shows the overall layout of the detector, with the various subsystems indicated.

Since the colliding partons do not in general have the same momenta along the z direction, the scattering process occurs in a frame which moves longitudinally with respect to the laboratory frame. It is therefore convenient to describe the physics in terms of quantities that are invariant under a longitudinal boost. Two such quantities are the transverse momentum $p_T = p\sin\theta$ and the transverse energy $E_T = E\sin\theta$, where θ is the polar angle with respect to the z axis. Another convenient quantity is the *rapidity* $y = \frac{1}{2}\ln\left(\frac{E+p_Z}{E-p_Z}\right)$, where p_Z is a particle's momentum component with respect to the z axis. Rapidity has the desirable property of being additive under a longitudinal boost. Particles produced in soft interactions (so-called *minimum bias* events) have a uniform distribution in rapidity and in the azimuthal angle ϕ . For massless particles, it can be shown that the rapidity simplifies to the *pseudorapidity*

$\eta = -\ln\left[\tan\frac{\theta}{2}\right]$. The ATLAS detector was designed to have uniform segmentation in η and ϕ to exploit these properties of hadronic collisions.

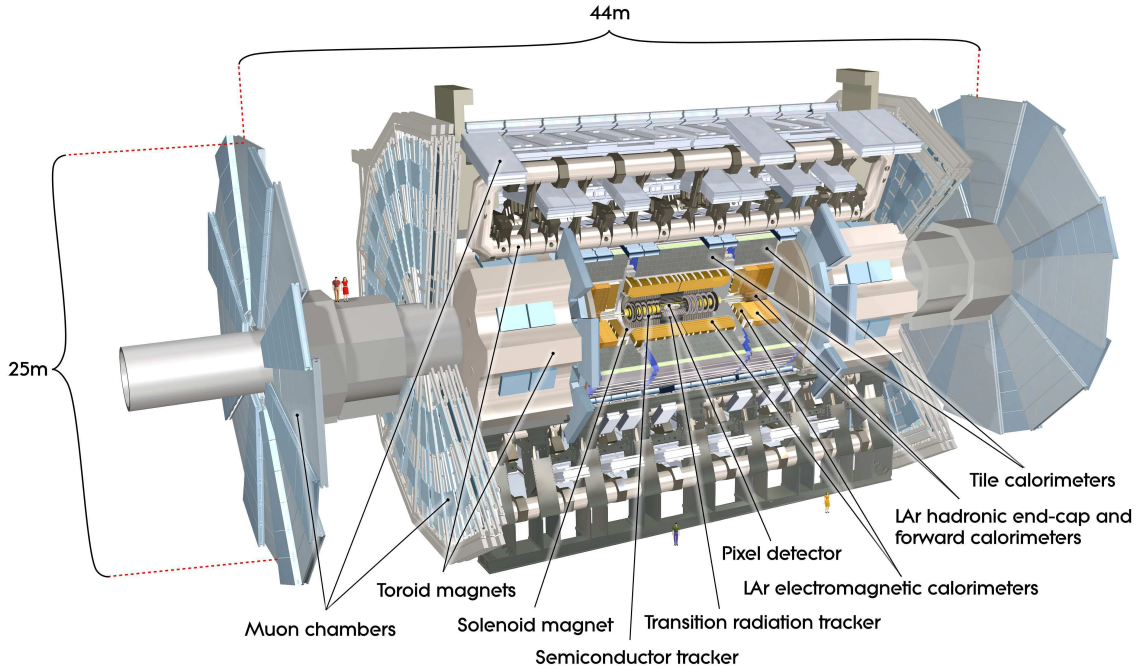


Figure 2.2: A cutaway view of the ATLAS detector. The dimensions and the different subsystems are indicated.

Reference [98] presents an extensive overview of all aspects of the detector. The following sections summarize the salient features of each subsystem and of the trigger and data acquisition systems.

2.2.1 The magnet system

The overall design of ATLAS was largely determined by the choice of the magnet system, which consists of a superconducting solenoid surrounding the inner detector and a superconducting air-core toroid for the muon system that has a barrel and

two endcap sections. Together, they provide the magnetic field necessary for charged particle momentum measurement over a volume of 12,000 m³. A schematic of the ATLAS magnet system is shown in Figure 2.3.

The central solenoid provides a 2T axial magnetic field for the inner detector. Charged particles bend in the $r - \phi$ plane. The winding is made of Al-stabilised NbTi alloy, cooled to 4.5 K using liquid helium. The diameter and axial length of the solenoid are 2.5 m and 5.3 m respectively, and stores 40 MJ of energy at the full current of 7330 A. The material of the solenoid is equivalent to ≈ 0.66 radiation lengths at normal incidence.

In the toroid, the magnetic field is along the ϕ coordinate, so that charged particles bend in the $r - z$ plane. The barrel toroid has eight racetrack-shaped coils arranged symmetrically in the azimuth. It has inner and outer diameters of 9.4 m and 20.1 m respectively, and a length of 25.3 m. The endcap toroids each contain eight flat coil units and eight keystone wedges bolted and glued together. Each unit is 5 m in length. At the peak current of 20.5 kA, the barrel and endcap toroids provide average fields of 0.5 T and 1 T respectively, and have a combined stored energy of 1.58 GJ. In order to minimize multiple scattering, the toroids were designed with a air core rather than using iron to enhance the magnetic field.

During operation, each coil of the barrel toroid experiences an inward Lorentz force of about 1400 tons [98]. This force is balanced by Al alloy struts in between the eight coils. In the case of the endcap toroids, the force is counteracted by stops mounted on the eight barrel toroid coils.

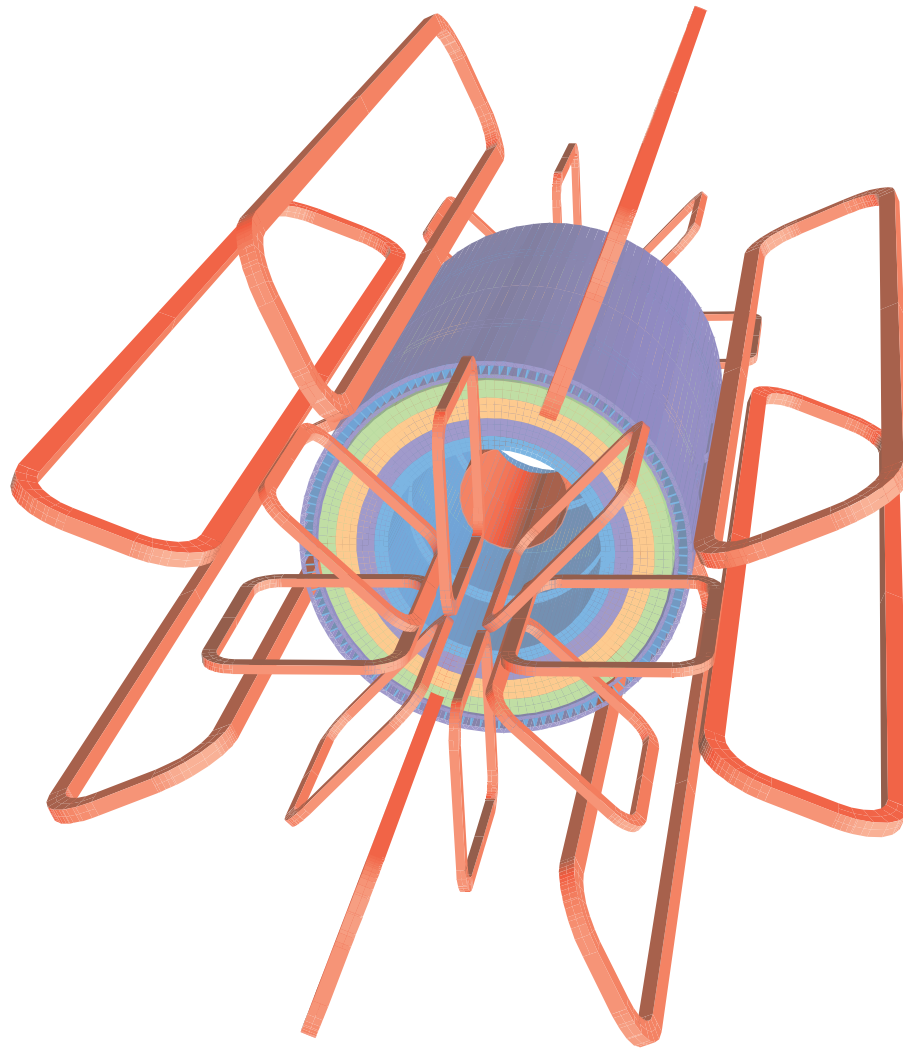


Figure 2.3: Schematic of the ATLAS magnet system. The windings of the barrel and endcap toroids can be seen. Also visible is the tile calorimeter steel, which acts as the flux return for the solenoid. The solenoid is housed inside the calorimeter volume.

2.2.2 The Inner Detector (ID)

The primary purpose of the inner detector is to perform pattern recognition for track finding in a very dense environment. At full design luminosity, $\mathcal{O}(10^3)$ particles will be produced per bunch crossing at 25 ns intervals. To successfully reconstruct charged particle tracks in this environment, the ID must use high-granularity detector elements with a fast response time close to the interaction region. To accurately estimate the momenta of these tracks, the magnetic field inside the ID must be well-mapped¹. In addition, the ID must be capable of precise primary and secondary vertex reconstruction to enable tagging of heavy flavor and τ leptons.

To realize these goals, the ATLAS inner detector has been designed with three components: a silicon pixel detector closest to the beampipe, a silicon microstrip tracker (SCT), and a transition radiation tracker (TRT). The pseudorapidity coverage of the ID is $|\eta| < 2.5$. Figure 2.4 shows a schematic of the ID. The three subdetectors are briefly described below.

The Pixel Detector

The silicon pixel detector largely determines the impact parameter resolution and vertex reconstruction capabilities of ATLAS. The pixel detector contains ≈ 80.4 million pixels, each of dimension $50 \times 400 \mu\text{m}^2$, covering an area of 1.7 m^2 . In the barrel region, there are three pixel layers, with distances from the nominal beam axis of 50.5 mm, 88.5 mm and 122.5 mm. In each endcap region, there are three disks of pixels. The axial coverage of the pixel detector is up to 650 mm on each side of the nominal

¹Since the axial length of the solenoid is smaller than that of the ID, the magnetic field in the ID is non-uniform.

interaction point (IP).

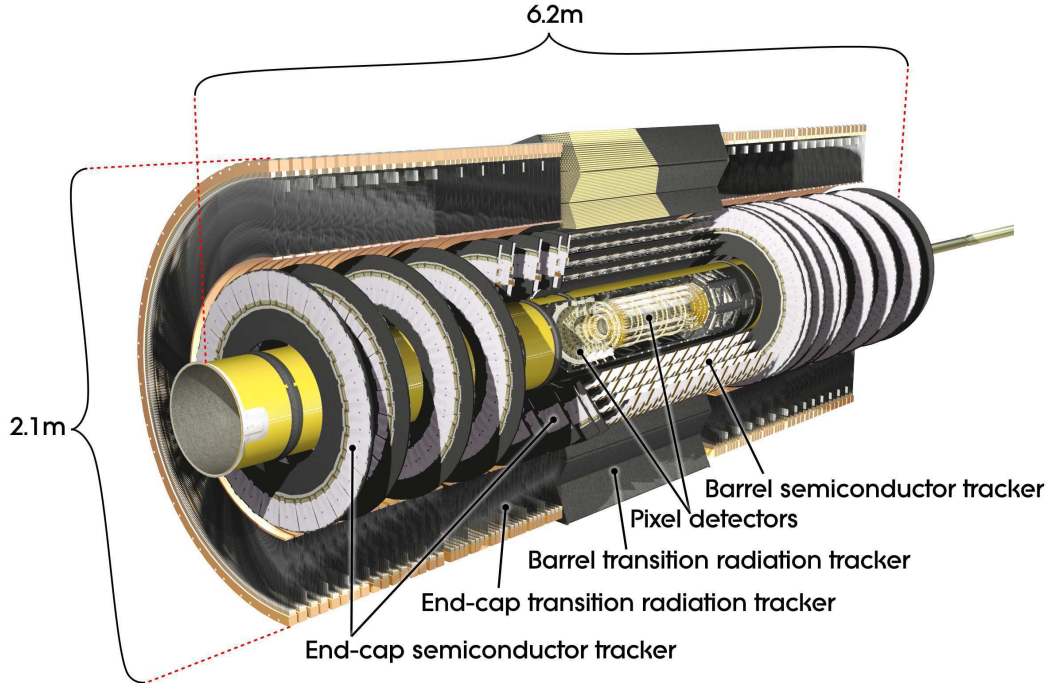


Figure 2.4: A cutaway view of the ATLAS inner detector, showing the various components.

Charged particles passing through the silicon generate electron-hole pairs. A bias voltage applied to the pixel causes the pairs to drift to one side of the pixel where a readout electrode picks up the signal. A track typically crosses three layers of pixels, which provide three-dimensional (3D) space point measurements with $10 \mu\text{m}$ accuracy in $r - \phi$. The barrel layers measure the z coordinate with $115 \mu\text{m}$ precision, while the endcap disks measure the r coordinate with the same accuracy.

The pixels work in a very high-radiation environment: they must withstand a radiation dose equivalent to a 1 MeV neutron fluence of $\approx 8 \times 10^{14} \text{ cm}^{-2}$. In order to keep the noise level minimal after radiation damage, the pixels are operated at

temperatures of -5 to -10°C . Notwithstanding, the innermost layer (the ‘B-layer’) must be changed after three years of operation at design luminosity.

The Semiconductor Detector (SCT)

The SCT consists of four double-sided layers of silicon strips in the barrel, and nine double-sided disks in each endcap region. Each strip is 6.4 cm in length and $80\ \mu\text{m}$ in width. The radial extent of the SCT is up to $r = 560$ mm, and the axial coverage is up to $|z| = 2735$ mm. The SCT has ≈ 6.3 million readout channels. The signal generation process is the same as that for the pixels and, as with the pixels, the SCT is operated at a low temperature in order to maintain a low noise level in spite of radiation damage.

A track typically traverses four SCT layers. In each SCT layer in the barrel region, the strips on one side run parallel to the beamline and provide $r - \phi$ coordinate measurement. The strips on the other side are set at a 40 mrad stereo angle. Because of this relative angle, measurements from strips on the two sides can be combined to obtain z coordinate information. The endcap disks have one set of strips running radially and the other set at a 40 mrad stereo angle to measure the r coordinate. In both regions, the $r - \phi$ resolution is $17\ \mu\text{m}$. The z coordinate is measured to $580\ \mu\text{m}$ in the barrel, and the r coordinate to the same accuracy in the endcap.

The Transition Radiation Tracker (TRT)

The TRT consists of 4 mm diameter straw tubes containing a $Xe/CO_2/O_2$ gas mixture. The body of the tubes is Al-layered polyimide, and the anode is a gold-layered tungsten wire of diameter $31\ \mu\text{m}$. There are 73 planes of tubes in the barrel,

and 160 planes in the endcaps in 18 wheels on each side. The radial extent of the TRT is $r = 1066$ mm. Notably, unlike the silicon detectors, the TRT provides a pseudorapidity coverage only up to $|\eta| = 2.0$. It has $\approx 351,000$ readout channels. Unlike the silicon, the TRT operates at room temperature.

A typical charged particle track is expected to cross 36 straw layers, though this is often not the case in reality, as we will see in Chapter 6. As its name suggests, the TRT acts as both a tracker and a transition radiation detector. Charged particles ionize the gas in the tubes and thereby produce a signal. The straws are interleaved with polypropylene fibers or layers, such that charged particles traversing them emit transition radiation (TR). A TR photon produces a much larger signal in the gas than does a charged particle, and can therefore be easily distinguished from the latter with a higher signal threshold. The probability of a particle emitting a TR photon is proportional to the Lorentz factor $\gamma = E/m$ of the particle. Since, for a given energy, electrons have a much larger γ than other charged particles, the TRT can identify electrons over a large range of energies. Typically, 7-10 high-threshold hits are expected in the straws for electrons with $E > 2$ GeV.

The TRT provides position measurements in $r - \phi$ only, with a precision of $130 \mu\text{m}$ per straw layer. Although the precision of a single measurement is relatively poor, the large number of measurements compensates for it. In addition, the large lever arm of the TRT in the magnetic field significantly improves the track momentum resolution.

The overall transverse momentum resolution of the ID can be parametrized [82] as:

$$\frac{\delta p_T}{p_T} \approx \left(\frac{1.6}{\sqrt{\sin\theta}} \oplus 0.034 \times p_T(\text{GeV}) \right) \% \quad (2.1)$$

where the first term is due to multiple scattering, and the second term corresponds to the intrinsic resolution of the detector components. Therefore, for a 100 GeV track, the p_T resolution is $\approx 5\%$, while it degrades to $\approx 35\%$ for a 1 TeV track².

2.2.3 The Calorimetry

The main purposes of the ATLAS calorimetry are to measure the energies of electrons, photons and jets with as high a precision as possible, and to provide missing transverse energy (E_T^{miss}) measurements. Jet reconstruction in complex multijet environments is a crucial requirement. These goals are important for most physics programs, requiring very good hermeticity of the calorimeters. In addition, the calorimetry must ensure that showers are well-contained within its volume, and that leakage of hadrons (hadronic *punch-throughs*) into the muon system is minimal.

The design of the sampling calorimeters in ATLAS is based on repeated units consisting of absorber layers, in which particles produce showers, followed by sensitive volumes that estimate the energy of shower particles. As usual, the calorimetry has an electromagnetic (EM) component and a hadronic component, with a pseudorapidity coverage $|\eta| < 4.9$. Figure 2.5 shows a cutaway view of the ATLAS calorimetry. It has four subsystems, the main features of which are described below.

The Liquid Argon (LAr) Electromagnetic Calorimeter

The electromagnetic calorimeter measures the energy and position of electrons and photons. It has a barrel section, covering $|\eta| < 1.475$, and two endcap sections,

²Using cosmic tracks, the momentum resolution of the ID was found to be $\approx 5\%$ for 100 GeV tracks. See Figure 23 in [97].

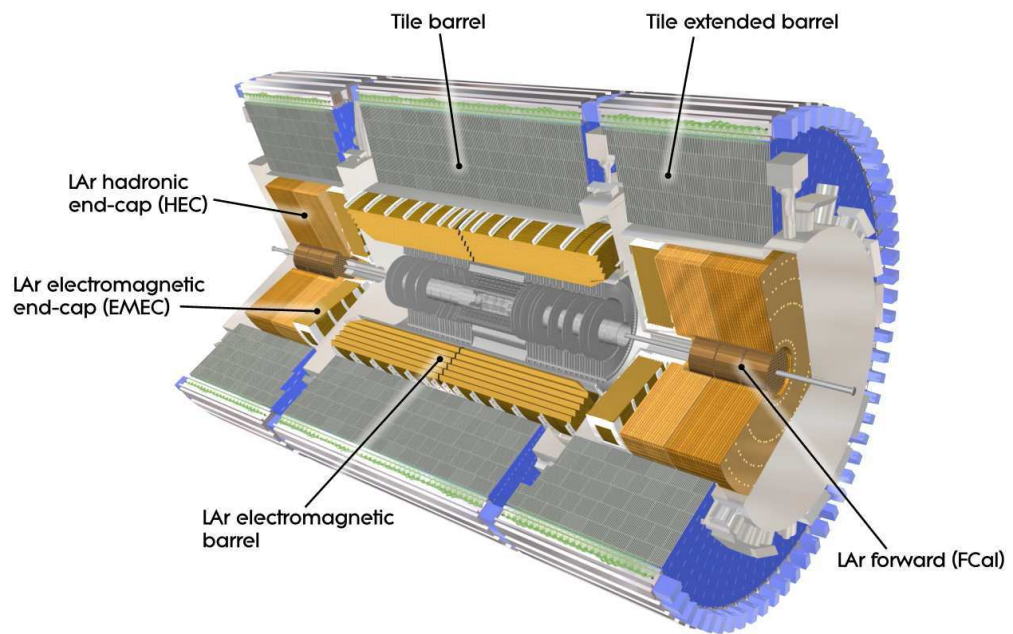


Figure 2.5: Structure of the ATLAS calorimetry, showing the various subsystems.

covering $1.375 < |\eta| < 3.2$. The absorber material is lead, and the active medium is liquid argon. The lead plates and the copper/kapton readout electrodes are arranged in an accordion shape (Figure 2.6). In terms of the *radiation length*³ X_0 , the depth of the EM calorimeter is more than $22 X_0$ in the barrel, and $24 X_0$ in the endcap. The barrel contains about 100,000 readout channels, while the endcaps have about 62,000 channels.

Electrons and photons create showers in the lead plates. The shower particles ionize the liquid argon, the amount of ionization being proportional to the energy of the incident particle. The copper/kapton electrodes collect the signal. The advantage of using liquid argon as the active medium is that it is intrinsically radiation-hard and has a linear behavior with respect to particle energy. The accordion geometry provides full symmetry in the ϕ coordinate without cracks, and allows fast signal extraction at the ends of the electrodes.

The EM calorimeter has three radial segments or *layers*. Layer 1 (Figure 2.6) has a depth of $4.3 X_0$. Its main purpose is to provide excellent resolution in η in order to separate π^0 decay showers from prompt photon showers. The readout is done in fine η strips, the strip size being $\Delta\eta \times \Delta\phi = 0.003 \times 0.1$. Layer 2 has a depth of $16 X_0$ and a cell size of $\Delta\eta \times \Delta\phi = 0.0245 \times 0.0245$. This layer measures shower position. The third layer, of depth $\approx 2X_0$ and cell size $\Delta\eta \times \Delta\phi = 0.05 \times 0.0245$, samples the highest energy electrons and photons.

The energy resolution of the EM calorimeter can be expressed as:

³For a given material, the radiation length is defined as the distance after traversing which an electron has $1/e$ of its original energy left. It is also $7/9$ of the mean free path of pair production for a photon.

$$\frac{\delta E}{E} = \frac{10\%}{\sqrt{E(\text{GeV})}} \oplus 0.17\% \quad (2.2)$$

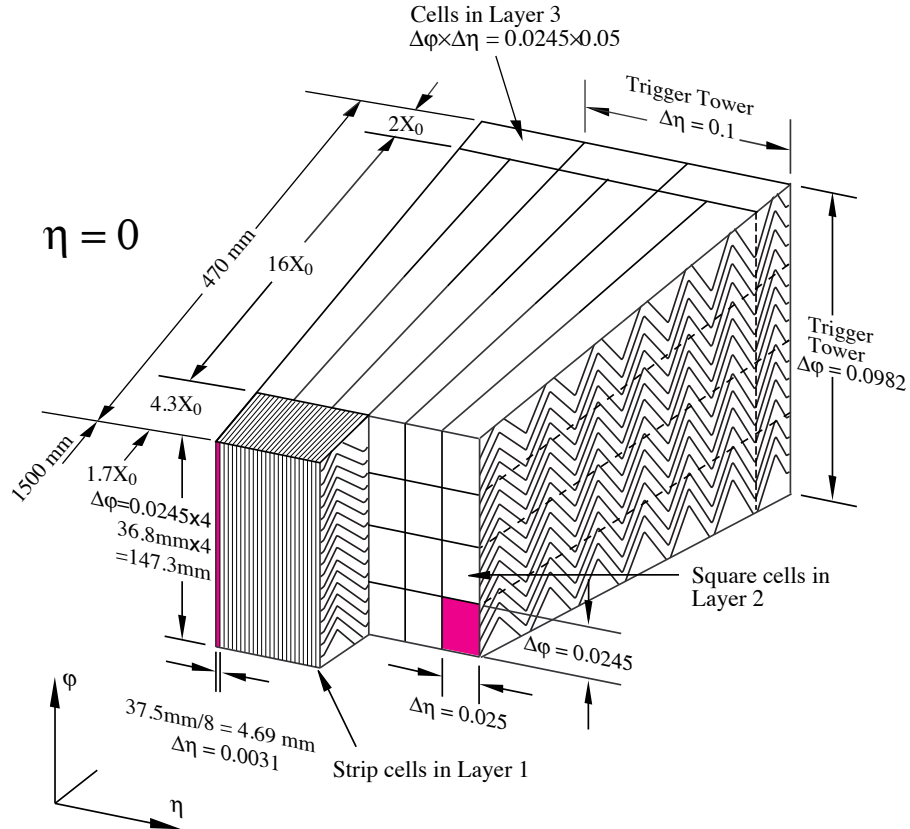


Figure 2.6: Schematic of a liquid argon barrel module in the EM calorimeter. The radial segmentation and the readout cell structure in each segment are visible. The accordion shape of the absorber plates and electrodes are also shown.

where the first term reflects statistical fluctuations in the signal and the second term describes (constant) local inhomogeneities in the calorimeter response [38]. These numbers were obtained from test-beam studies using electrons of various energies.

The presence of the inner detector and the solenoid in front of the EM calorimeter results in a considerable amount of material in which electrons and photons lose energy. This loss results in a systematic error in the energy measurement, and neces-

sitates a shower sampling preceding the calorimetry. This is accomplished by having a *presampler* in front of the EM calorimeter. The presampler covers the region $|\eta| < 1.8$, and consists of an active layer of liquid argon of thickness 1.1 cm in the barrel and 0.5 cm in the endcap. Signal readout occurs via interleaved cathodes and anodes.

The Hadronic Calorimeter

The hadronic calorimeter measures jet energy and position. It has three sections along the z coordinate: a barrel section, which covers $|\eta| < 1.0$, two extended barrel sections, covering $0.8 < |\eta| < 1.7$, and two endcap sections that cover $1.5 < |\eta| < 3.2$. Adjacent sections have some overlap in order to ensure that the material density does not drop near the ends. In the barrel and extended barrel sections, the absorber is steel and the active material is plastic scintillator tiles. The endcaps use copper absorber and liquid argon. In terms of the *interaction length*⁴ λ , the depth of the hadronic calorimeter is $\approx 10\lambda$ in the barrel, between 7 and 14 λ in the extended barrel [14], and between 12 and 16 λ in the endcap.

In the barrel and extended barrel regions, charged particles in hadronic showers produce light in the tiles in the ultraviolet wavelengths, which is converted to visible light by scintillator dyes. The light propagates to the edges of the tiles, where it is absorbed in *wavelength shifting (WLS)* fibers and converted to longer-wavelength light. The fibers guide the light to photomultiplier tubes (PMTs) where it is amplified and measured. Readout cells are built by grouping fibers into the PMTs such that the cells are approximately projective toward the interaction region. The measurement

⁴In a given material, the interaction length of hadrons is the mean free path between successive nuclear interactions.

principle in the endcap is the same as for the EM calorimeter.

The barrel and extended barrel sections each have three radial segments. The cells have dimensions $\Delta\eta \times \Delta\phi = 0.1 \times 0.1$ in the first two layers and $\Delta\eta \times \Delta\phi = 0.2 \times 0.1$ in the third layer. The endcap wheels each have two segments in z .

The energy resolution of the hadronic calorimeter can be expressed as

$$\frac{\delta E}{E} = \frac{52\%}{\sqrt{E(\text{GeV})}} \oplus 3.0\% \quad (2.3)$$

where the first and second terms reflect stochastic fluctuations and constant local inhomogeneities respectively [98]. These numbers were obtained from combined test-beam studies of the tile and liquid argon sections, using pions with an energy-dependent proton component.

The Liquid Argon Forward Calorimeter

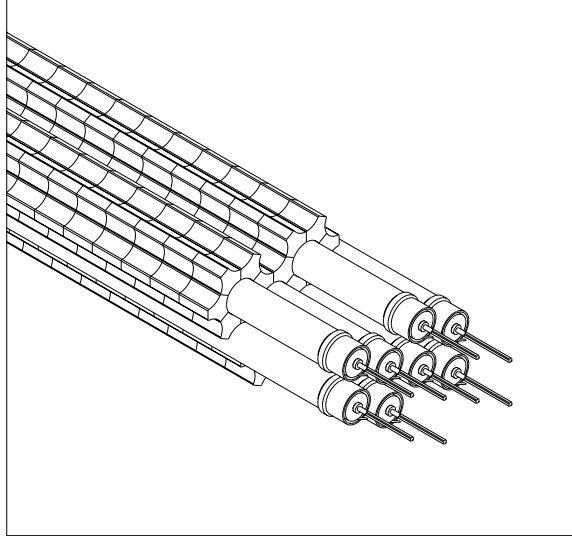


Figure 2.7: Structure of the ATLAS forward calorimeter, showing a set of tungsten rods and copper tubes in a tungsten matrix.

The forward calorimeter (FCal) covers the region $3.1 < |\eta| < 4.9$. It has three

longitudinal segments. The first segment is optimized for electromagnetic measurements, using copper as the absorber. The second and third segments make hadronic measurements and use tungsten absorbers. Each segment contains a metal matrix consisting of holes through which electrode structures have been inserted (Figure 2.7). An electrode is made of a coaxial copper rod and tube arrangement, the gap between the rod and the tube being filled with liquid argon.

Since the FCal is very close to the beampipe, it can potentially suffer from high occupancy. The rod-tube gaps are therefore made very small to minimize ion buildup. The total depth of the FCal is about 10λ .

2.2.4 The Muon Spectrometer

The muon spectrometer (MS) is the outermost subdetector of ATLAS, and determines its overall length and diameter. The function of the muon spectrometer is to measure the position and momenta of particles that exit the calorimetry. Most of these particles will be muons and, in what follows, the term ‘muons’ will refer to all particles traversing the muon system.

As discussed in Section 2.2.1, the muon system contains superconducting air-core toroidal magnets. Muon tracks bend in this magnetic field, so that their momenta can be reconstructed. The momentum measurement can be improved by matching tracks seen in the muon system with those reconstructed in the inner detector (Chapter 4). However, it is also possible to reconstruct tracks in the *standalone* mode using measurements from the muon spectrometer alone. Standalone track reconstruction is feasible over a wide range in transverse momentum from ≈ 4 GeV to ≈ 3 TeV.

The basic performance goal of the muon system, motivated by physics performance, is that the transverse momentum of a 1 TeV track be reconstructed with a resolution of 10% or better. The sagitta of such a track due to bending in the magnetic field will be $\approx 500 \mu\text{m}$, which requires that the sagitta be measured with an error of $\leq 50 \mu\text{m}$. In addition, it is vital that the tracks be associated with the correct bunch crossings. To achieve these goals, the muon system uses several detection technologies, both for precision measurement and for triggering (Figure 2.8). The various technologies will be briefly described below.

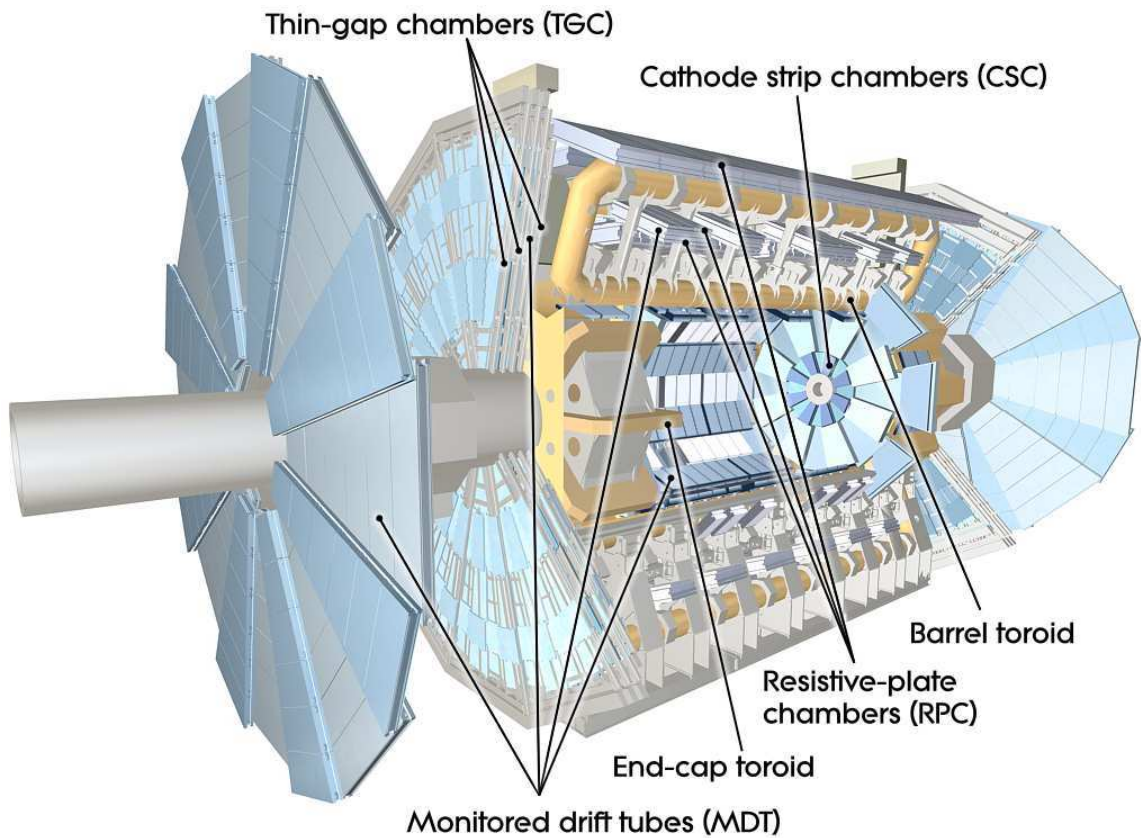


Figure 2.8: A cutaway view of the ATLAS muon system, showing the various technologies used.

Precision measurement technologies

Monitored Drift Tubes (MDTs): The MDTs form the principal component of the muon spectrometer precision measurement system. They cover the region $|\eta| < 1.0$ in the barrel, and $1.0 < |\eta| < 2.7$ in the endcap, except in the innermost endcap layer where the coverage is up to $|\eta| = 2.0$. Each chamber consists of several layers of drift tubes, usually arranged in two *multilayers* (Figure 2.9). Each drift tube has a diameter of 3 cm, with a body made of aluminum and a central (anode) wire made of gold-plated tungsten. The wire has a thickness of $50 \mu\text{m}$ and carries a potential of 3080 volts. The tube contains a gas mixture of Ar/CO_2 in the ratio 93/7, with a trace of water added to improve high-voltage stability.

A charged particle passing through the gas creates electron-ion pairs (Figure 2.10). The electrons accelerate toward the anode under the high voltage, creating further electron-ion pairs and leading to an avalanche. A measurable signal is thus formed. The time taken for the leading edge of the signal to arrive at the anode gives an estimate of the distance from the wire at which the muon passed, known as the *drift radius*. By fitting a straight line through the drift circles in a given multilayer, a segment of the muon track can be reconstructed.

The spatial resolution of a single drift tube is $\approx 80 \mu\text{m}$ in the precision coordinate (z in the barrel and r in the endcap). The resolution of a chamber is $\approx 35 \mu\text{m}$. In the barrel region, the MDTs are arranged in three concentric cylinders (*stations*) around the beampipe, at radii of $\approx 5 \text{ m}$, 7.5 m and 10 m . In each endcap, they are arranged in three wheels perpendicular to the beampipe, at distances of $|z| \approx 7.4 \text{ m}$, 14 m and 21.5 m . The arrangement is such that a muon coming from the interaction region

traverses at least three chambers, referred to as a projective *tower* (Figure 2.11). The total number of channels in the drift chambers is 339,000.

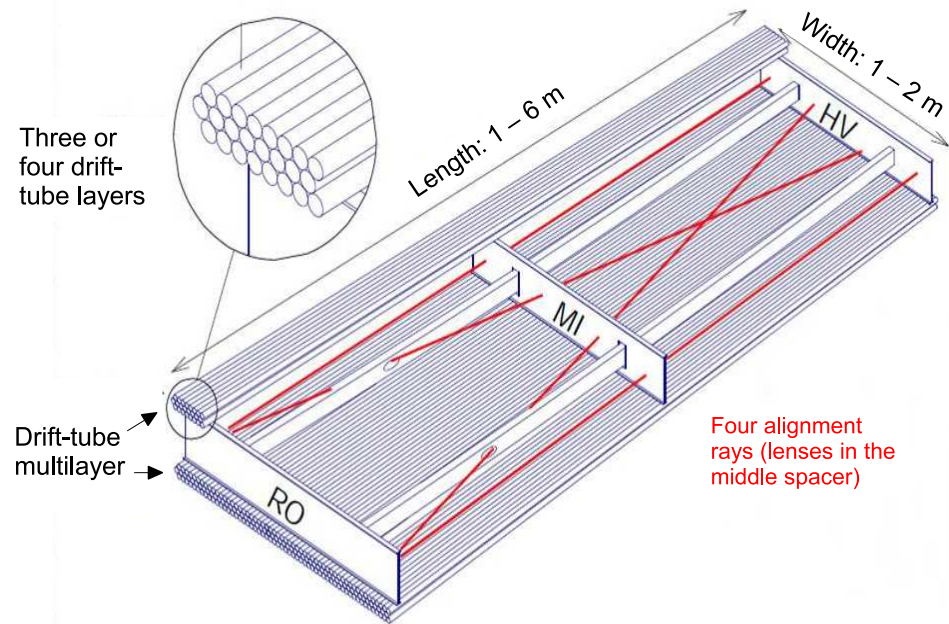


Figure 2.9: The structure of a barrel MDT chamber. Two multilayers of drift tubes and the spacer bars can be seen. The paths of the alignment rays are shown in red.

Cathode Strip Chambers (CSCs): In the very forward region, MDTs suffer from high occupancy because of the large particle flux⁵. In the pseudorapidity range $2.0 < |\eta| < 2.7$, CSCs are used instead of MDTs on the endcap wheel closest to the interaction point. The CSCs are *multiwire proportional chambers*. The mode of operation is similar to that of drift tubes in that charged particles create avalanches of electron-ion pairs in the gas. Each chamber contains four alternating planes of anode wires and cathode strips. The signal from a given track is collected on several

⁵The safe limit of operation for an MDT is a flux of ≈ 150 Hz/cm².

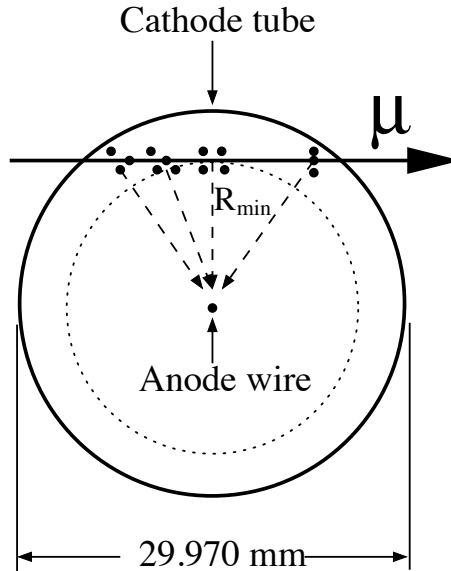


Figure 2.10: Schematic of a drift tube in cross-section. The process of electron-ion pair formation by a passing muon is shown. The dashed circle indicates the drift circle.

electrodes in each plane. By combining information from adjacent cathode strips, the position of the track can be determined with high accuracy.

Strips in the two cathode planes in a CSC chamber are arranged perpendicular to each other, such that both radial and azimuthal coordinates can be measured. The spatial resolution of a chamber is $\approx 40 \mu\text{m}$ in the radial (bending) direction and $\approx 5 \text{ mm}$ in ϕ . The CSCs also have an excellent time resolution of 7 ns. The total number of CSC channels is 30,700.

Trigger technologies

The main requirements on the muon trigger system are fourfold:

- It must be able to roughly estimate the momentum of a track within a few tens of nanoseconds after its passage. This requires fast signal generation and a fine

readout granularity.

- It must associate a track with a particular bunch-crossing, which necessitates a timing resolution better than the 25 ns bunch-crossing interval.
- It should measure the coordinate perpendicular to the precisely measured one (the *second coordinate*) with a resolution of 1 cm or better.
- The trigger chambers must perform well in the presence of a diffuse background of low-energy neutrons and photons in the experimental hall (the *cavern background*).

The ATLAS muon system uses resistive plate chambers for triggering in the barrel region and thin gap chambers in the endcaps. Both technologies satisfy the requirements mentioned above.

Resistive Plate Chambers (RPCs): RPCs are used for triggering in the region $|\eta| < 1.05$. An RPC unit is formed by two parallel plates made of a resistive material, Bakelite in this case, with a 2 mm gas-filled gap between the plates. An electric field of 4900 V/mm exists between the plates, so that a charged particle traversing the gas gap creates an avalanche. The signal is picked up via capacitive coupling by metallic strips mounted on the outer sides of the Bakelite plates. A chamber is formed of two rectangular detector units, each read out by two planes of metallic strips. The strips in the two planes are orthogonal to each other, so that the precision (η) coordinate as well as the ϕ coordinate can be measured⁶.

⁶The measurement of the ϕ coordinate is necessary for track reconstruction, since it gives an estimate of where along the length of an MDT tube the track passed.

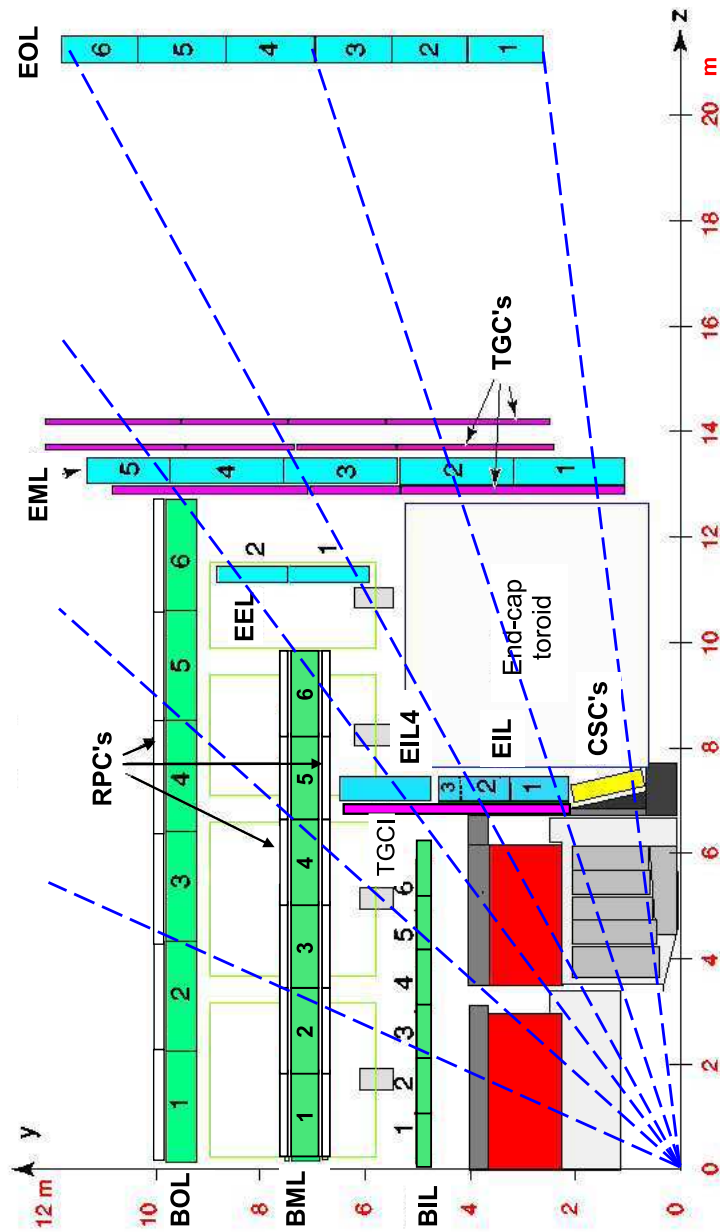


Figure 2.11: rz view of the ATLAS muon system. Trajectories followed by infinite-momentum tracks are shown.

The spatial resolution of an RPC chamber is 10 mm in both η and ϕ coordinates, while the time resolution is 1.5 ns. The signal width is only 5 ns, making accurate bunch-crossing identification possible. The total number of RPC channels is 359,000. Note that, because of space constraints due to the ‘feet’ of the detector, barrel toroid support structures and various services for the muon spectrometer, the $\eta - \phi$ coverage of the RPC chambers is about 80%.

The RPCs are arranged in three concentric stations around the beam axis. There is one station each on the bottom and top faces of the middle barrel MDT chambers, known respectively as the *low- p_T plane* and the *pivot plane*. The third station is on the outer barrel MDT chambers (Figure 2.12), known as the *high- p_T plane*. If there is a hit on the pivot plane, the trigger logic checks for hits in the low- p_T plane in a defined road and within the same 25 ns time window as that of the pivot plane hit. If a hit is found, the logic issues a low- p_T trigger, defined as $4 \text{ GeV} < p_T < 10 \text{ GeV}$. In order to minimize fake decisions, hits in at least three of the four RPC layers in the two stations are required. If a low- p_T trigger has been issued, the logic looks for at least one hit in the high- p_T plane in a defined road and within the same time window. If a hit is found, a high- p_T trigger is issued, defined as $p_T > 10 \text{ GeV}$.

Thin Gap Chambers (TGCs): In the endcap region, radiation levels are ≈ 10 times higher than in the barrel, so that finer granularity is needed of the trigger system than RPCs can provide. In addition, in the endcap the track momentum corresponding to a given value of p_T increases faster than the bending power of the magnetic field, which means an increased trigger granularity is needed to match the

p_T resolution of the barrel⁷. TGCs have the required high rate capability as well as good time resolution. They cover the region $1.05 < |\eta| < 2.7$, although signal from beyond $|\eta| = 2.4$ is not used for triggering. The TGCs are arranged in four wheels in each endcap, one before the endcap toroid, and three after the toroid (Figure 2.12). Only the three wheels after the toroid are used for triggering.

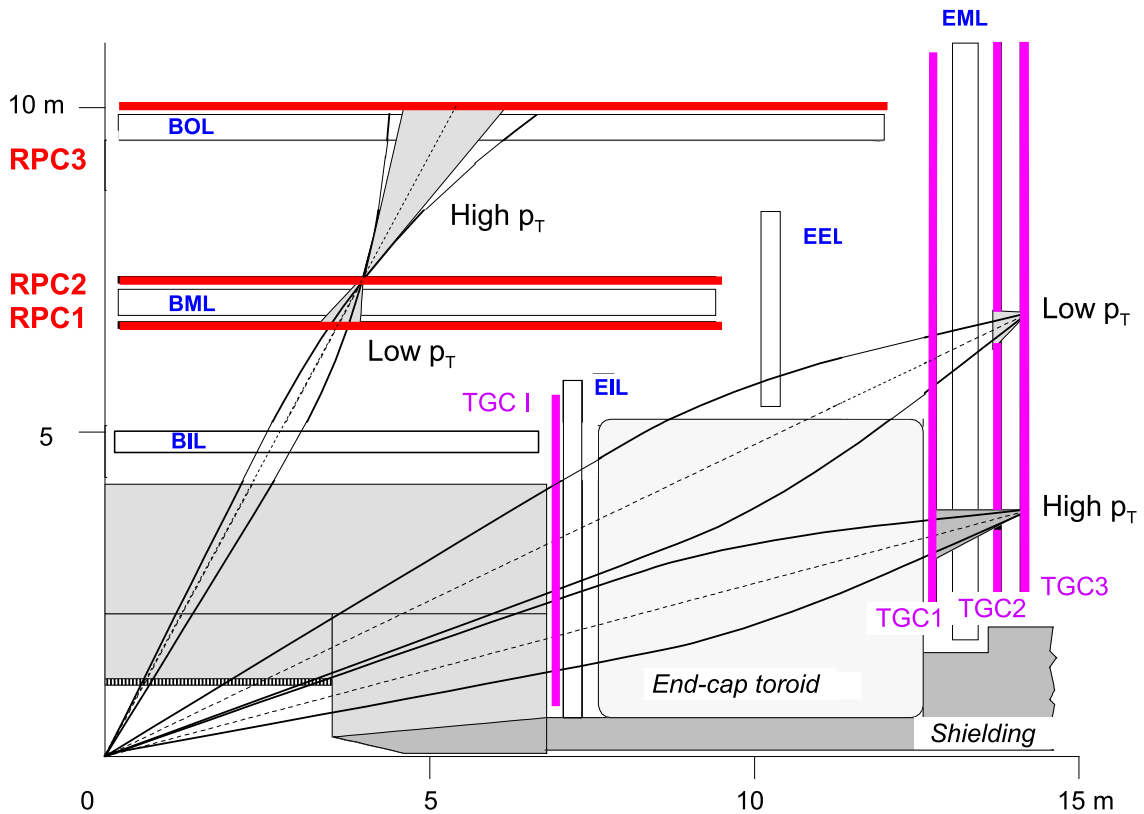


Figure 2.12: Schematic of the ATLAS muon trigger system. The triggering schemes for high- p_T and low- p_T tracks are indicated.

TGCs are multiwire proportional chambers, with the anode-cathode distance

⁷For example, at $|\eta| = 2.4$, the momentum of a track is $5.8 \times p_T$, while the integrated bending power⁸ of the magnetic field is only about twice that at $|\eta| = 0$ [98].

smaller than the distance between adjacent anode wires. This feature and the high applied potential of 3100 V ensure fast signal generation. The anode wires are arranged parallel to the MDT wires, while the cathode (readout) strips run in the radial direction. This configuration enables measurement of both the radial and azimuthal coordinates. The spatial resolution of a TGC chamber is 2-6 mm in r and 3-7 mm in ϕ . The time resolution is 4 ns. The signal arrives within a 25 ns time window with a probability of 99%. The total number of TGC channels is 318,000.

As in the case of the RPCs, triggering in the TGCs uses a coincidence condition in two or more trigger stations, depending on the track p_T . Coincidence is required in both the η and ϕ projections, thus minimizing the probability of accidental triggers caused by random combinations of converted photons.

Magnetic field in the muon system

The toroids that provide the magnetic field for the muon spectrometer have been briefly described in Section 2.2.1. The barrel toroid covers the pseudorapidity range $|\eta| < 1.4$, and has a bending power of 1.5-5.5 Tm. The endcap toroids cover the region $1.6 < |\eta| < 2.7$, providing a bending power of 1-7.5 Tm. In the *transition region* $1.4 < |\eta| < 1.6$, the field is provided by both the barrel and endcap toroids, which leads to considerable field inhomogeneity. The bending power is smaller in the transition region than in the barrel and endcaps.

In order to satisfy the precision required of the muon system, the magnetic field in the spectrometer must be accurately reconstructed. To this end, all three components of the field are continuously monitored by ≈ 1800 Hall sensors throughout

the spectrometer. Readings from the Hall sensors, accurate to 5 gauss, are stored in the Detector Control System (DCS) database. By comparing the measurements with a simulation, it is possible to fit for the position of the toroid coils. The goal is to estimate the bending power along a muon trajectory to a few parts in a thousand.

Alignment of muon chambers

As mentioned before, physics performance goals require that the accuracy of position measurement on a muon track be better than $\approx 50 \mu\text{m}$. Given that the position resolution of a precision chamber is $\approx 35 - 40 \mu\text{m}$, the alignment of the chambers themselves must be known to an accuracy of $\approx 30 \mu\text{m}$. Since it is not possible to keep the chambers stable to this accuracy, an optical alignment system is in place to continuously monitor the positions and deformations of the precision chambers. The optical alignment system has been shown to satisfy the accuracy required. Using the alignment data, displacements of up to $\approx 1 \text{ cm}$ can be corrected for during offline track reconstruction [15].

About 12,000 precision-mounted optical sources and cameras monitor the internal deformation of chambers as well as their relative positions. The MDT chambers are equipped with an in-plane alignment system which monitors MDT wire displacement at the level of $10 \mu\text{m}$ 2.9. Alignment of chambers within a projective tower is accomplished by defining a grid of optical lines that monitor the position of chambers. The required accuracy for the relative positioning of different towers is \approx few mm, which was achieved during the initial positioning of the chambers.

Not all MDT chambers are connected by the optical grid. Some chambers in the

barrel, for example, must be aligned using straight tracks that pass through overlap regions between these chambers and others that are connected to the optical grid⁹. Track-based alignment must also be used to monitor the relative alignment of the barrel and the endcap muon systems, and of the muon system and the inner detector. Finally, track-based alignment provides a cross-check on the optical alignment system.

2.2.5 Trigger and Data Acquisition System (TDAQ)

The goal of the trigger system is to select physically interesting events for permanent storage. It also reduces the high event rate to an acceptably small value that the storage hardware can handle. At the design LHC luminosity of $10^{34} \text{ cm}^{-2} \text{ s}^{-1}$, about 20 hard interactions are expected to occur per bunch-crossing. At a bunch-crossing rate of 40 MHz, this implies 10^9 events per second. On the other hand, available resources limit output to the storage to about 300 Hz. Hence, the trigger system must decrease the event rate by up to seven orders of magnitude. To accomplish this, ATLAS has three levels of trigger: Level-1, a hardware trigger, and Levels -2 and -3, both software triggers.

The DAQ system is responsible for data movement, starting from the front-end readout electronics to the transfer of raw events to the permanent storage. Figure 2.13 shows a block diagram of the ATLAS trigger and data acquisition system. The various parts of the system are summarized below.

The Level-1 (L1) trigger is implemented in the calorimetry and the muon system. Using information from muon trigger chambers and reduced-granularity information

⁹A large number of straight tracks were obtained during runs with the magnetic fields turned off.

from the calorimeters, the L1 trigger looks for signatures that may indicate physics of interest, such as high-energy electrons, photons, jets, τ leptons, large missing energy and/or total energy, and high- p_T muons. Another function of the L1 trigger is to define *Regions of Interest* (RoI's), *i.e.*, regions of the detector in which interesting activity has been found. RoI's are used for seeding the Level-2 trigger. The L1 trigger takes about $2.5 \mu\text{s}$ to make an accept/reject decision, which is equivalent to 100 bunch crossings at the 25 ns crossing interval. This duration is known as the trigger *latency*. The maximum L1 accept rate which the readout systems can accommodate is 75 kHz, upgradeable to 100 kHz.

The front-end readout electronics of each subdetector contains data buffers known as *pipelines*. Pipelines in the muon system and the calorimetry have enough depth to hold data for the L1 latency of $2.5 \mu\text{s}$. Upon an L1 accept decision, data from the relevant cells is transferred to *Readout drivers* (RODs).

The Level-2 (L2) trigger looks only at the RoI's defined by L1. It has access to full-granularity information from all subdetectors within the RoI's. The information, extracted from the relevant RODs, amounts to $\approx 2\%$ of the total event data for a typical event [98]. The L2 trigger has a latency of about 40 ms, and decreases the event rate to 3.5 kHz.

Events selected by the L2 trigger are transferred to the event builder, which is the first stage of the Level-3 (L3) trigger. The event builder uses elaborate algorithms to fully reconstruct events using information from the entire detector. The reconstructed events are then moved to the Event Filter (EF), which performs the final selection of events to be written to mass storage. The EF typically takes 4 seconds to process

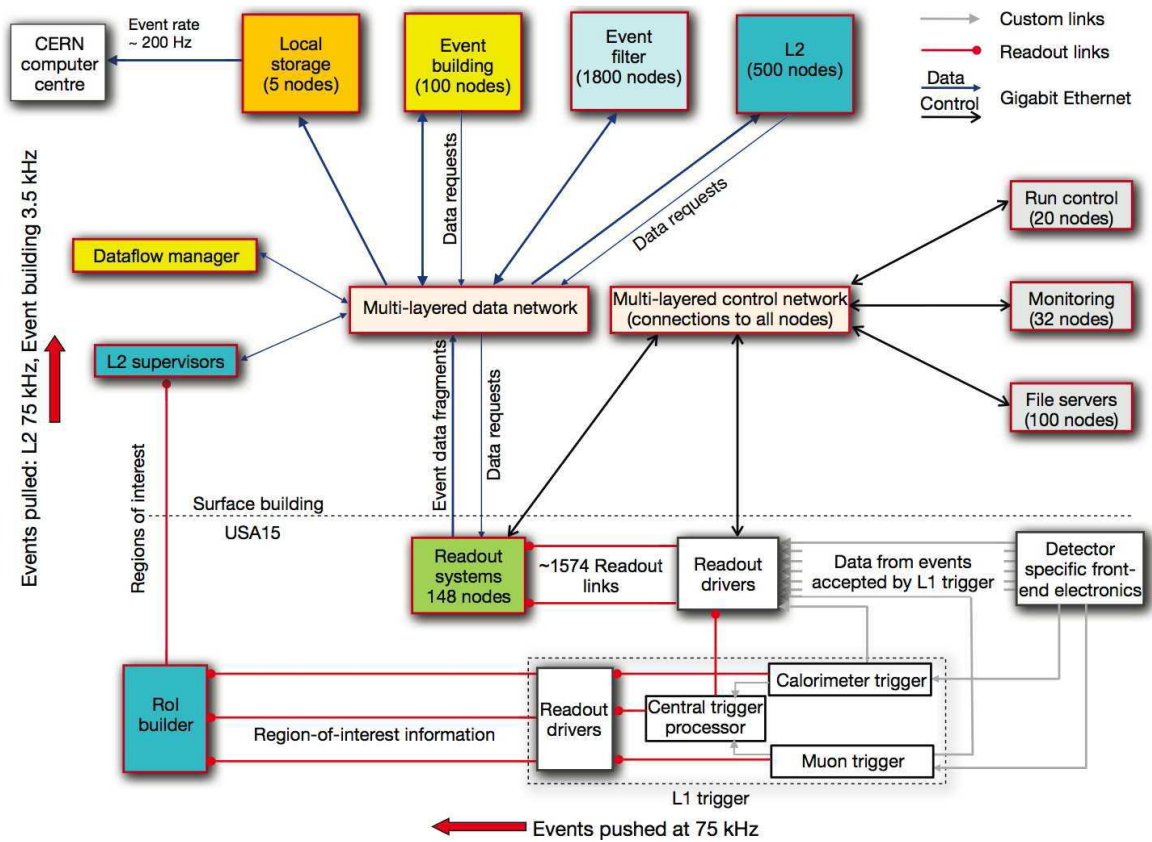


Figure 2.13: Block diagram of the ATLAS trigger and DAQ system. The accept rates at various trigger stages are shown.

an event, and reduces the event rate to 300 Hz. The size of a raw event is $\mathcal{O}(1 \text{ MB})$. The amount of data recorded by ATLAS in a year is of the order of a Petabyte (10^{15} bytes).

Besides controlling data movement among the trigger levels, the TDAQ system manages the configuration, control and monitoring of the detector via the *Detector Control System* (DCS). The DCS is an interface to all the subdetectors and the infrastructure of ATLAS. It monitors operational parameters such as temperature, magnetic field, high- and low-voltage systems and gas systems, and provides for bidirectional communication with the TDAQ.

Chapter 3

Luminosity Measurement at the LHC and in ATLAS

For a physics process p , the instantaneous luminosity L is the proportionality factor between the event rate $\frac{dR_P}{dt}$ and the cross-section σ_P :

$$\frac{dR_P}{dt} = L\sigma_P \quad (3.1)$$

The integral L_{int} of the instantaneous luminosity with respect to time is an estimate of the total amount of ‘data’ in a given run or set of runs. Knowledge of L_{int} is therefore vital for measuring the cross-sections of physics processes. The uncertainty in L_{int} is often the dominant source of uncertainty in such measurements and, therefore, the accurate determination of integrated luminosity is of prime importance in any high-energy physics experiment.

A number of methods exist for determining the luminosity at hadron colliders. The following are routinely used:

- parameters of the colliding beams
- purpose-built detector systems integrated with the experiments

- physics processes for which the cross-sections are known with high accuracy

In this chapter, we review the basic concepts underlying these three methods and describe their implementation at the Large Hadron Collider and in the ATLAS experiment. In Section 3.1, we derive an expression for instantaneous luminosity in terms of beam parameters, and discuss modifications due to several factors. Section 3.2 is an overview of the technologies used by the Beams Division to monitor the beam parameters necessary to compute instantaneous luminosity. In Section 3.3, we present a summary of the various detectors and processes that are or will be used by ATLAS for luminosity monitoring.

3.1 Luminosity measurement using beam parameters

In the 2010 run, instantaneous luminosity was measured using parameters of the beams, so that we will discuss this technique in some detail. For two colliding beams, it can be shown [58] that the instantaneous luminosity L is proportional to an overlap integral:

$$L \propto K \int \int \int \int_{-\infty}^{+\infty} \rho_1(x, y, s, -s_0) \rho_2(x, y, s, s_0) dx dy ds ds_0 \quad (3.2)$$

where ρ_1 and ρ_2 are time-dependent density distribution functions for the two beams, s is the longitudinal coordinate (along the beampipe), and $s_0 = ct$ is the distance of each beam from the central collision point, equivalent to a time-variable. K is a kinematic factor which equals 2 for head-on collisions. If we assume that the densities are uncorrelated in all three planes, $\rho_{1,2}$ can be factorized to give the expression:

$$L = 2N_1N_2fN_b \int \int \int \int_{-\infty}^{+\infty} \rho_{1x}(x)\rho_{1y}(y)\rho_{1s}(s-s_0)\rho_{2x}(x)\rho_{2y}(y)\rho_{2s}(s+s_0)dx dy ds ds_0 \quad (3.3)$$

where N_1 and N_2 are the number of particles in each bunch of the two beams, f is the beam revolution frequency and N_b is the number of bunches in each beam. We assume here that each bunch in each beam contains the same number of particles, which is not strictly true¹.

In hadron colliders, the bunches have approximately Gaussian profiles in all three coordinates². In the case of perfectly Gaussian profiles, Eq. 3.3 can be written as:

$$L = \frac{2N_1N_2fN_b}{(\sqrt{2\pi})^6\sigma_s^2\sigma_x^2\sigma_y^2} \int \int \int \int_{-\infty}^{+\infty} e^{-\frac{x^2}{\sigma_x^2}} e^{-\frac{y^2}{\sigma_y^2}} e^{-\frac{s^2}{\sigma_s^2}} e^{-\frac{s_0^2}{\sigma_s^2}} dx dy ds ds_0 \quad (3.4)$$

where σ_i is the Gaussian width of the beam in the i th coordinate, for $i = x, y, s, s_0$.

Performing the integrations, we get:

$$L = \frac{N_1N_2fN_b}{4\pi\sigma_x\sigma_y} \quad (3.5)$$

This expression applies to the ideal case of Gaussian beams colliding head-on. In practice, there can be several effects that require modifications to the ideal case. We will discuss three such effects:

- crossing angle
- offset beams

¹In particular, the so-called ‘pacman’ bunches degrade faster, and hence have a smaller number of particles, than ‘regular’ bunches during the lifetime of a beam. Pacman bunches are bunches at the extreme ends of a bunch train. However, bunch trains were not used during the data-taking period that our measurement is based on, and consequently this effect was not present.

²In reality, the shapes deviate from the ideal Gaussian. In the LHC, such deviation is expected to reduce the luminosity by up to 5% compared to the ideal case [21]. We will not discuss this point further.

- hourglass effect

3.1.1 Crossing angle

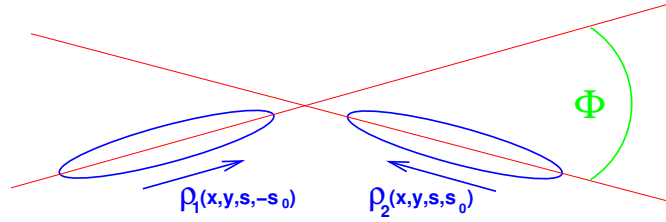


Figure 3.1: Schematic view of two bunches colliding at a non-zero crossing angle.

In machines with a large number of bunches per beam, the bunches are made to collide at an angle in order to avoid unwanted (‘parasitic’) collisions between bunches (Figure 3.1). For example, the LHC will have 2808 bunches in each beam at design luminosity, and a crossing angle of $285 \mu\text{rad}$ will be used. Obviously, a non-zero crossing angle leads to a smaller instantaneous luminosity compared with the ideal case.

Assuming that the crossing angle is in the horizontal plane and consists of two rotations of $\phi/2$ and $-\phi/2$ of the two beams in the x - s plane, the overlap integral in expression 3.4 can be written as:

$$L = \frac{N_1 N_2 f N_b}{(8\pi)^2 \sigma_s \sigma_x^2 \sigma_y} \int \int \exp\left(-\frac{x^2 \cos^2 \frac{\phi}{2} + s^2 \sin^2 \frac{\phi}{2}}{\sigma_x^2}\right) \exp\left(-\frac{x^2 \sin^2 \frac{\phi}{2} + s^2 \cos^2 \frac{\phi}{2}}{\sigma_s^2}\right) dx ds \quad (3.6)$$

Since x and $\sin \frac{\phi}{2}$ are both small, and assuming $\sigma_s \gg \sigma_{x,y}$, the result of the integrations can be simplified [21] to the form:

$$L = \frac{N_1 N_2 f N_b}{4\pi\sigma_x\sigma_y} S, \quad (3.7)$$

where

$$S = \frac{1}{\sqrt{1 + \left(\frac{\sigma_s}{\sigma_x} \tan \frac{\phi}{2}\right)^2}} \approx \frac{1}{\sqrt{1 + \left(\frac{\sigma_s}{\sigma_x} \frac{\phi}{2}\right)^2}}. \quad (3.8)$$

No crossing angle was used during the data-taking period that this analysis is based on, but was introduced later in the 2010 run as the number of bunches per beam increased and the bunch spacing decreased.

3.1.2 Offset beams with finite crossing angle

A further complication arises when the beams collide with a small offset in the transverse plane. In the following treatment, we assume without loss of generality that the offset is along the x -axis only. If the beams are offset by d_1 and d_2 from their reference orbits, the luminosity can be expressed as

$$L = \frac{N_1 N_2 f N_b}{8\pi^{\frac{3}{2}} \sigma_s} 2 \cos^2 \frac{\phi}{2} \int_{-\infty}^{+\infty} W \frac{e^{-(As^2 + 2Bs)}}{\sigma_x \sigma_y} ds \quad (3.9)$$

where

$$W = \exp\left(-\frac{1}{4\sigma_x^2} (d_1 - d_2)^2\right), \quad (3.10)$$

$$A = \frac{\sin^2 \frac{\phi}{2}}{\sigma_x^2} + \frac{\cos^2 \frac{\phi}{2}}{\sigma_s^2}, \quad B = \frac{(d_1 - d_2) \sin \frac{\phi}{2}}{2\sigma_x^2}. \quad (3.11)$$

We can now rewrite the luminosity as:

$$L = \frac{N_1 N_2 f N_b}{4\pi\sigma_x\sigma_y} S W e^{\frac{B^2}{A}}. \quad (3.12)$$

Note that the last factor $e^{\frac{B^2}{A}}$ is different from unity only in the simultaneous presence of a crossing angle and a transverse offset.

3.1.3 Hourglass effect

Up to now we have assumed that the transverse size of a bunch is constant over the entire collision region. However, the beams are usually focused near the interaction point (IP) to decrease the transverse size and thereby increase instantaneous luminosity. In other words, the β -functions of the beams have minima at the IP³ and increase with distance from the IP (Figure 3.2). When the β -function at the IP approaches the longitudinal bunch size σ_s , the two colliding bunches do not cross the entire length of each other with the minimum transverse size, and this results in a decrease of the luminosity.

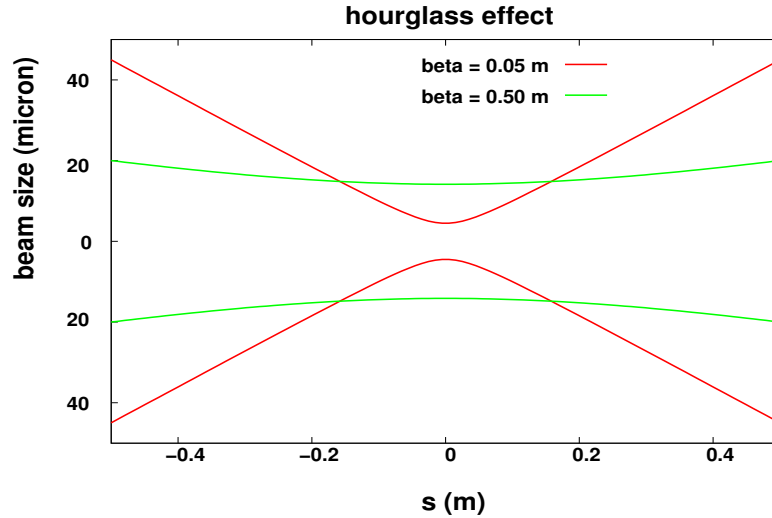


Figure 3.2: Illustration of the hourglass effect. The shape of the beam at the IP is shown for two different values of β^* .

³Near a collision region, there are quadrupole magnets which focus the beam toward the IP. The paths taken by the particles in a bunch form a hyperbola, whose shape is determined by the parameter β^* . More formally,

$$\beta(s) = \beta^* \left(1 + \left(\frac{s}{\beta^*} \right)^2 \right)$$

where s is the longitudinal coordinate.

In the presence of the hourglass effect, the luminosity can be expressed as:

$$L = \frac{N_1 N_2 f N_b}{8\pi\sigma_x\sigma_y} \frac{2\cos^2\frac{\phi}{2}}{\sqrt{\pi}\sigma_s} \int_{-\infty}^{+\infty} \frac{e^{-As^2}}{1 + \left(\frac{s}{\beta^*}\right)^2} ds, \quad (3.13)$$

where

$$A = \frac{\sin^2\frac{\phi}{2}}{\sigma_x^2[1 + \left(\frac{s}{\beta^*}\right)^2]} + \frac{\cos^2\frac{\phi}{2}}{\sigma_s^2}. \quad (3.14)$$

Usually, this expression has to be evaluated numerically.

Note that during the April-July 2010 run, the LHC used $\beta^* 3.5 \text{ m} \gg \sigma_s$, so hourglass effects were negligibly small.

3.2 Determination of beam parameters relevant to luminosity measurement

From expression 3.5, the parameters needed to measure the instantaneous luminosity are the number of bunches per beam, the revolution frequency, the number of particles per bunch and the transverse beam sizes. The first two parameters are accurately known in a collider. The uncertainty in the luminosity determination comes from knowledge of the number of particles per bunch, measured using beam current transformers, and the determination of beam sizes. In this section, we discuss the methods employed for these measurements at the LHC. In addition, we briefly review the technologies used for beam profile measurement and beam pickups.

3.2.1 Beam current measurement at the LHC

The LHC employs two types of beam current transformers to measure the intensity of circulating beams, namely fast beam current transformers and DC beam current

transformers.

Fast beam current transformers (FBCTs): The FBCTs are capable of integrating the current of each LHC bunch. Their operating principle is illustrated in Figure 3.3 [66].

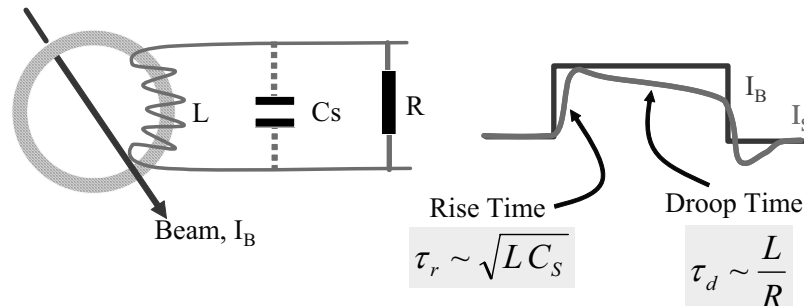


Figure 3.3: Operating principle of a fast beam current transformer.

The beam current, I_B , acts as the primary winding of the transformer. The secondary winding has an inductance L , resistance R and (stray) capacitance C_s . It generates an output voltage $V = L \frac{dI_B}{dt}$, with a risetime proportional to $\sqrt{LC_s} \approx 10$ ps [55]. The output waveform closely resembles the beam current, with a DC offset due to the transformer droop which can be corrected via software upon digitization. Fast integrators, working at repetition rates of up to 40 MHz, enable the estimation of the total charge in each bunch.

Two FBCTs with separate acquisition chains are used in the LHC in each ring. Each beam dump line also has two FBCTs to monitor the intensity of ejected beams.

DC beam current transformers (BCTDCs): BCTDCs measure the mean current of an entire circulating beam, and can also be used to measure the beam lifetime. The basic principle is to make use of the hysteresis in a pair of toroidal ferromagnetic

cores.

The two cores are driven into saturation with a current at frequency F_{mod} in the modulation windings. With no beam present, when equal but opposite modulation currents are applied to the cores, the induced voltages on the detection windings are also equal but opposite. However, when there is a beam, the beam current generates a static magnetic field in the cores, which offsets the hysteresis loop for zero modulation current. Consequently, since the modulation is opposite in the two cores, the time spent in saturation is different for the two branches of the hysteresis loop. When the induced voltages in the two detection windings are combined and demodulated, the result is a series of voltage pulses with the pulse width being directly proportional to the beam current.

Each LHC ring has two BCTCDs. Their current resolution is $2 \mu\text{A}$, corresponding to $\approx 10^9$ protons [66]. At design luminosity, each LHC beam will have 4.8×10^{14} protons [1], corresponding to a circulating current of $0.582 \mu\text{A}$, so that the measurement accuracy will be $\approx 10^{-6}$. A beam lifetime of about 25 hours because of pp collisions implies a decay rate of $\approx 5 \times 10^9$ protons/s. With a measurement time of 10 s, the BCTDCs are able to measure this rate, and therefore the expected beam lifetime, with a precision of $\approx 1\%$.

Note that comparison between bunch-by-bunch current measurements from the fast transformers, summed over all bunches, and the total beam current measured with the DC transformers gives information about the size of longitudinal beam tails.

3.2.2 Beam size measurement using Van der Meer scans

An accurate method of measuring the transverse beam size is to displace the beams against each other and monitor the relative luminosity as a function of the beam separation (Figure 3.4). Known as separation scans or Van der Meer scans, this method can also be used to minimize the beam separation in order to maximize instantaneous luminosity.

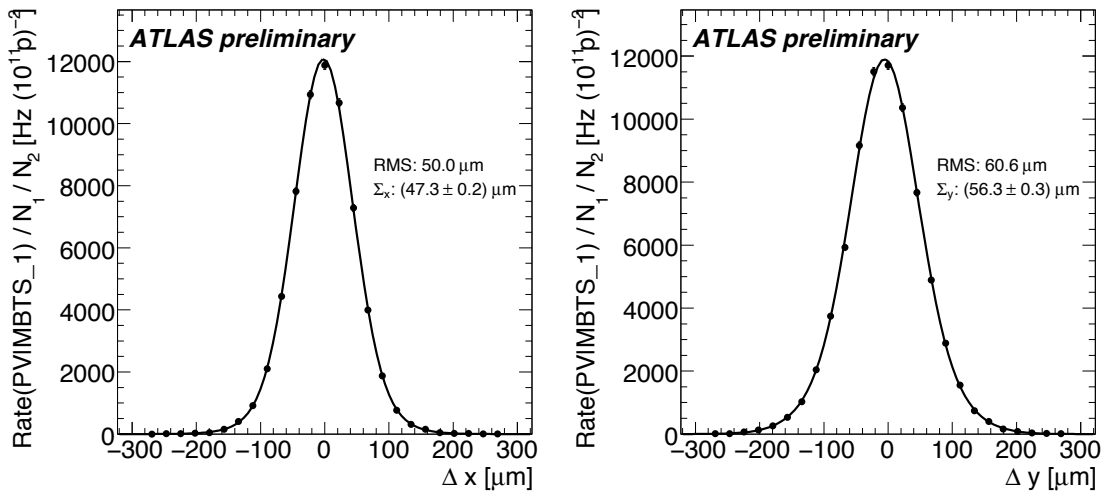


Figure 3.4: Variation in the rate of primary vertices seen in the ATLAS inner detector as the two beams are displaced relative to each other in the horizontal plane (*left*) and in the vertical plane (*right*). The beam size in each direction obtained from the double Gaussian fit is shown.

The luminosity reduction due to offset beams is given by formula 3.10:

$$W = \exp\left(-\frac{d^2}{4\sigma_i^2}\right) \quad (3.15)$$

where d is the beam separation along the i th axis, and $i = x, y$. A fit of the observed variation in luminosity, as shown in Figure 3.4 [58], to the above expression gives the beam size. The scans are performed separately in the horizontal and vertical

directions. Several sets of scans have been performed in ATLAS during the 2010 data-taking [94], the results from one of which is shown in Figure 3.4. In this case, the rate of production of primary vertices was monitored in the ATLAS inner detector as the beams were displaced against each other. Each distribution was fitted with a double Gaussian with a common mean. The beam sizes thus determined were $47.3 \pm 0.2 \mu\text{m}$ and $56.3 \pm 0.3 \mu\text{m}$ respectively in the horizontal and vertical planes. We see that the accuracy from the fits is at the per mille level.

3.2.3 Beam profile measurement

Several technologies are used at the LHC for measuring beam profile (bunch shape) in the transverse and longitudinal directions. We will briefly discuss three of them:

- scintillator and optical transition radiation monitors
- wire scanners
- synchrotron light monitors

Scintillator and optical transition radiation (OTR) monitors: The basic concept here is to place a thin metal screen in the beam path. A scintillator screen is usually a doped alumina foil, usable only for low-intensity beams. Beam particles produce scintillation photons, which can be observed on a TV screen. An OTR monitor consists of a very thin titanium screen. Charged particles traversing the interface between vacuum and the metal screen emit transition radiation photons. Two cones for backward OTR are produced around the angle of reflection, as well as

two cones of forward OTR (Figure 3.5) [66]. Consequently, if the screen is placed at 45° to the beam direction, the photons can be collected as shown.

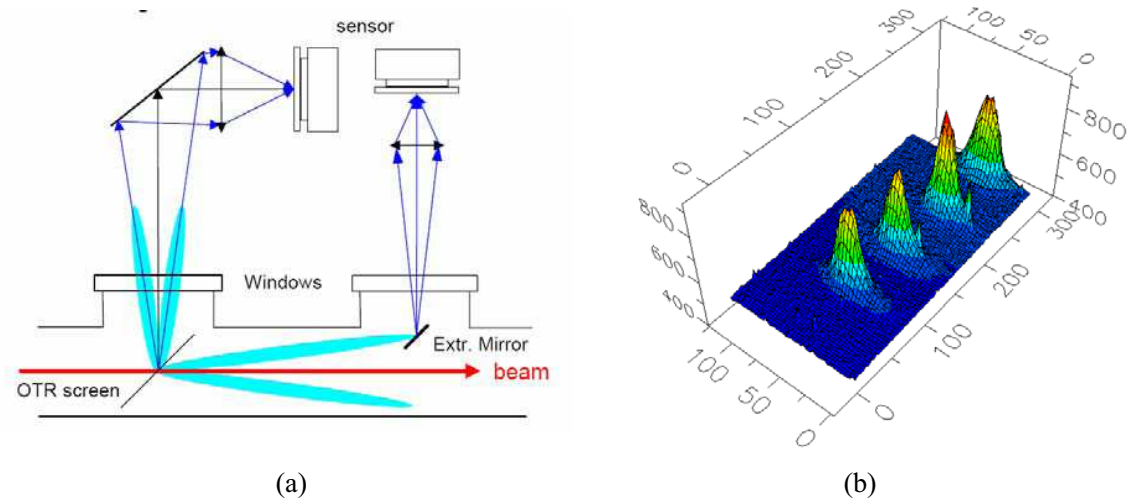


Figure 3.5: (a) Backward and forward optical transition radiation patterns, (b) An example of a 2-dimensional OTR image taken every four turns at injection at the CERN SPS. The transverse beam dimensions can be determined from the image.

The photon emission probability scales with γ_p , the Lorentz factor of the beam particles. The angular distribution of the emitted photons is peaked at $\frac{1}{\gamma_p}$. Hence, OTR screens are suitable for high-energy beams. They can also withstand higher intensities compared to scintillator screens. The LHC employs scintillator and OTR monitors in the injection lines, in the ring and in the beam dump lines [5].

Figure 3.6 shows the image of a beam spot in the transverse plane after a single-bunch beam has passed through a scintillator screen. The image is produced on a so-called BTV (Beam TeleVision). The bunch contained 2×10^9 protons, and was in fact the first beam circulated in the LHC, on September 10, 2008.

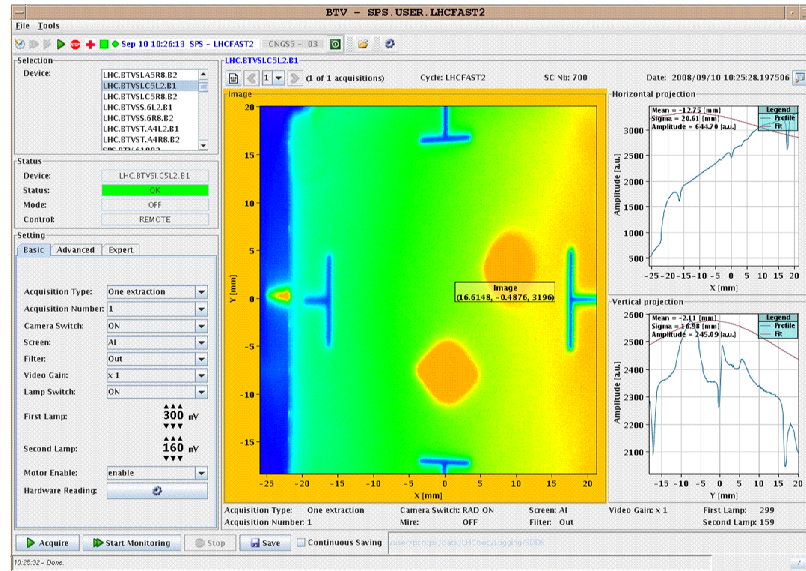


Figure 3.6: Image of an LHC beam spot produced with a scintillator screen and viewed on a TV. This image was taken at the LHC Interaction Point 3 on September 10, 2008.

Wire scanners: Wire scanning involves shooting a thin wire through the beam. As the beam particles hit the wire, secondary particles are emitted which lead to a current in the wire. Measuring this current as a function of the wire position yields a profile of the beam. Another way to map the beam profile is to measure the flux of the secondary particles using scintillators and photomultipliers placed downstream of the scanner. Wire scanners can be of two types: rotative scanners, in which the wire is mounted on a fork attached to a rotating motor, and linear scanners, in which the motor pushes or pulls the wire across the beam.

Wire scanners can be used over a wide range of beam energies, with resolutions as good as a few microns [66]. The LHC uses them in IP4. Their principal use is for absolute calibration of other profile monitors, but they can also be used as beam tail

monitors⁴ [1].

Synchrotron radiation monitors: Monitors based on synchrotron radiation emission provide a non-destructive and continuous way to map out the transverse density distribution of the beam. In the LHC, synchrotron light is produced by 5T superconducting undulators⁵ or ‘wiggler’ magnets that deflect the beam several times in the transverse plane within a short interval [1]. Their positioning in IP4 is shown in Figure 3.7. The synchrotron light is extracted 10 m downstream of the D3 magnets using a telescope assembly and recorded with a CCD camera [39], providing a 2-dimensional transverse image of the beam. The transverse beam size resolution using synchrotron monitors is expected to be 15-18%.

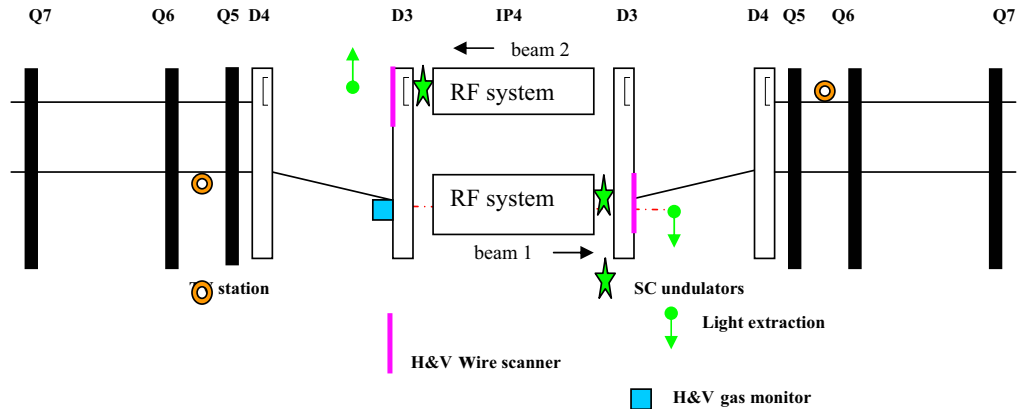


Figure 3.7: Configuration of transverse profile monitors at LHC Interaction Point 4: wire scanners, undulator magnets and gas monitors.

⁴Particles in the tail of the beam transverse distribution are counted in the beam current measurement, but contribute marginally to the luminosity; the core of the distribution accounts for most of the luminosity. Hence, transverse tails introduce an error in the luminosity measurement, and monitoring them is crucial for reducing this error.

⁵An undulator is a periodic magnet structure that uses interference to concentrate synchrotron radiation in a cone in the forward direction along the beam path. For details, see [39].

The synchrotron light source can also be used to measure bunch length and the longitudinal beam profile. Part of the synchrotron radiation generated by the undulators is collected by a separate mirror located behind the transverse optics. About 2×10^6 photons are expected to be collected for each bunch of 1.15×10^{11} protons. The photon flux reproduces the time and intensity profiles of the beam, so that longitudinal measurements can be made.

3.2.4 Beam position monitors

Beam position monitors (BPMs) measure the transverse position of the beam, and are used extensively in any accelerator complex. Inside linacs and transfer lines, they are used to measure and correct beam trajectories. They also measure beam trajectories inside synchrotrons. In particular, the first turn trajectory measurement is vital for closing the orbit on itself. Once a closed orbit has been established, BPMs continuously monitor beam position on a turn-by-turn or even bunch-by-bunch basis. Data from the BPMs is used for beam-related measurements such as Van der Meer scans.

The basic concept behind most BPMs is electrostatic or electromagnetic pickup from the beam by devices placed inside the beam-pipe. We will briefly describe the most commonly used beam pick-up technology at the LHC, namely button pickups.

Button pickups: These are electrostatic pickups with button-shaped electrodes, thus the name (Figure 3.8). As a beam of charged particles travels along the metal beampipe, it induces an image charge on the pipe wall. The image charge mimics the longitudinal profile of the beam and travels at the same speed as the beam. A button

pickup collects this charge at certain locations in the beampipe. The amplitude of the signal is proportional to the beam (or bunch) intensity and inversely proportional to the distance of the beam from the pickup device.

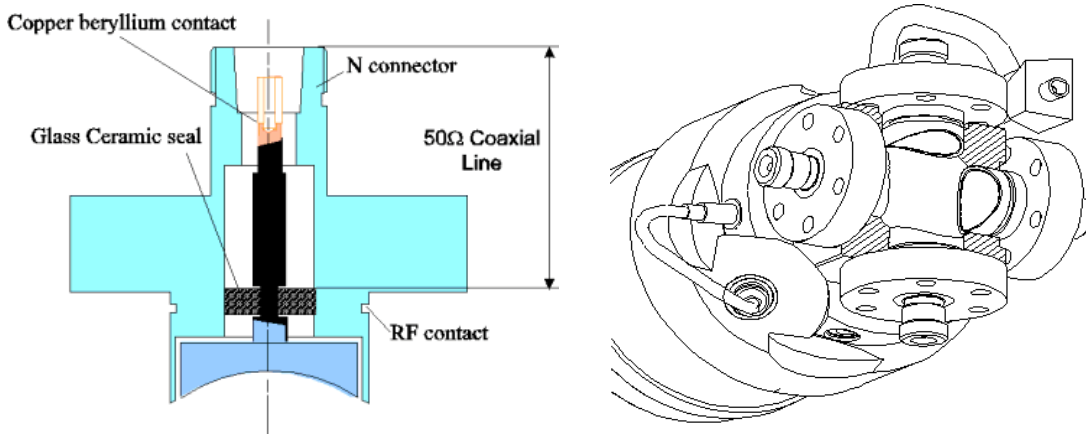


Figure 3.8: (*Left*) Structure of a 24 mm LHC button electrode; (*right*) configuration of a mounted BPM consisting of four button electrodes, two each for horizontal and vertical beam position monitoring.

The button-type BPM used in the LHC consists of two pairs of button electrodes placed symmetrically in the beam pipe, one pair for measuring the horizontal beam position and the other for the vertical position. Since the signal induced in each electrode in a pair depends on the distance of the beam from the electrode, the beam position can be determined by comparing the signals from the two electrodes. First, however, the signals must be normalized in order to make them independent of beam intensity. At the LHC, this is done by a process known as Wide Band Time Normalization (WBTN) [66]. The signal from each electrode is split and recombined with a delayed signal from the other electrode. This results in two signals whose relative zero-crossing time depends on the beam position. The electronics works at 40 MHz, enabling bunch-by-bunch position monitoring.

A total of 1058 BPMs are used in the LHC ring: 922 in the main arcs and beam dispersion suppressors, 68 in the interaction regions, 44 in the beam cleaners at IP3 and IP7, and 24 special BPMs for transverse damping and tune and chromaticity measurements at IP4. In addition, the beam transfer lines from the SPS to the LHC contain 100 BPMs.

3.2.5 The BRAN detectors for relative luminosity measurement

The BRAN (Beam RAtE Neutrals) detectors are relative luminosity monitors installed in the four LHC collision points (IP1, IP2, IP5 and IP8). They reside inside the TAN (Target Absorber Neutrals) on each side of a collision point. Figure 3.9 shows the layout of a collision point and the location of the BRAN monitors.

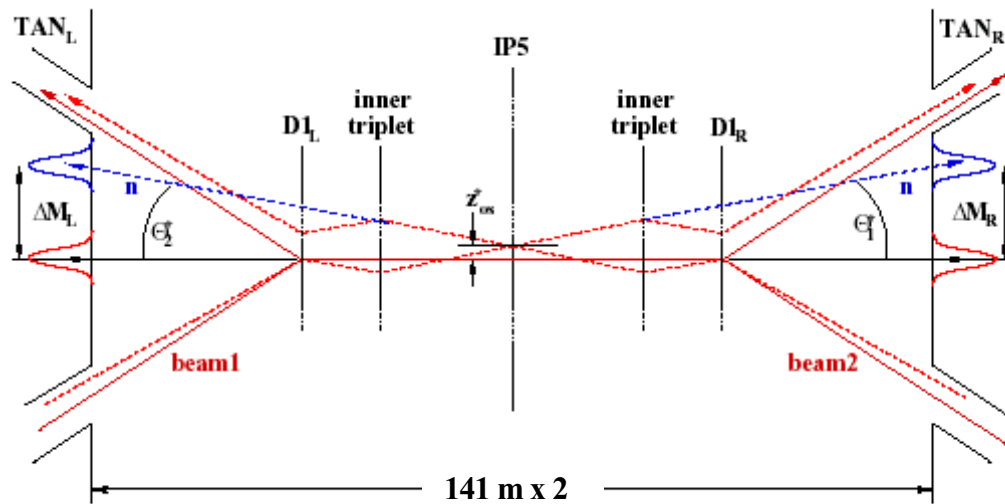


Figure 3.9: Layout of Interaction Point 5 (CMS), showing the TAN absorbers and signals in the BRAN monitors (*not to scale*).

The purpose of the BRAN monitors is to provide a relative luminosity estimate for machine optimization, *not* for use by the experiments to calculate physics cross-

sections. Hence, calibration for absolute luminosity is not essential. The monitors are used to estimate bunch-to-bunch variation in luminosity, so that they have the bandwidth of individual bunch crossings, namely 40 MHz. The physics process to monitor was chosen to be diffractive events in which at least one incoming proton dissociates into a neutron and other secondary particles. The properties of this process are well known, so that the cross-section at LHC design energies can be estimated with a precision of about 10% [66].

The neutrons are emitted into a small solid angle in the forward direction. Forward-going charged particles from the interaction are deflected away by the dipole magnets $D1_L$ and $D1_R$ (Figure 3.9), but the neutrons continue in a straight line collinear with the incoming bunches. Detectors placed in a direct flight path from the IP therefore intercept neutral particles only.

The BRAN detectors consist of two designs. The BRAN-A, used at IP1 and IP5 (ATLAS and CMS), are pressurized gas ionization chambers installed inside the TAN at a depth where the hadronic energy deposition is maximal (behind ≈ 30 cm of copper [1]). The BRAN-B are cadmium-telluride solid-state detectors used at the low-luminosity interaction points IP2 and IP8.

3.3 Luminosity monitoring in ATLAS

From 2011 onward, ATLAS is expected to use ALFA, a fiber tracker installed in Roman Pots, for absolute luminosity calibration. Two other subdetectors, namely LUCID and BCM, can deliver relative luminosity information, LUCID being the detector used for this purpose during the 2010 run. Additionally, a number of methods

can be used to determine relative integrated luminosity offline. In this section, we will briefly describe the subdetectors used for online luminosity monitoring and some of the processes potentially useful for offline luminosity estimation.

3.3.1 ALFA

The ALFA (Absolute Luminosity For Atlas) detector measures the elastic scattering rate at very small angles, and uses the optical theorem to relate this rate to the total cross-section and the luminosity. The total inelastic and elastic collision rates measured in an experiment are related to the luminosity and the total cross-section:

$$\dot{N}_{inel} + \dot{N}_{el} = L\sigma_{tot} \quad (3.16)$$

For small values of momentum transfer t^6 , the total cross-section is related to the elastic cross-section by the optical theorem:

$$\lim \frac{d\sigma_{el}}{dt} = \frac{1}{L} \frac{d\dot{N}_{el}}{dt} \Big|_{t=0} \quad (3.17)$$

But the elastic scattering amplitude can be expressed as a superposition of the Coulomb scattering amplitude f_c and the strong scattering amplitude f_s . So we can write:

$$\lim \frac{d\sigma_{el}}{dt} = \frac{1}{L} \frac{d\dot{N}_{el}}{dt} \Big|_{t=0} = \pi |f_c + f_s|^2 \approx \pi \left| \frac{2\alpha_{em}}{-t} + \frac{\sigma_{tot}}{4\pi} (\rho + i) e^{B\frac{t}{2}} \right|^2 \approx \frac{4\pi\sigma_{em}^2}{t^2} \Big|_{|t| \rightarrow 0} \quad (3.18)$$

where ρ is the interference parameter between the Coulomb and strong interference terms [58] and B is the nuclear slope parameter. If $\frac{d\sigma_{el}}{dt}$ is measured accurately,

⁶ t is a Mandelstam variable, defined as $t = (p_1 - p_3)^2 = (p_2 - p_4)^2$, where p_1, p_2 are the 4-momenta of the particles incoming to a collision, and p_3, p_4 are the 4-momenta of the particles outgoing from a collision.

σ_{tot} , L , ρ and B can be determined from a fit.

This method has been applied by various collaborations to measure the total elastic cross-section. Figure 3.10 shows measurements of $\frac{d\sigma_{el}}{dt}$ down to very small values of $|t|$ made by a number of experiments. The predicted measurements at the LHC are shown as well, together with estimations of the number of events expected per day at nominal luminosity in two different beam conditions [102].

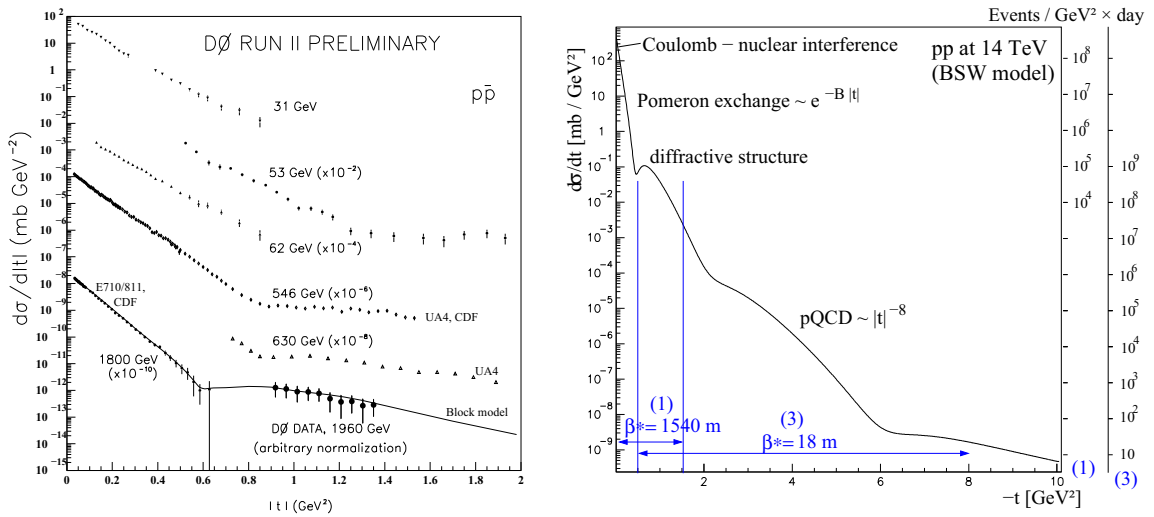


Figure 3.10: Elastic scattering cross-section measurements as a function of the momentum transfer t : (left) in proton-antiproton collisions in various experiments from the ISR to the Tevatron; (right) prediction for proton-proton collisions at the LHC at $\sqrt{s} = 7 \text{ TeV}$.

Access to the Coulomb-strong interference region requires measurement at very small angles from the beam direction, down to $\approx 3 \mu\text{rad}$, so that detector elements must be placed very close to the beam. The measurement also demands low beam intensity ($L \approx 10^{27} - 10^{28} \text{ cm}^{-2}\text{s}^{-1}$) and zero crossing angle. In addition, the beam divergence must be small, so that special runs with a high β^* at the IP are needed, e.g., with $\beta^* = 2630 \text{ m}$ at IP1 (ATLAS) [16].

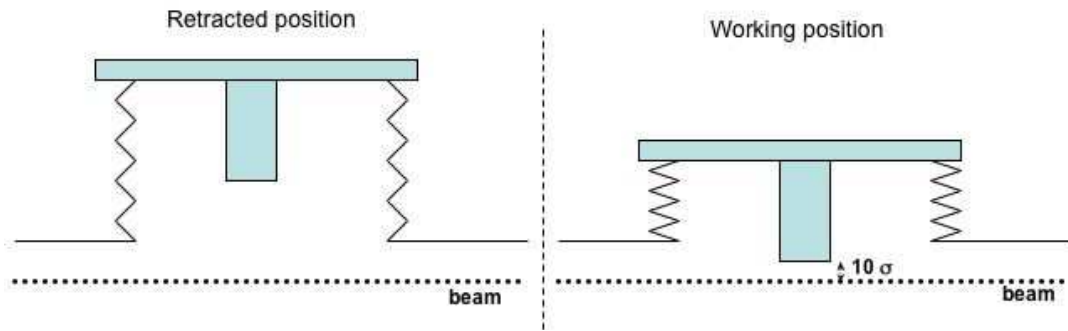


Figure 3.11: Concept of a Roman Pot. The detector is attached to a movable frame. In the working position during the special runs (*right*), the detector approaches the beam very closely, within $10\sigma_{x/y}$ or about 1 mm. During normal running, it is retracted away from the beam (*left*).

The ALFA detector consists of plastic scintillator fibers housed in so-called Roman Pots, whose working principle is illustrated in Figure 3.11. Each Roman Pot unit contains two pots, which approach the beam from top and bottom in the special runs. There are two Roman Pot units separated by 4 m on each side of the IP about 240 m away. The pseudorapidity coverage of ALFA is $11 < |\eta| < 13.5$.

The sensitive area in each Roman Pot consists of ten ceramic plates, each supporting two layers of 64 fibers. The two layers are rotated by 90° with respect to each other. The achievable spatial resolution from a single plane is $14.4\ \mu\text{m}$ [16]. The scintillation light from the fibers is routed to multi-anode photomultipliers. Figure 3.12 shows a cut-away view of a Roman Pot unit with the various parts indicated.

The precision of the luminosity measurement from ALFA is expected to be 2-3% [13]. The Roman Pots have already been installed in the LHC tunnel. Fiber tracker construction is complete, and testbeam measurements were taken during 2010. The complete installation will take place during the LHC shutdown in winter 2010-11.

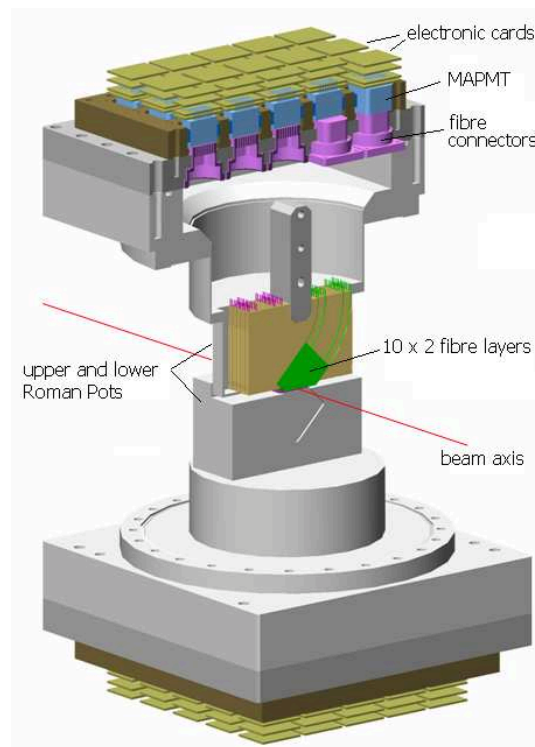


Figure 3.12: An ATLAS Roman Pot unit, with the upper and lower pots shown. Also indicated are the fiber layers, the multi-anode photomultiplier tubes (MAPMTs) and the front-end electronics [16].

3.3.2 LUCID

LUCID (*LU*minosity measurement with a *Cherenkov Integrating Detector*) is the dedicated luminosity monitor for ATLAS, designed to operate over the full dynamic range of the LHC. It measures relative luminosity by detecting inelastic pp scattering in the forward direction. The detector consists of two aluminum vessels, 1.5 m long and ≈ 30 cm in diameter, placed around the beampipe ≈ 17 m from the IP. Each vessel contains 20 aluminum tubes filled with C_4F_{10} gas, arranged in two concentric circles, and projective to the IP (Figure 3.13). The pseudorapidity coverage is $5.5 < |\eta| < 6.1$. LUCID can operate independently of the Level 1 trigger, and indeed of the trigger and data acquisition system. This implies that it can measure the delivered luminosity in addition to the luminosity recorded by ATLAS.

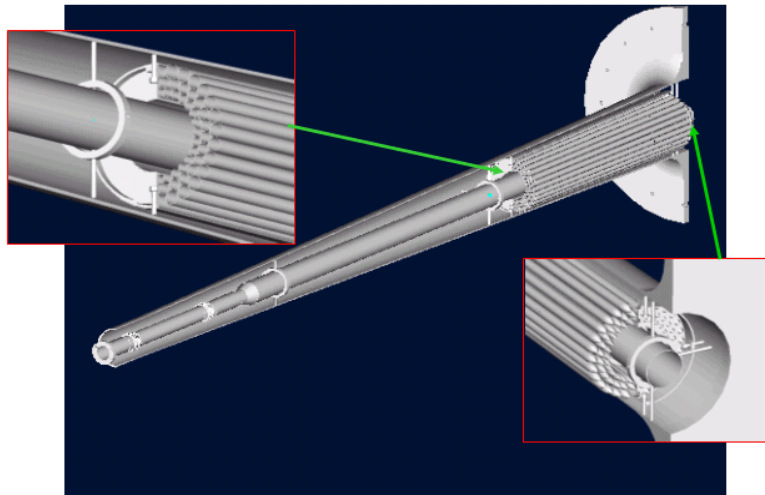


Figure 3.13: Configuration of the LUCID tubes. Their positioning between the beampipe and the conical beampipe support tube is shown.

A charged particle passing through a tube gives off Cherenkov radiation, which reaches the end of the tube after 3 reflections on average. The Cherenkov detection

threshold is 2.5 GeV for pions and 10 MeV for electrons. The tubes are read out by PMTs. When the instantaneous luminosity increases above $10^{33} \text{ cm}^{-2}\text{s}^{-1}$, the plan is to increase the number of tubes on each side to 168, and to replace the PMTs by scintillation fibers [23].

The fast response time of LUCID ($\approx 3 \text{ ns}$) allows it to measure bunch-by-bunch luminosity. Signals due to secondary particles are minimal owing to two factors: firstly, the Cherenkov threshold suppresses low-energy particles; secondly, the projective geometry leads to a shorter path length in the gas for secondary particles than for primary particles from the IP. Since the number of Cherenkov photons is directly proportional to the path length in gas, secondaries produce a relatively small signal.

LUCID measurements must be calibrated with absolute luminosity measurements obtained in parallel from some other source. Once LUCID has been calibrated, its measurements can be used over a wide range of beam conditions that may not be suitable for absolute measurement devices such as ALFA. As discussed before, in the 2010 run the calibration to absolute luminosity was done using beam parameters. Upon calibration, the overall accuracy of the luminosity measurement was 11%, the dominant contribution coming from beam current measurement [94]. From 2011 onwards, the calibration is expected to use ALFA measurements, with an achievable accuracy of $\approx 3\%$. Over the long term, physics processes with well-measured cross-sections can also be used for the calibration, but the accuracy of this method depends on theoretical uncertainties in the cross-sections, as discussed in Section 1.5.

3.3.3 BCM

The main purpose of the BCM (*Beam Conditions Monitor*) is to protect ATLAS and vital beamline components in the event of beam instabilities. For example, several proton bunches hitting a TAS (*Target Absorber Secondaries*) collimator can lead to very high secondary particle densities that will damage the experiment. The BCM can detect the initial stage of such an incident and abort the beam. The particle showers in these anomalous cases originate well away from the ATLAS IP, so that if two BCM detectors are placed symmetrically about the IP, the shower particles will reach them with a time difference Δt (Figure 3.14). By contrast, particles from collisions at the IP will reach both detectors simultaneously. A coincidence condition can therefore distinguish between the two types of events. This configuration also enables the BCM to provide bunch-by-bunch collision rate and instantaneous luminosity, making it potentially useful as a luminosity monitor.

Each BCM station is suspended from the beampipe support structure at a radius of ≈ 55 mm from the nominal beam axis. They are located at $z = \pm 183.8$ cm, corresponding to a pseudorapidity of ≈ 4.2 . For a particle coming from one side of the IP, such as from a TAS event, the time difference between the signals at the two stations will be 12.5 ns.

A BCM station consists of four diamond sensor modules each of area 10×10 mm², placed symmetrically about the beampipe at an angle of 45° (Figure 3.15). Diamond sensors have a large drift carrier velocity, enabling a fast signal rise-time (≈ 1 ns) and a narrow pulse (≈ 3 ns), so that operation at the nominal collision frequency of 40 MHz will be possible. In addition, leakage current due to radiation damage should

be very small so that no cooling is needed to minimize noise.

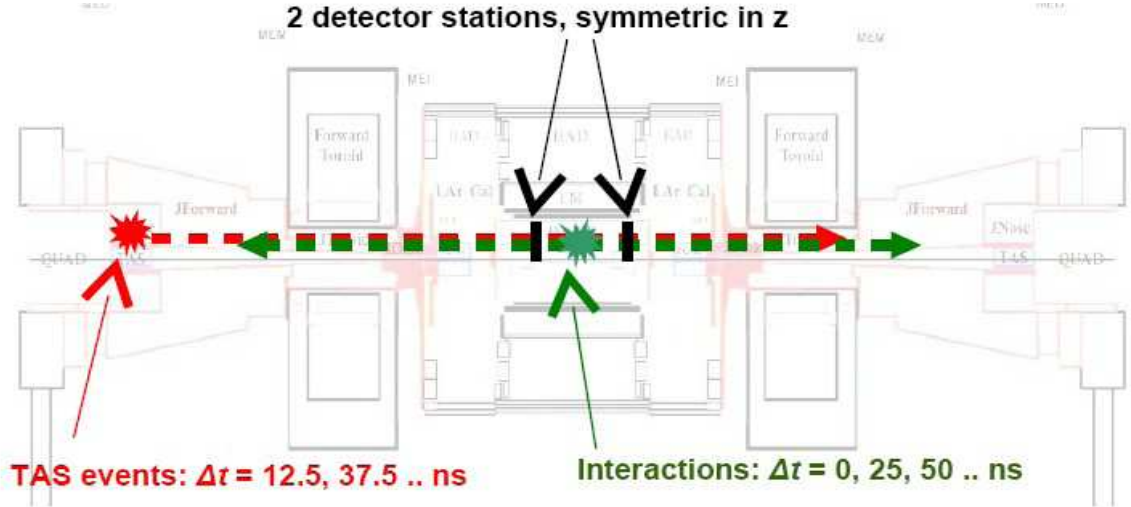


Figure 3.14: The ATLAS interaction region with the positions of the BCM stations shown. The time differences due to anomalous events in the TAS and normal events at the IP are indicated.

In addition to monitoring luminosity and providing emergency beam abort signals, the BCM can provide minimum bias trigger [51]. Also, a comparison of single module count rates in a station can provide a crude but fast estimate of the collision point location in all three coordinates. The resolution of this position determination is ≈ 1 mm [104].

3.3.4 Offline relative luminosity monitoring in ATLAS

Several methods of offline luminosity estimation exist, some of which are being used currently while others are potentially useful. We briefly describe three of them in this section.

Silicon spacepoint counting: The number of spacepoints in the Pixel and SCT subdetectors was used to monitor instantaneous luminosity in the early part of the

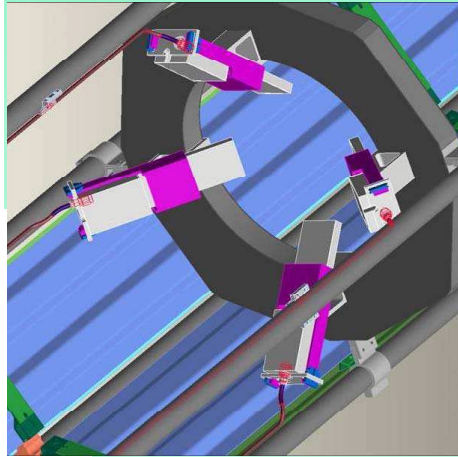


Figure 3.15: GEANT4 simulation showing an ATLAS BCM station with the four sensors placed symmetrically about the beam pipe on the support structure.

2010 running when the mean number of interactions per bunch-crossing was small. A spacepoint-based minimum bias trigger was used to reject bunch-crossings with no interactions. The trigger used spacepoint multiplicity in the silicon detectors to determine whether a hard interaction occurred [70]. The total number of spacepoints in triggered events in a given luminosity block⁷ scales with the integrated luminosity, after correction for trigger deadtime and prescales.

Primary vertex counting: The number of non-diffractive events per bunch crossing has a Poisson distribution with a mean λ given by:

$$\lambda = \sigma_{nd} L_b \quad (3.19)$$

where σ_{nd} is the non-diffractive cross-section and L_b is the bunch luminosity. Once σ_{nd} at the LHC is measured independently of ATLAS (e.g., using the TOTEM de-

⁷A *luminosity block* is the smallest length of time during which the integrated luminosity can be calculated, with corrections for trigger deadtime and prescales. The exact duration of a luminosity block depends on operational conditions; in particular, the duration must be long enough that the statistical uncertainty in the integrated luminosity measured for the block is smaller than the systematic uncertainty. In the 2010 proton run, 2-minute long blocks were used.

tector [99]), the mean number of vertices per bunch crossing can be used to estimate bunch-by-bunch luminosity [79].

Resonance counting: The number of resonances of a specific type produced in a run can be used as an estimate of the relative integrated luminosity in that run. Potentially useful physics processes include J/ψ , W , and Z (see Chapter 1). Decay modes into electrons and muons are optimal for this purpose since they are relatively easy to isolate from the background.

3.3.5 Summary

Accurate measurement of absolute luminosity is going to be crucial for cross-section estimations at the LHC. In this chapter, we have reviewed the various methods by which luminosity can be measured. We have summarized the theoretical underpinnings of luminosity measurement from machine parameters, and discussed the technologies and the current status of LHC beam monitoring systems which are being used to measure the relevant parameters. We have also given estimates of the accuracy of these monitors.

We have presented an overview of several ATLAS subdetectors that contribute to the measurement of both instantaneous and integrated luminosity. For each subsystem, we have discussed the basic concepts and the expected measurement accuracy. Additionally, we have given brief overviews of several methods of offline luminosity monitoring.

Chapter 4

Data Collection and Event Reconstruction

The electronics associated with the various detector subsystems output raw data in units of ADC (analog-to-digital converter) and TDC (time-to-digital converter) counts. Before we can perform a physics analysis on the data, it must go through an elaborate software chain which reconstructs each event. The reconstruction software attempts to identify all final-state particles in the event, including leptons, photons and quark/gluon jets. For each particle, it traces the spatial origin and gives an estimate of the four-momentum. In this chapter, we discuss the data collection and reconstruction procedure for various collision products.

4.1 Data Collection and Integrated Luminosity

This thesis is based on data collected between April 11 and July 19, 2010, the corresponding run range being 152844-159224. Data collected with stable beam operation is used; additionally, we require that all detector components were at full operational voltage for the data to be usable. The various quality criteria are applied

at the luminosity block level. By filtering the luminosity blocks in each run through a *Good Runs List* (GRL), we ensure that only those blocks that pass the quality criteria are used in the analysis. To eliminate events from the beam halo, beam-gas interactions and cosmic particles, we subsequently select events 6.1 which came from the crossing of bunches that were known to collide in ATLAS.

The integrated luminosity in the selected luminosity blocks is 331 nb^{-1} , with an uncertainty of 11% [94]. Figure 4.1 shows the integrated luminosity delivered and recorded vs. the day for this run duration. The duration was divided into several periods, labelled A to D6. Table 4.1 shows the run range and the integrated luminosity corresponding to each period. Note that $\approx 95\%$ of the data was taken during period D.

Period	Run range	Integrated luminosity (nb^{-1})
A-C	152844-156682	17.60
D1	158045-158392	28.64
D2	158443-158582	31.76
D3	158632-158975	34.71
D4	158041-159086	87.82
D5	159113	28.38
D6	159179-159224	101.85
Total: 152844-159224	330.8	

Table 4.1: Integrated luminosity for the runs in periods A to D corresponding to the *Z* Good Runs List. The total integrated luminosity for the dataset is 330.8 nb^{-1} .

4.2 Event Reconstruction in ATLAS

Event reconstruction starts with raw data from the front-end electronics. The reconstruction procedures vary between the inner detector (ID), the calorimeters and

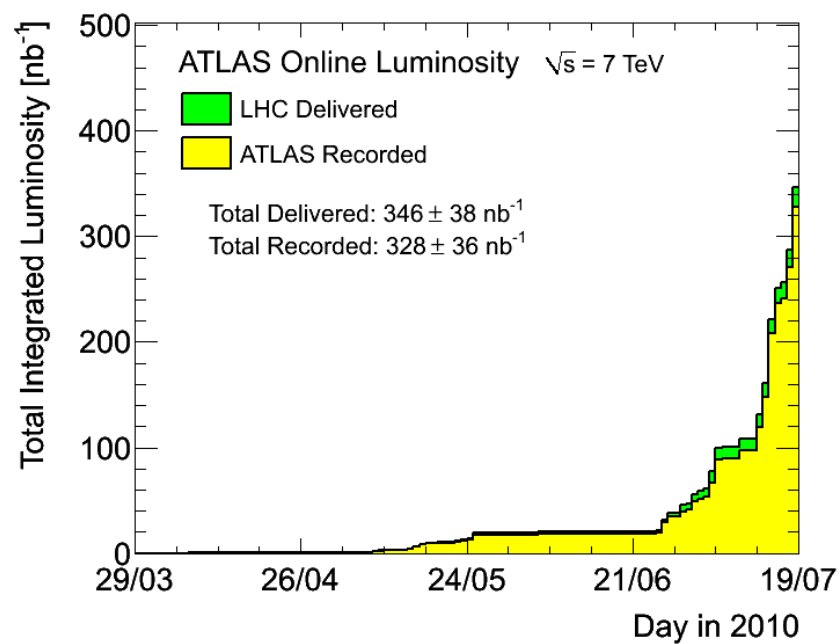


Figure 4.1: Integrated luminosity of our dataset from online measurements as a function of the day. Luminosity delivered by the LHC (green) and luminosity recorded by ATLAS (yellow) are shown. Note that the offline luminosity used in our analysis is slightly higher than the online estimate shown in this plot.

the muon spectrometer (MS), but the basic strategy is to convert ADC/TDC counts into energy, time and/or distance estimates. The reconstruction software is part of the ATLAS offline software framework, known as *Athena*. The raw data input to the reconstruction chain is in the so-called *bytestream* format. The output of reconstruction are Event Summary Data (ESD) and Analysis Object Data (AOD) files.

The ESD contains the detailed output of reconstruction, including sufficient information to enable jet calibration, track re-fitting etc. (discussed below). It has been designed to allow quick tuning of reconstruction algorithms and extraction of calibration constants. The AOD contains a summary of the reconstructed event, including all physics objects in the event as well as event-level *metadata*¹. AODs can be produced from ESDs. Our analysis used collections of variables extracted from ESDs or AODs, known as *D3PDs*, that allow efficient, CPU-economic access to data.

4.2.1 Reconstruction in the Inner Detector

Inner detector reconstruction includes the reconstruction of tracks, vertices, the beamline, and electron bremsstrahlung recovery. Track reconstruction in the inner detector has three main components: the primary *inside-out* reconstruction, the subsequent *outside-in* reconstruction, and a final *TRT-only* reconstruction. The various steps involved in each will be briefly described below.

¹Event metadata consists of such information as the run and luminosity block the event belongs to, the bunch crossing which produced it etc.

Inside-out track reconstruction

Inside-out tracking starts with the silicon detectors, namely the Pixel and the SCT (see Chapter 2). This technique takes advantage of the very high granularity of the silicon detectors, which is especially useful at high track multiplicities. In the first stage, the raw data from the silicon layers is converted into *clusters*, and the TDC output from the TRT into calibrated drift circles. The silicon clusters are transformed into 3-dimensional *space-points*. In the SCT, cluster information from opposite sides of a module is combined to form a 3D space-point. Pixel clusters are obviously 3-dimensional.

The second stage involves track-finding, in which the algorithm searches for prompt tracks coming from the interaction region. First, track seeds are formed by combining three space-points, each space-point originating in a unique Pixel or SCT layer. Figure 4.2 shows the number of track seeds per event in data and in Monte Carlo. The seeds are extended to the remaining silicon layers to form track candidates, which are fitted using a combinatorial Kalman fitter/smoothing technique [90]. Outlying clusters are removed based on their large contribution to the fit χ^2 .

The third stage is termed ambiguity-resolving. Some track candidates share clusters, or are *fakes* resulting from random cluster combinations. In order to resolve cluster-to-track association ambiguities and reject fake tracks, each candidate track is *scored*, the score indicating the likelihood that the track reproduces the path of an actual charged particle². The highest scoring track candidates are refitted, shared

²Track scoring takes into account the number of silicon clusters associated with a track candidate, the number of shared clusters and the number of *holes*, *i.e.*, layers where a cluster is expected but none is found.

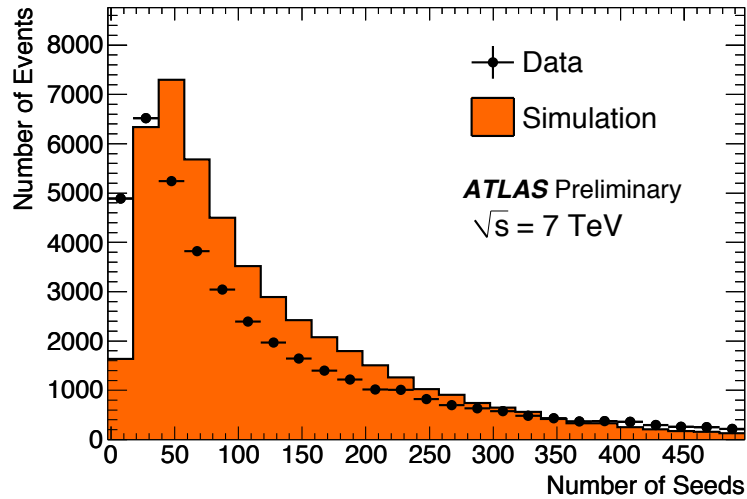


Figure 4.2: Number of tracks seeds per event in data and simulation. The data is not expected to agree with the simulation because, firstly, the track multiplicities are different between the two and, secondly, the simulation did not include diffractive events.

clusters removed and the tracks refitted again. Low-scoring tracks are then rejected and the remaining candidates are extended into the TRT.

All TRT hits in a *road* around an extrapolated track candidate are associated with the track. The track is then refitted and rescored. If the full track scores higher than the original silicon-only track, the TRT extension is added to the silicon-only track, forming a global inner detector track. Otherwise, only the silicon part of the track is fitted; the TRT extension is kept as part of the track, but not used in the fit. The final tracks are stored in a dedicated track collection³.

³Note that, since the TRT extends only to $|\eta| < 2.0$, while the silicon extends to $|\eta| < 2.5$, some inner detector tracks have no TRT extension.

Outside-in track reconstruction

Since inside-out reconstruction requires a minimum number of silicon hits to form track seeds, it is inefficient for tracks that originate in the tracker after the Pixel layers. In particular, it can miss tracks from K_s decays and photon conversions. Such tracks can be recovered using an outside-in tracking algorithm which starts in the TRT. In the first stage, TRT track segments are formed using a histogramming technique [17]. Only those TRT hits that have not been assigned to tracks in the inside-out reconstruction are used. Rough estimates of the transverse track parameters, namely ϕ , r in the barrel and ϕ , Z in the endcap, are associated with the segments.

In the second stage, the segments are extended into the silicon detectors, and space-point seeds are formed in a narrow $r - \phi$ road. Space-points that have already been associated with a track during the inside-out reconstruction are not used in the seed search. Only the three outermost layers of SCT are used, a minimum of two space-points being required within the road. The space-points yield improved track parameters, which are then used to redefine the road in the silicon detectors. As in the case of inside-out tracking, a combinatorial Kalman fitter/smoothen algorithm is used to add clusters and produce silicon track extensions, which are extended into the TRT as before to form a global track. After ambiguity-resolving and track refitting, the final tracks are stored in a dedicated track collection.

TRT-only track reconstruction

Following outside-in tracking, the remaining TRT segments that have not been assigned silicon extensions form the basis of TRT-only tracks. Tracks parameters

are computed for these tracks, but no refitting is performed. The tracks are scored, resolved for ambiguities, and stored in a third track collection.

Once all the track reconstruction sequences have run, the three separate track collections are merged. Ambiguity-resolving is performed once more to select unique tracks from the three collections, and the final tracks stored in one collection. At this point, post-processing steps such as vertex finding, photon conversion reconstruction and beam-spot finding can be executed.

Vertex reconstruction

At the LHC design luminosity of $10^{34} \text{ cm}^{-2}\text{s}^{-1}$, each bunch crossing is expected to have > 20 events on average, of which in general only one will be interesting, the others being mostly low- p_T events⁴. Hence, there will be a number of primary vertices in the interaction region, as well as secondary vertices, vertices from photon conversions, long-lived neutral particles such as K_S , and decay chains. The various vertex topologies are shown in Figure 4.3 [35].

The correct reconstruction of vertices is important for many physics studies. Primary vertices arise from promptly decaying particles, while displaced vertices indicate the decay of long-lived particles. Distinguishing between the different vertex types is crucial for discovery channels such as $H \rightarrow 4l$, $H \rightarrow \gamma\gamma$, b -tagging, τ -jet identification, measurement of the lifetime of long-lived particles, and so on. ATLAS inner detector reconstruction includes dedicated vertex finders for the different vertex types, including full decay chains. The various reconstruction techniques will be discussed in some

⁴As of the writing of this thesis, the maximum instantaneous luminosity reached is $2.07 \times 10^{32} \text{ cm}^{-2}\text{s}^{-1}$, the peak number of interactions per bunch crossing being 3.78.

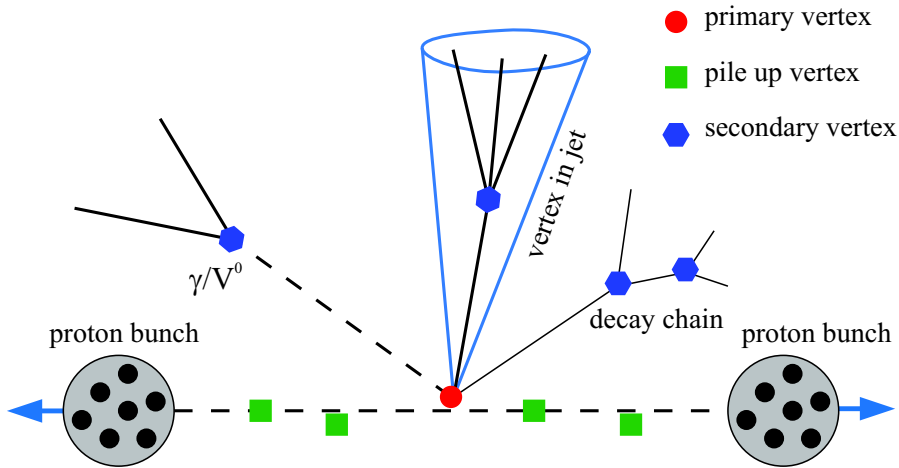


Figure 4.3: Vertex topologies expected in a typical bunch crossing at the LHC: the primary vertex of interest, pile-up vertices, vertices in jets, secondary and tertiary vertices from decay chains, and vertices from photon conversions and decays of long-lived neutrals (V^0 s).

detail in this section.

Primary vertex reconstruction

There are two approaches to primary vertex finding in ATLAS, the first of which involves using a ‘sliding window’ approach to locate vertices. A number of tracks compatible with the expected luminous region are selected and ordered by z_0 , the z projection of the track impact parameter. Then track clusters are looked for in the region using a sliding window along the z axis. All clusters thus found form candidates for primary vertices. Each candidate is iteratively fitted using one of several vertex fitters [47], outlying tracks being rejected at each iteration based on their contribution to the fit χ^2 . The vertex with the highest p_T -sum of tracks is defined as the primary vertex.

In this approach, a track rejected from one vertex candidate is not included in any

other vertex. The *Adaptive Multi-vertex Fitter* avoids this problem, in which *all* pre-selected tracks are used to form one vertex candidate. The candidate is fitted; tracks that are considered to be outliers in this first fit are not rejected but rather used to form a second vertex candidate. The two candidates are then simultaneously fitted, each track being weighted down with respect to the two vertices. The procedure is repeated so that the number of vertices grows at each iteration, but the vertices compete with one another to gain tracks. At the end of the process, a track that does not enter any vertex with a χ^2 probability greater than 1% does not influence the fit result [47]. This approach is the default one used for primary vertex finding in ATLAS.

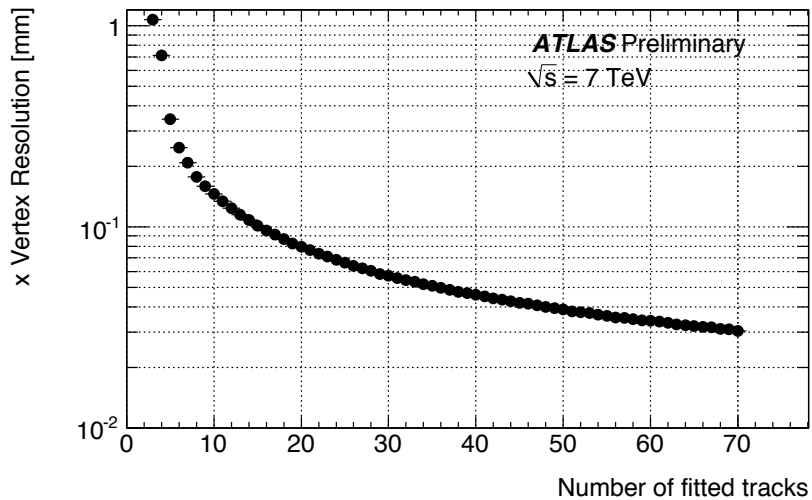


Figure 4.4: Position resolution in the x direction of reconstructed primary vertices as a function of the number of tracks associated with the vertex.

Figure 4.4 shows the position resolution of reconstructed primary vertices in the x direction as a function of the number of tracks associated with the vertex [96]. We see that the resolution is $\approx 150 \mu\text{m}$ for vertices built from as few as 10 tracks.

Reconstruction of secondary vertices and decay chains

The high granularity of the silicon detectors allows the identification of b -jets by finding tracks from a displaced b -hadron decay vertex in the neighborhood of the primary vertex. A b quark can decay into a c quark, giving rise to a secondary vertex from the b hadron decay and one or more tertiary vertices from the c hadron decay. Sophisticated algorithms are necessary to reconstruct such a decay chain. Two vertex finding mechanisms exist for b -tagging in ATLAS, namely the *inclusive* and the *topological* vertex finders.

Each vertex finder starts with a selection of displaced tracks that originate away from the beamline. The *inclusive* finder attempts to fit all selected tracks into one geometrical vertex [35]. Tracks with a large χ^2 contribution are iteratively removed until the overall χ^2 falls below a threshold.

The *topological* vertex finder relies on identifying the *primary vertex* (PV) $\rightarrow b \rightarrow c$ decay chain topology. By assuming that all selected tracks intersect a common $PV \rightarrow b \rightarrow c$ flight axis, the algorithm reduces the track clustering problem to one dimension. The first fit⁵ takes the b -hadron flight direction from the axis of a calorimeter jet that is likely to have resulted from a heavy flavor decay. Intersection of a track with this axis is searched for which, if found, gives the location of the second vertex. This procedure is repeated, vertices being clustered in pairs, until a well-defined decay chain has been reconstructed. In addition to b -tagging, this approach is likely to be very useful for identifying decay chains of supersymmetric particles.

⁵Note that the reconstruction of displaced vertices and decay chains in ATLAS employs constrained vertex fitting. The constraint usually takes the form of the mass of the decaying particle according to a particle hypothesis.

Reconstruction of photon conversions

About 60% of all photons produced in pp collisions in ATLAS converts to an electron-positron pair before reaching the calorimeter [17]. The conversion very often happens outside the volume of the Pixel detector, giving rise to a vertex far removed from the primary event vertex. The identification of conversion vertices is therefore vital for physics studies involving final-state photons.

The conversion reconstruction mechanism proceeds in three steps. The first step involves a preselection of track pairs as conversion candidates. Electron tracks are selected by requiring that a large fraction of the TRT hits be *high threshold* hits⁶. Tracks passing this criterion are grouped into oppositely charged pairs. The difference in polar angle θ between the two tracks must be small, since the photon is massless⁷. In addition, the distance of closest approach of the two tracks to each other must be small.

In the second step, an initial estimate of the conversion vertex position is derived using the perigee parameters of the track pair. The perigee parameters were defined with respect to the primary vertex, and are not accurate for photon conversion tracks. Once the vertex position has been roughly estimated, the perigee is redefined using this estimate and the track perigee parameters are recomputed. These tracks are now

⁶An electron emits transition radiation (TR) in passing through the TRT, while heavier particles do not emit TR below a Lorentz factor of ≈ 100 . In a TRT straw tube, a TR photon loses most of its energy in a single Compton scattering interaction, thereby giving a large ionization pulse. By contrast, the passage of the primary electron or other charged particle through the tube produces a smaller ionization pulse. The two types of pulses can be distinguished by having two separate detection thresholds. An electron traversing the TRT is therefore expected to give to a large number of high threshold hits, while heavier charged particles should generate few such hits.

⁷In the axial magnetic field of the inner detector, oppositely charged tracks will diverge in the azimuthal angle ϕ , so that the tracks are not expected to have a small difference in this angle.

passed to a vertex fitter which uses a collinearity constraint, taking advantage of the massless nature of the photon⁸. The fitter returns a new conversion vertex candidate with the track parameters redefined with respect to the new vertex. The procedure is repeated until the fit converges.

The next step is the rejection of fake conversion vertices. Cuts based on the fit χ^2 and the invariant mass of the reconstructed photon eliminate a large fraction of fakes. During the next level of event reconstruction, the use of calorimeter information for electron track identification further improves the purity of the vertices.

This procedure can reconstruct conversion vertices up to a radial distance of 800 mm from the beam axis, beyond which track reconstruction efficiency drops drastically owing to insufficient hits [35]. However, because of the limited spatial resolution of the TRT, the efficiency for conversion track pair reconstruction suffers significantly after a radial distance of 400 mm.

Figure 4.5 shows the conversion radii of reconstructed photon conversions in data. The material layers at which conversions take place are mapped out by the photons.

Beamline reconstruction

The proton beams collide inside the beampipe in a luminous region that is approximately linear along the z -axis. This is referred to as the *beamline*. A precise knowledge of the position, shape and size of the beamline is important for many physics studies such as b -tagging, as we have seen above. Ideally, the beamline would

⁸For the decay of a massive long-lived neutral such as $K_S \rightarrow 2\pi$, the mass of the parent particle is used in the fitter. If the mass of the parent is not known, as in the search for long-lived new particles, an unconstrained fit can be used.

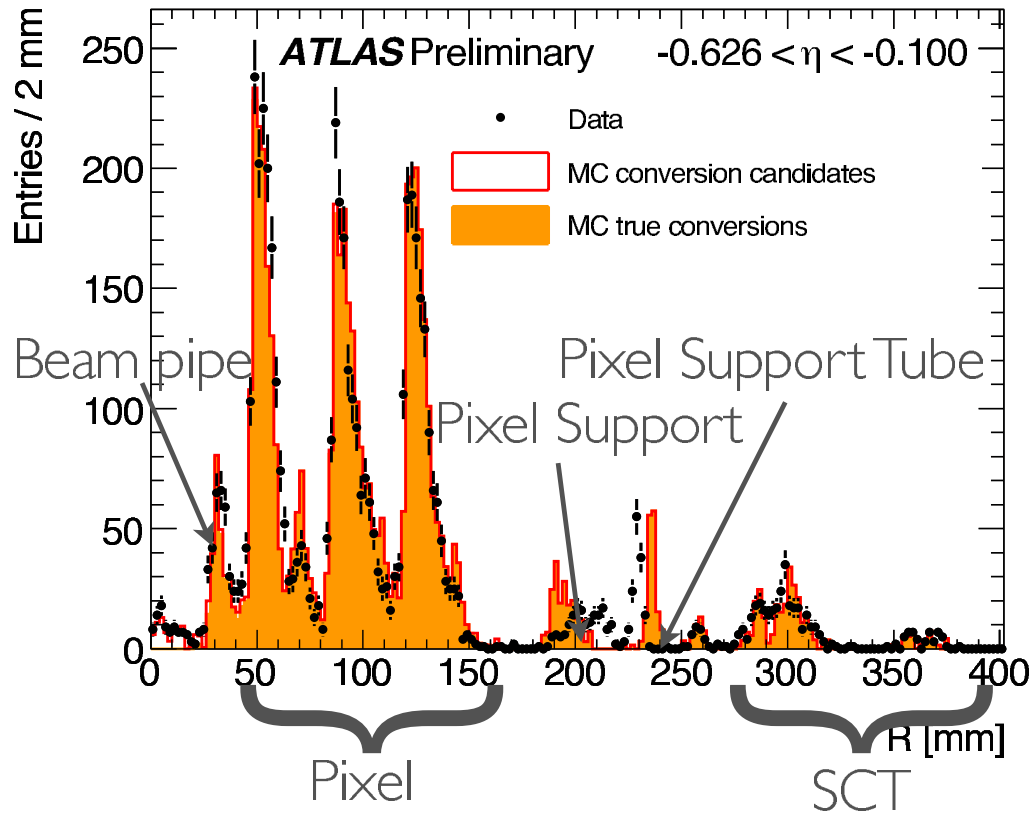


Figure 4.5: Radius of conversion of converted photons in 2010 data up to $R = 400$ mm. The material of the beampipe, the Pixel and SCT layers, and the support material are clearly mapped out by the photons.

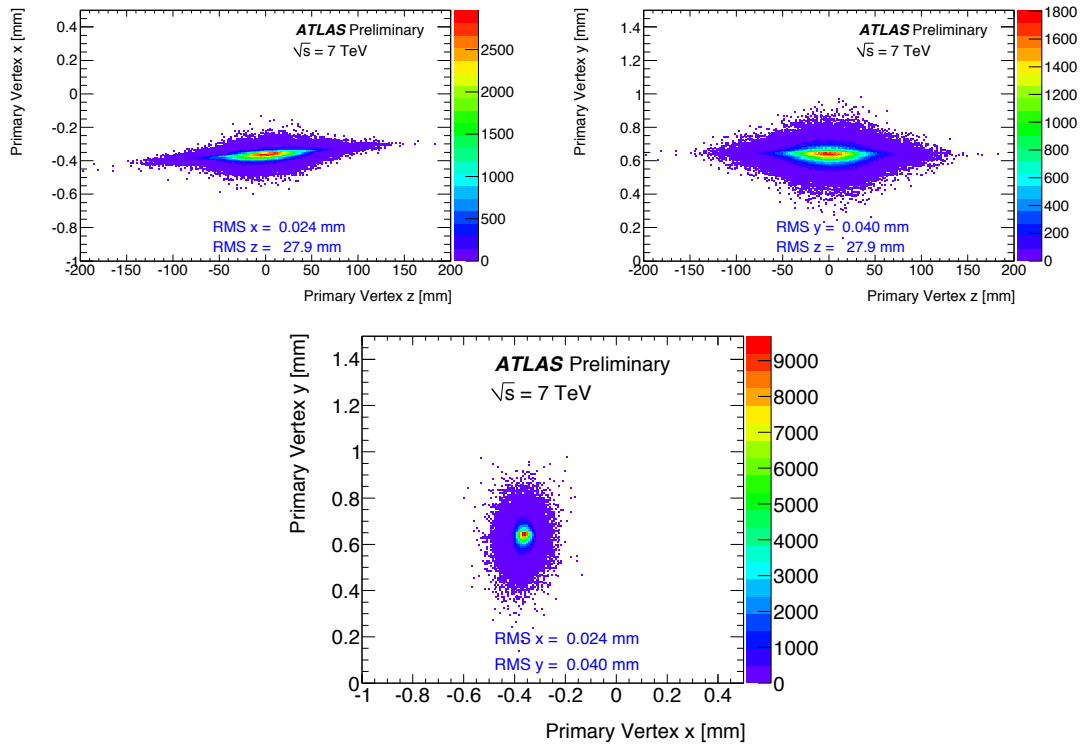


Figure 4.6: Distribution of primary vertices in data in the xz (top left), yz (top right) and xy (bottom) planes.

be parallel to the beampipe and centered on the nominal interaction point (IP), defined as the origin in global detector coordinates. In reality, the beamline often has a finite slope, and is off-center with respect to the nominal IP. For example, Figure 4.6 shows the distribution of primary vertices in 2010 data in the xy , xz and yz planes. We see that the beamline is significantly displaced from the nominal position along both x - and y -axes; additionally, a substantial slope is present in the xz plane [96]. Large jumps in the beam position of \approx mm can occur at the start of a run, while during a run it can shift by up to $50 \mu\text{m}$ [4]. Accurate reconstruction of the beamline is therefore necessary at least on a run-by-run basis, or even per luminosity block.

ATLAS uses two methods for offline beamline reconstruction: one based on primary vertices, and the other on tracks. The vertex-based method estimates the position and the Gaussian width of the beamline in all three coordinates and determines the slope along the x and y coordinates. Starting with primary vertices from a suitably large number of bunch crossings, the algorithm first performs a simple χ^2 minimization to roughly estimate the position and slope of the beamline. Then it carries out a full parameter estimation using an unbinned log-likelihood method, with specific selection criteria being applied to the positions and error matrices of the primary vertices.

The track-based method determines the position and slope of the beamline, but does not give width information. It starts with a suitably large number of tracks and performs a χ^2 minimization [3]. Only tracks associated with primary vertices are used in the fit.

Note that simplified versions of these two algorithms can also run online at Level-3 for fast beamline reconstruction on short time scales (\approx few seconds) and feedback to the LHC.

Electron reconstruction in the inner detector

Depending on the pseudorapidity, electrons lose between 20% and 50% of their energy in the form of bremsstrahlung before leaving the SCT [17]. Energy loss leads to change in the track curvature of electrons, with the result that it becomes difficult to reconstruct the tracks and accurately measure track parameters. The measurements can be improved substantially, however, if the track fit takes possible bremsstrahlung losses into account.

Two bremsstrahlung recovery mechanisms exist in the inner detector reconstruction framework, namely, the *dynamic noise adjustment* (DNA) method and the *Gaussian-sum filter* (GSF) method. The basic concept of both methods is to take into account the change in track curvature due to bremsstrahlung, and thereby follow the track accurately. Both methods use inner detector information only and significantly improve electron reconstruction for energies below ≈ 25 GeV. So as not to degrade the reconstruction of non-electrons, these algorithms are run only on tracks that are likely to correspond to electrons, based on TRT and EM calorimeter information.

The DNA algorithm runs during the Kalman filtering/smoothing process described earlier. At each silicon layer, the algorithm performs a simple one-parameter fit to estimate an increase in track curvature due to bremsstrahlung in that layer. If no bremsstrahlung is found, the track fitting reverts to the default Kalman filter. Otherwise, the algorithm returns a single parameter, namely, the fraction of energy retained by the electron. This parameter is passed to the Kalman filter as a noise term [105], which is adjusted dynamically according to the estimated z^9 and the thickness of the layer, hence the name *dynamic noise adjustment*.

The GSF method is a non-linear generalization of the Kalman filter [89]. Energy-loss due to bremsstrahlung follows a *Bethe-Heitler distribution* [53], which is very non-Gaussian, so that approximating it with a Gaussian would be quite inaccurate. A weighted sum of Gaussians is found to give a much better estimate. The Gaussian-sum filter uses this estimate at each material surface traversed by the electron track and determines the probability of bremsstrahlung. This technique has a slightly better

⁹ z is a parameter in the Bethe-Heitler equation, which describes electron energy loss due to bremsstrahlung [53].

performance than the DNA method, but is much slower.

4.2.2 Reconstruction in the Calorimeters

Information from the calorimetry is used for identifying and measuring the energies of electrons, photons, and hadronic and τ jets, as well as missing transverse energy. The strategies used for reconstructing the various objects will be discussed in this section, starting at the cell level.

An incoming particle creates a shower in the calorimeters, depositing its energy in a number of cells both in the longitudinal and lateral directions¹⁰. When an event is accepted by a Level-1 calorimeter trigger, the analog signal from each calorimeter cell is digitized and sent to a set of digital signal processors (DSPs). The DSPs convert the signals into an energy deposition value for each cell, taking into account electronic and pile-up noise¹¹. To estimate the energy in a shower from the cell energies, the cells are first grouped into *clusters* and the total energy in each cluster summed up. ATLAS uses two different clustering techniques, namely, *sliding window* clustering and *topological* clustering.

Sliding window clustering technique

The sliding window method is based on summing energies of cells within a fixed window in $\eta - \phi$ space. Two types of sliding window clusters (also called *towers*)

¹⁰In this context, the *longitudinal* direction is the direction of shower development, *i.e.*, along the path of the incoming particle. Similarly, the lateral direction is that perpendicular to the path of the particle.

¹¹‘Pile-up noise’ in the calorimetry can arise from multiple ‘pile-up’ events in the same bunch-crossing in which the primary interaction occurred, or from interactions in bunch-crossings close in time to that of the primary interaction. The latter is possible because the response time of the calorimeters is longer than the 25 ns bunch-crossing interval.

are built: EM clusters, used for electron and photon identification, and combined clusters, using information from both EM and hadronic calorimeters, and used for jet finding. The clustering proceeds in three steps.

In the first step, the available $\eta - \phi$ space is divided up into a grid of *towers* of size $\Delta\eta \times \Delta\phi$. For EM clusters, $\Delta\eta = \Delta\phi = 0.025$, while for combined clusters, $\Delta\eta = \Delta\phi = 0.1$ [107]. Within each tower, the energy of cells in each longitudinal layer is summed into a tower energy. In the second step, a window of a fixed size is moved across each element of the tower grid in steps of $\Delta\eta$ and $\Delta\phi$, and the transverse energies of all towers in the window is summed. If the window transverse energy is a local maximum and above a threshold, a cluster seed is formed. The threshold is 3 GeV for EM clusters and 15 GeV for combined clusters. At this point, for combined clusters, the seeds are directly transformed into clusters; cluster quantities such as position and energy deposition per layer are calculated based on the cells encompassed by the sliding window. For EM clusters, however, there is an additional step in which clusters of different sizes are built depending on the hypothesized particle type and the location of the cluster in the calorimeter. In general, the cluster must be large enough so that it contains most of the energy deposited by the particle. But including more cells in a cluster also means potentially including more noise, so the actual number is a trade-off between these two factors.

Topological clustering technique

Topological clustering attempts to reconstruct three-dimensional ‘energy-blobs’ in the calorimeter. It starts with a seed cell, and adds to the cluster any neighboring cell if its energy is significantly above the noise level. The resulting clusters have a

variable number of cells, in contrast to the sliding window approach. Separate EM and hadronic clusters are built.

In the first step, all cells with a signal-to-noise ratio above a threshold t_{seed} are put into a seed list; $t_{seed} = 6$ and 4 for EM and hadronic calorimeter cells respectively [107]. The noise is defined as the expected RMS of the electronics noise added in quadrature to the expected pile-up noise. The cells in the seed list are ordered according to their t_{seed} , and form *proto-clusters*. Next, all neighboring cells of a seed cell are considered. If a neighboring cell is not in the seed list and has a signal-to-noise ratio above a threshold $t_{neighbor}$, it is added to the proto-cluster. $t_{neighbor} = 3$ and 2 for EM and hadronic calorimeter cells respectively. If the neighbor is adjacent to more than one proto-cluster, the proto-clusters are merged. A neighbor of a neighbor is added to the cluster if it has a signal-to-noise ratio above a threshold t_{cell} ; $t_{cell} = 3$ and 0 for EM and hadronic calorimeter cells respectively. The procedure is repeated until the seed list is empty.

In a busy environment, especially in the endcap and forward calorimeters, clusters thus formed can grow very large if some energy is deposited between incoming particles. However, overlapping showers can be separated by identifying local maxima in a cluster. After the initial clusters are formed, they are therefore searched for local maxima. If multiple local maxima are found in a cluster, that cluster is split between them.

After they have been formed, the energies of both types of clusters are at an uncalibrated scale, often referred to as the *raw* or *EM* scale. At this point, topological clusters can be calibrated to the local hadronic energy scale. The clusters are first

characterized as EM, hadronic or noise clusters based on their position and shape. They are then weighted with a calibration function depending on their location and energy. Next, a correction for energy loss in dead material in or near the cluster is applied. Finally, a correction is made for signal losses due to the clustering procedure.

Note that all tower and topological clusters are defined as pseudo-particles with four-momenta, computed using the reconstructed energy and the cluster direction. This is important, for example, for jet finding algorithms, discussed below.

Jet reconstruction

The goal of jet reconstruction is to first find a calorimeter-level jet, then estimate the energy and shape of the particle-level (*i.e.*, hadron-level) jet, and eventually reproduce the kinematics of the original parton at the interaction-level. Because of the widely varying nature of the physics processes that result in jets, there is no optimal way to reconstruct jets from the hadronic final states of all interesting topologies. In general, any jet finding mechanism should be *infrared-safe*, that is, the presence of soft particles between two particles belonging to the same jet should not influence the inclusion of the two particles into the jet. It should also be *collinear-safe*, *i.e.*, it should reconstruct a jet correctly independent of the fact that a certain amount of energy may be carried by one particle or by two collinear particles. From a detector viewpoint, jet finding should be independent of detector technologies, and should not be affected by changing conditions such as underlying event activity and instantaneous luminosity.

Two jet finders are commonly used in ATLAS, namely, the *seeded fixed cone jet*

finder and the *sequential recombination* algorithm. Both algorithms can use sliding window clusters or topological clusters as well as reconstructed tracks. The main features of each technique are discussed below.

The seeded fixed cone jet finder

This technique attempts to reconstruct jets using a fixed-size cone around a seed cluster. First, all input clusters are arranged in descending order of p_T . If the cluster with the highest p_T is above a seed threshold of 1 GeV, all clusters within an $\eta - \phi$ cone of fixed size is combined with the seed cluster. The size of the cone is given by $R_{cone} = \sqrt{\Delta\eta^2 + \Delta\phi^2}$; the algorithm can be run with various cone options from $R_{cone} = 0.4$ to $R_{cone} = 0.7$. A new direction is computed from the four-momenta of the clusters in the first cone, and a new cone is formed. Clusters are then recollected in this cone, and the direction updated. The procedure continues until the cone direction is stable, at which point it is called a jet.

The next seed cluster is then taken from the seed list and a new cone jet formed. The process continues until all seeds have been used up. The jets thus formed can share clusters. Since the cone size is fixed, this procedure is not infrared-safe. For example, a jet from a single hadron can get split into two jets with a large overlap. To remedy this problem, a split-and-merge step is performed after the jet finding. If the clusters shared between two jets contain more than 50% of the p_T of the less energetic jet, the two jets are merged. Otherwise, they are kept as separate jets. However, the method is still not collinear-safe, since it uses seeds¹².

¹²An algorithm which starts by forming seed objects passing a threshold can miss some jets. Suppose a quark emits a gluon at a small angle such that the two jets end up in adjacent calorimeter clusters. If the energy in each cluster is below the seed threshold, neither jet will be reconstructed.

Sequential recombination jet finder

Sequential recombination schemes are inherently infrared- and collinear-safe. The default implementation of this scheme in ATLAS is the anti- k_T algorithm. This algorithm starts by analyzing all pairs of input clusters with respect to their relative inverse transverse momentum squared, defined as:

$$d_{ij} = \min(P_{T,i}^{-2}, P_{T,j}^{-2}) \frac{\Delta R_{ij}^2}{R^2} = \min(P_{T,i}^{-2}, P_{T,j}^{-2}) \frac{\Delta \eta_{ij}^2 + \Delta \phi_{ij}^2}{R^2} \quad (4.1)$$

and the inverse squared p_T of cluster i : $d_i = p_{T,i}^{-2}$ [17]. $\Delta \eta$ and $\Delta \phi$ are the η, ϕ differences between the two clusters. R , the only free parameter in this definition, is the distance parameter and allows control of the size of the jets formed. The algorithm finds the minimum d_{min} of the d_{ij} and the d_i . If d_{min} is a d_{ij} , the algorithm combines the clusters i and j into one object by adding their four-momenta. Both clusters are removed from the input list, and the new object k added to it. If, by contrast, d_{min} is a d_i , the cluster itself is considered to be a jet, and removed from the input list. The procedure is repeated for updated sets of d_{ij} and d_i until the input list is empty. Consequently, all clusters in the original list become either a jet by itself or part of a jet.

Since no clusters are shared between jets, this method is infrared-safe. Since no seeds are used, it is also collinear-safe. ATLAS uses distance parameters $R = 0.4$ for narrow jets and $R = 0.7$ for wide jets.

One important difference between using sliding window (tower) clusters versus topological clusters for jet finding is in the number of cells used in the jet. The former uses all cells in the calorimeter, while the latter leaves noisy cells out. Hence, the noise contribution per cell is significantly smaller for topological cluster jets than

for tower jets. Another difference is that the two types of clusters may reproduce the shape of the particle-level jet better in certain regions of the calorimeter than in others. Figure 4.7 [83] shows an example. In the central and endcap regions ($|\eta| \lesssim 3$), topological cluster jets reproduce the particle jet shapes better than the tower jets. In the forward region ($|\eta| \gtrsim 3$), the situation is reversed and tower jets do a better job of reproducing the particle-level jets.

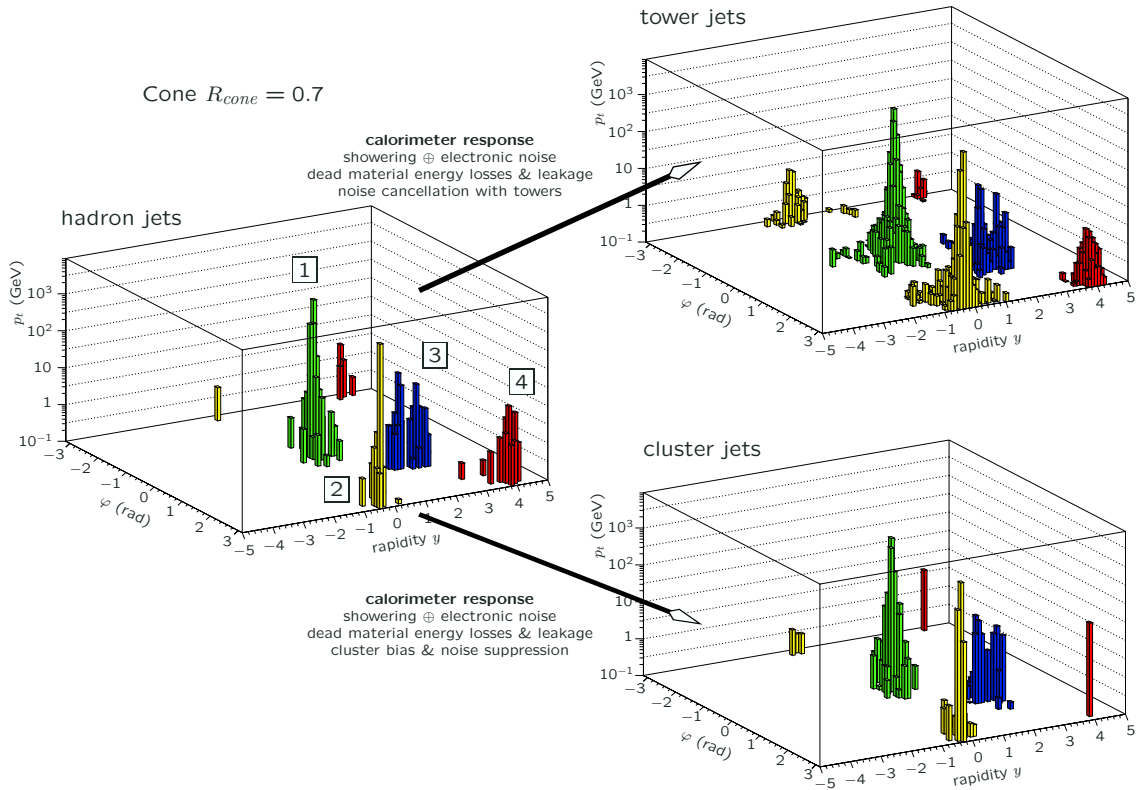


Figure 4.7: A simulated QCD event with four jets in the final state, at the particle level (*left*) and as reconstructed in the calorimeters (*right*). The reconstructed shapes and energies of the jets are shown for sliding window clusters (‘towers’) and for topological clusters. The seeded cone algorithm was used for jet finding in both cases, with $R_{cone} = 0.7$.

Reconstruction sequence for sliding window and topological cluster jets

Figure 4.8 shows the various steps in jet reconstruction starting from the two types of clusters. For sliding window clusters, the first step is a ‘resummation’ step. Because of cell signal fluctuations due to noise, some towers can end up with a net negative energy. The resummation step combines such towers with nearby positive-energy towers to ensure that all towers that are input to jet finding have physically meaningful four-momenta. The output of the jet finding algorithms are jets at the raw energy scale, which are then calibrated with a cell-signal based weighting function¹³. Further corrections for pile-up, electronic noise and algorithm effects are applied in order to reproduce the hadron-level jet shape and energy. Finally, all jets with $p_T < 7$ GeV are discarded. Calibration to the interaction-level parton requires further corrections for the physics environment, and is usually done during specific physics analyses.

Topological clusters at the raw energy scale yield jets at the same scale, which are then calibrated to the hadronic scale as before and the usual corrections applied to recover the particle-level jet. Clusters that have been locally calibrated to the hadronic scale lead to jets at this scale, which have to be further corrected for the fact that local calibrations and correction factors have been derived from single pion response [17]. After all corrections, jets with $p_T < 7$ GeV are discarded as before.

One powerful way to improve the energy resolution of jets is to match a calorimeter cluster with a charged inner detector track pointing to it. If the track momentum resolution is better than the calorimeter energy resolution, the cluster E_T is replaced with the track P_T . This technique is known as *energy flow* reconstruction.

¹³In a non-compensating calorimeter, such as the ATLAS calorimeters, low cell signal densities indicate energy deposition by charged hadrons. The observed energy can be calibrated to the actual hadronic energy by weighting the cell signal with a factor of the order of the electron/pion signal ratio [101].

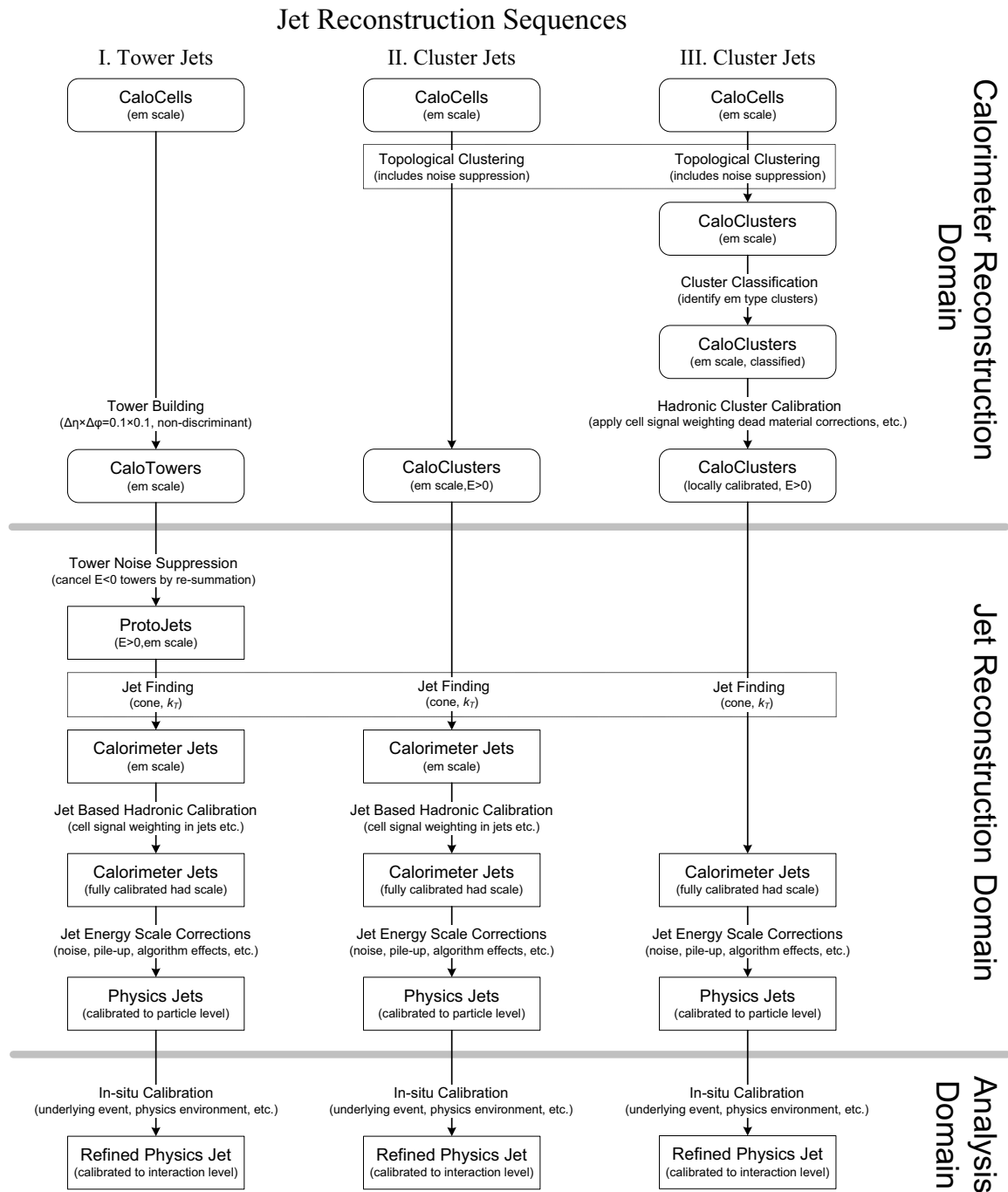


Figure 4.8: Flowchart of jet reconstruction sequence using sliding window clusters ('towers') and using uncalibrated and calibrated topological clusters.

The default jet reconstruction in ATLAS uses topological clusters and the anti- k_T jet algorithm.

Electron reconstruction in the calorimeter

Electron reconstruction can be track-seeded or calorimeter-seeded; the track-seeded approach has been described earlier in the context of inner detector reconstruction. In the calorimeter, electron-induced showers are identified using EM clusters formed with the sliding window technique¹⁴. Electron showers are in general broad compared to photon showers, since electrons have a larger probability of interaction than photons in the material upstream of the calorimeter, and because they emit bremsstrahlung photons while bending in ϕ inside the inner detector. Several cluster collections are therefore built with different window sizes for electron and photon identification.

Electron reconstruction starts by building a seed-list of EM clusters with $E_T > 3$ GeV. For each seed, a matching inner detector track is looked for within a $\Delta\eta \times \Delta\phi$ window of 0.05×0.10 . If such a track is found, the algorithm looks for an associated conversion, and checks that the ratio E/p of the cluster energy to the track momentum is smaller than 10. If no conversion is flagged and the E/p criterion is satisfied, an electron candidate is created. If no matching track is found or if the matched track belongs to a conversion pair, a photon candidate is created.

At this point, various refined identification criteria can be applied to an electron candidate, incorporating calorimeter and inner detector quantities, to distinguish jets

¹⁴Topological clusters are not used in electron and photon reconstruction by default.

and δ -electrons¹⁵ from signal electrons. A cut-based electron identification scheme is used by default. Three standard sets of cuts have been defined: loose, medium and tight. This approach provides flexibility in physics analyses; for example, the user can choose electrons that pass the loose cuts if the analysis demands high electron identification efficiency but is insensitive to a relatively large fake rate.

The loose cuts use simple calorimeter quantities, namely, shower shape variables in the middle layer of the EM calorimeter and the amount of leakage energy into the hadronic calorimeter. The medium cuts improve the identification by adding cuts on the strips in the first EM calorimeter layer (see Chapter 2) and on track quantities. The tight cuts use additional quantities such as the number of hits in the vertexing layer, the number of TRT hits and the ratio of high threshold TRT hits to all TRT hits. The tight cuts provide very high jet rejection. Details of the cuts can be found in the electron identification chapter of the ATLAS CSC note ([17], p. 73).

In addition to the cut-based approach, multivariate approaches using a likelihood discriminant, boosted decision tree and neural network have been implemented in ATLAS. Analyses involving electrons with the early 2010 data used cut-based electron definitions only.

Photon reconstruction in the calorimeter

As mentioned above, photon candidates are created from EM clusters that do not have an associated track or is matched with a track in a conversion pair. At this point, three photon identification techniques are available: a cut-based method, a

¹⁵A δ -electron or δ -ray is an energetic electron that has been knocked out of an atom by a charged particle.

log-likelihood based method and a covariance matrix based method.

The cut-based method uses longitudinal and lateral shower shape variables to reject jets. Since photons produce narrow showers well-contained within the EM calorimeter, they are easily separated from jet-induced fake photons which are broader and have substantial leakage of energy into the hadronic calorimeter. Following these cuts, the remaining fakes are mostly from low track multiplicity jets containing π^0 s, which are rejected using a track isolation criterion.

In the log-likelihood ratio based method, the distribution of each shower shape variable is normalized to unity to obtain a probability density function (PDF). The same variables are used as in the cut-based method. The log-likelihood ratio is defined as:

$$LLR = \sum_{i=1}^n \ln \frac{L_{s,i}}{L_{b,i}} \quad (4.2)$$

where $L_{s,i}$ and $L_{b,i}$ are the PDFs of the i th variable for the photon and the jet background respectively.

The covariance matrix method takes advantage of the fact that the shower shape variables associated with a photon shower in the calorimeter are correlated. The algorithm uses five longitudinal and five lateral shower shape variables to construct a covariance matrix. A χ^2 quantity defined using the matrix estimates the probability that a given object is a photon.

Reconstruction of missing transverse energy

To a fair approximation, the colliding partons do not carry energy/momentum transverse to their direction of motion, so that the net transverse energy upon col-

lision is \approx zero. If the net *measured* transverse energy is different from zero, it can indicate undetected particles, which can be neutrinos, neutralinos from supersymmetric theories, or particles that escape into an extra dimension. A robust estimation of missing transverse energy (E_T^{miss}) is crucial for discovery physics as well as for Standard Model measurements.

E_T^{miss} can be mismeasured owing to finite detector coverage, finite resolution, dead and noisy calorimeter channels, and various noise sources. The ATLAS calorimeters extend to large pseudorapidities ($|\eta| < 5$), but energy deposited in the transition regions between detector segments can go undetected. Various techniques have been developed to recover energy thus lost, as well to suppress calorimeter noise. Details of the latter can be found in [17]. Two techniques are used for E_T^{miss} reconstruction in ATLAS: cell-based and object-based. They are summarized below.

The cell-based method uses calorimeter cells that pass noise suppression criteria. It includes contributions from energy deposits in the calorimeter, and corrects for energy lost in the cryostat and measured energies of muons¹⁶:

$$\vec{E}_{x,y}^{\text{Final}} = -\vec{E}_{x,y}^{\text{Calo}} - \vec{E}_{x,y}^{\text{Muon}} - \vec{E}_{x,y}^{\text{Cryo}} \quad (4.3)$$

The calorimeter term is estimated by taking the vector sum of the energies of cells that belong to reconstructed topological clusters. Local hadronic calibration is applied to the cells. The muon term is calculated using the measured transverse momenta of muons and adding vectorially. The cryostat term is important because the cryostat thickness between the EM and hadronic calorimeters in the barrel is ≈ 0.5 interaction length, so that hadrons can lose a significant fraction of their energy

¹⁶Muons are minimum ionizing particles, and hence deposit little energy in the calorimetry.

there. The lost energy can be recovered by comparing energy deposits in the last layer of the EM calorimeter and the first layer of the tile calorimeter.

The motivation for the object-based method is to reconstruct E_T^{miss} for analyses sensitive to low- p_T deposits from pions, soft jets, the underlying event and pile-up events. The algorithm starts with all reconstructed, calibrated and identified objects in the event. In the first step, it classifies the objects into two groups: high- p_T objects such as electrons/photons, muons, tau's and jets, and low- p_T objects such π^\pm , π^0 and unclustered energy deposits from the various sources listed above. It finds all topological clusters associated with one or more of the high- p_T objects and removes them from the list. Cells in topological clusters that are not associated with any high- p_T object are classified as low- p_T deposits.

In the second step, an object-based calibration optimized for E_T^{miss} calculation is applied, and the E_T^{miss} calculated as

$$\cancel{E}_{x,y} = -\vec{E}_{x,y}^{\text{high}} - \vec{E}_{x,y}^{\text{low}} \quad (4.4)$$

4.2.3 Reconstruction in the Muon Spectrometer

The ATLAS muon reconstruction framework identifies muons and measures their position, direction and momentum with high accuracy over a large range of energies, from a few GeV into the TeV range. Several different strategies have been developed for muon reconstruction. The simplest strategy is to reconstruct *standalone* muons by looking for tracks in the muon spectrometer, and then extrapolating them to the interaction region. More sophisticated strategies take advantage of the muon signature in the inner tracker and the calorimetry. Thus, *combined* muon tracks are reconstructed by associating standalone muon tracks with inner detector tracks and

combining the measurements from the two systems. *Tagged* muons are inner detector tracks that have been extrapolated into the muon spectrometer and associated with track segments in the spectrometer. *Calorimeter tagged* muons are inner detector tracks that have been associated with calorimeter energy deposits consistent with a muon.

There are two independent algorithms for muon track reconstruction, resulting in two collections of muon tracks as the reconstruction output. The families are named after the corresponding standalone reconstruction algorithms: *Moore* and *Muonboy*. In the following section, we describe the concept and implementation of the Moore algorithm in detail. The Muonboy algorithm, which is conceptually similar to Moore but differs from it in particular aspects of implementation, is described in brief.

Standalone muon reconstruction

In standalone muon reconstruction, track segments are built using hits in the various measurement technologies (see Chapter 2), and then the segments are linked to form tracks.

Reconstruction by Moore

Muon track reconstruction by Moore (Muon Object-Oriented REconstruction) [6] proceeds in three distinct steps:

- pattern recognition
- segment building
- track finding and fitting

Each step is implemented in several stages, as shown in Figure 4.9, and described below.

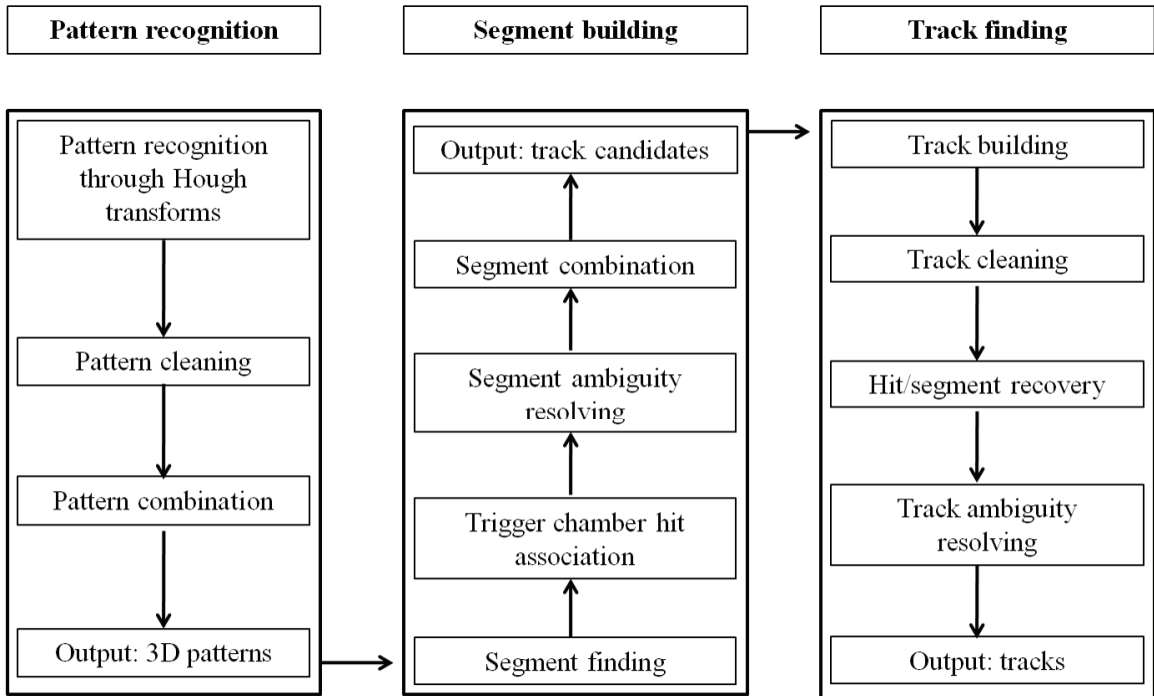


Figure 4.9: Flowchart of the various stages of muon track reconstruction by the Moore algorithm.

Pattern recognition

In this step, the algorithm looks for hits in the precision measurement technologies that appear to arise from the passage of a charged particle. Such a set of hits forms a *pattern*. A typical event can contain $\mathcal{O}(10^4)$ hits in the muon spectrometer, so that a strategy is needed for fast pattern recognition to minimize the required CPU time. The strategy employed is the *Hough transform* [88], also known as the histogramming technique.

The Hough transform method was originally developed at CERN for analyzing

bubble chamber photographs. In essence, a Hough transform is a function that transforms points in N -dimensional space into a *Hough space* H :

$$f_H : \mathfrak{R}^n \rightarrow H \quad (4.5)$$

where \mathfrak{R}^n can, for example, be 2- or 3-dimensional real space, while H typically has two dimensions. A point (e.g., a hit) in \mathfrak{R}^n corresponds to a curve in the Hough space, while an intersection of curves in the Hough space corresponds to a trajectory in \mathfrak{R}^n (e.g., a track). Consequently, our aim is to find intersection points in the Hough space. An analytical approach can be very CPU-intensive; however, we can define the Hough space such that it can be filled as a 2-dimensional histogram, whereupon we look for local maxima in the histogram. In the case of track reconstruction, the histogram is filled with hits, and the maxima are found by scanning over the axes. For each maximum, the distance in real space of every hit to the maximum is calculated. A hit is associated with a maximum if the distance is below a specified value¹⁷.

In its implementation in ATLAS muon reconstruction, the Hough transform is performed separately in the $r - \phi$ and $r - z$ planes. For a given track, this process results in two 2-dimensional patterns, known as a ϕ pattern and an η pattern. A χ^2 fit is performed on each pattern, yielding a position and a direction. If two patterns in the same plane share more than 80% of hits, they are merged. Hits that are considered to be outliers based on the distance from the pattern are rejected. ϕ and η patterns that should correspond to the same track are then combined to form 3-dimensional patterns. The combination is done by associating hits in the ϕ pattern to the η pattern based on a specified distance [88]. The pattern is assigned crude estimates

¹⁷For more details on the concept and implementation of the Hough transform, see Chapter 3 of [88].

of position, direction and momentum. Note that a pattern typically contains hits in multiple MDT stations.

Segment building

In this step, hits in the patterns from the pattern recognition step are used to form short, straight track segments in each MDT chamber. As shown in Figure 4.10 (*top left*), for a pair of hits in the two outermost layers of a multilayer, the four possible tangent lines connecting the drift circles are drawn. A tangent line is kept if its direction is within 0.2 radian of the direction of the corresponding pattern, and if there are at least three hits within 1.5 mm of the tangent line. A χ^2 fit is performed using distances to the drift circles. If a segment has a χ^2 per degree of freedom larger than 10, the hit which has the largest contribution to the χ^2 is rejected, and the segment refitted. This sequence is repeated until the χ^2 per degree of freedom is less than 10, or there are less than three hits left. At this point we have a *segment candidate*.

Trigger chamber hits are now added to the segment. In the barrel, hits in RPC chambers located on the middle and outer MDT stations are added to segments in the corresponding MDT chambers without any refit. In the endcap, TGC hits are similarly added to segments in the inner and middle MDT stations.

A fraction of the segment candidates at this stage can be ambiguous owing to hit sharing. To resolve ambiguities, segments are scored using a set of quality criteria in the following order of priority:

1. number of hits in precision chambers
2. number of missed hits (*holes*) in precision chambers

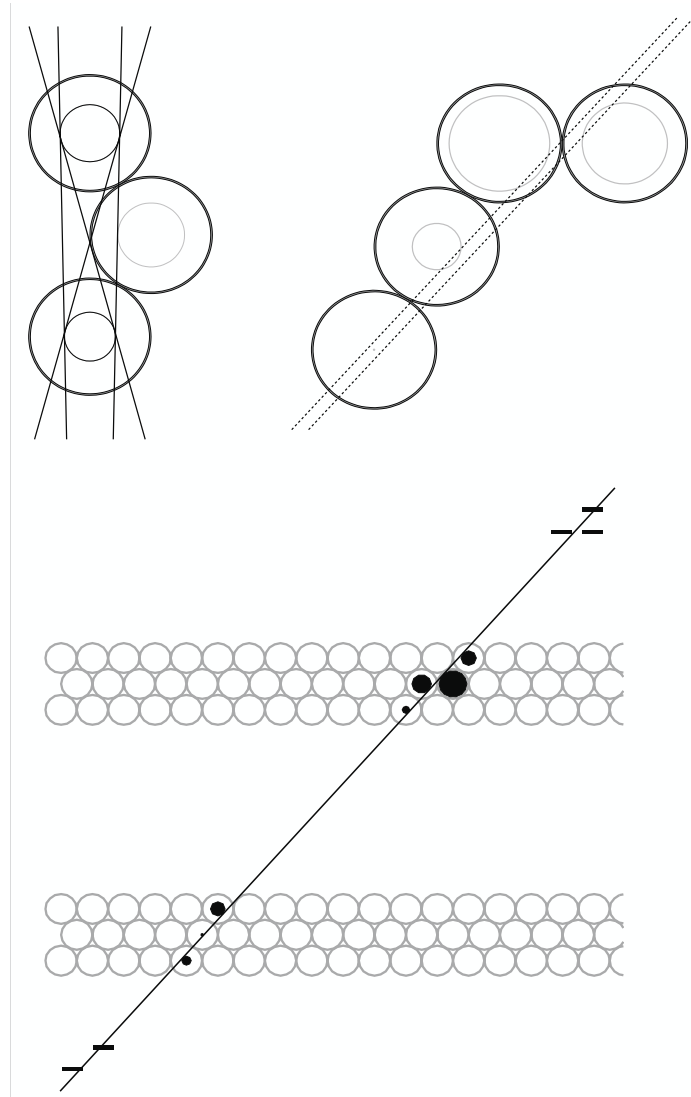


Figure 4.10: *Top*: building of segment seeds in the MDT by connecting drift circles; *bottom*: a reconstructed MDT segment in two multilayers.

3. number of hits in trigger chambers

If two segment candidates are ambiguous, the lower-scoring one is rejected.

In the segment combination stage, a second pattern recognition step is performed using segments. First, the segments are ranked according to a second set of criteria including isolation in the chamber and the crude momentum estimation from the initial pattern recognition [88]. Compatibility between pairs of segments is then estimated starting with the highest-ranked segment. Two segments are said to be compatible if they come from the same initial pattern and have consistent position and direction. If they are compatible and do not already belong to a *track candidate*, they form a track candidate. If one segment belongs to a track candidate, the other segment is assigned to the same candidate.

Once this process is complete, each track candidate is fitted using χ^2 minimization with respect to the segments on it, and with the constraint that a track must pass close to the interaction point. Material effects are not taken into account at this stage. If two track candidates share 50% or more segments, they are merged.

Track finding

The first stage of track finding is track building, which is similar to the segment combination described above except that material effects are taken into account and more stringent quality criteria are applied. A track is built up segment by segment starting from the outer MDT station to the inner stations¹⁸.

For a given track candidate, the segment in the outer MDT station with the high-

¹⁸Since the outer muon stations suffer from less combinatorial background than the inner ones, starting with segments in the outer stations results in a smaller number of possible combinations and therefore faster track building

est quality, as described in the previous section, is taken as a track seed. Next, a segment from the middle station that is on the track candidate is tested for compatibility with the first segment 4.11. The pair of segments are fitted with the `GlobalChi2Fitter` [31] and, if the fit results indicate compatibility, the middle station segment is added to the track. This procedure is repeated for all middle station segments on the track candidate in order of decreasing quality, and then for all inner station segments on the track. Note that a track must have at least two segments on it, and that multiple tracks can result from one track candidate at this stage.

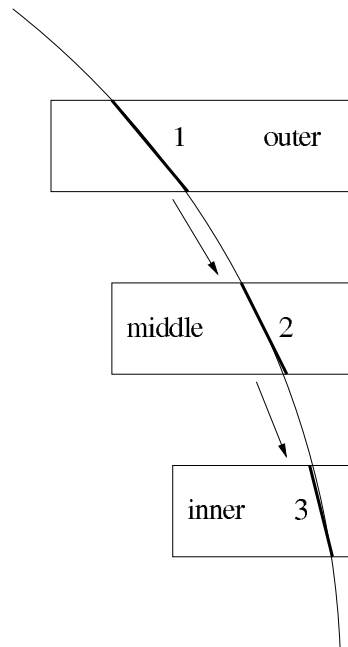


Figure 4.11: The sequence in which track segments are added to a muon track candidate [88].

In extrapolating the track through the detector, the `GlobalChi2Fitter` takes into account material effects which result in multiple scattering and energy loss of the charged particle. The material description is taken from a database which includes a

detailed description of both active and inactive material.

The next stage is track cleaning, which is itself a two-step procedure. In the first step, an entire MDT station is removed from a track if the average pull of the hits on track in that station is larger than 3.5, and if this pull does not result from any single hit. In the second step, the drift circle belonging to each MDT hit is tested. A track could have traversed on either side of a drift circle; in some cases the wrong side may have been chosen during segment-making (see Figure 4.10). For each hit, it is assumed that the track traversed on the other side of the drift circle from the one originally chosen, and the pull due to that hit recomputed. If the pull is now lower than the previous value, the new direction is kept and the track refitted.

For various reasons, a muon can traverse a layer in a chamber without registering a hit (see Section 4.2.4 below). An attempt is made to add some of these hits back to the track. In all chambers that have at least one hit on a track, layers without hits are searched for. If such a layer has a channel that registered a signal, a hit in that layer is added to the track provided that it has a pull smaller than a specified value. Otherwise, the layer is flagged as a *hole* on that track. A search for missed segments is then performed by checking that the track has segments in all three muon stations. If one station is missing, a segment search is done in that station using the parameters of the fitted track as a seed. If a segment is found, the hit/hole search as described above is performed on it, following which the segment is either discarded or added to the track.

At this stage, tracks can share hits. To assign each hit unambiguously to a track, the tracks are ranked according to quality criteria using the number of hits and the

fit χ^2 . Starting with the highest-ranked track, if it shares hits with a lower-ranked track, these hits are removed from the latter and the track is refitted. If the fit now fails, the track is removed. This process results in shared hits being assigned to the track that is most likely to be a muon. At this point we have a set of standalone muon spectrometer tracks, their parameters being expressed at the entrance to the spectrometer, *i.e.*, at the layer on which the track has its innermost hit.

The *MuIDStandalone* algorithm is used to extrapolate standalone muon spectrometer tracks through the calorimeters to the interaction region. A refit is performed, Coulomb scattering and energy loss in the calorimeters being represented by five additional fit parameters¹⁹. After the fit, the track parameters are expressed with respect to the distance of closest approach to the interaction point.

Reconstruction by Muonboy

The reconstruction strategy used by Muonboy [2] is basically similar to that of Moore, but there are some differences in the implementation. Muonboy starts by building patterns from precision chamber hits in regions of interest defined by trigger hits. Unlike Moore, three different classes of segments are built. The first class is the result of a strict segment search employing stringent χ^2 criteria and requiring that each segment candidate be associated with a second coordinate (ϕ) hit. The second class ensues from a looser search with no ϕ hit requirement. The third class contains segments which cross only one multilayer in an MDT station. Only hits not used in the previously made segments are used in the single-multilayer segment search.

In the next step, positions and directions of ‘strict’ segments in the outer and

¹⁹The algorithm uses the measured energy deposit in the calorimeter if it is significantly larger than the expected value.

middle stations are used to roughly compute the momentum of the corresponding muon. Each segment is then extrapolated to the next station using three-dimensional continuous tracking for several values of the momentum around the crude estimate, taking the magnetic field and any dead material into account. If the extrapolated segment matches one or more ‘loose’ segments in the new station, the latter are added to the track candidate. A fit is then performed on the segments already in the candidate, yielding a better estimate of the momentum.

The track candidate is then extrapolated to any remaining MDT station, and matching segments are added. At this point, a track candidate is kept only if it contains at least two segments. A new fit is performed to extract refined estimates of the position, direction and momentum. A global fit is then performed using all hits on the segments. Finally, the candidate is backtracked to the interaction region. Multiple scattering in the calorimeters is taken into account using a set of scattering centers, while energy loss is derived from a parametrization. Unlike Moore, Muonboy does not use the measured energy deposit in the calorimeter in any situation.

Combined muon reconstruction

Because of multiple Coulomb scattering in the calorimetry, the momentum resolution of the muon spectrometer degrades substantially for low- p_T muons. For these muons, combining spectrometer measurements with inner detector measurements provides improved resolution as well as more robust fake rejection. Specifically, the inner detector momentum resolution is better than that of the spectrometer for muons with $p_T < \approx 100$ GeV in the barrel and $p_T < \approx 20$ GeV in the endcap. Once standalone muon

tracks have been formed, an attempt is therefore made to match them with corresponding inner detector tracks. The Moore family algorithm that does the matching is *MuIDCombined*; the corresponding Muonboy family algorithm is *Staco*.

Combined reconstruction by MuIDCombined

MuIDCombined starts with a spectrometer track and attempts to match it with an inner detector track using a χ^2 quantity comprising the five track parameters and their covariances from each system:

$$\chi_{match}^2 = (T_{MS} - T_{ID})^T (C_{MS} + C_{ID})^{-1} (T_{MS} - T_{ID}) \quad (4.6)$$

where \mathbf{T} is a vector of the five track parameters expressed at the perigee, \mathbf{C} is the covariance matrix, and \mathbf{ID} and \mathbf{MS} denote the inner detector and the muon spectrometer respectively. For matches with χ^2 probability greater than 0.001, a partial refit is performed starting with the inner detector track vector and adding hits from the spectrometer track, taking into account material effects and the magnetic field [7]. If no matches are found, a combined fit is attempted with a road about the spectrometer track, and all measurements from the inner detector and spectrometer are used in a global χ^2 fit.

Combined reconstruction by Staco

Staco (STATistical COMbination) attempts to statistically merge the ID and MS tracks to obtain a combined track vector:

$$\mathbf{T} = (C_{MS} + C_{ID})^{-1} (C_{MS} T_{MS} + C_{ID} T_{ID}) \quad (4.7)$$

where the \mathbf{C} s and the \mathbf{T} s are defined as before. A combination is accepted if it is below an upper limit on the χ^2 , as defined in Eq. 4.6 above. If more than one combination satisfies this criterion, the one with the lowest χ^2 is kept. The corresponding tracks

are removed from the two track lists, and the procedure repeated until no more combinations are possible.

Note that, since the muon spectrometer covers the region $|\eta| < 2.7$ and the inner detector coverage extends only up to $|\eta| < 2.5$, not all spectrometer tracks can be matched to an inner detector track.

The results presented in this thesis use muons reconstructed with the Staco algorithm, unless otherwise stated.

Inner detector based muon tagging

Tagging of inner detector tracks as muon tracks is an *inside-out* approach. There are some muons that have well-measured tracks in the inner detector, but only isolated segments in the spectrometer. This can happen for two reasons. Very low- p_T muons, after they have traversed the calorimetry, may not have enough energy to traverse multiple spectrometer stations and may leave hits in the inner station only. Also, energetic muons that pass through acceptance gaps in the spectrometer (e.g., at $\eta \approx 0$) fail to be reconstructed by the outside-in approach.

The muon tagging algorithms propagate inner detector tracks to the inner muon stations and look for nearby segments. The Moore and Muonboy family algorithms that implement this scheme are known respectively as *MuGirl* and *MuTag*.

MuGirl

For all extrapolated inner detector tracks above ≈ 3 GeV, *MuGirl* tries to form segments in the muon spectrometer using a Hough transform-based pattern recogni-

tion [7]. Importantly, MuGirl uses all four muon spectrometer technologies to identify segments, employing an artificial neural network (ANN) to combine information from the different technologies. If a reconstructed segment is close to the predicted track position based on the ANN discriminant, the track is tagged as a muon. Although the algorithm was initially designed to find low- p_T muons, it is highly efficient for all muons, and has a low fake rate.

MuTag

MuTag does not do any segment-finding, but rather tries to associate an extrapolated inner detector track with existing muon segments using a χ^2 quantity based on the $\eta - \phi$ difference between the track and the segment. Unlike MuGirl, MuTag only uses inner detector tracks and spectrometer segments that have not already been associated with muon tracks by Muonboy and/or Staco. A χ^2 value below a cut-off tags the inner detector track as a muon.

Calorimeter-based muon tagging

Since the calorimeters have a significantly larger coverage ($|\eta| < \approx 5$) than the muon spectrometer, tagging muons via calorimeter energy deposit offers a way to identify muons that would otherwise be missed. Such tagging algorithms can also reconstruct muons that do not have sufficient energy to exit the calorimetry. This strategy is particularly useful for physics channels with multimMuon final states. There are two calorimeter based muon taggers in ATLAS, namely, *TileMuId* and *CaloTrk-MuId*, which are not associated with the Moore and Muonboy families.

TileMuId

TileMuId was originally designed to run as a Level-2 trigger algorithm, but has been adapted to run offline [48]. As its name implies, it searches for muon-like energy deposit signatures in the Tile hadronic calorimeter. It starts by looking at the outermost radial layer of the TileCal. If it finds an energy deposit compatible with the passage of a minimum ionizing particle (MIP), it continues the search in the middle layer along a direction pointing to the interaction region. If this search yields MIP-like energy deposit, it moves to the inner layer. A MIP-like energy deposit in this segment confirms a muon, the direction of which is estimated using the average coordinates of the cells in the three layers.

CaloTrkMuId

CaloTrkMuId provides two algorithms: one which returns a likelihood value, and the other a tag. The former uses a likelihood ratio function incorporating longitudinal energy deposits in all layers of the EM and hadronic calorimeters. The tagging algorithm starts with an inner detector track, propagates it through the calorimetry, and computes the energy deposit in a cone around the track. If the energy deposit is consistent with a MIP, the track is tagged as a muon.

4.2.4 Efficiencies in the muon system

Since we are interested in muons in the final state for our analysis, it behooves us to study the hardware and software efficiencies associated with the muon system. The most important hardware efficiencies are drift tube efficiency for detecting hits from single muons and trigger chamber efficiency for triggering on muons passing the preset thresholds. Crucial software efficiencies include reconstruction efficiency for muon tracks and efficiencies of the Level-2 and Level-3 trigger algorithms. In this

section, we look at MDT tube efficiency and muon track reconstruction efficiency. Trigger efficiencies will be addressed in Chapter 6²⁰.

Drift tube efficiency

As discussed in Chapter 2, a monitored drift tube registers a hit from a passing muon by detecting the leading edge of the electron avalanche. There are two ways in which the tube can fail to register a muon hit.

- The ionization from a charged particle has statistical fluctuations. For a given particle passage, the ionization can be small enough that the charge collected at the anode does not exceed the discriminator threshold. Therefore, the passage of the particle does not register. This is particularly true of muons passing close to the tube wall such that the path length in the gas is small.
- Following the arrival of a signal at the anode, a drift tube goes into a *dead time* of the order of 800 ns during which interval it does not record further hits. If a δ -electron traverses the tube almost concurrently with the muon, and the signal from the δ -electron arrives at the anode before the signal from the muon, the tube registers the δ -electron and fails to register the muon. Indeed, the inefficiency of single drift tubes is expected to be mostly due to δ -electrons.

The hit efficiency of a drift tube is defined as the ratio of the number of hits found in the tube in a sample of events to the number of hits expected. A hit is expected in a tube if a reconstructed track passes through the tube.

²⁰Since we use only a hardware (Level-1) trigger in our analysis, we will not discuss efficiencies of the Level-2 and Level-3 triggers.

The MDT tube hit efficiency in ATLAS has been estimated using cosmic muons. Figure 4.12 shows the tube hit efficiency in one MDT chamber (BML2A03) as a function of the distance of the particle trajectory from the anode (the *drift radius*) [26]. Efficiency curves are shown for three different cuts on the hit residual R , requiring $R < n\sigma$, for $n = 3, 5$ and 10 , where σ is a convolution of the tube spatial resolution and the track extrapolation error given by the extrapolator, and R is defined as:

$$R = d_i - r_i \quad (4.8)$$

where d_i is the distance of the reconstructed track from the anode and r_i is the measured drift radius. As can be seen, even in the most conservative case (red curve), the hit efficiency is $\approx 94\%$ or better over most of the drift radius.

Figure 4.13 shows the distribution of tube efficiencies for the tubes in all chambers in the middle MDT station. Distributions are shown separately for the four longitudinal segments of the muon spectrometer: barrel A and C and endcap A and C. In each segment, the overall tube efficiency is 93-94%, as expected from studies with test beam and drift tube simulation [110].

The MDT tube hit efficiency has a systematic uncertainty, due mainly to the presence of dead tubes. To estimate the number of dead tubes, we used monitoring histograms from events accepted by the Level-1 trigger produced by the **Gnam** application [41]. We found 590 tubes to be consistently dead, while a further 48 tubes were dead in about half the runs used in this analysis. Comparing these results with an offline database containing a list of dead tubes, we found 339 additional tubes to be dead. Hence, 939 tubes were dead for at least part of the data we use. This is $\approx 0.3\%$ of the total number of MDT tubes, and consequently we take this number as a

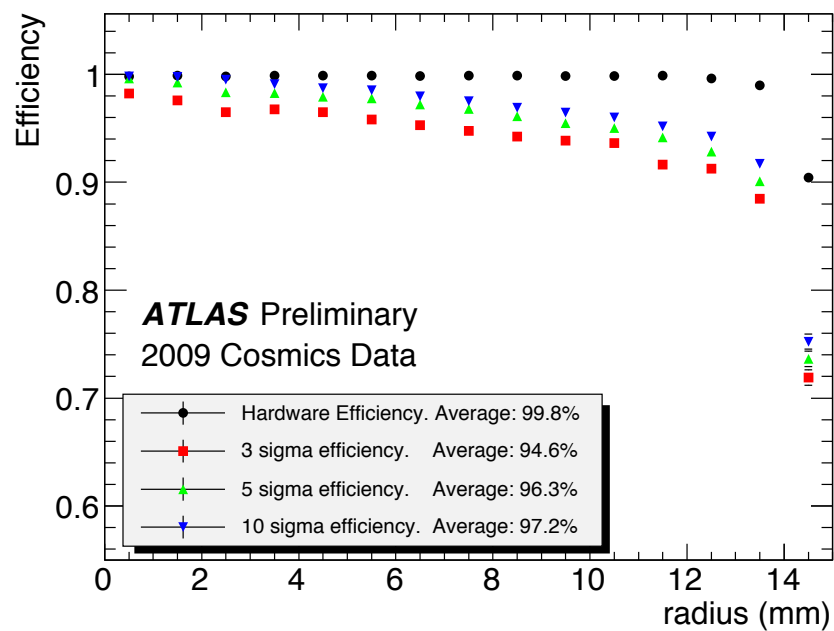


Figure 4.12: Efficiency vs drift radius in the tubes in one MDT chamber. The black curve corresponds to no cut on the residual R . The blue curve corresponds to $R < 10\sigma$, where $\sigma(r)$ is a convolution of the track extrapolation error and the tube resolution. The green and red curves correspond respectively to $R < 5\sigma$ and $R < 3\sigma$.

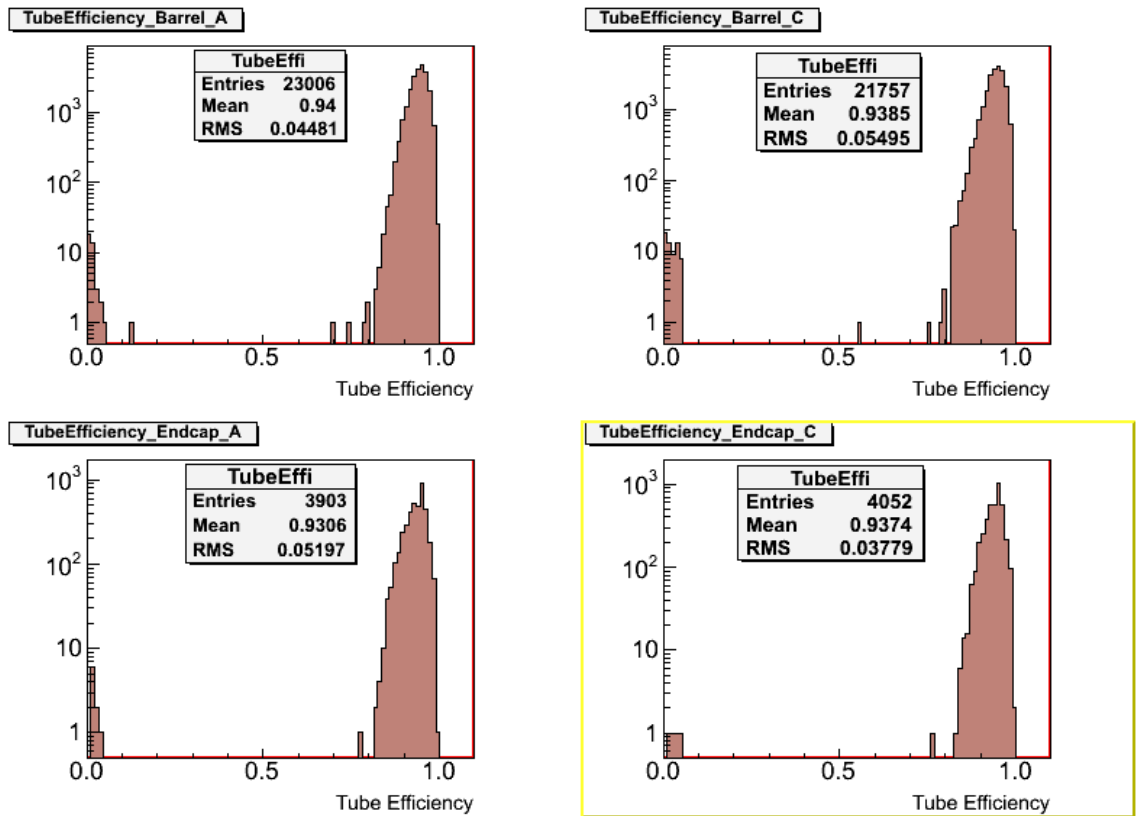


Figure 4.13: Overall efficiency of drift tubes in all MDT chambers of the middle station in barrel A (*top left*), barrel C (*top right*), endcap A (*bottom left*) and endcap C (*bottom right*). Note that the efficiency values close to zero are due to disconnected tubes or mezzanine cards being turned off.

systematic on the tube hit efficiency.

Reconstruction efficiency of combined muon tracks

In principle, the efficiency with which objects are reconstructed in a particular subdetector can be obtained from a Monte Carlo study. For example, the reconstruction efficiency for muons can be estimated from a simulated sample by comparing the number of generated muons to the number of reconstructed muons. However, a detector simulation will generally not be very accurate and, in particular, realistic background conditions cannot be modeled with precision. Hence, it is preferable to derive reconstruction efficiencies from real data with minimal reliance on simulation.

As stated in Section 4.2.3, we use combined muons from the Staco algorithm in our analysis, so that we want to estimate the efficiency of this particular reconstruction path. We derive the efficiency using two independent approaches, both of which measure the combined muon reconstruction efficiency relative to the inner detector track reconstruction efficiency. In the MS hit method, ID tracks are tagged as muon tracks using hits in the muon spectrometer, while in the tag-probe method, ID tracks are tagged as muon tracks by identifying them as coming from $Z \rightarrow \mu\mu$ decays. Both methods are described below.

The MS hit method

The selection criteria for events and for inner detector tracks used by this method are summarized in Table 4.2. The event selection criteria maximize the probability that the events are from collisions, while the kinematic and quality cuts on the tracks select well-reconstructed tracks that have similar characteristics to tracks from Z

decays (see Chapter 6).

Event selection	
Quality	Good runs list
Primary vertex	$N_{vtx} \geq 1$ with $N_{tracks} \geq 3$ $ z_{vtx} < 150$ mm
Trigger	L1_MU6
Inner detector track selection	
p_T	> 20 GeV
Pixel Hits	≥ 1
Silicon Hits	≥ 6
TRT Hits	≥ 10
Isolation	$\sum p_T^{ID}/p_T < 0.2$

Table 4.2: Event and track selection for muon reconstruction efficiency measurement using MS hit method.

A selected inner detector track is tagged as a muon if it is associated with a sufficient number of hits in the muon spectrometer. To determine this number, the track is extrapolated to each MDT tube layer. If a hit is found in a given layer, it is scored by its significance, defined as:

$$S_{assoc} = \frac{r_{ex} - c_{tube}}{\sqrt{\sigma_{ex}^2 + (w_{tube}/\sqrt{12})^2}} \quad (4.9)$$

where r_{ex} is the extrapolated track position along the precision dimension, c_{tube} is the center of the tube in that dimension, σ_{ex} is the extrapolator error and w_{tube} is the tube width. If a hit has $S_{assoc} < 3.0$, it is considered to be associated with the track [62]. If more than one hit in a layer satisfies this requirement, the one with the smallest value of S_{assoc} is used. The track is tagged if at least two of the following criteria are satisfied by the number of associated hits N_{assoc} :

- N_{assoc} in the inner MDT station ≥ 4
- N_{assoc} in the middle MDT station ≥ 3

- N_{assoc} in the outer MDT station ≥ 3

The combined muon reconstruction efficiency is defined as the fraction of tagged inner detector tracks within a cone of $\Delta R < 0.4$ of a combined muon track. Figure 4.14 shows the efficiency as a function of the p_T and η of the tagged inner detector tracks.

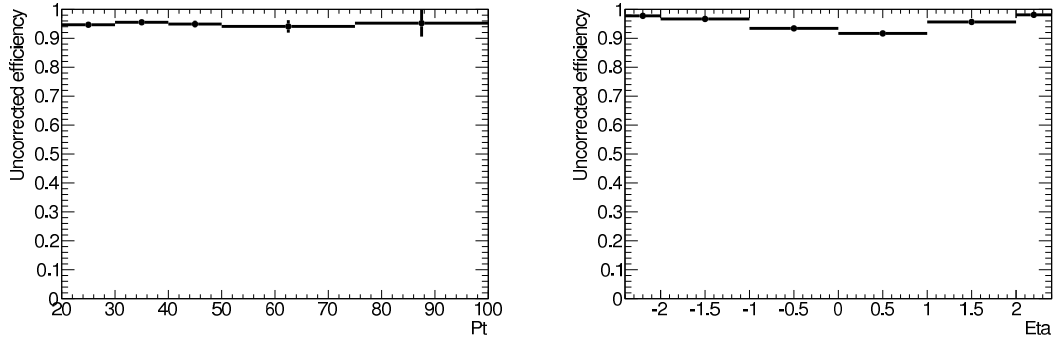


Figure 4.14: Measured combined muon reconstruction efficiency from the MS hit method in bins of tag p_T (*left*) and tag η (*right*).

The efficiency thus computed is likely to be an underestimation, however, because the sample of tagged tracks contains muons from pion decays in flight in addition to prompt muons. Decay-in-flight muons will often not be successfully combined, so that they will contribute to the denominator of the efficiency but not the numerator. We correct for this contamination by using templates of MDT hit residual distributions obtained from simulation. We obtain the template for prompt muons from a $W \rightarrow \mu\nu$ Monte Carlo sample, while that for decay-in-flight muons comes from a charged pion sample produced using a single-particle generator. We fit the templates to the hit residual distribution of tagged inner detector tracks and combined muon tracks in data, thus obtaining the fraction of prompt muon tracks in each [62]. The results are shown in Table 4.3.

Track type	Tagged InDet tracks	Combined muons
Prompt muon fraction	0.793 ± 0.003	0.830 ± 0.003

Table 4.3: Prompt muon fractions in data samples extracted using template fitting with Monte Carlo templates. Errors are statistical only.

Both the numerator and the denominator of the efficiency estimation are now corrected using the prompt muon fractions. The resulting combined muon reconstruction efficiency is found to be $0.994 \pm 0.006(stat)$ in data and 0.986 in $W \rightarrow \mu\nu$ Monte Carlo.

The systematic error on the efficiency is largely due to decay-in-flight contamination. We estimate this error by comparing the result from the template fitting with a second method in which the efficiency is computed as a product of two factors without the decay-in-flight correction. The two factors are:

- the reconstruction efficiency of standalone muon tracks with respect to tagged inner detector tracks
- the reconstruction efficiency of combined muon tracks with respect to the standalone tracks

The standalone muon track reconstruction efficiency is estimated as the fraction of tagged inner detector tracks within a cone of $\Delta R < 0.6$ of a standalone muon track. A subset of the standalone tracks is selected by requiring $p_T^{MS} > 10$ GeV, $|p_T^{ID} - p_T^{MS}| < 15$ GeV, and $\Delta R_{ID,MS} < 0.1$. This selection reduces the decay-in-flight contamination in the sample, although it does not eliminate them. The fraction of selected standalone tracks which are within a cone of $\Delta R < 0.4$ of a combined track is taken to be the combined track reconstruction efficiency with respect to standalone

tracks. The results are summarized in Table 4.4.

	Standalone tracks	Combined tracks	Overall
Data efficiency	0.981 ± 0.003	0.991 ± 0.002	0.972 ± 0.003
MC efficiency	0.993	0.997	0.991

Table 4.4: Measured relative muon reconstruction efficiency in data and Monte Carlo using a factorized method. Errors on the data measurement are statistical only. Errors on the Monte Carlo numbers are negligibly small.

Since the samples used in this method contain decay-in-flight contamination, the difference between these results and those from the template fit corrected method is a measure of the uncertainty arising from the contamination. The overall data efficiency in Table 4.4 differs from the decay-in-flight corrected efficiency by $\approx 2\%$. We take this number as a conservative estimate of the systematic from this source.

Other sources of systematic error on the combined reconstruction efficiency include the error on inner detector track reconstruction efficiency (1%), the error in MDT hit efficiency (0.3%), selection bias due to the tagging criteria (0.4%) and cut stability (0.5%) [62]. The various contributions are added in quadrature, leading to an overall systematic error on the measured efficiency of 2.4% (Table 4.5).

Data efficiency	0.994 ± 0.006 (stat) ± 0.024 (syst)
MC efficiency	0.986
Data/MC scale factor	1.008 ± 0.006 (stat) ± 0.024 (syst)

Table 4.5: Final results, including the data/MC scale factor, for the MS hit method of estimating combined track reconstruction efficiency.

The tag-probe method

The tag-probe method utilizes the correlation between the two muons in $Z \rightarrow \mu\mu$ decays. The first step is to define a sample of tagged events which contain at least

one high- p_T combined muon²¹. In these events, an inner detector track (the ‘probe’) is searched for using a set of criteria such as to ensure that it comes from a $Z \rightarrow \mu\mu$ decay²². The combined muon reconstruction efficiency is defined as the fraction of probe tracks that can be matched to a combined muon. Figure 4.15 illustrates the tag-probe method using $Z \rightarrow \mu\mu$ events.

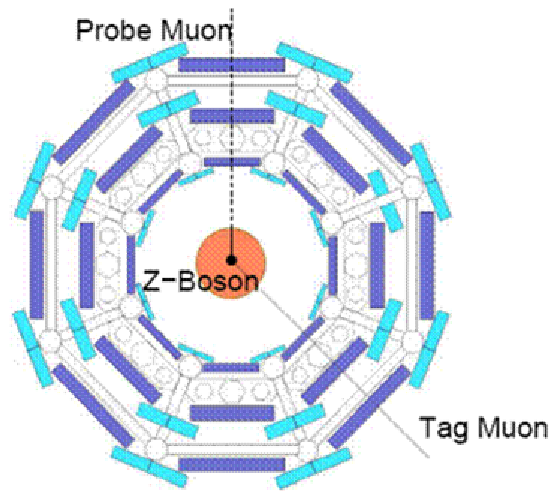


Figure 4.15: Schematic illustration of the tag-probe method using a $Z \rightarrow \mu\mu$ event.

The criteria used to select the tag muon and probe track are listed in Table 4.6. Note that only events containing at least one tag and at least one probe are used in the efficiency estimation.

114 events pass the selection criteria, containing 157 probe tracks. Matching the probes with combined muons using the condition $\Delta R < 0.01$, we find the measured

²¹Note that ‘tag’ has a different meaning in the context of this method from its meaning in the MS hit method.

²²Since we want to measure the reconstruction efficiency of the muon spectrometer, the probe selection criteria are chosen to be independent of that subsystem.

Tag selection	
Trigger	L1_MU6
Combined muon kinematics	$p_T \geq 15 \text{ GeV} \ \& \ \eta \leq 2.4$
Combined muon quality	$p_T^{\text{MS}} > 10 \text{ GeV}$ $ p_T^{\text{MS}} - p_T^{\text{ID}} < 15 \text{ GeV}$
Probe selection	
Track kinematics	$p_T \geq 20 \text{ GeV} \ \& \ \eta \leq 2.4$
Isolation	$\sum p_T^{\text{ID}} / p_T < 0.2$
InDet hit requirement	Pixel ≥ 1 , SCT ≥ 4 , Pixel+SCT ≥ 6 , TRT ≥ 10 for tracks with $\eta < 1.96$
$(\Delta d0)_{TP}$	$< 2 \text{ mm}$
$(\Delta z0)_{TP}$	$< 2 \text{ mm}$
$(\Delta \phi)_{TP}$	2.14 radians
Charge	$c_{\text{Tag}} \cdot c_{\text{Probe}} < 0$
Invariant mass	$ M_Z - M_{TP} < 15 \text{ GeV}$

Table 4.6: Selection criteria for tag muons and probe tracks in the implementation of the tag-probe method with $Z \rightarrow \mu\mu$ events. $z0$ and $d0$ are respectively the longitudinal and transverse components of the impact parameter measured at the distance of closest approach of a track to the primary vertex.

efficiency to be $0.922 \pm 0.006(\text{stat})$ in data and 0.924 in $Z \rightarrow \mu\mu$ Monte Carlo [62].

Figure 4.16 shows the combined muon reconstruction efficiency thus calculated as functions of probe p_T and η .

As with the MS hit method, the data sample used in the tag-probe study suffers from background contamination. In this case, events with a single reconstructed combined muon affect the measured efficiency. Such events can contribute to the denominator of the efficiency estimation but not the numerator, thus lowering the measured value. We estimate the single-muon event contribution using Monte Carlo, and find it to be 1.1% of the sample. We correct the measured efficiency by this amount. In addition, to account for uncertainties in the background simulation, we treat the single-muon event fraction as a systematic error on the efficiency.

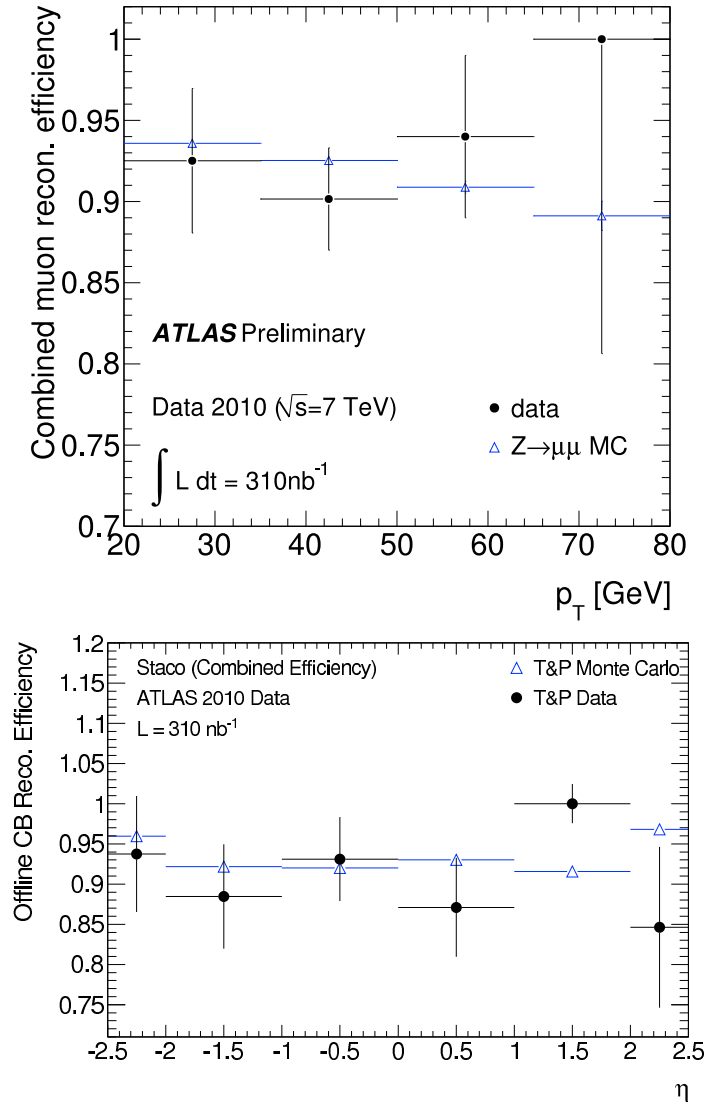


Figure 4.16: Measured combined muon reconstruction efficiency from the tag-probe method as a function of transverse momentum (*left*) and pseudorapidity (*right*) of the probes. Results are shown for both data and $Z \rightarrow \mu\mu$ Monte Carlo.

Because the tag and probe tracks are required to be largely back-to-back in the azimuthal coordinate, the tag-probe method can miss ϕ -symmetric inefficiencies in the detector. This effect can lead to an overestimation of the overall efficiency. The correct way to determine the efficiency is to compute it as a function of ϕ which, however, requires much larger statistics than we use for this analysis. Nevertheless, we obtain a crude estimate of this effect by measuring the efficiency with probes for which $(\Delta\phi)_{TP} < 3.0$. The result differs from the previously measured value by 0.4%, which we assign as a systematic.

Other sources of systematic error include that due to cut stability (0.6%) and data-MC efficiency differences (0.3%) [62]. The overall systematic error on the measured efficiency is 1.3% (Table 4.7).

Data efficiency	0.933 ± 0.022 (stat) ± 0.013 (syst)
MC efficiency	0.924
Data/MC scale factor	1.010 ± 0.022 (stat) ± 0.013 (syst)

Table 4.7: Final results, including the data/MC scale factor, for the tag-probe method of estimating combined track reconstruction efficiency.

Chapter 5

Monte Carlo Simulation

Monte Carlo (MC) simulation is an intrinsic part of experimental high-energy physics, mainly because of two reasons. Firstly, analyses are developed using simulated events, where we have knowledge of exactly what happened in the collision (the so-called ‘truth’ information), what subdetectors the particles propagated through, and therefore what we expect to see after event reconstruction. Secondly, theoretical predictions for the final result of an analysis can be obtained from MC simulation, such as the Z boson production cross-section in our case. The measurement can then be compared with the prediction.

We start this chapter with an overview of the various processes involved in MC simulation. Then we briefly describe the MC programs and samples we use in our analysis, and end the chapter a review of the ATLAS detector simulation.

5.1 Overview of Monte Carlo event generation and simulation

MC simulation consists of two basic steps. In the *generation* step, events that can occur in a collision are generated according to a theoretical modeling of the physics

involved. An event generator program can calculate cross-sections, *i.e.*, event rates, for a process. It can determine differential cross-sections as functions of kinematic variables, and then generates hypothetical events to populate the phase space of these variables. It provides energy-momentum four-vectors of primary particles produced in the hard interaction and of the decay products of all unstable particles. Differential cross-sections can be estimated using either exact matrix elements to a given degree of accuracy, or an ‘all-order’ approach such as parton showering or QCD resummation. At the end of the decay process, partons are grouped into hadrons using a hadronization model (Chapter 1). At a hadron-hadron collider such as the LHC, the underlying event must also be modeled¹.

A second class of MC generators are the so-called *cross-section integrators*. Unlike event generators, these programs do not output events with full kinematic information, but rather produce distributions of kinematic variables, *e.g.*, p_T spectra, with high precision. Cross-section integrators are often used for unambiguous interpretation of experimental results.

In the *simulation* step, final-state particles from the generation step are propagated through a realistic description of the detector. Ideally, all parts of the detector, including active detection volumes and inactive (‘dead’) material, would be included in the detector description. The simulation program knows what volume a particle is traversing at a given stage; interactions with the material in that volume are modeled according to the particle type, properties of the material and known physics. Elec-

¹The *underlying event* arises from interactions between partons in the colliding hadrons that did not participate in the hard process. These interactions can be significant and can lead to sufficient activity in the final state so as to affect the measurement of the hard process. It is therefore essential that the underlying event be accurately described in Monte Carlo.

tronic signals from active volumes are simulated such that they mimic the passage of real particles. From these signals, the full event can then be reconstructed in the same way as for real events, as described in Chapter 4.

By comparing simulation results with the truth information, we can determine quantities such as the acceptance of the detector and the smearing of kinematic distributions due to finite detector resolution.

5.2 Monte Carlo generators used in this analysis

The Monte Carlo datasets we use for our analysis were generated in the *Athena* [18] framework using two programs: PYTHIA [92] and POWHEG [44]. In addition, we use the FEWZ [67] program to compute the theoretical prediction for the $Z \rightarrow \mu\mu$ cross-section with which we compare our measurement. The main features of these programs are briefly described in this section.

5.2.1 Pythia

PYTHIA evaluates process cross-sections by using matrix elements that are leading-order in QCD. For many processes, including the $Z \rightarrow \mu\mu$ decay, it includes spin correlations of the decay products. PYTHIA uses the parton shower technique (see Chapter 1) to generate initial- and final-state gluon radiation. The PYTHIA parton shower is accurate to leading-logarithm, and leads to semi-realistic modeling of multipartonic final states.

PYTHIA models the underlying event by a set of separate $2 \rightarrow 2$ scatterings using leading-order matrix elements. Parton-parton interactions occur down to $q_T = 2$

GeV, below which color screening in the hadrons suppresses perturbative interactions. Note that the PYTHIA underlying event description has been tuned inside the ATLAS event generation framework such that event properties match measurements using the 900 GeV data from 2009 and 7 TeV data in 2010 [93]. As discussed in Chapter 1, hadronization is implemented in PYTHIA via the Lund string model.

External packages can be interfaced with PYTHIA where particle decay or radiation requires special treatment. These include TAUOLA [65] for τ decays with spin information and PHOTOS [77] for generating final-state photon radiation. PYTHIAB [87] is a modification of PYTHIA, used exclusively inside the ATLAS event generation framework, that allows fast generation of events containing b and/or c quarks.

Our analysis uses PYTHIA-generated datasets for the signal channel and four background channels, namely, $W \rightarrow \mu\nu$, $b\bar{b}$, $c\bar{c}$ and $Z \rightarrow \tau\tau$. For the $Z \rightarrow \mu\mu$, $W \rightarrow \mu\nu$ and $Z \rightarrow \tau\tau$ samples, the MRST LO* [86] PDF set was used, and final-state photon radiation was generated with PHOTOS. In the $Z \rightarrow \mu\mu$ sample, simulated minimum bias interactions were overlaid on top of the hard-scattering event to mimic the effect of event pileup 6.2. The $b\bar{b}$ and $c\bar{c}$ samples were generated with PYTHIAB, also using the MRST LO* PDF set.

5.2.2 POWHEG

POWHEG (*P*ositive *W*eight *H*ardest *E*mission *G*enerator) includes full next-to-leading-order QCD corrections in evaluating matrix elements. Additionally, it can be coupled to a parton shower-based Monte Carlo program. Since matrix elements accurately describe the high- p_T regime of a given process, and parton shower most

effectively describes soft (low- p_T) and/or collinear emissions, combining the two techniques results in a more accurate description of the process than either can provide by itself. All events generated by POWHEG have positive weights, unlike events from MC@NLO [84], which generates some events with negative weights since the approximate NLO process cross-section from the shower Monte Carlo must be subtracted from the exact NLO cross-section.

In implementing parton radiation, POWHEG generates the hardest parton first using NLO matrix elements by a method that yields only positive-weighted events [44]. The output can be passed to a shower Monte Carlo which then performs softer emissions, hadronization etc. If the shower Monte Carlo orders parton emissions by p_T , the showering starts with an upper limit on the scale which is just below the scale of the POWHEG emission. As a result, observables such as cross-section have NLO accuracy even if the shower algorithm starts from a leading-order matrix element. Moreover, if the shower Monte Carlo correctly treats emissions that are both soft and collinear (the so-called ‘double-logarithmic’ region), this accuracy is retained in the final event. We note that PYTHIA contains both of these features, *i.e.*, p_T -ordered parton emission and double-logarithmic accuracy.

The $t\bar{t}$ background sample used in our analysis was generated using POWHEG interfaced with PYTHIA for parton showering. The CTEQ6.6 PDF set was used, and PHOTOS was interfaced for final-state photon radiation.

5.2.3 FEWZ

FEWZ (*F*ully *E*xclusive *W* and *Z*) [67] is a cross-section integrator. It computes

production cross-sections for W and Z bosons produced in hadronic collisions to NNLO accuracy in QCD. As mentioned in Chapter 1, FEWZ takes into account quark masses, finite width effects, spin correlations of boson decay products and $\gamma - Z$ interference in the case of Z bosons.

We use FEWZ to derive the theoretical prediction for the $Z \rightarrow \mu\mu$ cross-section, to which we compare the final result of our analysis. In addition, we normalize the cross-sections of the PYTHIA-generated W and Z signal and background samples to the NNLO cross-sections of the corresponding processes obtained from FEWZ. The MSTW2008NNLO PDF set was used with FEWZ.

5.2.4 Monte Carlo samples used in this analysis

Table 5.1 gives a summary of the Monte Carlo datasets used in our analysis, together with the cross-sections and the number of events in each sample. For the $b\bar{b}$ and $c\bar{c}$ samples, the leading-order cross-sections from PYTHIA are used. The cross-sections of the W and Z samples are normalized to the corresponding NNLO cross-section values obtained using FEWZ. The $t\bar{t}$ cross-section is taken from [71].

5.2.5 The ATLAS detector simulation

As discussed above, an accurate detector description is crucial for developing an analysis, and especially for optimizing the various selection criteria. The ATLAS detector simulation is based on the GEANT4 [60] simulation toolkit, which is used by a large number of projects in various domains. The ATLAS GEANT4 simulation contains over a million volumes including active and inactive material.

Process	Dataset	Generator	Cross-section (pb)	$N_{\text{evt}} (\times 10^6)$	Note
$Z \rightarrow \mu\mu$	106047	PYTHIA	989	7.9	$\sqrt{\hat{s}} > 60$ GeV
$W \rightarrow \mu\nu$	106044	PYTHIA	10 454	7	
$Z \rightarrow \tau\tau$	106052	PYTHIA	989	7.9	$\sqrt{\hat{s}} > 60$ GeV
$t\bar{t}$	105861	POWHEG	161	0.2	$m_t = 172.5$ GeV/ c^2 , single lepton filter $\epsilon = 0.538$
$b\bar{b}$	108405	PYTHIA	7.39×10^4	4.4	15 GeV/ c single muon filter
$c\bar{c}$	106059	PYTHIA	2.84×10^4	1.5	15 GeV/ c single muon filter

Table 5.1: Monte Carlo samples used in this analysis. The cross-sections quoted are the ones used to normalize estimates of expected event numbers. The cross-sections for the $b\bar{b}$, $c\bar{c}$ samples are taken directly from PYTHIA. Sources for the other cross-sections are discussed in the text.

The active material description is contained in two databases: one containing the size and coarse position of each detector element, and the other detailing the variations in their positions as a function of time. A third database contains descriptions of the inactive (‘dead’) material such as support structures. Most of the dead material is located toward the edges of the detector, so that the inner detector and the calorimetry are not much affected by it. But dead material description is vital for the muon system since muons typically traverse large volumes of such material.

The actual geometry of ATLAS at runtime is different from the ‘as-built’ geometry. The shape of the detector is distorted by its own weight; the large magnetic fields in the solenoid and the toroids also change the shape. These changes are monitored and the detector description databases regularly updated. The magnetic field map, built using information from a large number of B -field sensors, is also updated frequently. The detector description and magnetic field map are input to track reconstruction in

both real and simulated events.

Chapter 6

Event Selection

After event reconstruction, the four-vectors of leptons and jets are available, together with a number of other quantities helpful in identifying these objects. Since we want to study $Z \rightarrow \mu\mu$ events, the primary aim of our event selection is to identify events with isolated muons that have high transverse momenta. In addition to the signal, various types of background events will pass our selection criteria, and we must eliminate as many of these events as possible. In this chapter, we describe the criteria for selecting muons and $Z \rightarrow \mu\mu$ events, and then discuss the acceptance and efficiencies of these criteria. Background estimation will be described in Chapter 7.

6.1 Z event selection

The Z event preselection is divided into two parts. First, we apply collision candidate selection criteria to maximize the likelihood that the events are from pp collisions:

- We require each event to have a bunch crossing index which corresponds to bunches that collide in ATLAS. This criterion largely eliminates events from

beam halo and beam-gas interactions.

- Then we require that the events pass the L1_MU6 trigger. At this stage, the data sample contains 5464740 events.
- Events are then required to have at least one reconstructed primary vertex which has at least three inner detector tracks associated with it. In addition, we require that the primary vertex be located within 15 cm from the nominal interaction point along the beam pipe. This requirement takes the finite size of the beam spot into account, at the same time reducing contamination from cosmic events. 5103785 events pass the vertex cut.

The ‘high- p_T muon event’ selection eliminates low-quality, low- p_T and possibly fake muons. We require that the events have at least one combined muon, reconstructed in both the inner detector and the muon spectrometer, having p_T greater than 15 GeV and within $|\eta| < 2.4$. The later cut is motivated by the fact that the muon trigger coverage ends at $|\eta| = 2.4$.

A detailed study of high- p_T muons in collision data [61] showed that requiring a muon spectrometer track extrapolated to the primary vertex to have p_T greater than 10 GeV largely rejects muons from pion/kaon decays-in-flight as well as poorly matched tracks between the inner detector and the muon spectrometer. Additionally, requiring the difference in p_T between the spectrometer and inner detector tracks, $|p_T^{MS} - p_T^{ID}|$, to be less than 15 GeV significantly reduces fake muons while losing very little of the signal. We therefore impose these two criteria on the muon track. 22075 events are left in the data sample at this stage.

The sample now contains $Z \rightarrow \mu\mu$ events as well as events from other high- p_T physics sources. To select a sample of pure $Z \rightarrow \mu\mu$ events for the cross-section measurement, we apply the additional ‘ Z selection’ criteria, requiring two isolated, oppositely charged high- p_T muons with an invariant mass consistent with the hypothesis that they originate from the decay of a Z boson. These criteria are described below and summarized in Table 6.1.

Collision event selection	
Primary vertex	$N_{vtx} \geq 1$ with $N_{tracks} \geq 3$ $ z_{vtx} < 150$ mm
Trigger	$L1_MU6$
High- p_T event selection	
Muon selection	combined tracks $p_T > 15$ GeV, $ \eta < 2.4$
Muon quality	$p_T^{MS} > 10$ GeV $ p_T^{MS} - p_T^{ID} < 15$ GeV $ z_0 - z_{vtx} < 10$ mm
$Z \rightarrow \mu\mu$ event selection	
Tight kinematics (both muons)	$p_T > 20$ GeV, $ \eta < 2.4$
Muon quality (both muons)	(as above)
ID isolation (both muons)	$\sum p_T^{ID}/p_T < 0.2$
Charge	$c_1 \cdot c_2 < 0$
Invariant Mass	$66 < m_{\mu\mu} < 116$ GeV

Table 6.1: Event selection for Z candidates.

- Combined muon requirement: we require the event to have at least two combined muons. The measurement can also be made using a less strict selection requiring one or both muons to be standalone or tagged 4.2.3. The looser selection would increase our signal acceptance. However, standalone and tagged muons have a number of problems which combined muon do not suffer from:

- In the muon momentum range relevant to the Z analysis, the momentum resolution of combined tracks using information from both the inner detector and the muon spectrometer is expected to be better than that of standalone muon tracks. In particular, standalone tracks can suffer from dead material that is not accounted for in the material database, uncorrected misalignment at both chamber and stations levels, and low bending power of the magnetic field in certain regions of the spectrometer.
- Tagged muons do not require hits in more than one muon station, so that tagged tracks typically have a small number of precision hits in the spectrometer. This strategy also fails to take advantage of the large bending power of the spectrometer. As a result of both these factors, the fraction of fake tracks is expected to be high among tagged tracks.

1879 data events satisfy the combined muon requirement.

- Muon η and p_T cuts: We require $|\eta| < 2.4$ and $p_T > 20$ GeV for both muons¹.
- Muon quality cuts. To ensure that both muons have high quality, we require both to have $p_T^{MS} > 10$ GeV, $|p_T^{MS} - p_T^{ID}| < 15$ GeV and $|z_0 - z_{vtx}| < 10$ mm. The sample contains 144 events at this stage.
- Isolation cut: Z decay muons will in general be isolated, while muons from many of the background processes are non-isolated. We impose an inner detec-

¹In principle, the η cut on the second muon can be loosened to 2.5, where the inner detector coverage ends, thus increasing signal acceptance. In addition, the p_T cut on the second muon can be loosened to 15 GeV. For this first measurement, however, we decided to keep these cuts symmetric on the two muons for the sake of simplicity. These cut values are expected to change for subsequent Z -related measurements.

tor track-based isolation requirement to minimize background event contamination. A relative isolation quantity is constructed by summing the p_T of all inner detector tracks in a cone around the muon track that have $p_T > 1$ GeV, excluding the muon track itself, and dividing by the combined muon p_T :

$$\text{isol}_\mu = \frac{\Sigma \text{track}_{p_T}}{\mu_{p_T}} \quad (6.1)$$

To determine the optimal cone size, we studied the background rejection and signal efficiency of isol_μ for three different cone sizes, namely, $\Delta R = 0.2, 0.3$ and 0.4 . For each cone size, we looked at the rejection of non-prompt muons as a function of the efficiency for Z decay muons for $\text{isol}_\mu < 0.2$. The results are shown in Figure 6.1. We see that $\Delta R = 0.4$ provides the largest background rejection and the smallest signal loss, so that this is the cone size we use. We require $\text{isol}_\mu < 0.2$ for each muon. 117 events are left in the sample after this cut.

- Opposite charge: We require that the muons have opposite charge. All 117 events satisfy this requirement, that is, no same-sign dimuon events exist in our data sample after the isolation requirement.
- The final Z selection cut is on the invariant mass $M_{\mu\mu}$ of the muon pair. We require the invariant mass to lie in the range 66-116 GeV. We have 109 events passing this cut.

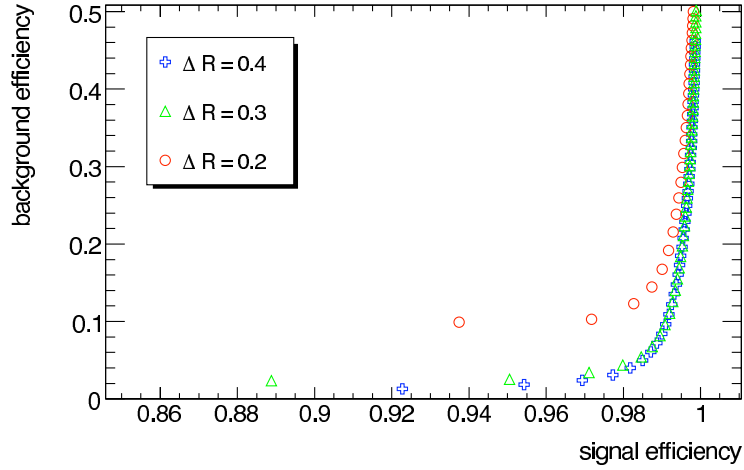


Figure 6.1: Background versus signal efficiency for three different cone sizes used to define the relative track isolation. Monte Carlo samples are used for both background and signal.

6.1.1 Properties of the preselected sample

In this section, we present some properties of the data events, Monte Carlo signal and Monte Carlo background events after the preselection criteria have been applied. The backgrounds we consider include $t\bar{t}$, QCD ($b\bar{b}$ and $c\bar{c}$), $Z \rightarrow \tau\tau$ and $W \rightarrow \mu\nu$. These channels will be discussed in some detail in Chapter 7.

Hit distributions

We show below the distribution of hits on muon tracks in the various subsystems of the muon spectrometer and the inner detector. Figure 6.2 shows the number of MDT hits per track. The distribution peaks at 20 hits, which is expected for tracks that traverse all layers of all three MDT stations (Section 2.2.4). However, we see a significant number of tracks with 12 hits, *i.e.*, tracks that go through two stations. Since at least 2 segments are required for a track to be reconstructed, and each

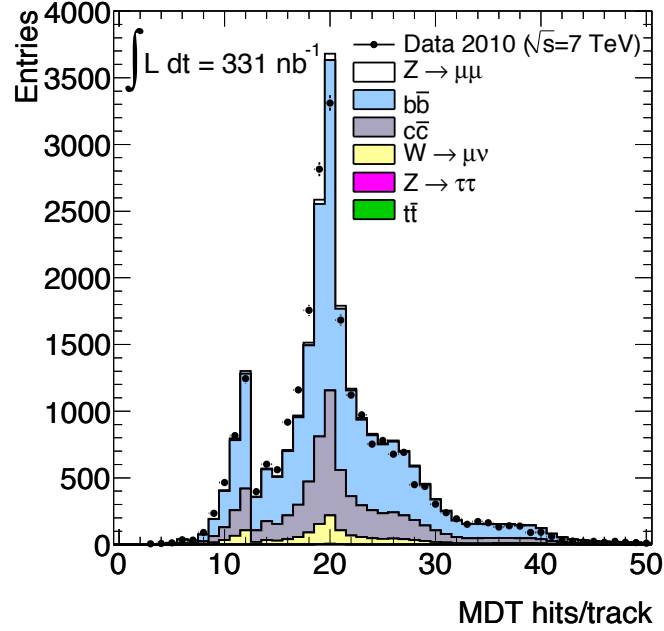


Figure 6.2: MDT hits per muon track for signal Monte Carlo, background Monte Carlo and data after event preselection. The total Monte Carlo event number has been normalized to the number of events in data.

segment must have at least 3 hits on it, in principle there should be no track with less than 6 hits. We see a very small number of tracks with 3-5 hits, which are most likely badly reconstructed tracks with two segments that share one or more MDT hits.

A track can have more than 20 MDT hits owing to two reasons:

- It traverses the overlap region between adjacent ϕ sectors. Such a track can have a maximum of 40 hits, assuming that it does not have more than one hit in any MDT tube layer.
- It traverses multiple tubes in the same tube layer. Because of the geometry of the multilayers, there should be very few such tracks in collision events.

We see that a small number of tracks have more than 40 hits, which are tracks

with multiple hits in the same layer.

We note that, in the peak region, the data is systematically shifted toward lower number of hits compared to Monte Carlo. This is primarily due to misalignment among the MDT stations that is not taken into account in the simulation. The misalignment can result in some MDT hits not being assigned to a track, thus shifting the hit spectrum toward lower values.

Figure 6.3 shows the number of RPC η and ϕ hits per track. Since there are 3 RPC stations, and each station has 2 readouts in η and 2 in ϕ , 6 hits are expected in each coordinate for a track that traverses all three RPC stations. This is where the peak occurs in each coordinate. Tracks with more than 6 hits in η or ϕ have gone through the overlap region between adjacent sectors. In both coordinates, we see good agreement between data and Monte Carlo. We note that the 0-hit bin is due to tracks in the endcap which are not expected to traverse the RPCs.

Figure 6.4 shows the number of TGC η and ϕ hits per track. The expected number of hits per track in each of the η and ϕ coordinates is determined by the arrangement of doublet and triplet gas gap configurations, as described in [15] (see also Figures 1-20 and 4-30 in [15]). In Figure 6.4, we see that the data is significantly above the Monte Carlo expectation in some bins. For the η coordinate, we see this discrepancy in the 1-, 5- and 15-hit bins, while for the ϕ coordinate this is the case in several bins. The discrepancy is explained by cross-talk between neighboring readout channels. In Monte Carlo, the amount of cross-talk is determined by a parameter that must be adjusted such that the Monte Carlo hit distribution agrees with that in data. This adjustment has not been done in the Monte Carlo samples we use, so that some

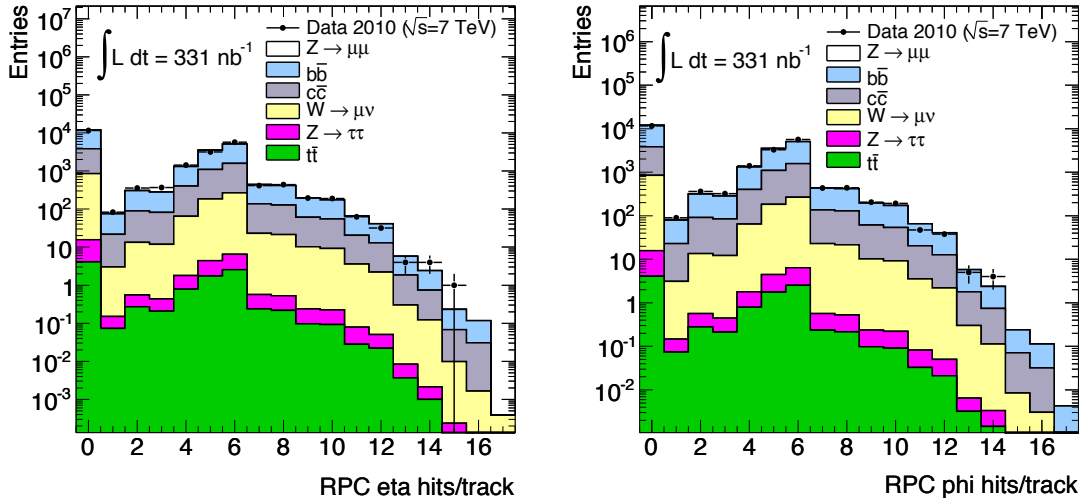


Figure 6.3: RPC η (*left*) and ϕ (*right*) hits per muon track for signal Monte Carlo, background Monte Carlo and data after event preselection. The total Monte Carlo event number has been normalized to the number of events in data.

disagreement is expected. In addition, the amount of cross-talk is expected to be worse in ϕ than in η [59], which is what we observe.

We note that the 0-hit bin is due to tracks in the barrel which, of course, do not traverse the TGCs.

Figure 6.5 shows the number of Pixel hits on the inner detector track associated with the combined muon track. Most tracks have at least 3 Pixel hits, as expected (Section 2.2.2). Tracks that traverse overlap regions between Pixel layers have more than 3 hits. In all bins, we see good agreement between data and Monte Carlo.

Figure 6.6 shows the number of SCT and TRT hits on the track. The SCT hit plot shows the sum of hits on the axial/radial sides and the stereo sides of the strips. Consequently, at least 8 hits are expected on a typical track from the 4 SCT layers. Smaller hit multiplicities result from hit association inefficiencies in the SCT.

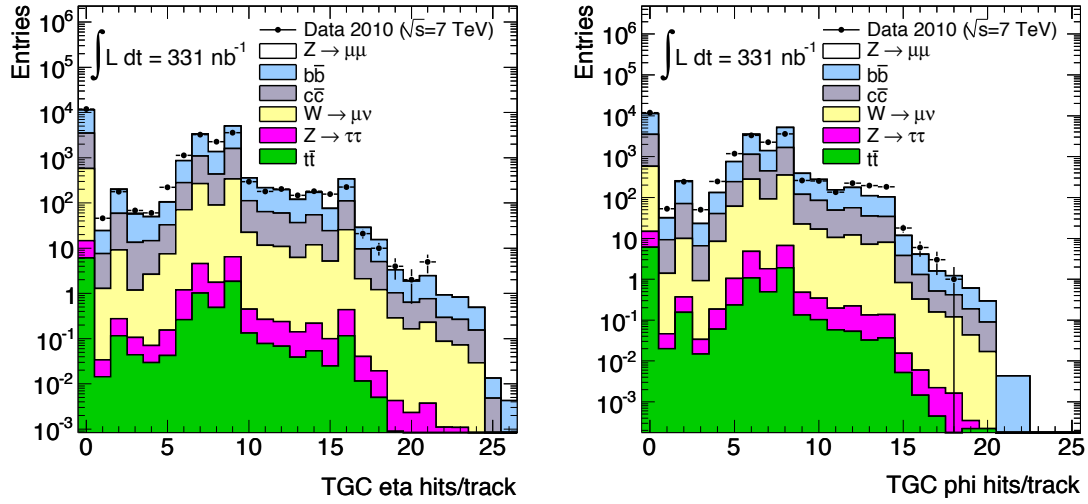


Figure 6.4: TGC η (*left*) and ϕ (*right*) hits per muon track for signal Monte Carlo, background Monte Carlo and data after event preselection. The total Monte Carlo event number has been normalized to the number of events in data.

Although the data agrees with Monte Carlo expectation in most bins, we see that it is significantly above expectation in the 0- and 2-hit bins. These tracks are most likely TRT-only tracks that were back-extrapolated into the silicon, and have few or no SCT hits [12]. We note that these tracks constitute $\approx 0.1\%$ of the total sample.

A track is typically expected to traverse 36 TRT layers in the barrel, which is where we see the peak in the hit distribution. The smaller peak at ≈ 20 hits is due to tracks in the TRT endcaps. The 0-hit bin is due to tracks outside the TRT acceptance of $|\eta| < 2.0$.

As with the MDT hit distributions, we see a migration toward lower bins in data compared to Monte Carlo expectation in the TRT hit distribution. As before, we understand this feature as a consequence of misalignment among the layers, so that the algorithm fails to associate some hits with the track.

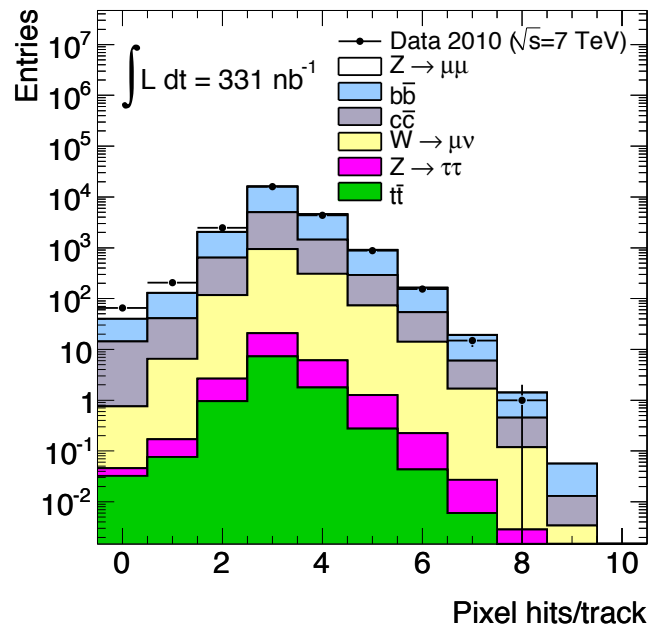


Figure 6.5: Pixel hits on inner detector tracks matched to muon spectrometer tracks for signal Monte Carlo, background Monte Carlo and data after event preselection. The total Monte Carlo event number has been normalized to the number of events in data.

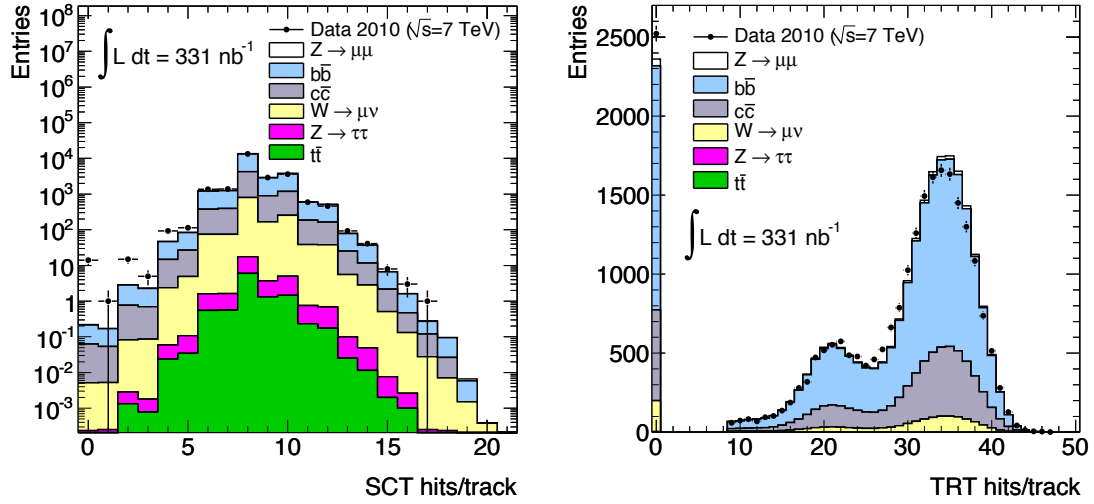


Figure 6.6: SCT hits (*left*) and TRT hits (*right*) on inner detector tracks matched to muon spectrometer tracks for signal Monte Carlo, background Monte Carlo and data after event preselection. The total Monte Carlo event number has been normalized to the number of events in data.

Kinematic distributions

Figure 6.7 shows muon kinematic distributions (p_T , η and ϕ) at the preselection stage. Figure 6.8 (*left*) shows the track isolation ratio versus muon p_T , while Figure 6.8 (*right*) shows the dimuon invariant mass distribution. The Monte Carlo predictions in these figures have been normalized to the number of data events. As expected, QCD backgrounds dominate the sample owing to their large cross-sections. The data and Monte Carlo show reasonably good agreement within the statistical uncertainty.

6.2 Z signal acceptance and efficiencies

The $Z \rightarrow \mu\mu$ production cross-section is given by:

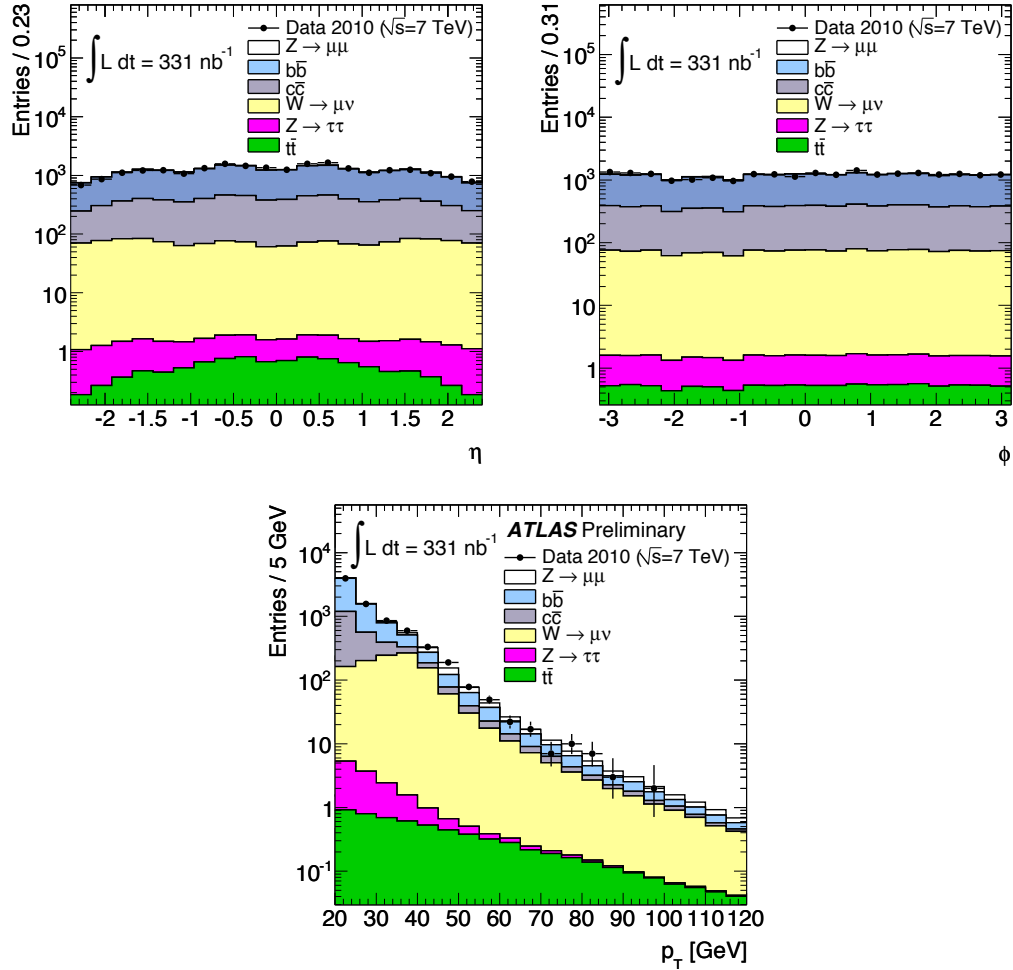


Figure 6.7: Muon η , ϕ , p_T distributions for signal Monte Carlo, background Monte Carlo and data after the event preselection. The total Monte Carlo event numbers have been normalized to the number of events in data.

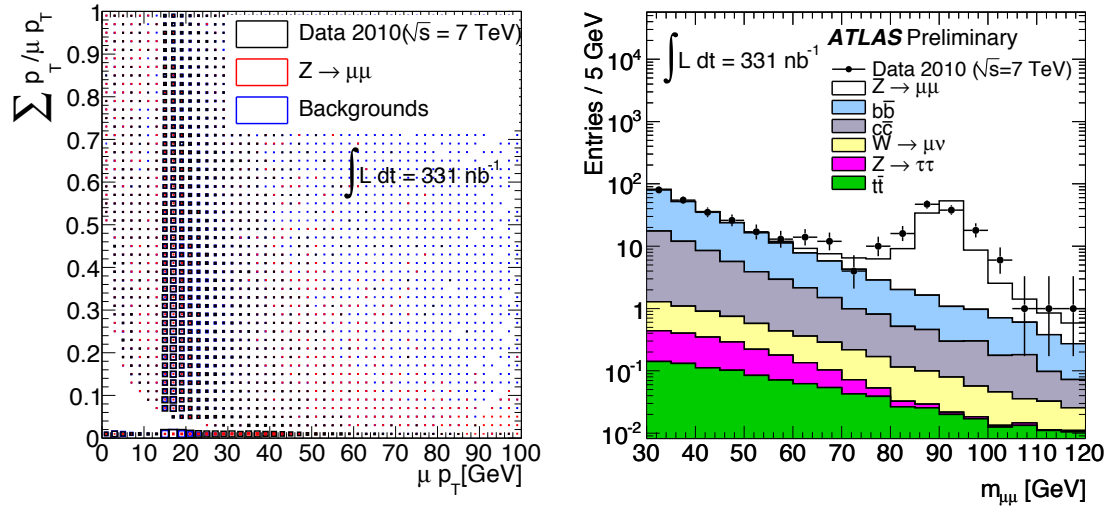


Figure 6.8: Track isolation ratio versus muon p_T (*left*) and dimuon invariant mass distribution (*right*) for signal Monte Carlo, background Monte Carlo and data after the event preselection. The total Monte Carlo event numbers have been normalized to the number of events in data.

$$\sigma_{tot} = \sigma_{Z/\gamma^*} \times BR(Z/\gamma^* \rightarrow \mu\mu) = \frac{N - B}{A_Z C_Z L_{int}}, \quad (6.2)$$

where σ_{tot} is measured within the invariant mass window $m_{\mu\mu} = 66 - 116$ GeV, and

- N is the number of candidate events observed in data,
- B is the expected number of background events,
- L_{int} is the integrated luminosity for the dimuon decay channel corresponding to the L1.MU6 trigger,
- A_Z and C_Z are factorized acceptances, defined below, and corrected for any discrepancy in reconstruction and trigger efficiencies between data and Monte Carlo.

By setting $A_Z = 1$ in Eq. 6.2 we obtain the cross-section σ_{fid} measured in the fiducial region defined by the geometrical acceptance of the detector and the kinematic acceptance of the selections used in the analysis. Before we describe the acceptance estimations in detail, however, there is a caveat due to event pile-up which we address.

6.2.1 Monte Carlo event reweighting owing to pile-up

For instantaneous luminosities in excess of $\approx 10^{30} \text{ cm}^{-2}\text{s}^{-1}$, there is a significant probability of more than one pp interaction per bunch crossing, *i.e.*, event pile-up. Pile-up events can affect the Z selection by introducing additional tracks in the inner detector and thus changing the value of the isolation variable. To take into account the effects of event pile-up on our signal selection, we use a signal Monte Carlo sample with simulated minimum-bias interactions overlain on top the hard-scattering event.

Figure 6.9 (*left*) [62] shows a comparison of the number of primary vertices per event in the early part of the data-taking (periods A-C) with that in the latter part (period D, instantaneous luminosity $>\approx 10^{30} \text{ cm}^{-2}\text{s}^{-1}$). The distributions are normalized to unit area. The increase in the number of vertices with instantaneous luminosity is clearly seen. Figure 6.9 (*right*) shows the number of vertices per event in the entire collision dataset compared to that in the Monte Carlo sample with event pile-up. We see that the mean number of vertices is considerably larger in the Monte Carlo than in data. We therefore reweight the Monte Carlo vertex distribution to match that in data, in all vertex bins except the zero bin [62].

An event in the pile-up Monte Carlo sample with N vertices is weighted by the ratio $\frac{N^{data}}{N^{MC}}$, where N^{data} is the fraction of events in data with N vertices, and N^{MC}

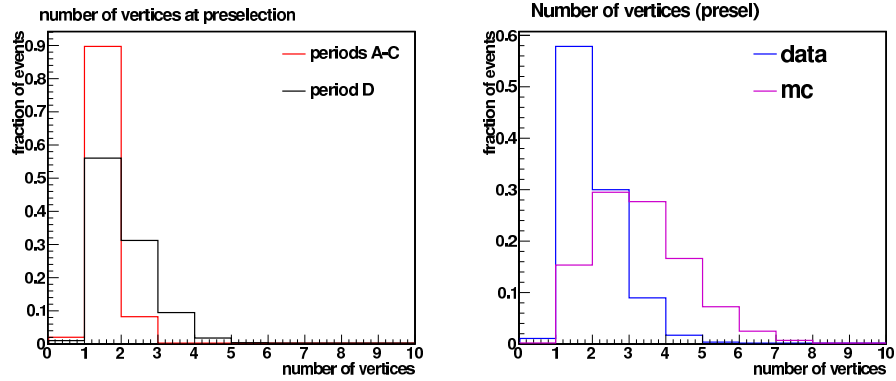


Figure 6.9: *Left*: Comparison of the number of reconstructed vertices per event in periods A-C with that in period D. *Right*: Comparison of the number of reconstructed vertices per event in data and Monte Carlo. The distributions are from after the muon pre-selection requirements. Vertices are required have $|z| < 150$ mm from the nominal interaction point and at least three inner detector tracks associated with it. The data-taking periods were defined in Chapter 4.

is the corresponding fraction in Monte Carlo. We use vertices after the event pre-selection that satisfy $|z_{vtx}| < 150$ mm from the nominal interaction point and have at least three associated inner detector tracks. The event weights used on the Monte Carlo as well as the fraction of events with each vertex multiplicity are summarized in Table 6.2. Further details of the weighting procedure can be found in [62].

6.2.2 Acceptance of Z selection from Monte Carlo cutflow

We can define the acceptance as the number of events passing our selection criteria divided by the total number of generated events. Table 6.3 shows the number of Monte Carlo $Z \rightarrow \mu\mu$ events passing each step of the selection as well as the efficiency of each step relative to the full sample and to the previous step.

Number of vertices	Fraction of events		Event weight
	In data	In simulation	
0	-	-	1
1	0.5848	0.1538	3.8027
2	0.3032	0.2956	1.0260
3	0.0907	0.2773	0.3270
4	0.01729	0.1666	0.1038
5	0.00374	0.0726	0.0514
6	0.000192	0.0250	0.0077
7	0.000048	0.00709	0.00675
8	0.	0.00165	0.
9	0.	0.00034	0.

Table 6.2: Fraction of events with N vertices in Monte Carlo and data for $N = 1 - 9$. The last column shows the weights that we use to correct the Monte Carlo. The weight for the 0-vertex case is set to 1, since the fraction of events in data without a reconstructed vertex is negligibly small.

Selection	Number of events	Relative eff.	Absolute eff.
Total Events	299249	-	-
L1_MU6	256943	85.9%	85.9%
Vertex	256422	99.8%	85.7%
High p_T muon	232787	90.8%	77.8%
2 combined muons	142226	61.1%	47.5%
$ \eta < 2.4$	135505	95.3%	45.3%
$p_T > 20$ GeV, MS $p_T > 10$ GeV, $dp_T < 15$ GeV	116938	86.3%	39.1%
ptcone40/pT < 0.2	114946	98.3%	38.4%
Opp charge	114945	1.00%	38.4%
Mass window	111805	97.3%	37.4%

Table 6.3: Effect of the $Z \rightarrow \mu\mu$ selection criteria on simulated $Z \rightarrow \mu\mu$ events. The relative efficiency is relative to the previous step of the selection, while the absolute efficiency is relative to the total number of events in the sample. The statistical uncertainty on the efficiency estimates are $< 10^{-3}$.

6.2.3 Factorizing the acceptance: A_Z and C_Z

The overall acceptance can be factorized into two parts: one that can be extracted from Monte Carlo generation-level quantities only (A_Z), and one that relies on reconstructed quantities (C_Z). With the acceptance thus factorized, we can report the $Z \rightarrow \mu\mu$ cross-section within a fiducial region or as an inclusive value, as already mentioned. The calculation of the acceptance factors and associated systematics are described in detail in the sections below.

Fiducial acceptance A_Z

A_Z denotes the fraction of generated $Z \rightarrow \mu\mu$ events that pass the kinematic and geometric selection of the analysis at the generator level. More explicitly, it is the fraction of generated events satisfying $p_T^{(l^+, l^-)} > 20$ GeV, $|\eta^{(l^+, l^-)}| < 2.4$, and 66 GeV $< M_{ll} < 116$ GeV, where all of these quantities pertain to truth-level muons before any final-state photon radiation. A_Z corrects the fiducial cross-section to the total cross section. Its value is estimated from PYTHIA Monte Carlo using the MRST LO* PDF set to be 0.486 ± 0.019 (stat). The statistical uncertainty on this value is negligible.

The systematic uncertainty on A_Z has been studied in detail in [85], and we describe it here briefly. There are three main sources of systematics:

- Uncertainties within a PDF set: these are determined using the 44 error eigenvectors of the CTEQ6.6 PDF set and $Z \rightarrow \mu\mu$ events generated with MC@NLO. For each error eigenvector i , values of the acceptance A_{Z+}^i and A_{Z-}^i are computed, and the uncertainty on A_Z estimated by the expression:

$$\Delta A_{Z_+} = \Delta A_{Z_-} = \frac{1}{2} \sqrt{\sum_i (A_{Z_+}^i - A_{Z_-}^i)^2} \quad (6.3)$$

The relative uncertainty from this source is found to be 1.60%.

- Uncertainties among different PDF sets: this component of the systematic is determined from the maximum difference of the value of A_Z estimated from the PYTHIA sample generated using MRST LO* and from PYTHIA samples using CTEQ6.6 and HERAPDF1.0 [111] NLO PDF sets. The relative uncertainty from this source is 2.01%.
- Uncertainty from the parton shower model: since PYTHIA and MC@NLO use different parton shower models, the uncertainty due to parton showering can be estimated by comparing values of A_Z from samples generated with the two algorithms using the same PDF set (CTEQ6.6 in this case). We find the relative error in this case to be 2.78%.

Table 6.4 summarizes the values of A_Z obtained with the different PDF sets and event generators, and the corresponding systematic errors. The components are added in quadrature to yield an overall systematic uncertainty of 3.78% on A_Z , which we conservatively round up to 4%.

Event detection efficiency C_Z

C_Z corrects the cross-section for the detector efficiency, resolution and QED radiation effects². It is estimated from the PYTHIA $Z \rightarrow \mu\mu$ Monte Carlo sample. The

²Final state QED radiation effects are taken into account thus: in computing the denominator of C_Z , we only use muons that come directly from a Z boson decay, and not from a muon which has

Event generator parameters	A_Z
PYTHIA MRST LO*	0.486
PYTHIA CTEQ6.6	0.496
PYTHIA HERAPDF1.0	0.492
MC@NLO CTEQ6.6	0.485
MC@NLO HERAPDF1.0	0.479
Relative uncertainties	
PDF eigenvector set	1.60%
Different PDF sets	2.01%
Model dependence	2.78%
Total uncertainty	3.78%

Table 6.4: Summary of geometrical acceptance values A_Z using different Monte Carlo generators and PDF sets. The estimated relative systematic errors from three different sources are also shown [85].

denominator of C_Z is the number of events passing the generator-level requirements that form the numerator of A_Z . The numerator of C_Z is the fraction of events passing the full $Z \rightarrow \mu\mu$ selection described in Sec. 6.1. The uncorrected value C_Z^{MC} is estimated to be $0.788 \pm 0.001(stat)$. It is then corrected to take into account data-driven corrections, namely, efficiency scale factors defined as $\epsilon_{data}/\epsilon_{MC}$.

The systematic uncertainty on C_Z derives from the uncertainties in the scale factors as well as those on the muon momentum scale and resolution and on the efficiency of the isolation requirement. The derivation of the various efficiencies, associated scale factors and their uncertainties is described below.

radiated a photon. This is ensured by requiring that the parent of each muon be a Z with PYTHIA status 3.

6.2.4 Estimation of efficiency scale factors

Trigger efficiency for single muons

Since we require the L1_MU6 trigger in our analysis, we must estimate the efficiency of this trigger, for single muons and for $Z \rightarrow \mu\mu$ events. We first note that, since the trigger technologies are different in the barrel and the endcap regions, we must measure the single muon trigger efficiency separately in each. The event selection for this purpose must be independent of any muon trigger so as not to bias the sample.

We perform the study on the same initial dataset as used in the cross-section analysis, using events that are in the $Z \rightarrow \mu\mu$ good runs list. We require the same primary vertex and high- p_T event selection as in the analysis, with the exception that the combined muon p_T is required to be greater than 20 GeV instead of 15 GeV. Events must pass the L1_J15 trigger, which requires a jet with $E_T > 15$ GeV, and is independent of any muon trigger. In applying the $|z_0 - z_{vtx}|$ cut on the muon, we use the primary vertex that has the largest Σp_T and satisfies the vertex selection criteria. Table 6.5 [62] summarizes the event selection criteria.

Event selection	
Primary vertex	$N_{vtx} \geq 1$ with $N_{tracks} \geq 3$ $ z_{vtx} < 150$ mm
Trigger	L1_J15
Muon selection	
Muon type	combined muons $p_T > 20$ GeV, $ \eta < 2.4$
Muon quality	$p_T^{MS} > 10$ GeV $ p_T^{MS} - p_T^{ID} < 15$ GeV $ z_0 - z_{vtx} < 10$ mm

Table 6.5: Event and muon selection criteria for single muon trigger efficiency measurement.

Following event and muon selection, each selected muon track is extrapolated to a nominal trigger chamber surface. In the barrel, this surface is defined as a cylinder centered on the beam axis, of length 32 m and radius 7.5 m, *i.e.*, roughly the position of the middle RPC station. In the endcap, the surface consists of two vertical disks of radius 20 m and $z = 15.53$ m from the interaction point. Now we search for RoIs (Regions of Interest, see Section 2.2.5) in the muon spectrometer in the vicinity of each extrapolated track. Each RoI has $\eta - \phi$ coordinates as well as a size defined as the half-diagonal length of the RoI in $\eta - \phi$ space. For the RoI nearest to an extrapolated track, we compute the distance ΔR defined as:

$$\Delta R = \sqrt{(\eta_{ex} - \eta_{RoI})^2 + (\phi_{ex} - \phi_{RoI})^2} \quad (6.4)$$

where η_{ex} and ϕ_{ex} are the coordinates of the extrapolated track, and η_{RoI} , ϕ_{RoI} those of the RoI. Next, for each track we define a search range as:

$$\text{search range} = \text{matching tolerance} \times \sqrt{\delta\eta^2 + \delta\phi^2} + \text{RoI size} \quad (6.5)$$

where $\delta\eta$ and $\delta\phi$ are the errors from the track extrapolation, and the matching tolerance is a number set to 3.0 [62]. For a given muon track, if we find an RoI with ΔR less than the search range, we consider that muon to have fired the trigger.

The RoI object contains an integer indicator for the p_T threshold of the muon that created the RoI, the p_T being estimated by the Level-1 trigger algorithm. The indicator corresponding to the L1_MU6 trigger is the integer 2. In case more than one RoI is matched to the same track, we accept one RoI using the priority ordering:

1. the RoI with the highest p_T indicator
2. the RoI closest to the extrapolated track

Once we have matched RoIs with muons in our event sample, we define the L1_MU6 trigger efficiency for single muons as:

$$\epsilon_{L1_MU6} = \frac{\text{Number of selected muons matched with RoIs with } p_T \text{ threshold } \geq 2}{\text{Number of selected muons}} \quad (6.6)$$

Figure 6.10 shows the measured single muon trigger efficiency as a function of muon p_T in both the barrel and the endcap. The data is compared with $W \rightarrow \mu\nu$ Monte Carlo. Since $W \rightarrow \mu\nu$ events have a single high- p_T muon, similar to those for $Z \rightarrow \mu\mu$ events, they provide a suitable comparison to data results for the purposes of our analysis. We see that the data efficiency is lower than that expected from Monte Carlo in both the barrel and the endcap, but that the discrepancy is quite marked in the endcap. This is a combined effect of the TGC chamber inefficiency and the fact that the trigger road was not well-calibrated at the time the measurement was performed.

Figure 6.11 shows the single muon trigger efficiency as a function of muon η , where again data results are compared with those from $W \rightarrow \mu\nu$ Monte Carlo. We see that the overall trigger efficiency in the barrel is significantly lower than that in the endcap. This difference is due to the insufficient coverage of the RPCs, as mentioned in Sec. 2.2.4. Figure 6.12 shows the trigger efficiency vs. ϕ in the barrel and in the endcap. The dip in the barrel efficiency owing to poor RPC coverage in the feet region ($\approx -2 < |\eta| < \approx -1$) is clearly visible.

The overall relative efficiency of the L1_MU6 trigger in data is $0.7602 \pm 0.0087(stat)$ in the barrel and $0.8628 \pm 0.0084(stat)$ in the endcap.

The systematic uncertainty in the single muon trigger efficiency comes mainly

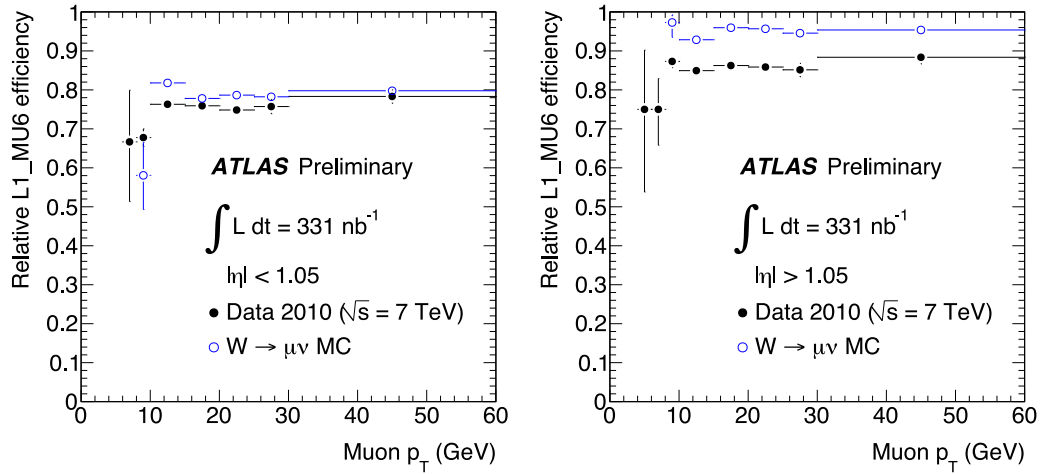


Figure 6.10: L1_MU6 trigger efficiency as a function of the p_T of selected muons in the barrel (*left*) and in the endcap (*right*). The data efficiencies are compared to those from $W \rightarrow \mu\nu$ Monte Carlo.

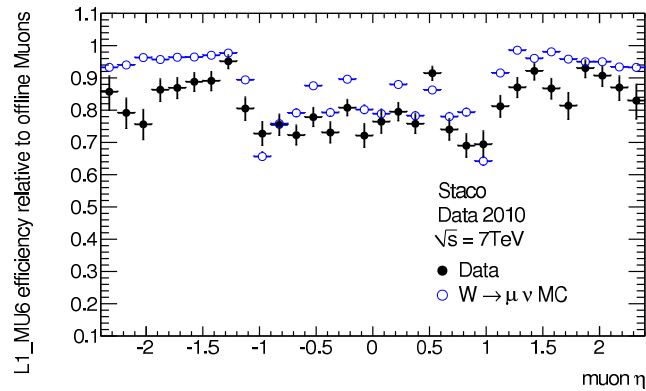


Figure 6.11: L1_MU6 trigger efficiency as a function of the η of selected muons. The data efficiency is compared to that from $W \rightarrow \mu\nu$ Monte Carlo.

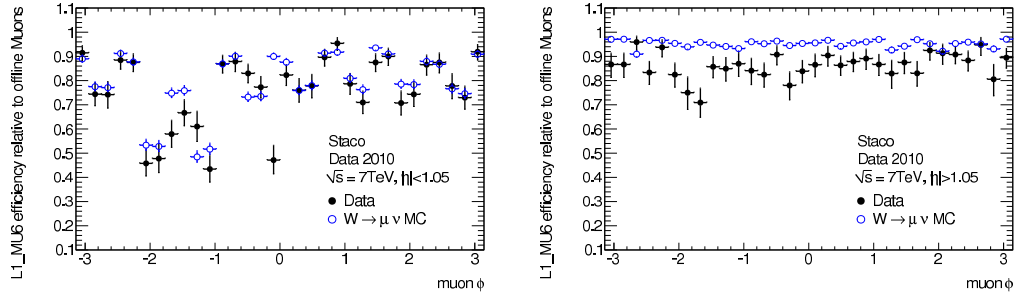


Figure 6.12: L1_MU6 trigger efficiency as a function of the azimuthal coordinate of selected muons in the barrel (left) and in the endcap (right). The data efficiencies are compared to those from $W \rightarrow \mu\nu$ Monte Carlo.

from the dependence on the muon reconstruction algorithm and the p_T cut on the combined muon. The Staco reconstruction chain requires at least one hit in trigger chambers in both η and ϕ , which can bias the efficiency measurement. The Muid chain does not have this requirement (Section 4.2.3), so that any possible bias can be estimated by re-measuring the trigger efficiency using Muid muons and taking the difference between the two measurements. We find this difference to be 1.38% in the barrel and 0.92% in the endcap, which we take as a systematic.

We estimate the effect on the measurement of the p_T cut on the combined muon. By varying the p_T cut by ± 5 GeV around the nominal value of 20 GeV, we found that the efficiency changed by 1.36% in the barrel and 0.46% in the endcap, which we assign as a systematic.

Other sources of systematic uncertainty include the value of the $|p_T^{ID} - p_T^{MS}|$ cut, the muon-RoI matching criteria, the size of the search range in RoI-finding and the dependence on the muon η distribution³. The various contributions to the systematic

³The muons used in this efficiency measurement are predominantly from heavy-flavor decays, which can have a different η distribution from W/Z decay muons. This can result in the trigger

are summarized in Table 6.6 [62]. The contributions are added in quadrature to yield absolute systematic uncertainties of 1.97% in the barrel and 1.77% in the endcap.

Source of systematic	Barrel	Endcap
Reconstruction algorithm dependence	1.38 %	0.92 %
p_T cut value	1.36 %	0.46 %
$ p_T^{ID} - p_T^{MS} $ cut value	0.20 %	0.30 %
Matching criteria dependence	0.01 %	1.18 %
Size of search range in RoI finding	0.16 %	0.77 %
η distribution re-weight	0.18 %	0.07 %
Total	1.97 %	1.77 %

Table 6.6: Various components of the systematic uncertainty on the L1_MU6 trigger efficiency in the barrel and the endcap. Numbers quoted are absolute errors.

Table 6.7 shows the results for the efficiency of the L1_MU6 trigger for single muons with respect to the muon reconstruction efficiency. Results for data, Monte Carlo, and the data/MC scale factors are shown for the barrel and the endcap.

barrel efficiency in data	$0.760 \pm 0.009(stat) \pm 0.020(syst)$
barrel efficiency in MC	$0.792 \pm 0.003(stat)$
barrel single muon SF	$0.959 \pm 0.012(stat) \pm 0.016(syst)$
endcap efficiency in data	$0.863 \pm 0.008(stat) \pm 0.018(syst)$
endcap efficiency in MC	$0.951 \pm 0.002(stat)$
endcap single muon SF	$0.907 \pm 0.009(stat) \pm 0.015(syst)$

Table 6.7: Final results, including the data/MC scale factors, for single muon efficiency of the L1_MU6 trigger.

Trigger efficiency and scale factor for $Z \rightarrow \mu\mu$ events

Now we estimate the trigger efficiency and associated data/MC scale factor for $Z \rightarrow \mu\mu$ events. Given that there are two muons in the final state, the event trigger

efficiency for these muons being different in particular regions of the detector compared to W/Z decay muons, and thus the overall efficiency can be different between the two cases.

efficiency and its uncertainty are given by:

$$\epsilon_{event} = 1 - (1 - \epsilon_1)(1 - \epsilon_2) \quad (6.7)$$

$$\delta\epsilon_{event} = (1 - \epsilon_1)\delta\epsilon_2 + (1 - \epsilon_2)\delta\epsilon_1 \quad (6.8)$$

where two efficiency parameters are used since:

- we have two muons, both of which can be in the barrel region (BB), or both in the endcap region (EE), or one in the barrel and the other in the endcap (BE)
- the single muon trigger efficiencies are significantly different in the barrel and in the endcap, for both data and Monte Carlo, as we saw in Section 6.2.4. Consequently, ϵ_1 and ϵ_2 will be the same for BB and EE events, but different for BE events.

We compute the overall trigger efficiency as a weighted average to take into account the three different possibilities. We adopt the following strategy:

1. Using Monte Carlo simulation, we estimate the fraction of Z events of each type BB, EE and BE. The events are required to pass all Z selection criteria except the trigger. The numbers and fractions of the three types of events are summarized in Table 6.8.
2. We apply Eq. 6.8 to each event type. Using the single muon trigger efficiencies from Table 6.7, we estimate the event trigger efficiency for each type in data and in Monte Carlo, summarized in Table 6.9.
3. Using the fractions from Step 1, we now average the efficiency values separately for data and for Monte Carlo. The overall efficiency is found to be 0.962 in data and 0.982 in Monte Carlo.

4. Finally, we take the ratio of these two values to obtain a trigger efficiency scale factor of 0.981.

Event type	Number in MC sample	Fraction
BB	32856	0.286
EE	26340	0.230
BE	55537	0.484

Table 6.8: Numbers and fractions of Z events in Monte Carlo in which the two muons go into each of the three possible combinations of barrel and endcap regions. The events are required to pass all Z selection criteria except the trigger.

Event type	Efficiency in data	Efficiency in MC
BB	$0.942 \pm 0.004\%$ (<i>stat</i>)	$0.956 \pm 0.001\%$ (<i>stat</i>)
EE	$0.981 \pm 0.002\%$ (<i>stat</i>)	$0.9976 \pm 0.0002\%$ (<i>stat</i>)
BE	$0.967 \pm 0.003\%$ (<i>stat</i>)	$0.9897 \pm 0.0006\%$ (<i>stat</i>)
Overall	$0.963 \pm 0.003\%$ (<i>stat</i>)	$0.9818 \pm 0.0007\%$ (<i>stat</i>)

Table 6.9: Event trigger efficiencies in data and Monte Carlo for $Z \rightarrow \mu\mu$ events in which the two muons go into each of the three possible combinations of barrel and endcap. The overall weighted efficiencies are also shown.

We obtain the statistical error on the scale factor by propagating the errors in Table 6.7 through the calculation process. The absolute statistical error is 0.003. The systematic error on the scale factor is computed by using the values from Table 6.6 and applying Eq. 6.8. The absolute systematic error is 0.006. Note that this is smaller than the systematic error on the single muon trigger scale factors (1.57% and 1.45% respectively in the barrel and the endcap). Ultimately, the smaller uncertainty derives from the fact that at least one of the two muons must trigger the event.

The trigger efficiency scale factor with errors is reported in Table 6.10.

Trigger eff. scale factor	Statistical error	Systematic error
0.981	0.003	0.006

Table 6.10: Trigger efficiency scale factor for $Z \rightarrow \mu\mu$ events with errors.

Reconstruction efficiency and scale factor for $Z \rightarrow \mu\mu$ events

Detailed descriptions of the techniques used to measure the (relative) muon reconstruction efficiency in data can be found in Section 4.2.4. Briefly, we measure the single muon reconstruction efficiency using two methods:

- the ‘direct’ or ‘MS hit’ method, associating inner detector tracks with muon spectrometer hits, using a template background subtraction technique to properly remove the π/K contamination in the sample of selected tracks
- the ‘tag-probe’ method, using one leg of the Z decay to tag the event as a Z event, and the other to estimate the efficiency

Given that $Z \rightarrow \mu\mu$ events have two combined muons, the event reconstruction efficiency and its uncertainty are given by:

$$\epsilon_{event} = \epsilon^2 \quad (6.9)$$

$$\delta\epsilon_{event} = 2\epsilon\delta\epsilon \quad (6.10)$$

This translates to a scale factor which is the square of the scale factor corresponding to single muon reconstruction efficiency. Taking into account all the systematics described in Section 4.2.4, we obtain a scale factor consistent with unity from both methods (Tables 4.5 and 4.7):

Reconstruction eff. scale factor	Statistical error	Systematic error
1.000	0.012	0.048

Table 6.11: Reconstruction efficiency scale factor for $Z \rightarrow \mu\mu$ events with errors.

6.2.5 Muon momentum scale and resolution

In general, muon momentum scale and resolution are not expected to be well-reproduced by Monte Carlo simulation, so that these quantities must be determined from data. A frequently-used technique for scale and resolution determination is to use a distribution that depends on these quantities. The momentum scale and resolution are varied in Monte Carlo until the predicted distribution agrees with that observed in data; the scale and resolution that achieve this agreement are the values of these quantities in data.

The Z boson mass peak is an ideal distribution for this purpose: the position of the mean of the distribution depends on the muon momentum scale, while the width is partially determined by muon momentum resolution. We use the Z event sample obtained using our selection criteria. For this study, we fit the dimuon invariant mass distribution in the signal region with a convolution of a Breit-Wigner and a Gaussian function, the width of the Breit-Wigner component being fixed to the Z boson decay width. The mean of the distribution is given by the fitted mean of the Breit-Wigner component, while the resolution due to detector effects is indicated by the width of the Gaussian component.

For the p_T range in which most of our Z decay muons lie, *i.e.*, $20 \text{ GeV} < p_T < \approx 50 \text{ GeV}$, the momentum resolution is mainly due to the intrinsic resolution of the detector

technologies and misalignment effects⁴. We note that the quantity that is actually measured in the muon spectrometer is the curvature $1/p_T$, and so we determine the scale and resolution of this quantity. We use the following expression [62] to modify (‘smear’) the curvature of single muons:

$$(1/p_T)_s = (1/p_T)_{MC} \times 1/C_1 \times (1 + x \times C_2) \quad (6.11)$$

where $(1/p_T)_s$ is the smeared muon curvature, $(1/p_T)_{MC}$ is the muon curvature in the default Monte Carlo sample, and the parameters:

- C_1 is the scale term
- C_2 is the curvature smearing term
- x is a random number with a Gaussian distribution, mean = 0 and width = 1

We vary the parameter C_1 from 0.97 to 1.02 in steps of 0.01, while keeping C_2 fixed. Then we vary C_2 from 0.01 to 0.08 in steps of 0.01, keeping C_1 fixed. For each permutation, we reconstruct the Z mass peak, fit it to a Breit-Wigner convolved with a Gaussian, and extract the mean and width as described above. We perform the sequence three times: for all muons and separately for muons in the barrel and in the endcap. Figure 6.13 (*left*) shows the mean of the fitted Z mass distribution as a function of the scale parameter. The intersection of the solid red line and the black line gives the curvature (momentum) scale in data. Figure 6.13 (*right*) shows the fitted width of the Z mass distribution as a function of the resolution smearing parameter. Again, the intersection of the solid red and black lines gives the extra

⁴The component of the resolution owing to multiple scattering is significant for $p_T < \approx 10$ GeV. See Figure 6.18.

smearing needed in Monte Carlo to reproduce the data. Figure 6.14 shows the fitted width vs. the smearing parameter separately for Z events with both muons in the barrel (*left*) and both in the endcap (*right*).

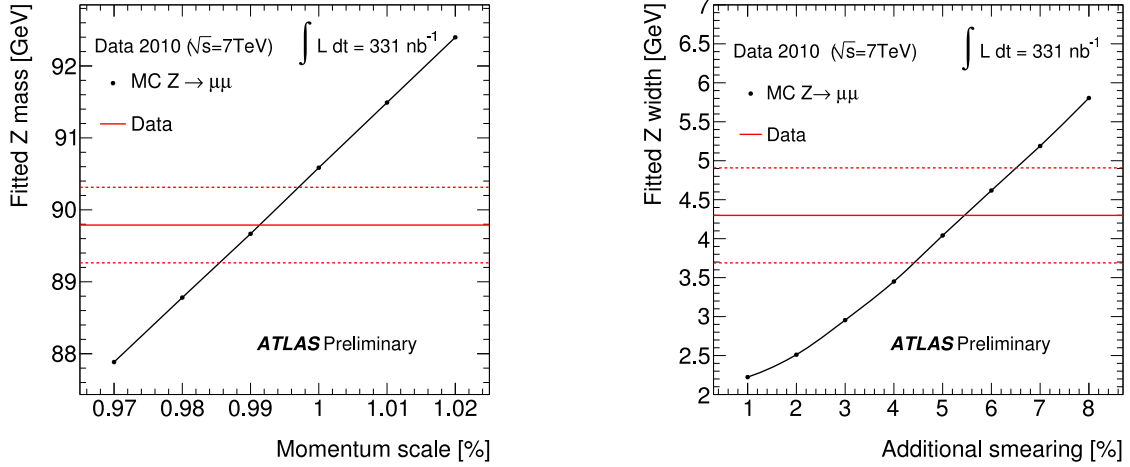


Figure 6.13: Muon momentum scale (*left*) and additional smearing (*right*) needed in the Monte Carlo simulation to reproduce data, using all $Z \rightarrow \mu\mu$ events in the sample. Red lines denote the fitted peak position (width) and its statistical uncertainty in data. Black points denote the fitted peak position (width) from Monte Carlo.

Table 6.12 shows the values of the parameters C_1 and C_2 separately for the case of all Z events and for Z events with both muons in the barrel and both in the endcap. We see that the muon momentum scale and resolution in data are consistent between the barrel and the endcap within statistical errors. Instead of correcting our measurement with these values, we take them as uncertainties on the muon momentum scale and resolution and determine their effect on the $Z \rightarrow \mu\mu$ event acceptance.

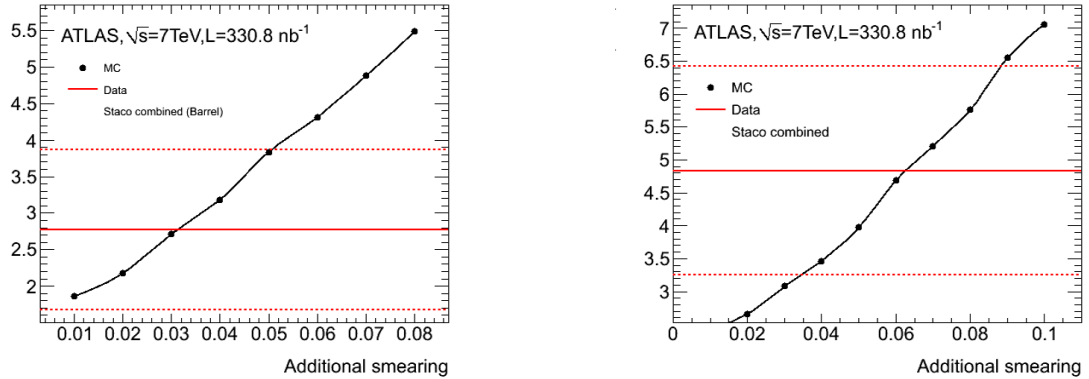


Figure 6.14: Additional smearing needed in simulation using $Z \rightarrow \mu\mu$ events with both muons in the barrel (*left*) and both in the endcap (*right*). Red lines denote the fitted width and its statistical uncertainty in data. Black points denote the fitted width from Monte Carlo.

	C_1	C_2
All events	0.991 ± 0.005	0.055 ± 0.012
BB events	0.992 ± 0.010	0.031 ± 0.020
EE events	0.980 ± 0.012	0.063 ± 0.031

Table 6.12: Scale and extra resolution parameters measured in data by fitting the Z mass distribution and comparing with Monte Carlo events smeared according to Eq. 6.11. Errors are statistical only.

Muon momentum scale and resolution from cosmic events

During 2008-2009, ATLAS collected a substantial amount of cosmic muon events. A fraction of these muons traverse both the muon spectrometer (MS) and the inner detector (ID). We can derive an estimate of the muon momentum scale and resolution of the muon spectrometer by comparing the momentum measured in the MS with that measured in the ID. A detailed study to this effect can be found in [8]. We summarize below the measurement of muon momentum scale and resolution as a function of muon p_T using matched ID and MS tracks in cosmic events.

First, we produce distributions of a quantity P_{diff} defined as:

$$P_{diff} = \frac{p_T^{MS} - p_T^{ID}}{p_T^{ID}}, \quad (6.12)$$

in bins of p_T^{ID} . Fits of the P_{diff} distributions will provide us with an estimate of the momentum resolution and scale.

The selection criteria used for MS and ID tracks are as follows:

- MS tracks: The motivations for these cuts can be found in [8], together with definitions of and motivations for ‘mirror’ and ‘shadow’ tracks:
 - track fit $\chi^2/DoF < 10$
 - the track traverses all 3 muon stations
 - the track is in the top half of the detector
 - all MDT hits on the track are in the same sector
 - this sector is one of sectors 2-8
 - the track has at least 4, 3, 3 hits in the MDT BI, BM, BO layers respectively
 - it has hits in at least 2 RPC ϕ layers
 - track $p \geq 2$ GeV/ c
 - there are no more than 10 segments in the sector containing the track
 - the mirror track has all hits in the same sector after efficiency corrections
 - it has at least 4, 3, 3 hits in the MDT BI, BM, BO layers respectively
 - it has hits in at least 2 RPC ϕ layers
 - the mirror and shadow tracks both confirm offline the RPC trigger algorithm used in the run

- ID tracks:
 - the TRT event phase is non-zero, and lies in the interval $[-25, 25]$ ns
 - track fit $\chi^2/DoF < 5$
 - the track has at least 20 hits in the TRT
 - $2 \times \text{SCT hits} \geq 8$ (note that the Pixels were off in the run used for the measurement)
 - the transverse impact parameter $d_0 < 299$ mm
 - the longitudinal impact parameter $z_0 < 540$ mm
 - track $p \geq 2$ GeV/ c

For this study, we use events from the `IDCosmic`⁵ stream of the run. Only those events with exactly one ID track are used. The matching of an ID track with an MS track requires:

- the difference in the polar angle θ between the two tracks, $\delta\theta < 50$ mrad
- the difference in the azimuthal angle ϕ between the two tracks, $\delta\phi < 50$ mrad

Figures 6.15 and 6.16 show the fitted distributions of P_{diff} respectively for positive and negative muons, in bins of p_T^{ID} . The fit function is a Gaussian convoluted with a Landau distribution. A second Gaussian is added to describe the tails due to mismatched ID-MS pairs; its normalization is forced to be no more than 30% of the total number of entries.

⁵The `IDCosmic` stream contains events with a high probability of having at least one track traversing the ID, as estimated from the pattern of hits in the ID subdetectors at Level-2.

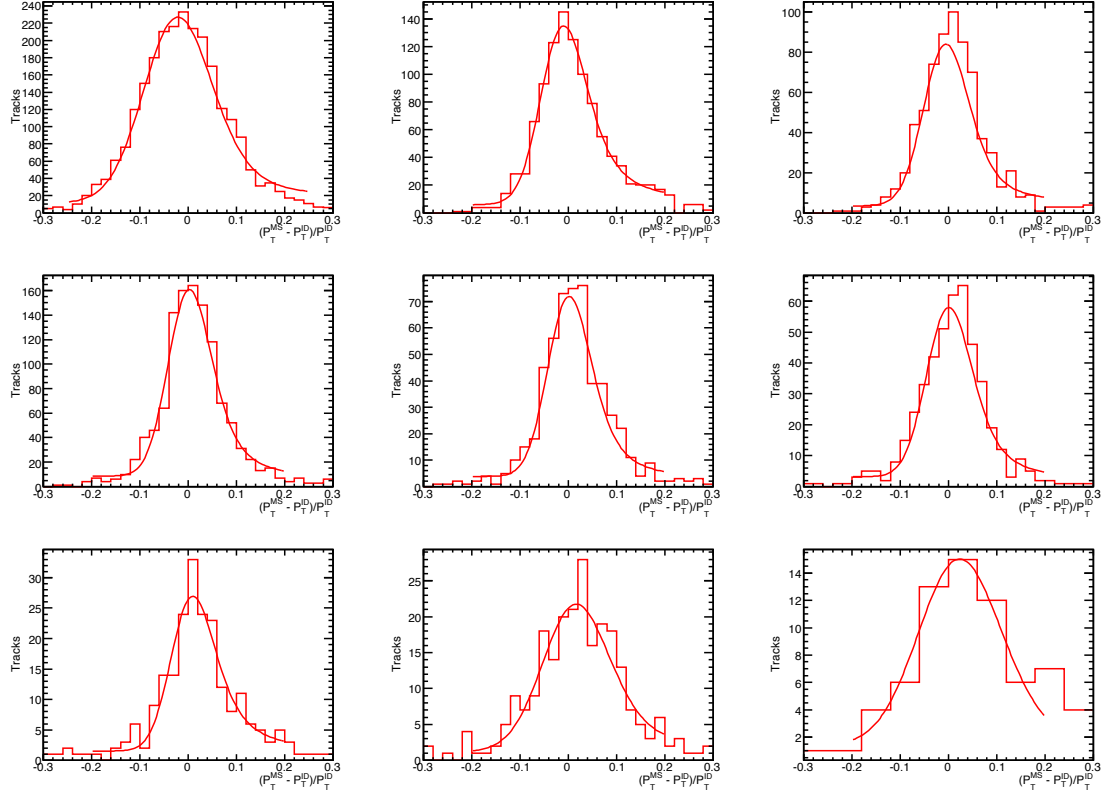


Figure 6.15: Distribution of $(p_T^{MS} - p_T^{ID})/p_T^{ID}$ in bins of p_T^{MS} , for positive muons. From top left to bottom right, the p_T bins are defined as follows: $[0, 10]$ GeV/ c , $(10, 15]$ GeV/ c , $(15, 20]$ GeV/ c , $(20, 35]$ GeV/ c , $(35, 50]$ GeV/ c , $(50, 75]$ GeV/ c , $(75, 100]$ GeV/ c , $(100, 200]$ GeV/ c , $(200, 300]$ GeV/ c . Each histogram is fitted with a Landau function convoluted with a Gaussian, plus a second Gaussian, with normalization limited to no more than 30% of the total number of histogram entries.

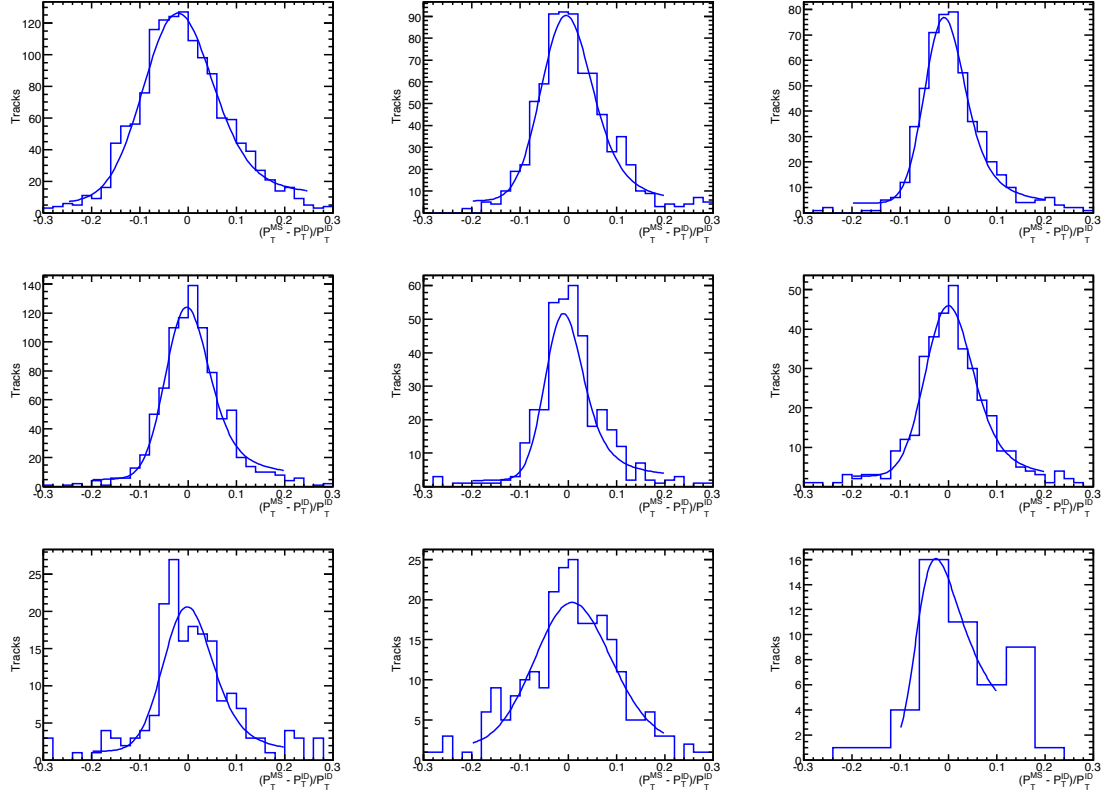


Figure 6.16: Distribution of $(p_T^{MS} - p_T^{ID}) / p_T^{ID}$ in bins of p_T^{MS} , for negative muons. From top left to bottom right, the p_T bins are defined as follows: $[0, 10]$ GeV/ c , $(10, 15]$ GeV/ c , $(15, 20]$ GeV/ c , $(20, 35]$ GeV/ c , $(35, 50]$ GeV/ c , $(50, 75]$ GeV/ c , $(75, 100]$ GeV/ c , $(100, 200]$ GeV/ c , $(200, 300]$ GeV/ c . Each histogram is fitted with a Landau function convoluted with a Gaussian, plus a second Gaussian, with normalization limited to no more than 30% of the total number of histogram entries.

Parameter		μ^+	μ^-
Energy loss	[GeV/c]	0.28 ± 0.09	0.43 ± 0.16
Multiple scattering	[%]	3.60 ± 0.21	2.95 ± 0.66
Intrinsic resolution	$[10^{-4}/(\text{GeV}/c)]$	3.07 ± 0.61	4.19 ± 0.87

Table 6.13: Result of the p_T resolution fits using MS-ID matched tracks, shown separately for positive and negative muons.

The p_T scale in each p_T^{ID} bin is taken to be the fitted mean of the first Gaussian. This choice corresponds to selecting the most probable value of the Landau distribution. The scale thus derived is shown in Figure 6.17 separately for positive and negative muons as a function of the muon p_T . As can be seen, in the p_T range of interest for $Z \rightarrow \mu\mu$ events (20-50 GeV), the scale is ≈ 1 -2% for muons of both signs, which approximately agrees with the measurement using fits to the Z peak.

The p_T resolution is taken to be the fitted width of the first Gaussian. The resolution thus derived is shown in Figures 6.18 separately for positive and negative muons. The resolution vs. p_T graphs are fitted with the following function:

$$\mathcal{F}(p) = a/p \oplus b \oplus c \cdot p, \quad (6.13)$$

where the coefficients a , b , and c respectively describe the contribution to the overall p_T resolution from energy loss, multiple scattering, and intrinsic detector resolution. The three components are added in quadrature. The results of the resolution fits are summarized in Table 6.13.

We see that the resolution thus derived is $\approx 4\%$ for both positive and negative muons in the p_T range of interest for $Z \rightarrow \mu\mu$ events, which again agrees within error with the values obtained from fits to the Z peak.

A comparison of the curvature (reciprocal of the momentum) between matched MS and ID tracks can be found in Appendix B, together with a brief discussion of

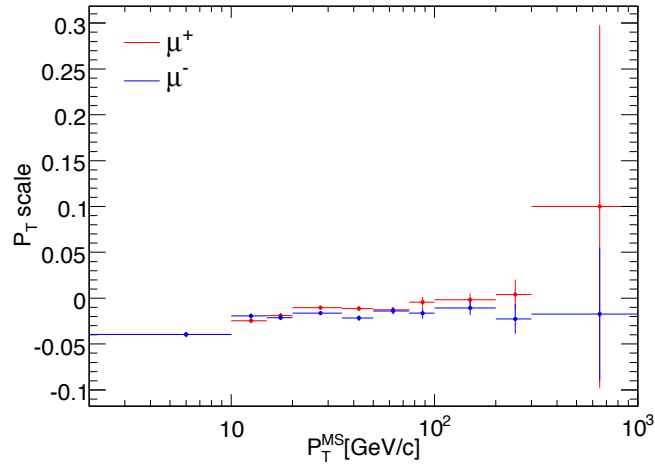


Figure 6.17: p_T scale, as a function of the muon p_T measured in the MS, for positive muons (red) and negative muons (blue).

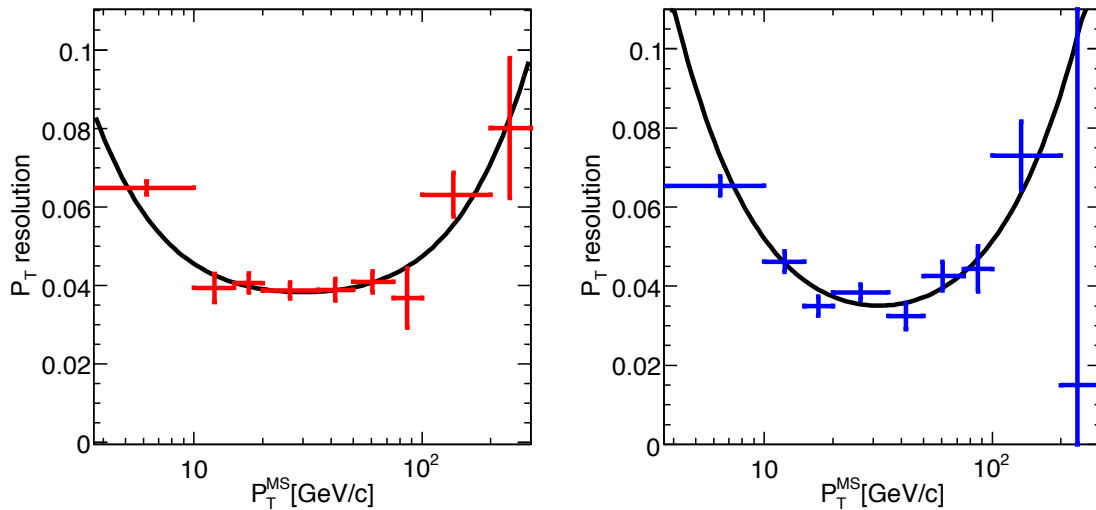


Figure 6.18: Fits to the p_T resolution distributions, as a function of the muon p_T measured in the MS. *Left*: positive muons (fit probability: 89.7%); *right*: negative muons (fit probability: 41.6%).

the effect of misalignment on track curvature.

Effect of momentum scale and resolution on $Z \rightarrow \mu\mu$ acceptance

From the values given in Table 6.12, we take the uncertainty in the muon momentum scale as 1%. To estimate its effect on the Z event acceptance, we change the curvature of muons in our $Z \rightarrow \mu\mu$ Monte Carlo sample up and down by this amount. The change in acceptance from the central value is seen to be +0.34% and -0.45% respectively in the two cases. We conservatively take the larger of the two values as the systematic uncertainty on C_Z from this source.

Since the smearing needed in the barrel and in the endcap differ by a factor of ≈ 2 , we estimate its effect on the acceptance separately in the two regions. To be conservative, we take as the central value the smearing correction plus the 1σ error, *i.e.*, 5% in the barrel and 9% in the endcap (Table 6.12). We smear the muon curvature by these amounts and recalculate the Z acceptance. The change in acceptance from the central value is found to be 0.48%, which we take to be the systematic error from p_T resolution.

By adding the two contributions in quadrature, we find the combined systematic uncertainty from muon momentum scale and resolution to be 0.66%.

The p_T spectrum of Z decay muons in Monte Carlo is shown in Figure 6.19 with and without the additional smearing.

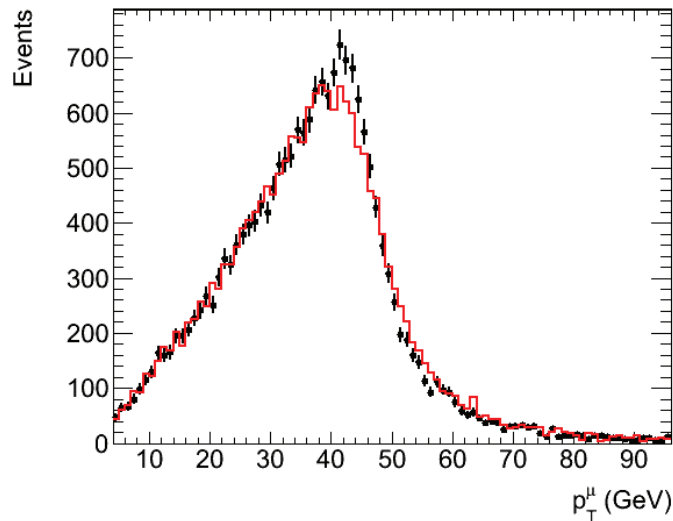


Figure 6.19: p_T distribution of Z decay muons in Monte Carlo without smearing (points) and with additional smearing (line).

6.2.6 Isolation cut efficiency for $Z \rightarrow \mu\mu$ events

We study the efficiency of the isolation cut on Z decay muons using a tag-probe approach similar to that used to determine muon reconstruction efficiency. The event selection criteria are the same as for the reconstruction efficiency study (Table 4.6). The tag is selected to be a high- p_T isolated combined muon, while the probe is required to be a high- p_T combined muon without any isolation requirement. The invariant mass of the tag and the probe must be in a 10 GeV window around the Z mass. The selection criteria for events, tags and probes are summarized in Table 6.14.

In determining the isolation cut efficiency, we must take into account the fact that either of the two muons from a Z decay can pass the isolation cut. We want to define the efficiency such that for an event in which the probe passes the isolation cut, both the tag and the probe contribute to both the numerator and the denominator of the

Event Selection	
Good runs list	same as for the Z analysis
Trigger	L1_MU6
Tags	≥ 1
Probes	≥ 1
Tag Selection	
Combined muons	
Kinematics	$p_T \geq 20 \text{ GeV} \ \& \ \eta \leq 2.4$
Muon quality	$p_T^{\text{MS}} > 10 \text{ GeV}$
	$ p_T^{\text{MS}} - p_T^{\text{ID}} < 15 \text{ GeV}$
Muon isolation	$\sum p_T^{\text{ID}} / p_T < 0.2$
Probe Selection	
Combined muon	
Kinematics	$p_T \geq 20 \text{ GeV} \ \& \ \eta \leq 2.4$
Muon quality	$p_T^{\text{MS}} > 10 \text{ GeV}$
	$ p_T^{\text{MS}} - p_T^{\text{ID}} < 15 \text{ GeV}$
Invariant mass	$ M_Z - M_{\text{TP}} < 10 \text{ GeV}$

Table 6.14: Event, tag and probe selection criteria used for the isolation efficiency measurement.

efficiency expression. By contrast, in an event in which the probe fails the isolation cut, only the tag contributes to the denominator. If N_{TP} is the number of events in the former category and N_T is that in the latter category, the isolation cut efficiency for single isolated muons is defined as:

$$\epsilon_{iso} = \frac{2N_{TP}}{2N_{TP} + N_T} \quad (6.14)$$

The results for ϵ_{iso} in data and $Z \rightarrow \mu\mu$ Monte Carlo are reported in Table 6.15. We see that the efficiency is $\approx 1\%$ lower in data than in Monte Carlo. We keep in mind, however, that a background contamination of $\approx 1\%$ is expected in the sample (Section 4.2.4) which would lower the efficiency. We consequently take the Monte Carlo efficiency as the true value of ϵ_{iso} . Instead of correcting our acceptance, we assign the 1% uncertainty as a systematic on the isolation cut efficiency for single

isolated muons.

ϵ_{iso} in data	ϵ_{iso} in MC
$0.984 \pm 0.010(\text{stat})$	0.993

Table 6.15: Isolation cut efficiency measured in data and in $Z \rightarrow \mu\mu$ Monte Carlo events.

Assuming the isolation efficiency to be fully correlated between the two Z decay muons, the systematic on C_Z from this source is 2%.

6.2.7 Theoretical uncertainty on C_Z

Uncertainties on C_Z arising from differences between PDF sets was investigated in [85]. The event yield from the nominal Monte Carlo sample generated with PYTHIA using the MRST LO* PDF set was compared with event yields using the CTEQ6.6 and HERAPDF1.0 sets. The difference after all selection cuts was found to be 0.3%, which we take as the theoretical error on C_Z .

6.2.8 Summary of systematic uncertainties

Apart from the 11% uncertainty in luminosity determination, all systematic uncertainties from experimental sources pertain to the event detection efficiency factor C_Z . The largest systematic is the 5.0% uncertainty in the reconstruction efficiency scale factor. The other contributions are from the isolation cut efficiency (2%), trigger efficiency scale factor (0.7%) and muon momentum scale and resolution (0.7%). The various contributions are assumed to be uncorrelated and added in quadrature. Table 6.16 summarizes the different components of the systematic uncertainty and their values.

Parameter	Parameter uncertainty (%)	Acceptance uncertainty (%)
Trigger efficiency	2.0 (barrel), 1.9 (endcap)	0.7
Reconstruction efficiency	2.5	5.0
Muon momentum scale	1.0	0.45
Muon momentum resolution	5.0 (barrel), 9.0 (endcap)	0.48
Isolation cut efficiency	1.0	2.0
Total experimental uncertainty		5.5

Parameter	δA_Z (%)
Theoretical uncertainty	3.0
Total uncertainty	6.2

Table 6.16: Systematic uncertainty on $Z \rightarrow \mu\mu$ acceptance from various sources. The precision in the measurement of each component is reported as the ‘parameter’ uncertainty.

6.2.9 Summary of acceptance and efficiency

We summarize the $Z \rightarrow \mu\mu$ signal acceptance in Table 6.17. The total acceptance and the factorized values A_Z and C_Z are reported. The value of C_Z has been corrected by the scale factors for trigger and reconstruction efficiencies to take into account differences between data and Monte Carlo. The scale factors are also summarized in the table.

Z	
A_Z	0.486 ± 0.019
C_Z	0.773 ± 0.043
Overall acceptance	0.376 ± 0.026
Trigger efficiency SF	0.981 ± 0.003 (stat) ± 0.006 (syst)
Reconstruction efficiency SF	1.000 ± 0.012 (stat) ± 0.048 (syst)

Table 6.17: Total and factorized acceptances for Z events. Trigger and reconstruction efficiency scale factors used to correct the Monte Carlo-derived acceptance to take into account differences between data and simulation are also shown.

6.2.10 Decomposition of C_Z

The correction factor C_Z for the cross-section measurement includes all detector effects as well as the effect of final-state photon radiation. C_Z can be interpreted [85] as a product of four factors:

$$C_Z = \epsilon_{event} \cdot \alpha_{reco} \cdot (\epsilon_{id})^2 \cdot [1 - (1 - \epsilon_{trig})^2] \quad (6.15)$$

The different factors and their extraction are summarized below.

1. ϵ_{event} is the efficiency of the event preselection cuts, in our case, the primary vertex requirement. From Table 6.3, its value is 99.8% with negligible error.
2. α_{reco} itself has several factors. It accounts for:
 - All kinematic and geometric cuts applied to reconstructed quantities instead of generator-level quantities. By applying the muon p_T , η and invariant mass cuts at the generator level, and comparing the event yield with that from the reconstruction level, we determine this component to be 106.4% with negligible error.
 - The effect of final-state photon radiation (FSR). In Section 6.2.3, we determined the denominator of C_Z using muons that come directly from Z boson decays. Instead, using muons after FSR, we find the change in C_Z to be 3.2% with an error of less than 0.1%. This component of α_{reco} is therefore 96.8%.
 - The inner detector track reconstruction efficiency. This quantity is 98.9% per muon, or 97.8% per Z event.

- Muon momentum scale and resolution. Since we do not correct C_Z for momentum scale and resolution, they contribute only to the error in α_{reco} .

Combining these factors, we have $\alpha_{reco} = 100.7 \pm 0.7\%$.

3. ϵ_{id} is the muon identification efficiency with respect to the muon reconstruction efficiency, and can also be factorized into several components:

- Combined muon reconstruction efficiency in Monte Carlo. This quantity is taken to be 92.4% from Table 4.7. and the 2.5% overall error for the corresponding efficiency in data is assigned to it.
- Muon quality criteria. The efficiency of the quality cuts in Monte Carlo is found to be 97.4% with an error of less than 0.1%.
- Isolation cut efficiency. This quantity is 99.3% from Section 6.2.6. The 1% error from the corresponding efficiency in data is assigned to it.

4. Finally, ϵ_{trig} is the single muon trigger efficiency in $Z \rightarrow \mu\mu$ events. It is calculated in Monte Carlo by weighting each Z decay muon with the single muon trigger efficiency for the barrel or the endcap depending on which region the muon traversed. Its value is found to be $80.8 \pm 1.9\%$, the error being derived from the systematic errors on single muon trigger efficiencies.

The decomposition of C_Z into the various factors is shown in Table 6.18 together with the values and errors for all components. This factorization will prove particularly useful, for example, when the quantities currently extracted from Monte Carlo are replaced by measurements from data.

Contribution	Central value	Relative uncertainty
Overall C_Z	77.3%	5.5%
ϵ_{event}	99.8%	< 0.2%
α_{reco} :	100.7%	0.7%
- kinematic cuts	106.4%	
- lepton momentum scale		0.5%
- lepton momentum resolution		0.5%
- FSR	96.8%	<0.1%
- ID reconstruction efficiency	97.8% (98.9% per μ)	
ϵ_{lep} :	89.4%	2.7%
- combined muon	92.4%	2.5%
- muon quality	97.4%	<0.1%
- isolation	99.3%	1.0%
ϵ_{trig} (MC)	86.5% (98.2% per Z)	
ϵ_{trig} (data)	80.8% (96.3% per Z)	1.9%
Theoretical uncertainty		0.3%

Table 6.18: Decomposition of C_Z and related systematic uncertainties. Note that the trigger efficiency term is shown per muon but also per event in parentheses. The muon identification efficiencies and their uncertainties are per muon.

Chapter 7

Background Estimation

The $Z \rightarrow \mu\mu$ decay results in two high- p_T muons, so that other physics processes with high- p_T muons in the final state are potential backgrounds. A major background is $t\bar{t}$ production. The top decays overwhelmingly to a W and a b quark¹; $t\bar{t}$ decays with two-muon final states can fake the signal. The $Z \rightarrow \tau\tau$ decay, with each τ decaying into a muon, is another potential background channel. The high- p_T muon from a $W \rightarrow \mu\nu$ decay can pair with a muon from a QCD jet to fake a $Z \rightarrow \mu\mu$ event. Finally, the very large cross-section of QCD dijets implies a substantial background due to high- p_T muons in jets.

If a process is theoretically well-understood, we can use Monte Carlo to estimate the amount of background expected from that process. Otherwise, we must devise methods to estimate the backgrounds from data with minimal reliance on Monte Carlo. In this chapter, we first discuss data-driven methods to estimate the QCD background. We then describe the extraction of backgrounds from W , Z , $t\bar{t}$ and cosmic sources.

¹The branching fraction into this channel is $\approx 99\%$ [40].

7.1 QCD background

Multijet production can lead to backgrounds to Z production in the dimuon channel via two principal processes: heavy-flavor production (b or c quarks) and decay-in-flight of pions and kaons. Heavy-flavor production of $b\bar{b}$ and $c\bar{c}$ leads to b/c hadrons. Muons can be produced in the subsequent decays of these hadrons. Since these muons are associated with jets and do not originate from the primary proton-proton hard scattering, these backgrounds can be reduced significantly by selecting muons associated with the primary vertex, isolated from hadronic activity, and with large transverse momenta. Nonetheless, because of the large multijet production cross-section, events in the tails of the distributions contribute to the background after our Z selection criteria and need to be estimated properly.

In view of the large cross-sections, these backgrounds should ideally be estimated from data, but the small number of high- p_T dimuon events from multijet sources in our dataset makes it difficult to do so. We nevertheless make an attempt to estimate the QCD background from data using two different methods, as detailed below.

7.1.1 Data-driven QCD background estimation

Exponential fit to the $M_{\mu\mu}$ distribution

The basic strategy underlying data-driven QCD background estimates is to use a sample of events with enriched QCD content to estimate the QCD contamination in the Z sample after isolation cuts. One implementation of this concept is to use a fit to the dimuon invariant mass spectrum shown at the bottom of Figure 6.8. This distribution contains events which have passed our high- p_T event selection criteria as

well as the requirement of at least two combined muons in the event, both of which pass the $|z_0 - z_{vtx}|$ cut. The event sample at this stage is dominated by QCD events.

We fit the mass spectrum from data in the range 30-120 GeV using:

- a convolution of a Breit-Wigner and a Gaussian function in the signal region $66 \text{ GeV} < M_{\mu\mu} < 116 \text{ GeV}$
- an exponential function for the background above and below the signal region

Figure 7.1 shows the fit superposed on the spectrum. From the exponential component, we estimate 38.5 ± 6.2 background events in the signal region. To obtain the number N_{BG} of background events in the signal region after the remaining Z selection cuts, we multiply this number by the acceptance of the cuts estimated from QCD Monte Carlo, which is $1.9 \pm 0.2 \times 10^{-4}$. Then we have:

$$N_{BG} = 0.0074 \pm 0.0014$$

We note that this method is not fully data-driven, since we do rely on QCD Monte Carlo to estimate the acceptance of the Z selection criteria for QCD events.

Template fitting with 3.37 pb^{-1}

A second method of data-driven QCD background estimation is a template fit. Since muons in QCD events are generally non-isolated, we can get a QCD-rich sample by requiring that the events contain non-isolated muons. We use the dimuon invariant mass distribution in this sample as a template for QCD events. We have a corresponding template for signal events from $Z \rightarrow \mu\mu$ Monte Carlo. Assuming that

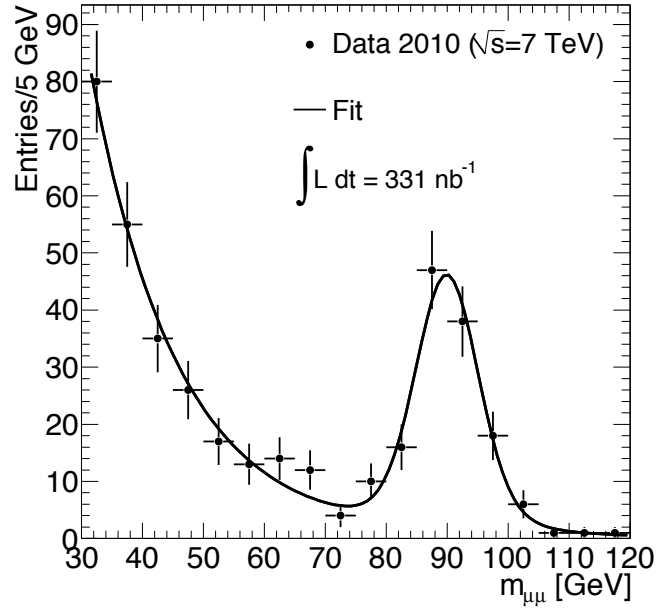


Figure 7.1: Dimuon invariant mass distribution in data after the high- p_T event selection criteria and the requirement of at least two combined muons in the event, both passing the $|z_0 - z_{vtx}|$ cut.

the dimuon invariant mass distribution has the same shape for both isolated and non-isolated muons from QCD sources, we can determine the fractions in which the two templates must be combined to reproduce the data. Multiplying the QCD fraction by the number of events in the QCD template then yields the QCD contamination in data.

Figure 7.2 shows the dimuon invariant mass spectra for isolated and non-isolated muons from $b\bar{b}$ and $c\bar{c}$ Monte Carlo. Note that, in order to obtain sufficient statistics for the invariant mass distribution of isolated muons, we loosened the p_T cut on the muons to 15 GeV. We still have limited statistics for isolated muons, but the general shapes of the two distributions are close enough that the above assumption is justified.

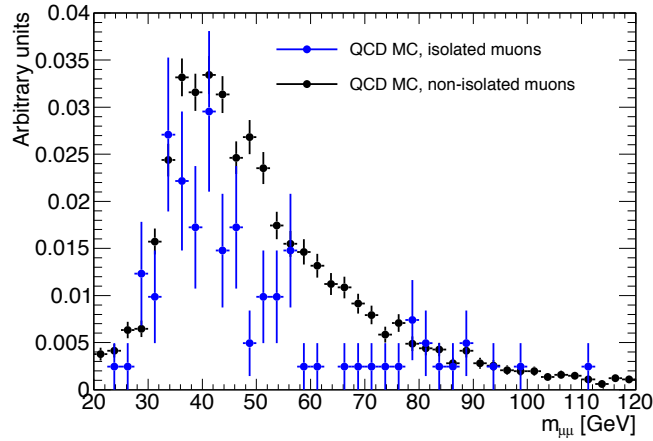


Figure 7.2: Dimuon invariant mass distributions for isolated and non-isolated muons in $b\bar{b}$ and $c\bar{c}$ events from Monte Carlo in the range $20 \text{ GeV} < m_{\mu\mu} < 120 \text{ GeV}$. The Monte Carlo samples have a 4 GeV generator-level filter on the p_T of *each* muon. Note that the cut applied on the reconstructed p_T of each muon is 15 GeV, instead of 20 GeV as in the cross-section analysis, so that sufficient statistics remained after the selection.

Figure 7.3 (*left*) shows the invariant mass distribution in data of non-isolated muons, obtained by using our $Z \rightarrow \mu\mu$ selection criteria except for the opposite charge and mass window requirements, and reversing the isolation cut. In 331 nb^{-1} data, we do not have enough events in this distribution to successfully perform the template fit, so that we use a larger dataset of 3.37 pb^{-1} to obtain the QCD template. In this amount of data, 88 events satisfy the selection criteria in the mass range $30 \text{ GeV} < m_{\mu\mu} < 120 \text{ GeV}$.

We carry out the fraction fit using the ROOT function `TFractionFitter`, which performs a likelihood fit by varying the normalizations of the template histograms. We note that the errors from the fraction fit are not quite reliable when the QCD template from data has limited statistics. Nevertheless, we perform the fit keeping in

mind this caveat.

Figure 7.3 (*right*) shows the invariant mass distribution of data events that satisfy all the $Z \rightarrow \mu\mu$ selection criteria including the isolation cut. It also shows the result of the fraction fit, that is, the signal and QCD background templates added in the respective fractions from the fit. We see that, within the statistical uncertainty, the prediction from the fit matches the data well.

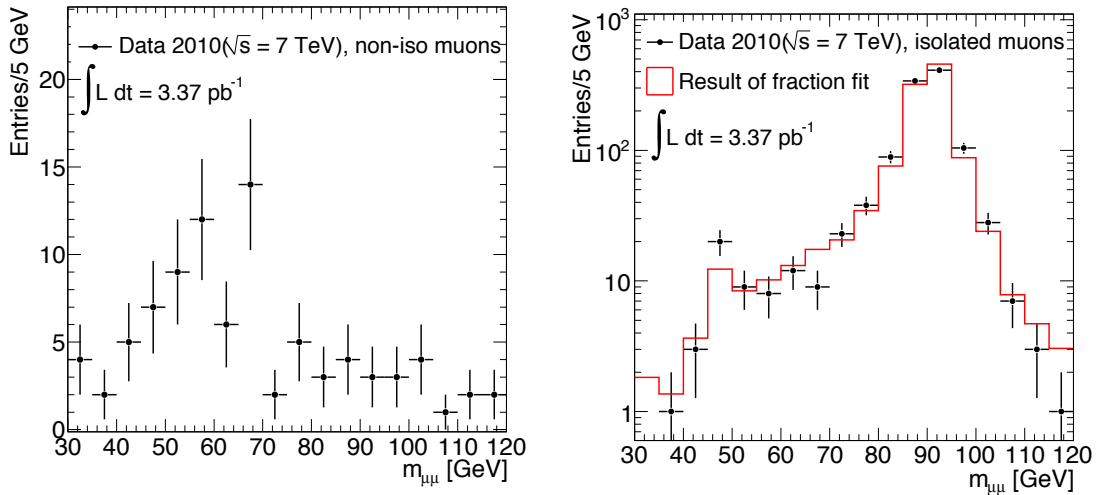


Figure 7.3: *Left*: Dimuon invariant mass distribution for events with non-isolated muons in 3.37 pb^{-1} of data. *Right*: Dimuon invariant mass distribution for data events with isolated muons (*black*) and from the template fit result (*red*) in the range $30 \text{ GeV} < m_{\mu\mu} < 120 \text{ GeV}$.

The QCD fraction from the fit is $6.5 \pm 1.4\%$. Since we have 88 events in the QCD template, this translates to 5.7 ± 1.3 events in 3.37 pb^{-1} of data. In our analysis sample of 331 nb^{-1} , therefore, the expected QCD background is 0.56 ± 0.12 event in the range $30 \text{ GeV} < m_{\mu\mu} < 120 \text{ GeV}^2$. Since this is a larger range than our Z mass

²Note that we cannot trivially obtain an estimate from the QCD background in the Z mass window $66 \text{ GeV} < m_{\mu\mu} < 116 \text{ GeV}$, because the result of the fraction fit is not a simple weighted

window, the QCD background estimate should be taken as an overestimation of the background within the window.

We test the robustness of the template fit method using Monte Carlo. We use $b\bar{b}$ events with non-isolated muons as our QCD template, and $b\bar{b}$ events with isolated muons as our QCD pseudo-data. Half of our $Z \rightarrow \mu\mu$ Monte Carlo sample is used as the signal template, while the other half is treated as signal pseudo-data. The invariant mass distributions for the QCD and signal pseudo-data events are added in known fractions to simulate the pseudo-data distribution.

We perform an ensemble test by simulating a number of pseudo-experiments. We take the invariant mass distributions for the $Z \rightarrow \mu\mu$ and QCD pseudo-data, and change the content of each bin within their Poisson fluctuation. Then we add the distributions and perform the template fit as described above. We repeat the procedure 1000 times, each time varying the bin contents of the signal and background pseudo-data distributions but using the same templates. We make two sets of distributions from the results of the pseudo-experiments:

- the signal and background fractions from the template fit in each experiment
- the quantity $p = \frac{\text{True fraction} - \text{fit fraction}}{\text{Error in fit fraction}}$ for both signal and background in each experiment

Figure 7.4 shows the distributions of the signal and QCD background fractions. We expect them to be Gaussian-distributed; Gaussian fits yield $99.10 \pm 0.09\%$ for the signal fraction and $0.90 \pm 0.09\%$ for the background fraction. Figure 7.5 shows the

sum of the input distributions. We need more statistics to be able to make the fit within the Z mass window.

distributions of the pull quantity p for the signal and background ensembles together with Gaussian fits. Ideally, both of these distributions would be centered around zero. We see that this is not the case, which points to a systematic overestimation of the background fraction by the template fit.

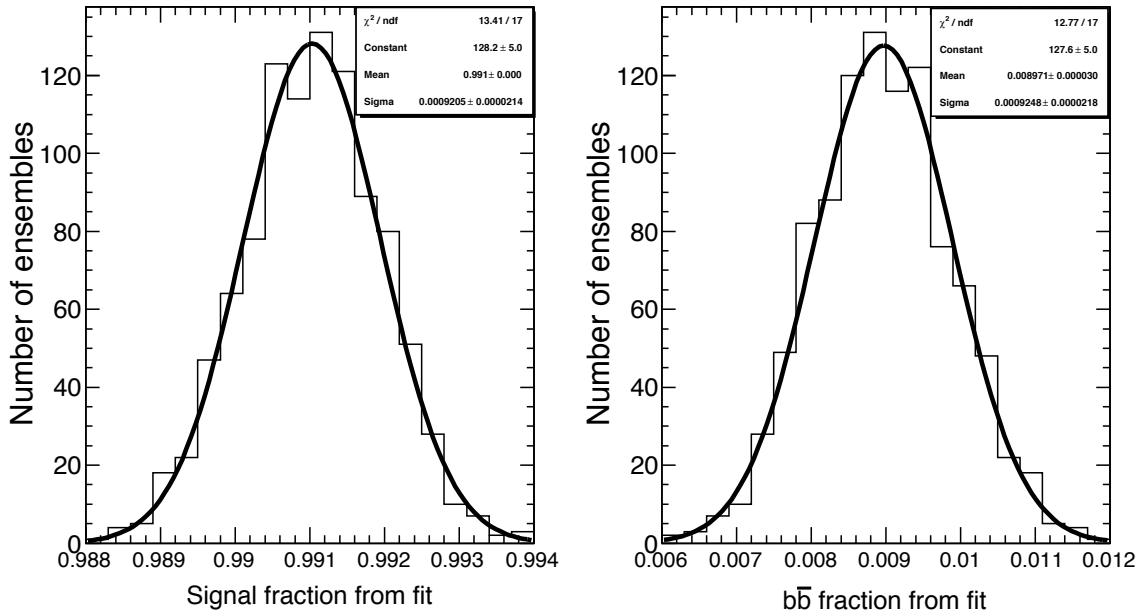


Figure 7.4: Distribution of Z fraction (*left*) and $b\bar{b}$ fraction (*right*) from the template fit in 1000 pseudo-experiments, in which the content of each pseudo-data bin is randomly varied within their Poisson fluctuation. Both distributions have been fitted to Gaussians.

To derive a correction factor for the systematic overestimation, we repeat the ensemble test several times, each time varying the input QCD fraction in the pseudo-data. For each input QCD fraction, we obtain a ‘measured’ fraction from the Gaussian fit to the distribution of template fit results *a la* Figure 7.4. Table 7.1 lists the input and measured QCD fractions in each test. Figure 7.6 shows a plot of the measured QCD fraction vs. the input fraction, with a straight-line fit. The fit has a slope of

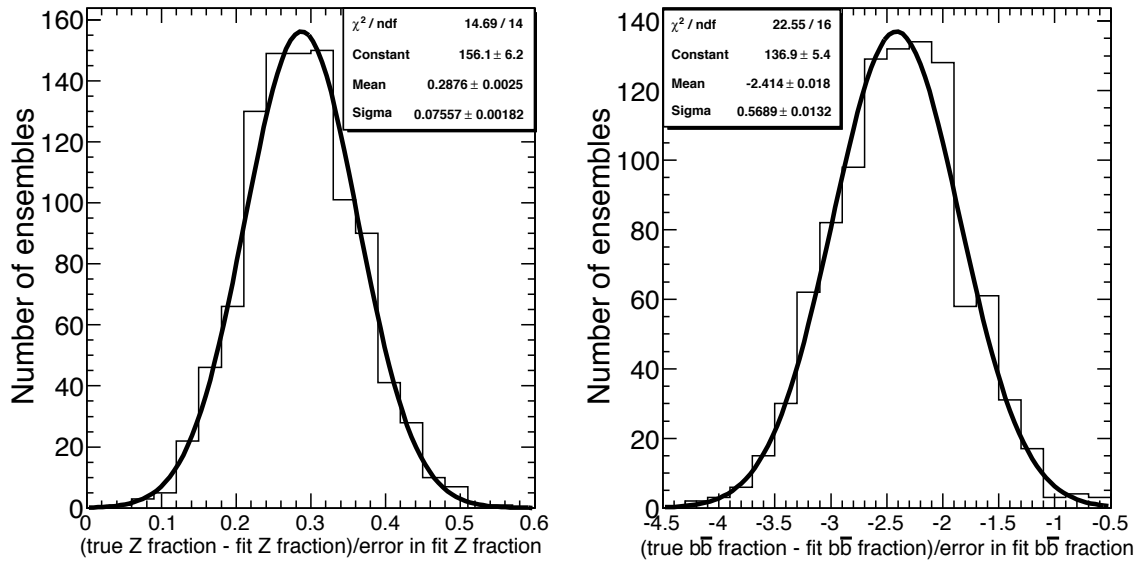


Figure 7.5: Distributions of the quantity $p = \frac{\text{True fraction} - \text{fit fraction}}{\text{Error in fit fraction}}$ for the Z ensemble (*left*) and the $b\bar{b}$ ensemble (*right*). Both distributions have been fitted to Gaussians.

1.123 ± 0.015 , which we use to correct the QCD fraction obtained from the template fit to data.

Ensemble	Input QCD fraction (%)	Measured QCD fraction (%)
1	0	0.0002 ± 0.0005
2	0.63	0.90 ± 0.09
3	1.3	1.66 ± 0.12
4	2.0	2.46 ± 0.13
5	3.0	3.59 ± 0.15
6	4.0	4.69 ± 0.17
7	5.0	5.76 ± 0.18
8	10.0	10.5 ± 0.2

Table 7.1: Input and measured QCD fractions from 8 ensemble tests, in each of which the input fraction to the QCD pseudo-data was varied.

Corrected QCD background from template fitting in $30 \text{ GeV} < m_{\mu\mu} < 120 \text{ GeV}$:
 0.50 ± 0.11 event.

We notice that the background estimations from the two data-driven methods described above do not agree. However, we re-emphasize that the estimate from the template fit method is an upper limit to the QCD background in our mass window, and that the error from this procedure is unreliable owing to the limited statistics in the QCD template.

For the cross-section analysis, we decided to use a purely Monte Carlo estimation for the QCD background. We use two `Pythia`-generated heavy-flavor jet production samples which contain $b\bar{b}$ and $c\bar{c}$ events. Since the QCD production cross-section is not known accurately³, we assign a conservative estimate of 100% to the cross-

³Using the dimuon invariant mass distribution at the preselection stage (bottom plot in Figure 6.8), we estimated a QCD scale factor of 1.6 between data and Monte Carlo.

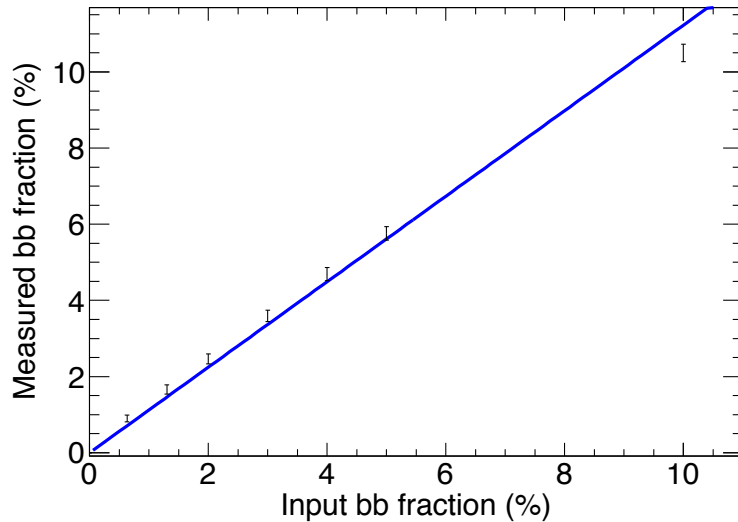


Figure 7.6: The measured QCD fraction as a function the input fraction from 8 ensemble tests. The slope of the first-degree polynomial fit gives the correction factor for the QCD fraction obtained from a template fit to data.

sections of these samples, and use it as a systematic on the Monte Carlo prediction of the QCD background.

In 331 nb^{-1} of data, we predict $0.038 \pm 0.015(\text{stat}) \pm 0.038(\text{sys}) \pm 0.04(\text{lum})$ events using simulated $b\bar{b}$ and $c\bar{c}$ samples.

7.2 Electroweak backgrounds

7.2.1 $t\bar{t}$ background

$t\bar{t}$ decays can fake the signal in two ways. One W can decay into a muon, which can combine with a muon in a jet to give a $Z \rightarrow \mu\mu$ decay topology, or both W 's can decay into muons which, being high- p_T and isolated, together resemble the signal channel. In the former case, the muon from the jet will generally be non-isolated, and

thus the events should be largely removed by the isolation requirement. The latter channel is a so-called *irreducible* background because of its very close similarity to the signal⁴. Irreducible backgrounds are difficult to remove by definition, but their size in the sample can usually be estimated.

The $t \rightarrow Wb$ and the $W \rightarrow \mu\nu$ decays are both theoretically well-understood, the cross-sections being known respectively to NLO and NNLO accuracy. Hence, we can use a fully-simulated Monte Carlo sample to estimate this background. Reconstruction and trigger efficiencies for muons from dileptonic and semi-leptonic $t\bar{t}$ decays should be close to the corresponding values for $Z \rightarrow \mu\mu$ events. We can therefore be confident in determining this background using simulation.

7.2.2 $Z \rightarrow \tau\tau$ background

The branching fraction for the $\tau \rightarrow \mu\nu_\mu\nu_\tau$ decay is $\approx 17.3\%$ [40], so that both τ 's decay into muons $\approx 3\%$ of the time. The processes involved are electroweak and are well-understood, so we can again use a Monte Carlo sample to deduce the background contribution from this channel. τ decay muons in general have lower p_T than muons from a direct $Z \rightarrow \mu\mu$ decay, so that most of the τ background should be eliminated by our event selection criteria.

7.2.3 $W \rightarrow \mu\nu$ backgrounds

As already mentioned, $W \rightarrow \mu\nu$ events fake the signal when a muon from a jet combines with the W decay muon. Since muons in jets are non-isolated, we expect

⁴The branching fraction $t \rightarrow \mu\nu_\mu$ is $\approx 9.4\%$ [40], so the $t\bar{t}$ decay probability into the irreducible channel is $\approx 0.9\%$.

isolation cuts to remove most of these events. The $W \rightarrow \mu\nu$ cross-section is known to NNLO accuracy in QCD, but jets cannot be modeled with any accuracy in a Monte Carlo program. Therefore, as with the QCD multijet background, the $W \rightarrow \mu\nu$ background is best extracted from data. However, again in view of the small size of our data sample, we use Monte Carlo to estimate this background.

To all electroweak backgrounds, we assign a 3% systematic owing to PDF uncertainty. In addition, we assign a further 5% theoretical cross-section uncertainty to the $W \rightarrow \mu\nu$ and $Z \rightarrow \tau\tau$ backgrounds, and a 6% theoretical uncertainty to the $t\bar{t}$ background.

7.3 Cosmic ray background

High- p_T muons from cosmic rays can potentially mimic the Z signal. Our collision event criteria, in particular the cut on primary vertex z_0 and the requirement that the event have at least one primary vertex with at least three tracks associated with it, largely reduce this background. However, cosmic muons that traverse the detector near the beam spot and within the time window for a bunch crossing can look like a $Z \rightarrow \mu\mu$ event by appearing to be two oppositely charged energetic muons from the interaction region. Since most bunch crossings lead to minimum-bias events, for a cosmic muon to fake a Z decay it must coincide with a minimum-bias event, the event must pass our muon trigger, and the muon track must be reconstructed as two combined muons which pass the Z selection criteria.

In this section, we estimate an upper limit to the in-time cosmic contamination

in our data sample using the relation:

$$N_{Cosmic} = \sigma_{mb} \times p_{trig}^{cosm} \times p_{reco}^{cosm} \times \mathcal{L} \quad (7.1)$$

where \mathcal{L} is the integrated luminosity and:

- σ_{mb} is the minimum bias cross-section at 7 TeV center-of-mass energy, which we take to be 50 mb
- p_{trig}^{cosm} is the probability that a cosmic muon will pass the L1_MU6 trigger in time with a bunch crossing
- p_{reco}^{cosm} is the probability that the muon will be reconstructed as a combined muon that passes all our Z selection criteria

The cosmic triggering probability for the L1_MU0 trigger was estimated in [62]. The rate of this trigger for colliding bunches in the run period of interest is about 2.96 Hz. We note that during period D, when most of the data used in this analysis was collected, there were 8 circulating bunches in the LHC. Given that the beam circulation frequency is 11.3 kHz (Chapter 2), the probability that a cosmic muon is triggered on during a bunch collision is:

$$2.96/(11300 \times 8) = 3.3 \cdot 10^{-5}$$

Given the fact that cosmic muons are mostly in the barrel region, and assuming that the L1_MU6 trigger efficiency in the barrel is similar to that of the L1_MU0 trigger for muons with $p_T > 20$ GeV, we take the cosmic trigger probability of L1_MU6 as being essentially the same as that of the L1_MU0 trigger.

We derive the probability of a cosmic muon passing our Z selection criteria using events in unpaired bunches⁵ through ATLAS. We eliminate the trigger requirement and the vertex cut, and relax the cut on $|z_0 - z_{vtx}|$ to be less than 150 mm for each muon. We then count events that pass the other selection criteria. We find that 40 events pass our high- p_T event selection, 6 events pass the requirement of at least two combined muons in the event, and 2 events pass the p_T , η , isolation and opposite charge requirements on the muons (Table 7.2). No event lies within the Z mass window.

Cut	Events	Fraction of selected events
GRL + BCID (non-colliding)	942492	-
High- p_T muon selection	41	$(43.5 \pm 6.8) \cdot 10^{-6}$
≥ 2 combined muons in event	6	$(6.4 \pm 2.6) \cdot 10^{-6}$
$p_T > 20$ GeV, $\Delta p_T(ID, MS) < 15$ GeV	2	$(2.1 \pm 1.5) \cdot 10^{-6}$
Isolation, opposite charge	2	$(2.1 \pm 1.5) \cdot 10^{-6}$
$66 < m_{\mu\mu} < 116$ GeV	0	

Table 7.2: Cutflow of events in unpaired bunch crossings with respect to the Z selection.

Supposing that one event were within the Z mass window, we can estimate an upper limit to the number of cosmic events that would pass the full selection:

$$1 \times (20/300) = 0.067$$

This result yields a value of $2.8 \cdot 10^{-8}$ for p_{reco}^{cosm} . We now plug the values in Eq. 7.1 and derive N_{Cosmic} :

$$N_{Cosmic} = 50 \cdot 10^6 \times 3.3 \cdot 10^{-5} \times 7.1 \cdot 10^{-8} \times 331 = 0.039$$

⁵An unpaired bunch with respect to the ATLAS detector is one that does not collide with a bunch in the other beam in the detector.

Since this is small compared to our total background prediction of 0.244 event (Table 7.3) and is an upper limit in any case, we conclude that the cosmic ray background is negligible for our analysis.

7.4 Summary of backgrounds

The total estimated background to $Z \rightarrow \mu\mu$ in 331 nb^{-1} of data is 0.244 ± 0.057 , where the uncertainty quoted includes statistical and systematic components, but not the uncertainty on the luminosity. All backgrounds are predicted based on the acceptance for the Z selection in simulation, so that the 5.5% uncertainty on C_Z is included in the systematic. This value includes all contributions to C_Z , namely, the uncertainties on trigger, reconstruction and isolation cut efficiencies as well as on muon momentum scale and resolution.

sample	Number of events
$W \rightarrow \mu\nu$	$0.013 \pm 0.003(\text{stat}) \pm 0.001(\text{sys}) \pm 0.001(\text{lum})$
$Z \rightarrow \tau\tau$	$0.086 \pm 0.004(\text{stat}) \pm 0.007(\text{sys}) \pm 0.0010(\text{lum})$
$t\bar{t}$	$0.107 \pm 0.004(\text{stat}) \pm 0.010(\text{sys}) \pm 0.012(\text{lum})$
EW Total	$0.206 \pm 0.006 (\text{stat}) \pm 0.017 (\text{sys}) \pm 0.023 (\text{lum})$
QCD	$0.038 \pm 0.015(\text{stat}) \pm 0.038(\text{sys}) \pm 0.04(\text{lum})$
Total Background	$0.244 \pm 0.016 (\text{stat}) \pm 0.055 (\text{sys}) \pm 0.027 (\text{lum})$

Table 7.3: Details of the background calculation. The Monte Carlo event predictions are normalized to 331 nb^{-1} , and the trigger and reconstruction efficiency scale factors derived in Section 6.2 have been applied. See Chapter 5 for a definition of the Monte Carlo samples.

Chapter 8

Properties of Z bosons and measurement of $Z \rightarrow \mu\mu$ cross-section

8.1 Z candidate events

In this section we look at the results of the $Z \rightarrow \mu\mu$ analysis. After full event selection, we have 109 candidate events. Table 8.1 shows the cutflow from data using the Z event selection. The expected number of signal events is 119.9 ± 7.6 over an expected background of 0.244 ± 0.057 , where the uncertainties include statistical and systematic components, but not the 11% uncertainty on the luminosity. The largest background contribution is from $t\bar{t}$ events (44%), followed by $Z \rightarrow \tau\tau$ (35%) and QCD (16%). The expected signal and background numbers with a breakdown of the background predictions, and the number of observed candidates in data are summarized in Table 8.2. Uncertainties in Table 8.2 include statistical, systematic, and luminosity contributions.

Cut	Number of Events
BCID+good runs list	35756532
Trigger	5464740
Preselection	22075
≥ 2 combined muons in event	1879
Comb $p_T > 20$ GeV, MS $p_T > 10$ GeV, $dp_T < 15$ GeV	144
Isolation	117
$66 \text{ GeV} < M_{\mu\mu} < 116 \text{ GeV}$	109

Table 8.1: Z selection cutflow on the data.

$W \rightarrow \mu\nu$	0.013 ± 0.003
$Z \rightarrow \tau\tau$	0.086 ± 0.013
$t\bar{t}$	0.107 ± 0.016
EW Total	0.206 ± 0.027
QCD	0.038 ± 0.041
Total background	0.244 ± 0.063
$Z \rightarrow \mu\mu$ signal	119.9 ± 15.2
Total predicted	120.1 ± 15.3
Number observed	109

Table 8.2: Summary of predicted number of events, including systematic and luminosity uncertainties, compared to the number observed. The number of predicted events is normalized to 331 nb^{-1} .

8.1.1 Properties of $Z \rightarrow \mu\mu$ events

In this section, we show properties of the data and signal Monte Carlo events after the full Z selection. Since the background is about 3 orders of magnitude below the signal, we do not show the background distribution in most plots.

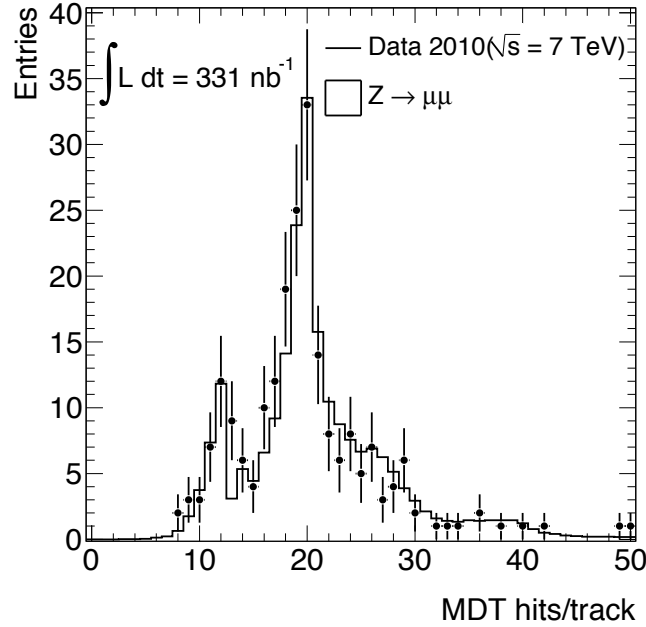


Figure 8.1: MDT hits per muon track for signal Monte Carlo and data after the full Z selection.

Hit distributions

Figure 8.1 shows the number of MDT hits per track. Unlike the corresponding plot at the preselection level (Figure 6.2), we no longer see tracks with less than 6 MDT hits. However, in spite of the large statistical uncertainty, we note the systematic migration of the data distribution to lower hit bins in the peak region, which we recognize as an effect of misalignment.

Figure 8.2 shows the number of RPC η and ϕ hits per track, where we see good data-Monte Carlo agreement. Figure 8.3 shows the TGC η and ϕ hit distributions. As in Figure 6.4 at the preselection stage, the effect of cross-talk shows up as several data bins being higher than corresponding Monte Carlo bins.

Figure 8.4 shows the number of Pixel hits on the inner detector track associated

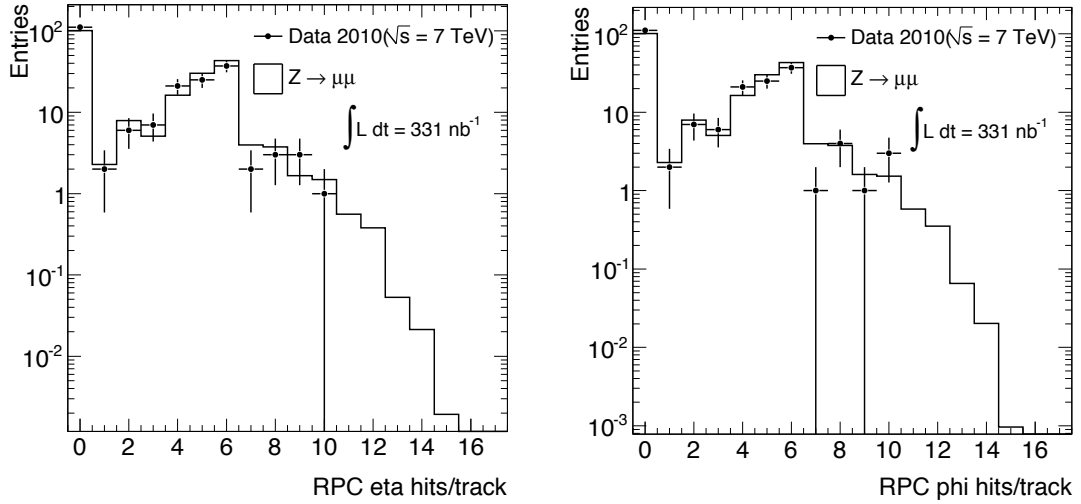


Figure 8.2: RPC η (*left*) and ϕ (*right*) hits per muon track for signal Monte Carlo and data after the full Z selection.

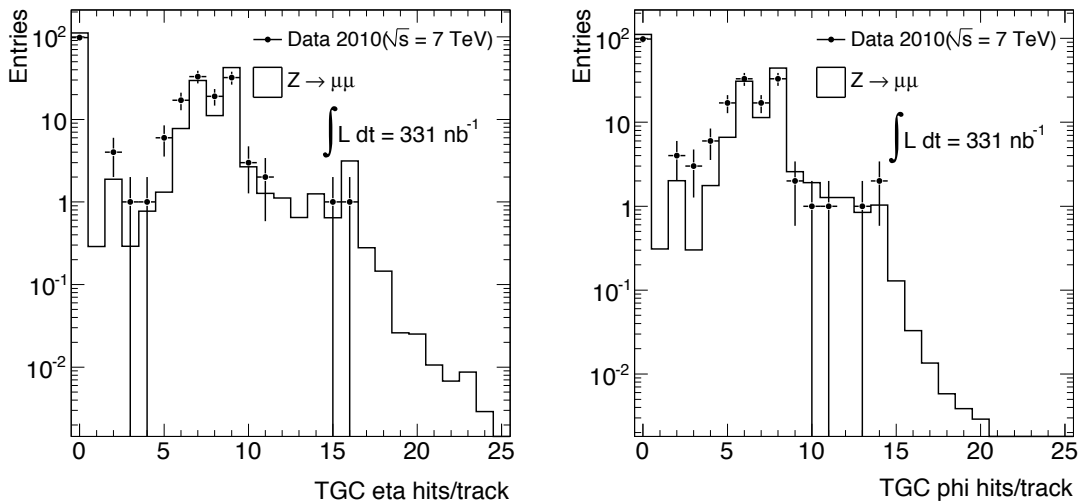


Figure 8.3: TGC η (*left*) and ϕ (*right*) hits per muon track for signal Monte Carlo and data after the full Z selection.

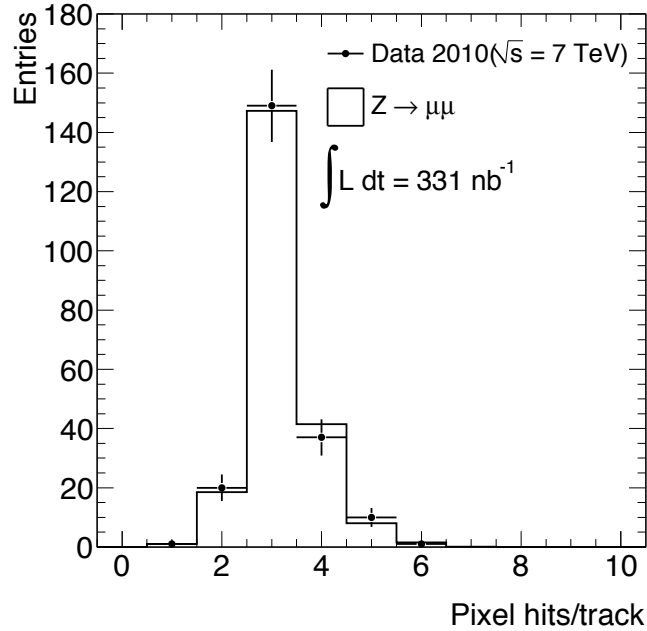


Figure 8.4: Pixel hits on inner detector tracks matched to muon spectrometer tracks for signal Monte Carlo and data after the full Z selection.

with the combined muon track, while Figure 8.5 displays the number of SCT and TRT hits on the track. We see good agreement between the data and the Monte Carlo expectation in all three plots.

Kinematic distributions

Figure 8.6 shows kinematic distributions (p_T , η and ϕ) for muons from the decay of the Z candidates.

Figure 8.7 shows the muon p_T versus dimuon invariant mass at two different stages of the Z selection cuts: after the muon p_T cut (*left*) and after the isolation cut (*right*) on the decay muons. We see that the Z events are concentrated in the expected band in this 2D phase space. As expected, the isolation cut removes a number of events

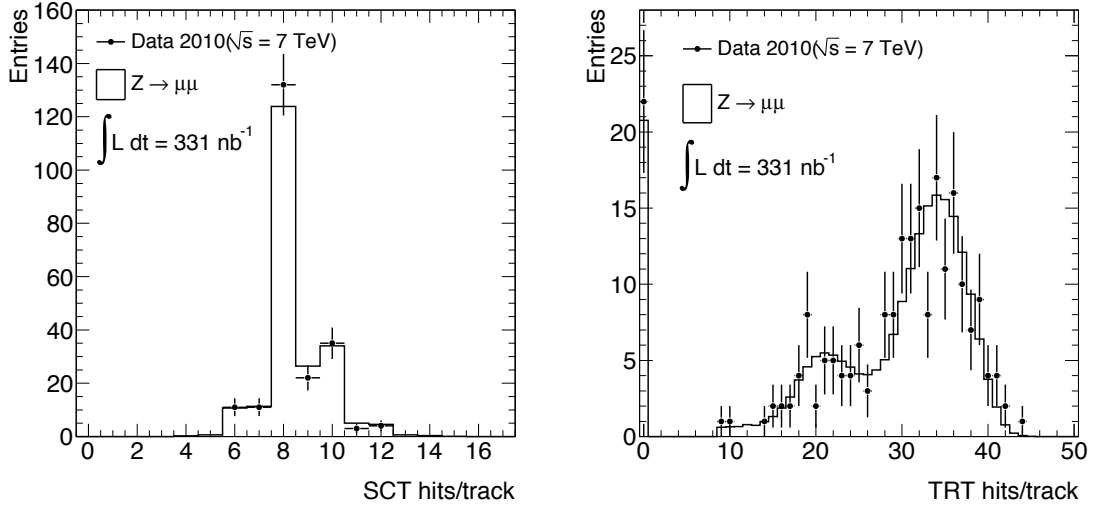


Figure 8.5: SCT (*left*) and TRT (*right*) hits on inner detector tracks matched to muon spectrometer tracks for signal Monte Carlo and data after the full Z selection.

outside the band, but very few within the band.

Figure 8.8 (*left*) shows the track isolation ratio versus muon p_T , in which all Z cuts have been applied except the isolation cut. Figure 8.8 (*right*) shows the dimuon invariant mass distribution from data and Monte Carlo after the Z selection.

Figure 8.9 shows the dimuon invariant mass distribution for signal Monte Carlo and data separately for events in which both muons are in the barrel, both in the endcap, and one muon in the barrel and one in the endcap.

Figure 8.10 shows the p_T and rapidity distributions of the Z bosons.

8.1.2 Fitting the Z peak and extraction of Z mass resolution

Figure 8.11 shows an unbinned fit to the dimuon invariant mass spectrum in data. The fitting function is a theoretical lineshape which includes both Z and virtual photon contributions to the Drell-Yan production, convolved with a Gaussian function

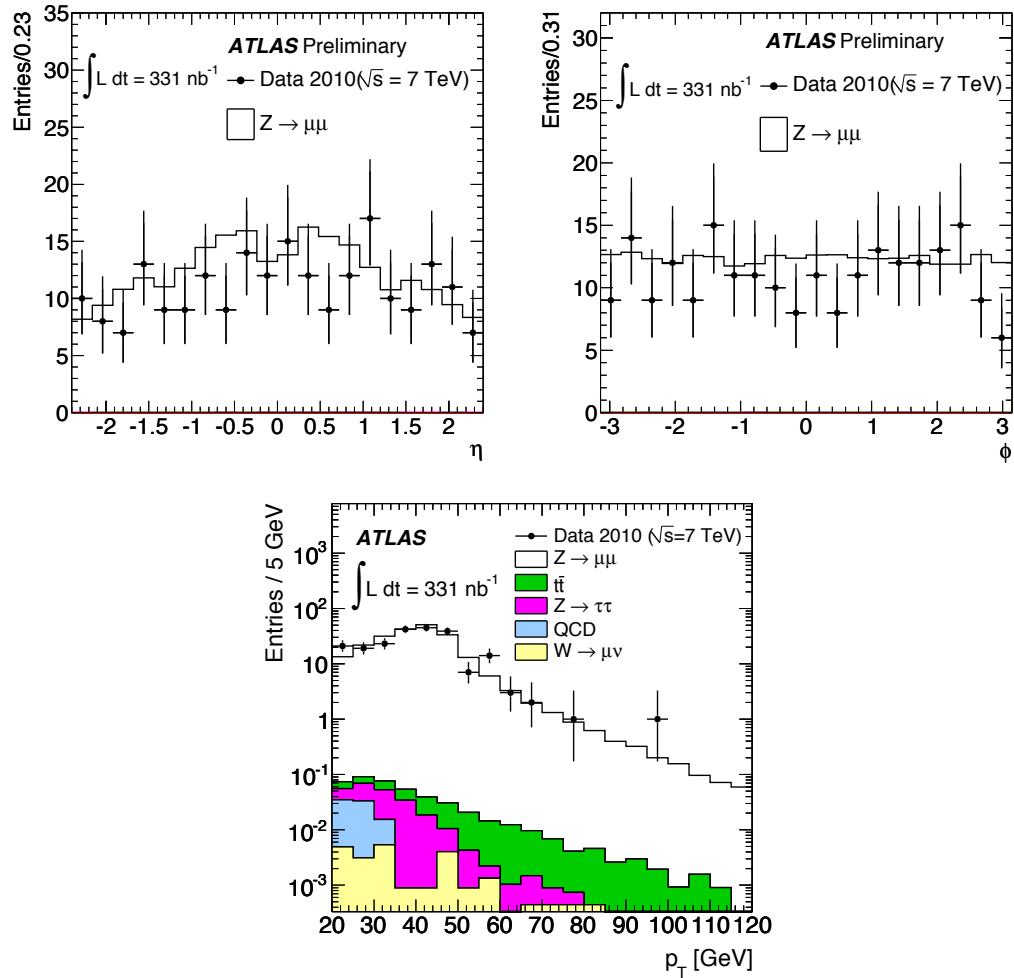


Figure 8.6: Muon η , ϕ , p_T distributions for signal Monte Carlo, background Monte Carlo and data after Z selection. The total Monte Carlo event numbers have been normalized to the integrated luminosity.

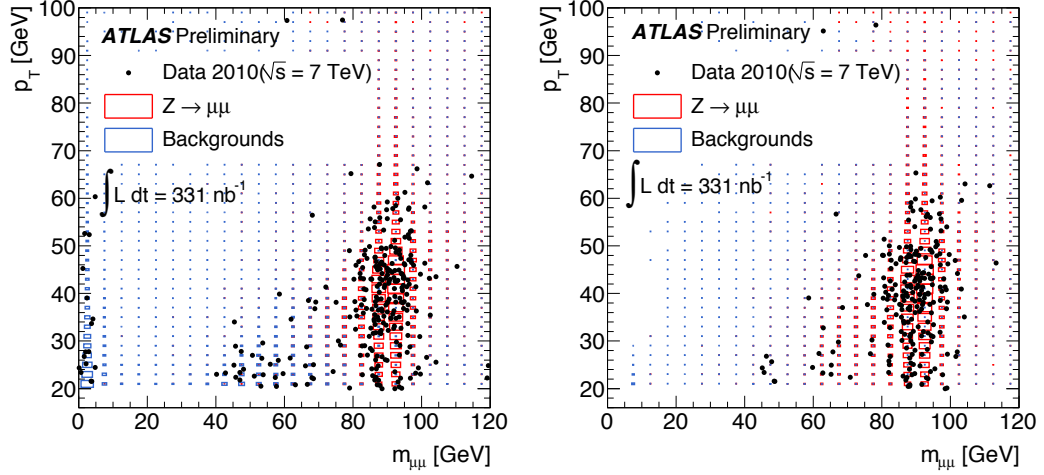


Figure 8.7: Muon p_T versus dimuon invariant mass for signal Monte Carlo, background Monte Carlo and data: after the muon p_T cut (*left*) and after the isolation cut (*right*).

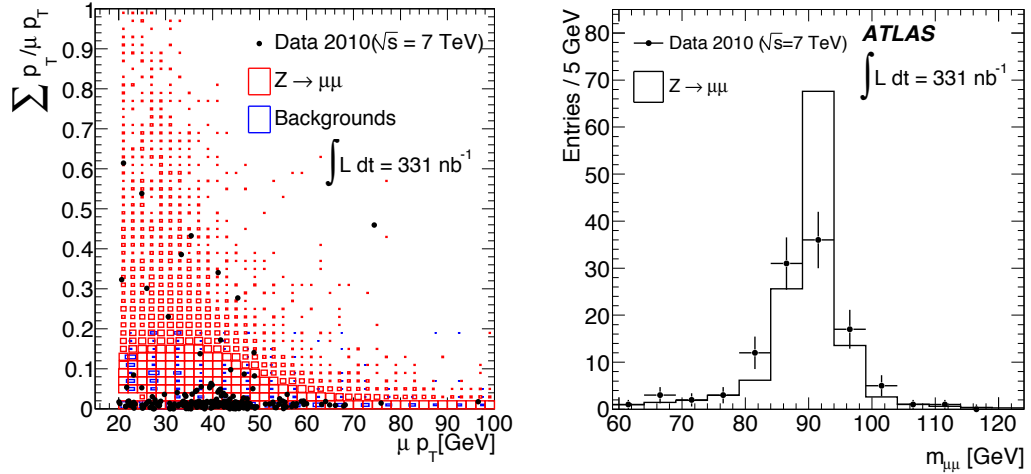


Figure 8.8: Track isolation ratio versus muon p_T (*left*) and the dimuon invariant mass spectrum (*right*) after the Z selection cuts. The track isolation ratio is defined as the sum of the p_T of all inner detector tracks in a cone of size $\Delta R < 0.4$ around the muon track divided by the muon track p_T .

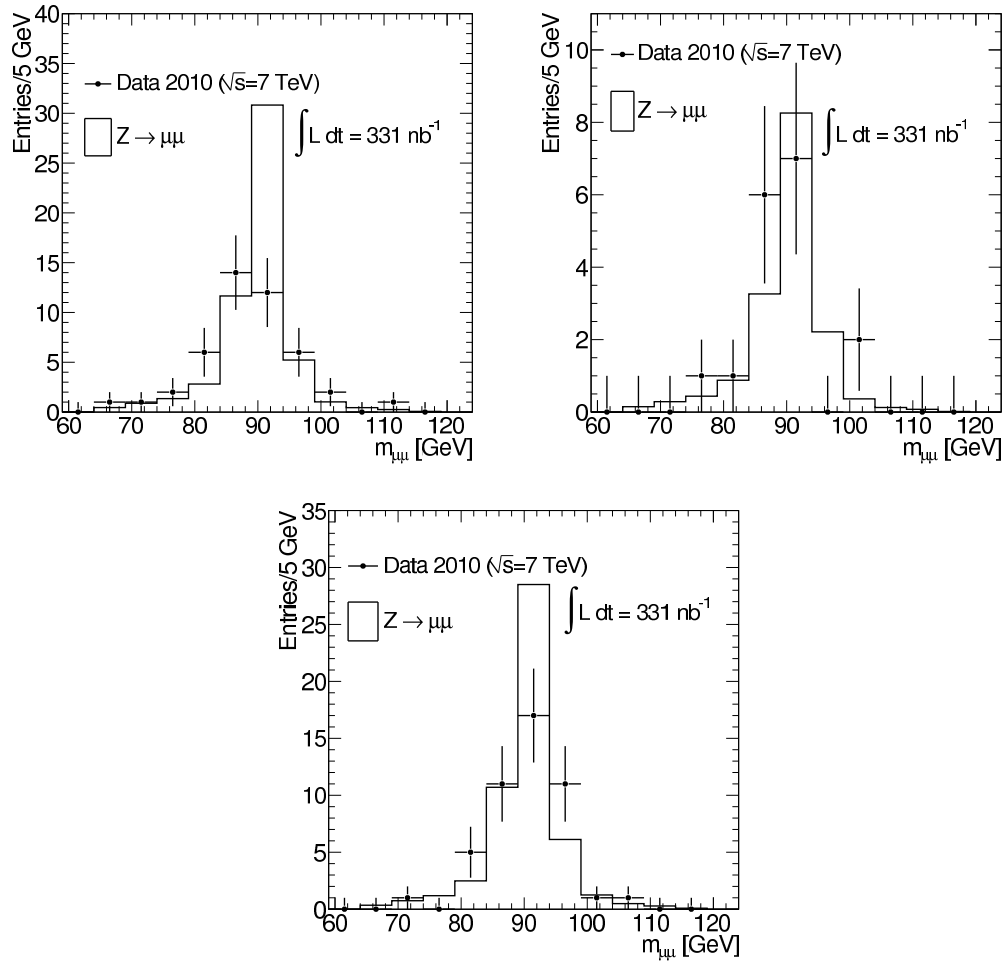


Figure 8.9: Dimuon invariant mass spectrum after the Z selection cuts for three cases: both decay muons in the barrel (*topleft*), both in the endcap (*topright*), and one muon each in the barrel and the endcap (*bottom*).

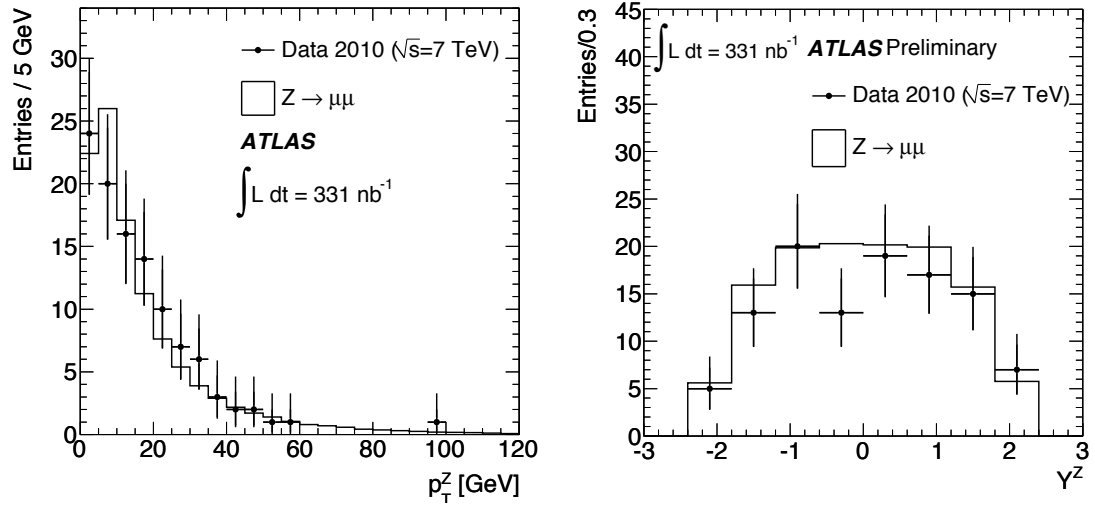


Figure 8.10: Z boson p_T and rapidity spectra after full event selection.

to take into account the finite detector resolution. A similar fit is made to the binned invariant mass spectrum from $Z \rightarrow \mu\mu$ Monte Carlo. The mean and width of the Gaussian component from each fit are reported in Table 8.3.

Fit parameter	Value from data [GeV]	Value from MC [GeV]
Mean	91.17 ± 0.56	91.30 ± 0.01
Width	4.19 ± 0.54	1.52 ± 0.01

Table 8.3: Mean and width of the Gaussian component of Z lineshape fits. The fit is made on unbinned data and binned Monte Carlo.

The Gaussian width gives an estimate of the Z mass resolution due to detector effects. We see from the values in Table 8.3 that the mass resolution in data is worse than that expected from simulation by a factor of ≈ 2.8 .

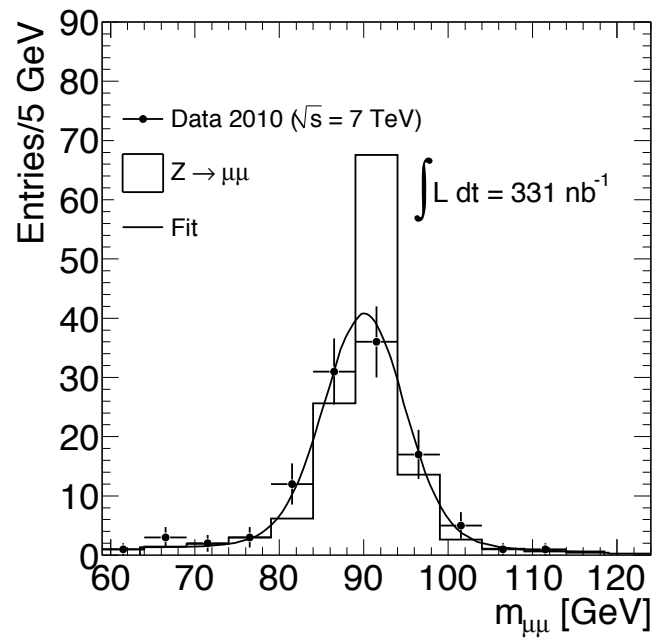


Figure 8.11: Unbinned fit to the Z boson mass peak using a theoretical lineshape function convolved with a Gaussian function.

8.2 Cross-section measurement

From the analysis described in this thesis, using 331 nb^{-1} of data, we expect 120.1 ± 15.3 events and observe 109. The resulting total and fiducial $Z/\gamma^* \rightarrow \mu^+\mu^-$ cross-sections are extracted using Eq. 6.2, and are reported in table 8.4 [95].

$$\sigma_{Z/\gamma^*} \times BR(Z/\gamma^* \rightarrow \mu^+\mu^-) \quad 0.87 \pm 0.08 \text{ (stat)} \pm 0.05 \text{ (sys)} \pm 0.10 \text{ (lum)} \text{ nb.}$$

$$\sigma_{Z/\gamma^*}^{fid} \times BR(Z/\gamma^* \rightarrow \mu^+\mu^-) \quad 0.43 \pm 0.04 \text{ (stat)} \pm 0.02 \text{ (sys)} \pm 0.05 \text{ (lum)} \text{ nb.}$$

Table 8.4: Measured values of the total and fiducial $Z \rightarrow \mu\mu$ cross-section, including statistical, systematic and luminosity errors.

We see that, even with the low statistics used in this measurement, the uncertainties in the cross-section values are dominated by systematics. The 11% uncertainty from the luminosity measurement comes primarily from the uncertainty in the beam current measurement 3. With the latest Van der Meer calibration (as of October 14, 2010), the luminosity uncertainty is expected to decrease to 5-10% [69]. The experimental uncertainties will improve as we collect more data and use the tag-probe approach to measure the various efficiencies.

Chapter 9

Discussion and Outlook

9.1 Comparison with theoretical prediction

We calculate the theoretical $Z \rightarrow \mu\mu$ cross-section with the FEWZ program to NNLO accuracy in QCD using the MRST2008 NNLO PDF set. The factorization and renormalization scales are both set at the Z mass [40], while the value of α_s used is 0.1171 [85]. We find the central value for the cross-section to be:

$$\sigma_{Z/\gamma^* \rightarrow l^+l^-}^{NNLO} = 0.964 \text{ nb} \quad (66 < m_{\ell\ell} < 116\text{GeV})$$

To estimate the systematic uncertainty on the theoretical cross-section, we use the FEWZ and ZWPROD [57] programs. There are three major sources of uncertainty, studied in detail in [85]. We summarize them below:

- Uncertainty due to factorization and normalization scales, μ_F and μ_R : to estimate the scale uncertainty, we compute the cross-section a number of times, varying one scale in the range $\frac{m_Z}{2} \leq \mu_{F,R} \leq 2m_Z$ while keeping the other constant. Then we vary both scales together within the constraint $0.5 \leq \mu_F/\mu_R \leq 2$. The largest deviation from the central value of the cross-section is taken to be

the uncertainty from this source, which we find to be $\pm 0.6\%$.

- PDF uncertainties: the uncertainties within the PDF set are determined using the 40 error eigenvectors of the MRST2008 NNLO PDF set. As with the calculation of the PDF uncertainty in the fiducial acceptance A_Z 6.3, the cross-section values σ_{Z+}^i and σ_{Z-}^i are computed for each error eigenvector i , and the uncertainty on the cross-section estimated using:

$$\Delta\sigma_+ = \Delta\sigma_- = \frac{1}{2} \sqrt{\sum_i (\sigma_+^i - \sigma_-^i)^2} \quad (9.1)$$

The uncertainty from this source is found to be 3.4%. Table 9.1 shows the cross-section obtained with ZWPROD using four different PDF sets. The relative difference between the value using each PDF set and that using the MRST2008 NLO PDF set is indicated.

Scale ($\mu_F = \mu_R$)	Parton density functions			
	MSTW2008	CTEQ6.6	CT10	HERA1.0(NLO)
m_Z	946	946(+0.1%)	941(-0.6%)	969(+2.3%)

Table 9.1: NLO $Z \rightarrow \ell\ell$ cross-sections in units of picobarns calculated with the ZWPROD program using different PDF sets. The numbers in parentheses indicate relative changes from the value obtained using the MSTW2008 NLO PDF set.

- Uncertainty from the strong coupling constant $\alpha_S(m_Z)$: the MRST2008 NNLO PDF set includes PDF fits obtained with $\alpha_S(m_Z)$ values that correspond to:
 1. variations from the central value up and down by one standard deviation
 2. values between 0.110 and 0.130

To estimate the uncertainty in the cross-section from $\alpha_S(m_Z)$, we compute the cross-section using MRST2008 NNLO PDFs corresponding to the 90% confi-

dence limit in $\alpha_S(m_Z)$. We find the deviation from the central value to be about 2.6%. Using HERAPDF1.0 NNLO PDF fits obtained with $\alpha_S = 0.1145$ and $\alpha_S = 0.1176$, we find the deviation in the cross-section value to be 1.9%.

The overall systematic uncertainties on the $Z \rightarrow \mu\mu$ cross-section from the several sources are summarized in Table 9.2 [85].

Relative uncertainty (%)			
Scale	90% C.L. PDF+ α_s	90% C.L. PDF error and HERA α_s	
+0.5	+4.5		3.8
-0.7	-3.9		

Table 9.2: Summary of scale and PDF+ α_s uncertainties on the $Z \rightarrow \mu\mu$ cross section to NNLO accuracy in QCD. The values have been obtained using the MSTW2008NNLO 90% confidence limits for both the PDF and α_s uncertainties. The last column shows the result obtained using averaged MSTW2008NNLO 90% confidence limit PDF errors and α_s uncertainties obtained from HERAPDF1.0 NNLO fits.

From these numbers, we decided to use a systematic uncertainty of 5% on the $Z \rightarrow \mu\mu$ cross-section. We then have¹:

$$\sigma_{Z/\gamma^* \rightarrow l+l-}^{NNLO} = 0.964 \pm 0.048 \text{nb} \quad (66 < m_{\ell\ell} < 116 \text{ GeV})$$

We see that our measured cross-section of $0.87 \pm 0.08(\text{stat}) \pm 0.05(\text{sys}) \pm 0.10(\text{lum})$ nb is in agreement with the theoretical prediction. Figure 9.1 shows the measured Z cross-sections in the electron and muon channels, as well as the combined value from the two channels, in addition to the theory prediction with its error band. Figure 9.2 shows the predicted and measured values of the $Z \rightarrow \mu\mu$ cross-section at various hadron colliders as a function of the center-of-mass energy. We see in these figures that all measurements to date are in good agreement with the theoretical prediction.

¹We note here that the cross-section $\sigma_{Z \rightarrow l+l-}^{NNLO}$ is 0.944 ± 0.047 nb, which is about 2% lower than $\sigma_{Z/\gamma^* \rightarrow l+l-}^{NNLO}$ [85].

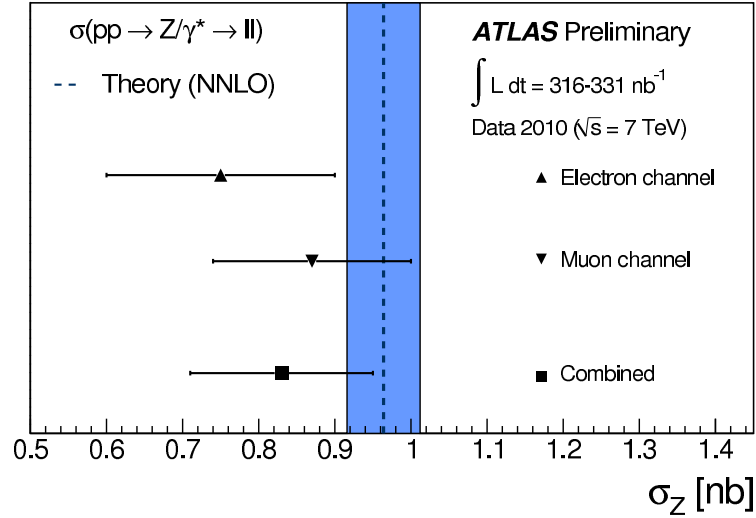


Figure 9.1: The measured values of the Z cross-section in the electron and muon channels as well as the combined value from the two channels. Note that the size of the dataset used for the electron channel measurement is 316 nb^{-1} . The theory prediction is from the FEWZ program using the MRST2008 NNLO PDF set. For the data points, the total uncertainties are shown.

We conclude that the modeling of the Z boson production cross-section using QCD calculations up to order α_s^2 is accurate in the limit of current measurements.

9.2 Outlook

In this section, we show distributions of Z boson kinematic variables obtained with a 3.37 pb^{-1} dataset, which is larger than the dataset used for the cross-section measurement by a factor of ≈ 10.2 .

Figure 9.3 shows an unbinned fit to the dimuon invariant mass spectrum in data, using the fitting function described in Section 8.1.2. The mean and width obtained from the fit are reported in Table 9.3, together with corresponding values from Monte

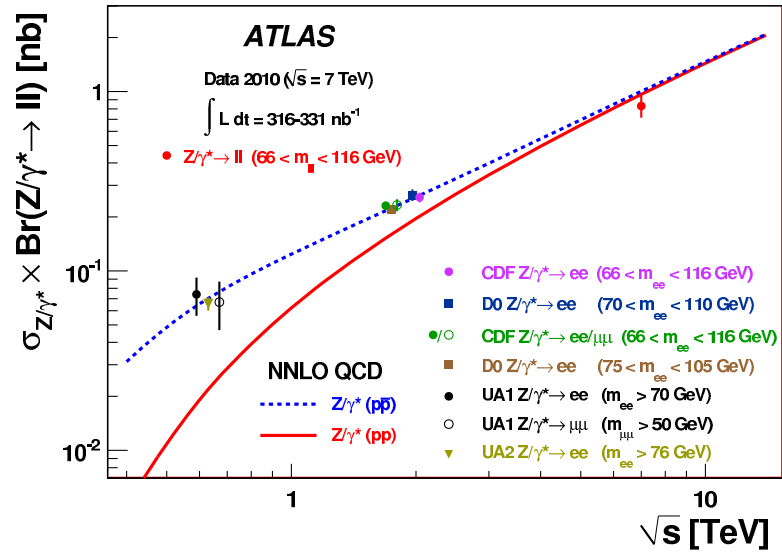


Figure 9.2: Combined measurements of the Z cross-section from the electron and muon channels, made at various pp and $p\bar{p}$ colliders. The measurements are compared with theoretical predictions at NNLO accuracy as a function of the center-of-mass energy, obtained with the FEWZ program using the MRST2008 NNLO PDF set. For the data points, the total uncertainties are shown. Note that the data points at the various energies have been staggered for better readability.

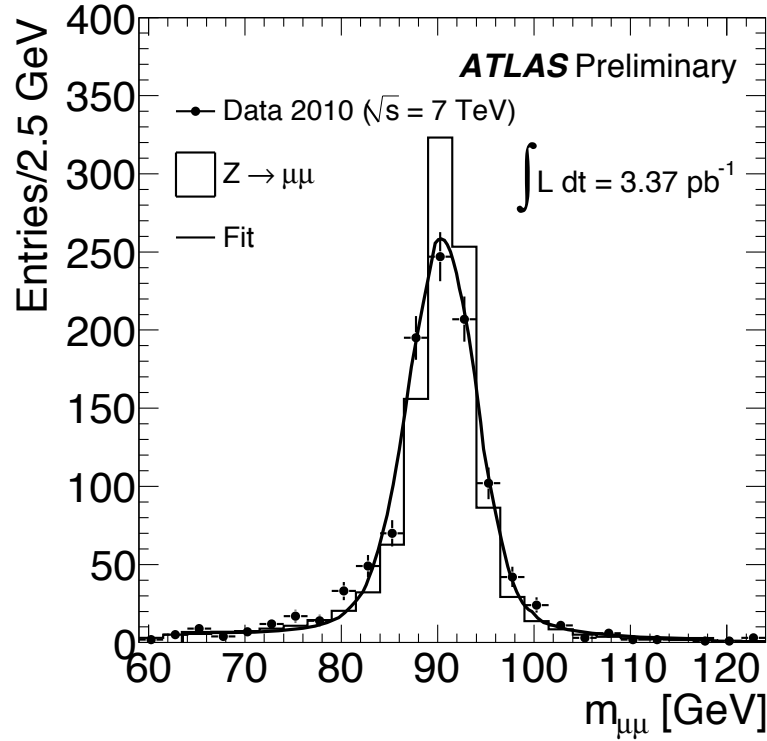


Figure 9.3: Unbinned fit to the Z boson mass peak using a theoretical lineshape function convolved with a Gaussian function. The Monte Carlo prediction, normalized to the total number of data events, is also shown.

Carlo.

Fit parameter	Value from data [GeV]	Value from MC [GeV]
Mean	90.85 ± 0.14	91.30 ± 0.01
Width	2.83 ± 0.17	1.52 ± 0.01

Table 9.3: Mean and width of the Gaussian component of Z lineshape fits. The fit is made on unbinned data events from a 3.37 pb^{-1} dataset and on binned Monte Carlo.

Figure 9.4 shows muon kinematic distributions (p_T , η and ϕ) for muons from the decay of the Z bosons. Figure 9.5 shows the muon p_T versus dimuon invariant mass at two different stages of the Z selection cuts: after the muon p_T cut (*left*) and after the isolation cut (*right*) on the decay muons. As with the lower-statistics dataset,

we see that the Z events lie in the expected band in this 2D phase space. Figure 9.6 shows the p_T and rapidity distributions of the Z bosons.

The Monte Carlo distributions in these figures are normalized to the number of events in data; consequently, we can only conclude that the shapes of the data distributions agree with Monte Carlo expectations.

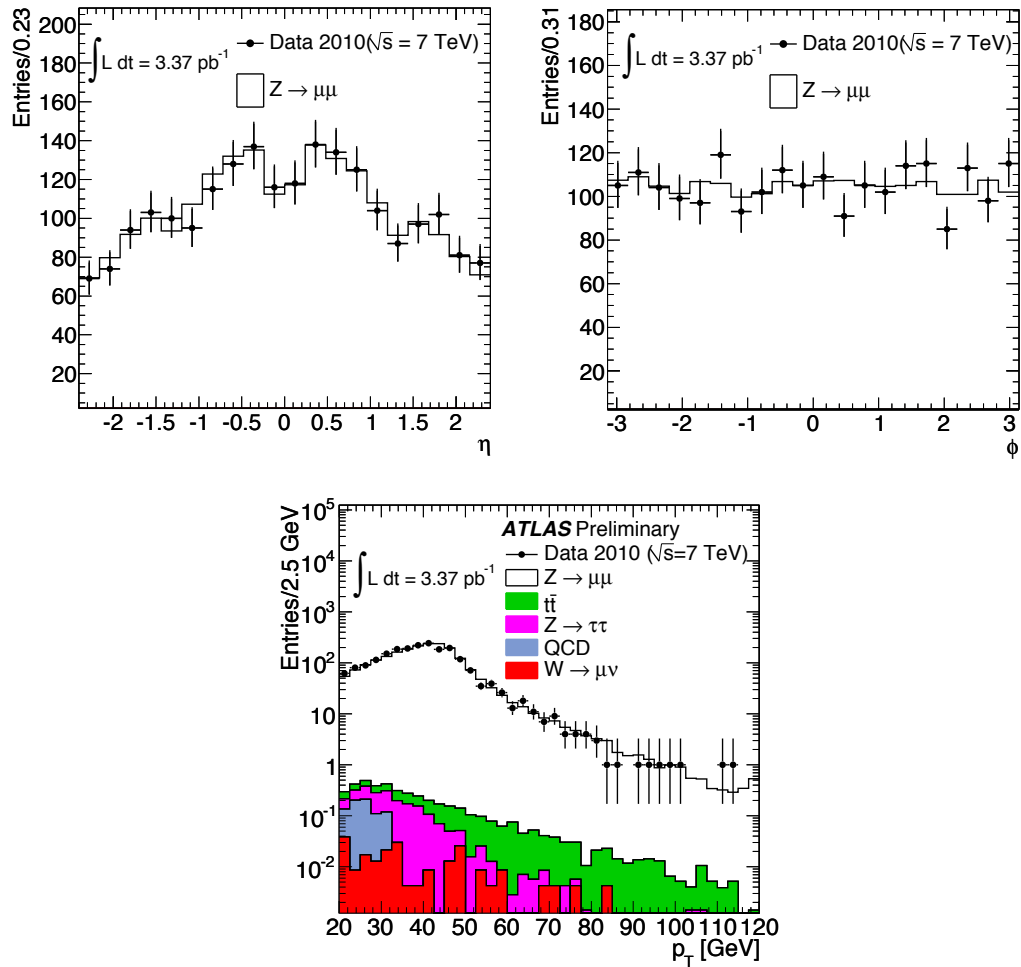


Figure 9.4: *Top:* Muon η (*left*) and ϕ (*right*) distribution for signal Monte Carlo and data after Z selection. *Bottom:* muon p_T distribution for signal Monte Carlo, background Monte Carlo and data after Z selection. The total Monte Carlo event numbers have been normalized to the number of data events.

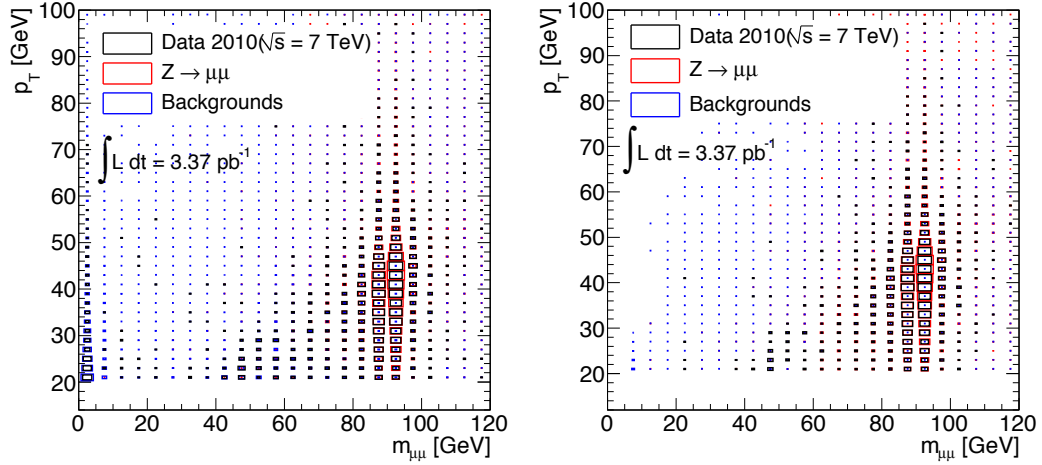


Figure 9.5: Muon p_T versus dimuon invariant mass for signal Monte Carlo, background Monte Carlo and data: after the muon p_T cut (*left*) and after the isolation cut (*right*).

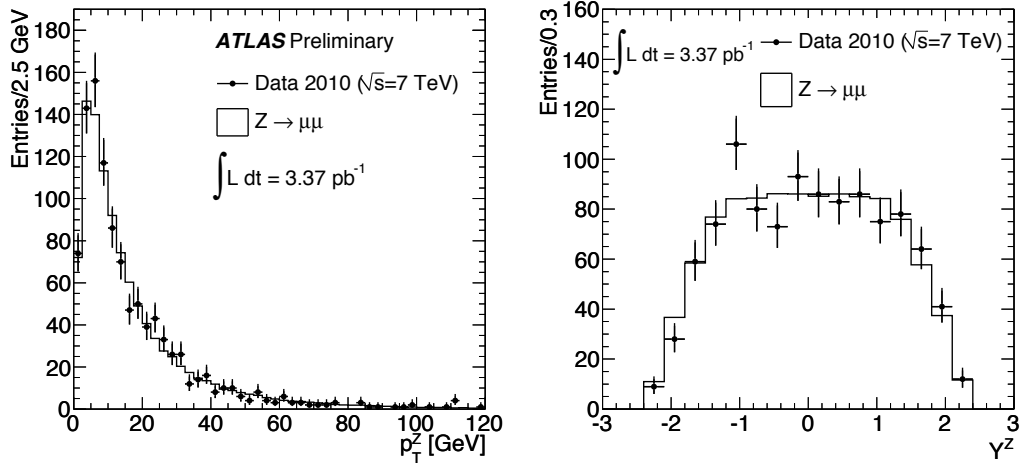


Figure 9.6: Z boson p_T and rapidity spectra after full event selection. The Monte Carlo event numbers have been normalized to the number of data events.

Appendix A

Event list

Tables A.1, A.2 and A.3 list the run, luminosity block and event numbers of the Z events in our dataset. They also show the invariant masses obtained using combined muon tracks, associated inner detector tracks, and muon spectrometer tracks extrapolated to the primary vertex.

Candidate	Run	LB	Event	$M_{\mu\mu}$ (GeV) (comb tracks)	$M_{\mu\mu}$ (GeV) (InDet tracks)	$M_{\mu\mu}$ (GeV) (ME tracks)
1	155112	430	79831531	82.7211	81.3091	98.1304
2	155569	233	2963628	99.5332	100.124	90.1982
3	155669	297	9723082	91.7341	93.8341	88.9622
4	155678	284	12897976	88.9719	89.0976	88.0877
5	155678	296	15529226	96.1388	96.5519	97.6974
6	155697	500	40092612	97.2669	97.0459	100.557
7	156682	488	15652763	84.9435	88.66	80.3552
8	158116	166	9280694	81.5023	80.4837	84.1518
9	158116	188	11985072	87.7801	86.9525	89.7637
10	158116	253	19521523	100.522	90.6267	100.876
11	158116	332	28142433	89.9145	89.032	91.5366
12	158116	117	2909609	86.924	82.7558	91.9704
13	158116	139	5795269	90.5658	79.8734	93.3409
14	158269	18	1433877	83.3648	85.8533	79.7057
15	158392	259	8540259	94.1101	89.7752	101.427
16	158392	409	24580205	93.1056	100.644	89.344
17	158443	227	4095112	69.0334	68.9478	69.592
18	158466	266	3863134	87.2786	99.3088	82.5852
19	158466	268	3999312	91.2185	95.1894	91.4222
20	158466	270	4174272	78.6584	77.6439	79.9327
21	158466	273	4566707	96.6974	98.4693	86.0168
22	158466	274	4687856	84.7348	86.5554	82.5617
23	158548	199	15974948	80.7139	80.8693	79.1509
24	158548	112	1499487	92.2508	90.4101	94.9343
25	158548	277	29399418	87.9503	86.9371	85.9255
26	158582	298	42733145	77.0333	76.0548	79.7024
27	158582	307	44184208	91.2384	90.4666	91.9552
28	158582	127	14524548	88.4564	86.0884	90.5149
29	158582	218	29798112	96.6137	97.8313	94.1887
30	158582	262	36972083	101.099	100.389	100.962
31	158632	201	9178181	93.2994	91.5784	95.9866
32	158632	214	11361744	92.8457	90.1325	95.4298

Table A.1: Run, luminosity block (LB) and event numbers of the Z candidate events. Corresponding dimuon invariant masses using combined muon tracks, associated Inner Detector tracks and Muon Spectrometer extrapolated (ME) tracks are also shown.

Candidate	Run	LB	Event	$M_{\mu\mu}$ (GeV) (comb tracks)	$M_{\mu\mu}$ (GeV) (InDet tracks)	$M_{\mu\mu}$ (GeV) (ME tracks)
33	158801	163	4054383	85.2209	86.3981	85.3666
34	158801	185	6999725	111.466	110.063	113.13
35	158801	242	14502419	90.6235	92.1369	86.5476
36	158801	297	26022799	84.712	86.7621	84.4159
37	158975	169	14619951	90.9091	94.1982	83.0452
38	158975	229	25445980	91.5897	89.4252	92.4182
39	158975	236	26635416	88.9176	90.0811	79.6241
40	158975	251	29890777	93.9227	95.8707	93.0327
41	158975	323	39615111	90.0331	89.8175	94.1603
42	158975	333	41763968	90.2624	93.1545	91.3966
43	154822	280	14321500	87.5746	75.8467	87.5766
44	159041	311	36579209	72.7728	77.0084	68.9924
45	159041	345	43460569	88.6226	86.3909	91.0375
46	159041	140	6713219	89.8465	88.8118	93.1003
47	159041	187	14072232	94.1493	93.9719	94.2356
48	159041	190	14674336	93.8343	91.7457	95.1232
49	159041	210	18504052	85.9677	87.3117	82.5433
50	159041	242	24288060	95.5719	97.2219	94.1498
51	159041	260	27541154	81.2372	81.9381	79.7931
52	159041	270	29246227	80.7331	86.98	75.4021
53	159041	117	2888031	89.8628	89.4522	93.5068
54	159086	328	34994657	104.538	103.695	106.524
55	159086	401	46810158	90.6399	93.6787	81.0671
56	159086	403	47149283	85.9526	85.7587	92.4555
57	159086	431	52107058	99.9009	100.179	101.876
58	159086	436	53104618	95.1428	97.1476	87.2979
59	159086	471	59556511	89.9563	92.6654	79.4243
60	159086	492	63385979	91.4919	91.3803	89.0277
61	159086	547	73527574	86.5524	86.4565	86.1078
62	159086	159	8546916	97.6506	98.136	93.4159
63	159086	162	9022982	93.8393	95.4874	89.4688
64	159086	121	2474127	66.7636	66.1659	66.4467
65	159086	206	15637749	82.8991	82.4947	82.649
66	159086	209	16161108	92.0042	93.4958	89.1605
67	159086	212	16604356	92.3584	92.4556	95.2744
68	159086	127	3417935	89.4442	90.3616	87.8527
69	159086	267	25054308	97.3791	99.3085	83.5884
70	159086	285	27844867	88.9286	89.2767	88.5194

Table A.2: Z candidate list *cont'd.*

Candidate	Run	LB	Event	$M_{\mu\mu}$ (GeV) (comb tracks)	$M_{\mu\mu}$ (GeV) (InDet tracks)	$M_{\mu\mu}$ (GeV) (ME tracks)
71	159086	307	31525892	88.106	92.986	79.0085
72	159113	299	9744787	81.5145	81.0818	86.133
73	159113	312	12152880	75.6768	77.3425	75.2314
74	159113	347	18728242	89.2129	88.1236	88.4897
75	159113	355	20191851	89.8638	90.0767	87.9949
76	159113	362	21578272	89.4172	88.9397	88.2873
77	159113	412	30062185	96.6542	96.709	94.8373
78	159113	414	30394614	82.4593	83.5846	82.6808
79	159113	416	30724230	85.8544	86.8118	84.581
80	159113	438	34832448	90.2513	90.8871	90.4884
81	159113	443	35764750	81.287	80.3091	82.5521
82	159113	453	37538727	92.1183	92.6807	91.311
83	159179	250	5584139	79.5987	77.3731	82.5398
84	159179	268	7612914	93.9897	93.4774	93.2529
85	159179	274	8290752	87.6681	88.4909	87.6575
86	159202	195	3362767	88.6461	90.8143	89.0242
87	159202	199	3758451	92.5774	90.6239	96.2003
88	159202	200	3823928	88.6112	81.358	90.8492
89	159202	256	8900710	87.4374	84.0253	93.95
90	159202	268	10001935	102.3	100.396	109.417
91	159203	11	686975	85.7993	84.8705	92.2655
92	159203	15	1133979	86.9704	90.2379	86.6562
93	159224	406	19277908	82.5367	83.3064	79.9598
94	159224	435	21583562	96.5334	97.4919	92.5467
95	159224	437	21751775	92.2754	95.2369	90.5132
96	159224	264	5055266	88.0602	88.7367	78.5341
97	159224	478	25249560	87.7798	86.84	90.384
98	159224	482	25534948	90.2717	90.8548	90.8304
99	159224	554	31656446	91.798	91.8042	91.5583
100	159224	575	33415906	96.5596	92.0012	100.275
101	159224	603	35906097	94.8577	94.4594	99.5776
102	159224	607	36204162	87.2796	87.775	85.5368
103	159224	653	40287931	90.3464	90.5796	89.6039
104	159224	675	42328132	95.8919	91.7512	98.3798
105	159224	707	45286755	87.5333	89.8607	79.4435
106	159224	311	10241283	95.6132	94.6983	98.959
107	159224	320	11207558	92.738	92.7919	91.9563
108	159224	254	3846135	88.7339	88.0692	88.466
109	159224	344	13630667	88.9226	89.0358	90.4782

Table A.3: Z candidate list *cont'd.*

Appendix B

Comparison of muon curvature in cosmic events

Figure B.1 shows the signed inverse momentum, *i.e.*, curvature of muon spectrometer tracks in bins of the momentum of inner detector tracks that have been matched to the spectrometer tracks. The criteria used for track selection in the MS and the ID as well as for the matching were described in Section 6.2.5.

If the ID and the MS measured exactly the same momentum for a track, each histogram would have two peaks of identical shape symmetrically on each side of $q/P = 0$. This is not seen to be not the case: events migrate to bins above and below those that correspond to $P_{ID} = P_{MS}$. Moreover, as the track momentum increases, we see a corresponding increase in the fraction of tracks that migrate out of bin. In particular, for $P_{ID} > 120$ GeV, a significant fraction of tracks migrate to higher momentum (*i.e.*, lower curvature) bins. This effect is most pronounced in the [400, 1000] GeV bin (lower right plot in Figure B.1).

The observed migration is believed mainly to be due to misalignments in both the ID and the MS, and in particular due to relative misalignment between the two systems. It points to the need for more precise alignment within and between the

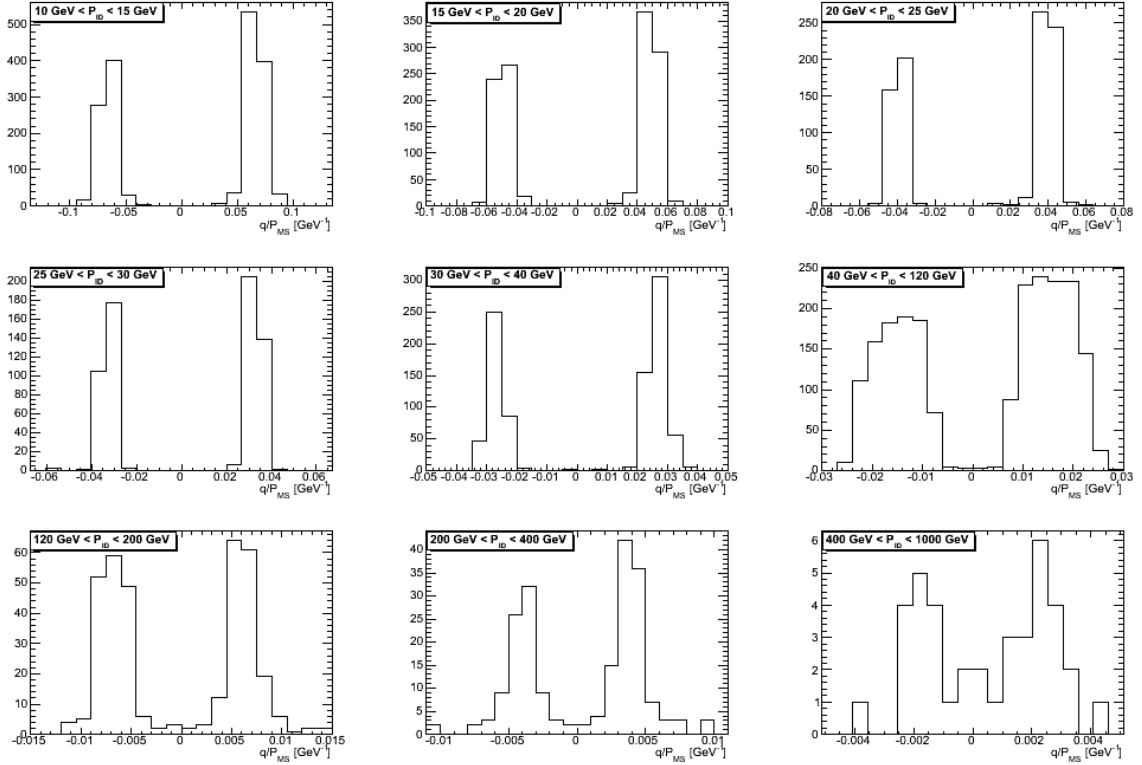


Figure B.1: Signed inverse momentum of muon spectrometer tracks in cosmic events in 9 bins of matched tracks in the inner detector. From top left to bottom right, the inner detector momentum bins are as follows: $[10, 15]$ GeV/ c , $(15, 20]$ GeV/ c , $(20, 25]$ GeV/ c , $(25, 30]$ GeV/ c , $(30, 40]$ GeV/ c , $(40, 120]$ GeV/ c , $(120, 200]$ GeV/ c , $(200, 400]$ GeV/ c , $(400, 1000]$ GeV/ c .

systems. The observed discrepancy between the measured width of the Z peak and that expected from Monte Carlo also underscores the importance of better alignment.

Bibliography

- [1] The LHC design report: Vol. 1. The LHC Main Ring. Technical Report CERN-2004-003, CERN, 2004. <http://ab-div.web.cern.ch/ab-div/Publications/LHC-DesignReport.html>.
- [2] <https://twiki.cern.ch/twiki/bin/view/Atlas/TrackingOverviewRecoMuonboy>, 2007.
- [3] InDetBeamSpot - ATLAS Offline Beam Spot Determination . <https://twiki.cern.ch/twiki/bin/view/Atlas/InDetBeamSpot>, 2008. ATLAS Twiki page for offline beamline reconstruction.
- [4] Online Beam Spot in HLT. <https://twiki.cern.ch/twiki/bin/view/Atlas/AtlasTriggerBeamSpot>, 2008. ATLAS Twiki page for online beamline reconstruction.
- [5] TV beam observation system for LHC. Technical report, CERN, 2008. <http://ab-dep-bi-pm.web.cern.ch/ab-dep-bi-pm/?n=Activities.BTVLHC>.
- [6] Twiki. <https://twiki.cern.ch/twiki/bin/view/Atlas/MooreMuidInfo>, 2008.
- [7] Twiki. <https://twiki.cern.ch/twiki/bin/view/AtlasProtected/MuonRecoPedia>, 2008.
- [8] A. Belloni et al. Measurement of the Cosmic Ray Muon Charge Ratio using the ATLAS Muon Spectrometer. ATL-COM-MUON-2010-012, Geneva, 2010.
- [9] G. Altarelli and F. Feruglio. Discrete flavor symmetries and models of neutrino mixing. 2010.
- [10] G. Altarelli and G. Parisi. Asymptotic freedom in parton language. *Nucl.Phys.*, **B126**:298, 1977.
- [11] C. Anastasiou, K. Melnikov, and F. Petriello. Fully differential higgs boson production and the di-photon signal through next-to-next-to-leading order. *Nucl.Phys.*, **B724**:197–246, 2005.
- [12] A. Andreazza. Private communication.

-
- [13] S. Ask. Status of the forward physics projects in ATLAS. In *Proceedings of DIS2007, Munich*, 2007.
- [14] ATLAS Collaboration. ATLAS Tile Calorimeter Technical Design Report. Technical Report CERN/LHCC/96-42, CERN, 1996.
- [15] ATLAS Collaboration. The ATLAS Muon Spectrometer Technical Design Report. Technical Report CERN/LHCC/97-22, CERN, 1997.
- [16] ATLAS Collaboration. ATLAS forward detectors for measurement of elastic scattering and luminosity. Technical Report CERN/LHCC/2008-004, CERN, 2008.
- [17] ATLAS Collaboration. Expected Performance of the ATLAS Experiment, Detector, Trigger and Physics. arXiv:0901.0512v1 [hep-ex], 2008.
- [18] ATLAS Computing Group. ATLAS Computing Technical Design Report. Technical Report CERN-LHCC-2005-022, CERN, 2005.
- [19] C. Balazs and C. P. Yuan. Soft gluon effects on lepton pairs at hadron colliders. *Phys. Rev. D*, **58**:5558–5583, 1997.
- [20] V. A. Bednyakov, N. D. Giokaris, and A. V. Bednyakov. On Higgs mass generation mechanism in the Standard Model. *Phys.Part.Nucl.*, 39:13–36, 2008.
- [21] H. Burkhardt and S. White. Absolute luminosity from machine parameters. Talk given in ATLAS Week, April 2008.
- [22] N. Cabibbo. Unitary symmetry and leptonic decays. *Phys. Rev. Lett.*, **10**:531, 1963.
- [23] D. Caforio. Luminosity measurement using Cherenkov integrating detector (LUCID) in ATLAS. In *Proceedings of WSPC2007*, 2007.
- [24] J.M. Campbell, J.W. Huston, and W.J. Stirling. Hard Interactions of Quarks and Gluons: a Primer for LHC Physics. *Rept.Prog.Phys.*, **70**:89, 2007.
- [25] C.M. Calame et al. Multiple photon corrections to the neutral-current Drell-Yan process. *Phys. Rev. D*, **69** 037301, 2004.
- [26] The ATLAS Collaboration. Commissioning of the ATLAS Muon Spectrometer with Cosmic Rays. 2010.
- [27] J. C. Collins. Sudakov form factors. *Adv.Ser.Direct.High Energy Phys.*, **5**:573–614, 1989.

- [28] J. C. Collins and D. E. Soper. The Theorems of Perturbative QCD. *Ann. Rev. Nucl. Part. Sci.*, **37**:383–409, 1987.
- [29] A. M. Cooper-Sarkar. An NLO QCD analysis of inclusive cross-section data and jet production data from the zeus experiment at HERA-I. In *Proceedings of the DIS'04, Strbske Pleso, Slovakia*, 2004.
- [30] A. M. Cooper-Sarkar. Impact of and constraints on PDFs at the LHC. In *Proceedings of DIS2007, Munich*, 2007.
- [31] T. G. Cornelissen. *Track fitting in the ATLAS experiment*. PhD thesis, NIKHEF, 2006.
- [32] B. Delamotte. A hint of renormalization. *Am.J.Phys.*, **72**:170–184, 2004.
- [33] Manuel Drees. An introduction to supersymmetry. 1996.
- [34] S. Drell and T. M. Yan. Partons and their applications at high energies. *Nucl.Phys.*, **66**:578, 1971.
- [35] E. Bouhova-Thacker et al. Vertex Reconstruction in the ATLAS Experiment at the LHC. ATL-INDET-PROC-2008-003, Geneva, 2008.
- [36] E. Eichten and K. Lane. Low-scale technicolor at the Tevatron and LHC. 2007.
- [37] J. Kuckei et al. Strong cp violation and the neutron electric dipole form factor. *Phys.Atom.Nucl.*, **70**:349–357, 2007.
- [38] M. Aharrouche et al. Energy linearity and resolution of the ATLAS electromagnetic barrel calorimeter in an electron test-beam. *Nucl. Inst. Meth*, **A568**:601–623, 2006.
- [39] R. Jung et al. The LHC 450 GeV to 7 TeV synchrotron radiation profile monitor using a superconducting undulator. Technical Report CERN-SL-2002-015 BI, CERN, 2002.
- [40] K. Nakamura et al. (Particle Data Group). The Review of Particle Physics. *J. Phys. G*, **37**, **075021**, 2010.
- [41] P. Adragna et al. GNAM: A low-level monitoring program for the ATLAS experiment. *IEEE Trans. Nucl. Sci.*, 53:1317–1322, 2006.
- [42] R. P. Feynman. Mathematical formulation of the quantum theory of electromagnetic interaction. *Phys. Lett.*, **80**:440–457, 1950.
- [43] R. D. Field and R. P. Feynman. A parametrization of the properties of quark jets. *Nucl. Phys.*, **B136**:1, 1978.

- [44] S. Frixione, P. Nason, and C. Oleari. Matching NLO QCD computations with Parton Shower simulations: the POWHEG method. *JHEP*, 11:070, 2007.
- [45] C.D. Froggatt and H.B. Nielsen. Trying to understand the Standard Model parameters. *Surveys High Energ.Phys.*, **18**:55–75, 2003.
- [46] G. Marchesini et al. HERWIG: A Monte Carlo event generator for simulating hadron emission reactions with interfering gluons. *Comp. Phys. Commun.*, 67:465, 1992.
- [47] G. Piacquadio and K. Prokofiev and A. Wildauer. Primary Vertex Reconstruction in the ATLAS Experiment at LHC. *Journal of Physics: Conference Proceedings*, **119 032033**, 2008.
- [48] G. Usai. Feasibility study of a level two low pT di-muon trigger based on Tile calorimeter. ATL-DAQ-2003-017, Geneva, 2003.
- [49] G. Watt and A. D. Martin and W. J. Stirling and R. S. Thorne. Recent progress in global PDF analysis. In *Proceedings of DIS2008, London*, 2008.
- [50] J. Goldstone. Field theories with "superconductor" solutions. *Nuovo Cimento*, 19:154–164, 1961.
- [51] A. Gorisek. ATLAS BCM status and plans. Talk given in ATLAS luminosity working group meeting, July 2008.
- [52] T. D. Gottschalk. An improved description of hadronization in the QCD cluster model for e+ e- annihilation. *Nucl. Phys.*, **B239**:349, 1984.
- [53] H. Bethe and W. Heitler. On the stopping of fast particles and on the creation of positive electrons. *Proc. Roy. Soc. Lond.*, **A146**:83–112, 1934.
- [54] H. J. Abreu Aguilar et al. First measurement of the inclusive isolated prompt photon cross section in pp collisions at $\sqrt{s} = 7$ TeV with the ATLAS detector. ATL-COM-PHYS-2010-802, Geneva, 2010.
- [55] H. Jacob et al. A 40-MHz bunch by bunch intensity measurement for the CERN SPS and LHC. In *Proceedings of DIPAC2003, Mainz, Germany*, 2003.
- [56] H.-L. Lai et al. New parton distributions for collider physics. 2010.
- [57] R. Hamberg, W. L. van Neerven, and T. Matsuura. A Complete calculation of the order α_s^2 correction to the Drell-Yan K factor. *Nucl. Phys.*, B359:343–405, 1991. Erratum-ibid. B644:403-404,2002.
- [58] W. Herr and B. Muratori. Concept of luminosity. In *Proceedings of CAS2003, Zeuthen, Germany*, page 361, 2003.

- [59] M. Ishino. Private communication.
- [60] J. Allison *et al.* Geant4 developments and applications. *IEEE Transactions on Nuclear Science*, **53**No.1 :270–278, 2006.
- [61] J. Barreiro Guimaraes da Costa *et al.* Observation of $W \rightarrow \mu\nu$ and $Z \rightarrow \mu\mu$ in proton-proton collisions at $\sqrt{s} = 7$ TeV with the ATLAS Detector. ATL-PHYS-INT-2010-087, Geneva, 2010.
- [62] J. Barreiro Guimaraes da Costa *et al.* $W \rightarrow \mu\nu$ and $Z \rightarrow \mu\mu$ cross-sections measurements in proton-proton collisions at $\sqrt{s} = 7$ TeV with the ATLAS Detector. ATL-COM-PHYS-2010-685, Geneva, 2010.
- [63] J. Pumplin *et al.* Uncertainties of predictions from parton distribution functions II: the Hessian method. *Phys. Rev. D*, **65** 014013, 2002.
- [64] J.C. Collins. Hard-scattering factorization with heavy quarks: a general treatment. *Phys. Rev. D*, **58** 094002, 1998.
- [65] J.H. Kuhn and Z. Was. τ Decays to Five Mesons in TAUOLA. *ActaPhys.Polon.*, B39:147–158, 2008.
- [66] R. Jones and H. Schmickler. Introduction to beam instrumentation and diagnostics. In *Proceedings of CAS2003, Zeuthen, Germany*, page 75, 2003.
- [67] K. Melnikov and F. Petriello. The W boson production cross section at the LHC through $O(\alpha_s^2)$. *Phys. Rev. Lett.*, 96 231803, 2006.
- [68] N. Kidonakis and G. Sterman. Resummation for QCD hard scattering. *Nucl.Phys*, **B505**:321–348, 1997.
- [69] W. Kozanecki. Private communication.
- [70] R. Kwee. Inner detector based MinBias trigger. Talk given in ATLAS luminosity working group meeting, May 2008.
- [71] U. Langenfeld, S. Moch, and P. Uwer. Measuring the running top-quark mass. *Phys. Rev.*, D80:054009, 2009.
- [72] G.P. Lepage. A new algorithm for adaptive multidimensional integration. *Journal of Computational Physics*, **27**:192–203, 1978.
- [73] A.D. Martin, R.G. Roberts, W. J. Stirling, and R.S. Thorne. Parton distributions and the LHC: W and Z production. *Eur.Phys.J.*, **C14**:133–145, 2000.
- [74] C. J. Maxwell. Perturbative and non-perturbative QCD. In *IPM-LPH06 School and Conference, Tehran, Iran*, 2006.

- [75] N. E. Adam and V. Halyo and S. A. Yost. Evaluation of the theoretical uncertainties in the $Z \rightarrow l^+l^-$ cross sections at the LHC. *J. High Energy Phys.*, 05:62, 2008.
- [76] Y. Nambu. QCD and the string model. *Phys. Lett.*, **B80**:372, 1979.
- [77] P. Golonka and Z. Was. Next-to-leading logarithms and the PHOTOS Monte Carlo. *Eur. Phys. J.*, **C50**:53, 2007.
- [78] P. M. Nadolsky et al. Implications of CTEQ global analysis for collider observables. *Phys. Rev. D*, **78** 013004, 2008.
- [79] K. Prokifiev. Counting primary vertices in a bunch crossing. Talk given in ATLAS luminosity working group meeting, May 2008.
- [80] J. Pumplin, A. Belyaev, J. Huston, D. Stump, and W.K. Tung. Parton distributions and the strong coupling strength: Cteq6ab pdfs. *J. High Energy Phys.*, **0602**:032, 2006.
- [81] Q.-H. Cao and C.P. Yuan. Combined effect of QCD resummation and QED radiative correction to W boson observables at the Tevatron. *Phys. Rev. Lett.*, **93** 042001, 2004.
- [82] F. Ragusa and L. Rolandi. Tracking at LHC. *New J. Phys.*, **9**:336, 2007.
- [83] S. D. Ellis et al. Jets in hadron-hadron collisions. *Prog. Part. Nucl. Phys.*, **60**:484–551, 2008.
- [84] S. Frixione, P.Nason and B.R. Webber. Matching NLO QCD and parton showers in heavy flavor production. *J. High Energy Phys.*, 0308:7, 2003.
- [85] M. Schott, D. Froidevaux, and M. Boonekamp. Total inclusive W and Z boson cross-section measurements, cross-section ratios and combinations in the electron and muon decay channels at 7 TeV based on 300 nb⁻¹. ATL-COM-PHYS-2010-703, Geneva, 2010.
- [86] A. Sherstnev and R. S. Thorne. Parton distributions for LO generators. *The European Physical Journal C*, 5(4):553–575, 2008.
- [87] Smizanska, M. PythiaB: Interface to Pythia6 dedicated to simulation of beauty events. phys-ds.physics.lsa.umich.edu/docushare/dsweb/Get/Document-2010/g6.ps, 2003.
- [88] J. Snuverink. *The ATLAS Muon Spectrometer: Commissioning and Tracking*. PhD thesis, University of Twente, 2009. <http://www.nikhef.nl/jsnuverink/thesis.pdf>.

- [89] T. Atkinson. Reconstruction of electrons with the Gaussian-Sum filter in the ATLAS inner detector. In *Proceedings of the 52nd IEEE Nuclear Science Symposium and Medical Imaging Conference, Puerto Rico*, 2005.
- [90] T. Cornelissen et al. Concepts, Design and Implementation of the ATLAS New Tracking. ATL-SOFT-PUB-2007-007, Geneva, 2007.
- [91] G. 't Hooft and M.J.G. Veltman. Regularization and renormalization of gauge fields. *Nucl.Phys.*, **44**:189–213, 1972.
- [92] T. Sjostrand, S. Mrenna and P. Skands. PYTHIA 6.4: Physics and manual. *J. High Energy Phys.*, 05:26, 2006.
- [93] The ATLAS Collaboration. Charged particle multiplicities in pp interactions at $\sqrt{s} = 0.9$ and 7 TeV in a diffractive limited phase space measured with the ATLAS detector at the LHC and a new Pythia6 tune. ATL-CONF-2010-031, Geneva, 2010.
- [94] The ATLAS Collaboration. Luminosity Determination Using the ATLAS Detector. ATL-CONF-2010-060, Geneva, 2010.
- [95] The ATLAS Collaboration. Measurement of the $W \rightarrow \mu\nu$ and $Z \rightarrow \mu\mu$ production cross sections in proton-proton collisions at $\sqrt{s} = 7$ TeV with the ATLAS detector. 2010.
- [96] The ATLAS Collaboration. Performance of primary vertex reconstruction in proton-proton collisions at $\sqrt{s} = 7$ TeV in the ATLAS experiment. ATL-CONF-2010-069, Geneva, 2010.
- [97] The ATLAS Collaboration. The ATLAS Inner Detector commissioning and calibration. 2010.
- [98] The ATLAS Collaboration, G. Aad et al. The ATLAS Experiment at the CERN Large Hadron Collider. *Journal of Instrumentation*, 3 S08003, 2008.
- [99] The CMS and TOTEM Collaborations. Prospects for diffractive and forward physics at the LHC. Technical Report CERN/LHCC-2006-039/G-124, CERN, 2006.
- [100] The D0 Collaboration. Measurement of the muon charge asymmetry from W boson decays. *Phys. Rev. D*, **77** 011106(R), 2008.
- [101] The H1 Collaboration, I. Abt et al. The Tracking, calorimeter and muon detectors of the H1 experiment at HERA. *Nucl.Instrum.Meth.*, **A386**:348–396, 1997.

-
- [102] The TOTEM Collaboration. Diffraction and total cross-section at the Tevatron and the LHC. In *Proceedings of the Hadron Collider Physics Symposium 2005, Les Diablerets, Switzerland*, 2005.
- [103] A. Tricoli. Structure function measurements at LHC. In *Proceedings of Workshop on Implications of HERA for LHC Physics*, 2005.
- [104] V. Cindro et al. ATLAS beam conditions monitor. *Journal of Instrumentation*, 3 P02004, 2008.
- [105] V. Kartvelishvili. Electron bremsstrahlung recovery in ATLAS. *Nucl. Phys. B (Proc. Suppl.)*, **172**:208–211, 2007.
- [106] W. K. Tung et al. Heavy quark mass effects in deep inelastic scattering and global QCD analysis. *J. High Energy Phys.*, 0702:53, 2007.
- [107] W. Lampl et al. Calorimeter Clustering Algorithms: Description and Performance. ATL-LARG-PUB-2008-002, Geneva, 2008.
- [108] S. Weinberg. A theory of leptons. *Phys. Rev. Lett.*, **19**:1264, 1967.
- [109] F. Wilczek. QCD and asymptotic freedom: Perspectives and prospects. *Int.J.Mod.Phys.*, **A8**:1359–1382, 1993.
- [110] M. J. Woudstra. *Precision of the ATLAS muon spectrometer*. PhD thesis, University of Amsterdam, 2002.
- [111] The ZEUS and H1. Combined Measurement and QCD Analysis of the Inclusive ep Scattering Cross Sections at HERA. *JHEP*, 1001:109, 2010.